UNIVERSITY OF PAVIA
Department of Nuclear and Theoretical Physics

# WARP
# An argon double phase technique for dark matter search

External Refereee: Prof. E. Bellotti

Doctoral Thesis of
L. Grandi

Dottorato di Ricerca in Fisica XVII Ciclo

**Abstract**

One of the most intriguing puzzles of modern physics involves the dark matter problem. Several experimental observations, obtained through very different experimental techniques, both at galactic and cosmic scale, suggest that the majority of matter, whose total amount is somehow fixed by the observed gravitational potentials, is not visible. This dark matter, to coherently satisfy the experimental results should be constituted by nonbaryonic, cold, neutral and relic elementary particles, known with the name of WIMPs (Weakly Interacting Massive Particles). These particles could be in principle detectable through their possible interaction, although with a very low cross section, with ordinary matter, leading to the production within a target of nuclear recoils in the range up to 100 $keV$. The most promising WIMP candidate is represented by the Lightest Supersymmetric Particle (LSP) called, in the MSSM model, neutralino.

The WARP programme (WIMP ARgon Programme) belongs to the so-called direct detection experiments class and it proposes to use liquid argon as target for WIMPs search. In order to be sensitive to the expected tiny energy depositions and to be able to discriminate nuclear recoils, eventually generated by WIMPs scattering, from the dominant electromagnetic background, the standard Time Projection Chamber technique has been modified, foreseeing a gaseous region above the sensitive volume where luminous multiplication can occur. An interaction in the medium produces scintillation light and a certain amount of ionization: the application of opportune electric fields is used to drift a fraction of ionization electrons towards the liquid-gaseous interface, to extract and accelerate them in order to induce electroluminescence light. Photomultipliers are hence used to detect both prompt scintillation light and the delayed secondary light associated with ionization. The ratio between the two intensities can be used to discriminate the nature of the ionizing particle: a second and decoupled identification technique is provided by prompt scintillation signal shape analysis. These experimental techniques have been tested by the means of a 2.3 $l$ double phase argon chamber prototype providing extremely good background rejection power.

On the basis of the results a 100 $l$ sensitive volume chamber has been projected. Material selection and the use of active and passive shielding strongly

reduce the otherwise overwhelming background, mainly associated with neutrons and electromagnetically interacting particles (photons and electrons) coming from outside and from inner materials. The most dangerous surviving background component is represented by the $\beta$-emitter $^{39}Ar$; this radioactive isotope is present in liquid argon with a typical activity, within the detection window, of about 0.76 $Bq/kg\ of\ Ar$. This not negligible contamination, directly measured by the means of the prototype, implies very performing rejection powers, in order to reduce as much as possible the number of $\beta$-events mislabeled as nuclear recoil (obviously the discrimination techniques will start to fails at some level). If the combination of the two proposed identification techniques is able to provide a rejection power of the order of $10^{-7}$-$10^{-8}$ (as it seems possible), the surviving background events should be kept to a rate lower than 1 *event in* $10 \div 100$ *days*, leading to *the possibility of exploring WIMP-nucleon cross sections approximately two orders of magnitude lower than actual limits*. The proposed technique seems really promising mainly due to argon low cost and to the fact that its treatment is well supported even at industrial level: as a consequence huge mass detectors can be imagined, leading to tremendous increase of the sensitivity to WIMP search.

*To my beloved family*
*and to my sweet and patient Giada*

# Aknowledgements

First of all I would like to thank the I.N.F.N. and in particular the section of Pavia (administrative office, mechanical and electronic laboratories) for having supported the experimental R.&D. activity we have started about four years ago in the Pavia laboratory that has led to the proposal of the WARP experiment. At the same time I would like to thank also the direction of the National Laboratory of Gran Sasso for the helpfulness shown to host the WARP programme.

A number of people have played a crucial role in the experimental activity that has provided the results shown in this Ph.D. thesis. I would like to thank my supervisor Prof. C. Rubbia for the opportunities he gave me. A great thank to Doc. C. Montanari for the job done together, for his helpfulness and for his tenacity. For his approach to physics and for the interesting discussions I would like to thank also Doc. N. Ferrari. A thank also to the whole WARP collaboration and in particular to the Pavia group: thank to Prof. E. Calligarich and to Prof. M. Cambiaghi.

Together with my collaborators, a lot of other people should be thanked: they are my family, my girlfriend and all my friends. Each of them knows exactly the special role he plays in my life. Thank to everyone.

# Contents

# Preface

In this PhD thesis I have tried to summarize the main results of almost four years spent to characterize the behaviour of a double phase argon chamber with the ultimate aim to develop a high performance particle discrimination technique, useful even for tiny energy depositions, to be eventually exported to a larger sized detector for dark matter search. Like in each small $R\&D$ activity, I have had the fortune to face almost every aspect of this research from the hardware to the data analysis.

As far as the layout given to this PhD work, I have decided to be as much exhaustive as possible, trying to give the reader the elements to fully understand the liquid argon technology and to minutely explain the motivations that have suggested the various experimental choices. These guidelines could sometimes result as pedantic but, according to my personal taste, a detailed description of the work is more useful for those people trying to really get into the experimental problem. The reverse of the medal is that, at the same time, this work could result too detailed for readers just looking for the main experimental results. Trying to solve this problem I have inserted at the end of each chapter (apart from Chap. 5) a brief summary to focus the main information presented in the chapter itself.

Due to the chosen layout my personal and original contributions to this research are not clearly evident. For this reason I will try to explicit them within this small preface. As far as the experimental activity is concerned I have essentially followed, together with very few collaborators (to which few units have recently added), the whole history of the so-called 2.3 $l$ WARP prototype, from its birth $(2000-2001)$ till now. This means that I have taken part to the hardware realization of the prototype and to the study of its re-

sponse to various radioactive sources, performing the correlated data analysis (referred in the text as *phase I*). In the same way I have followed also the *phase II*, foreseeing the installation of the prototype at the National Laboratory of Gran Sasso, to study its behaviour in a low background environment. I have performed the data analysis onto the collected data, leading to the evaluation of the discrimination power. The whole Chap. 4 is dedicated to the description of this work including both experimental and data analysis contributions.

Differently from Chap. 1, containing essentially a review of the general dark matter problem, both Chap. 2 and 3 present some original contributions. They consist essentially in the application of some theoretical models to the argon case: in the former the expected behaviour of argon as target for WIMP detection has been investigated while, in the latter, the so-called Lindhard theory have been applied to the description of ionization processes in gaseous and liquid argon, later on used for the data analysis.

As far as the last chapter is concerned, it essentially consist of the description of a 100 *liters* double phase argon detector. It represents the final goal that has guided throughout these four years the $R\&D$ activity, whose results are at the basis of the proposed WARP experiment (WIMP ARgon Programme). I have given an active contribution to its realization and to the background estimate, apart from the implementation of Monte Carlo simulations.

Once again I would like to stress that due to the small dimension of the WARP collaboration my own work is the result of continuous mutual interactions with colleagues and viceversa.

# Chapter 1

# The dark matter

## 1.1 Introduction

Modern cosmology has become a frontier land between two branches of physics which were very different up to a few decades ago: on the one hand general relativity which tries to explain the evolution of the Universe considered as a perfect fluid, according to the Friedmann-Robertson-Walker model (FRM), on the other hand elementary particle physics which, together with the classical thermodynamics and the theory of nucleosynthesis, tries to justify the abundances of relic particles which could play a dominant role in the formation and evolution of the whole Universe. The various experimental confirmations regarding the theoretical predictions given by the above listed models makes them a kind of cosmological standard, so that in this work about the problem of dark matter, they will never be debated. Nevertheless it is necessary to underline that a different gravitational theory could explain and justify the experimental data which imply, in the framework of the relativity theory, the introduction of dark matter. For the purposes of the present work it is necessary to present the FRW-model before considering the dark matter subject. It should be noted that the equations of this chapter will be obtained in a system for which $c = \hbar = 1$.[1]

[1] In such system $[length] = [time] = [energy]^{-1}$.

## 1.2 The Friedmann-Robertson-Walker Model

### 1.2.1 The Robertson-Walker metric

The core of general relativity is represented by Einstein's equation

$$G_{ab} = 8\pi G T_{ab} \tag{1.1}$$

which describes the relationship between the curvature tensor $G_{ab}$ of the differentiable manifold $V$, called spacetime, and the energy contained in the spacetime itself represented by the stress-energy tensor $T_{ab}$. The spacetime curvature can be expressed as function of the metric defined on the tangent spaces to the $V$ manifold, every time it exist a connection which satisfies the Levi-Civita equation. Without analysing further details, this last relationship allows to associate to each metric a unique covariant derivative operator and hence a unique Ricci tensor $R_{ab}$. Thus Einstein's equation can be rewritten as function of the global metric $g_{ab}$[2] and, once specified the stress-energy tensor $T_{ab}$, re-conducted to a differential equations system in the $g_{ab}$ variables. The conditions imposed on the stress-energy tensor permit to describe very different physical systems and the FRW model is obtained by a particular set of these conditions.

As a first step one should define the properties of the left-hand side of Eq. 1.1 and hence choose an opportune metric able to satisfy the experimental observations. Although the entire life of our planet represents a very small portion of spacetime, according to the *copernican principle*, it seems logical to assume that the Earth position in the Universe is not privileged and, even if it were in another sector of the spacetime, it would be surrounded by a similar contest (*spatial homogeneity*). Then, it is equally logical to assume that the Universe is *isotropic* that is to say that, on a large scale, the observations done in the one or the other direction give similar results: these theoretical speculations are supported by experimental data regarding, as an example, the Cosmic Microwave Radiation (CMR).

The imposition of the mathematical conditions of homogeneity and isotropy on the spacetime metric is enough to uniquely define the feature of the so-called *Robertson-Walker metric*. A spacetime is called *spatially homogeneous* if it exist a one parameter family of hypersurfaces $\Sigma_t$ foiling it so that, for every $t$ and every couple of points $p$ and $q \in \Sigma_t$, an isomorphism of the $g_{ab}$ metric

[2]For the $g_{ab}$ metric the sign $-+++$ will be used from now onwards.

mapping $p$ into $q$ exists. This condition implies that for each instant of time $t$, every point of the Universe ($\Sigma_t$) is "equivalent" to another. The concept of *spatial isotropy* is instead defined requiring that for each point $p$ of the spacetime a timelike curve with tangent $u_p$ passes which belongs to a congruence and satisfies the following condition: for each $p$ and for each couple of vectors $s_1$ and $s_2$, normal to $u_p$, and belonging to the tangent space of the manifold in $p$, an isometry of the metric exists which lets $p$ and $u_p$ fixed while rotating $s_1$ and $s_2$. From the previous definition it follows that for a comoving observer[3] $\mathcal{O}$ with four-velocity $u_p$, it is impossible to select a privileged spatial direction: every direction $s_1 \in \Sigma_t$ (for construction normal to $u_p$) is equivalent to another $s_2$. The request of homogeneity and isotropy implies that the tridimensional space is at a constant curvature, in other words the Riemann tensor ${R_{abc}}^d$, derived from the $h_{ab}$ metric induced on $\Sigma_t$ by $g_{ab}$, satisfies the equation

$$R_{abcd} = K h_{c[a} h_{b]d} \tag{1.2}$$

with $K$ constant.[4] As a consequence of the *Eisenhart theorem*, which demonstrates that *two spaces at constant curvature with the same dimension, the same metric sign and the same $K$, are locally isotropic*, it is possible to describe the geometry of an hypersurface $\Sigma_t$ with curvature $K$, introducing space with the same $K$ value but easier to be visualized. On the basis of the $K$ sign, the three possible solutions are:

- $K > 0$: all the positive values of $K$ can be obtained from a three-sphere $\mathcal{S}^3$ considered as a surface in the Euclidean space $\mathcal{R}^4$ which satisfies the equation

  $$x^2 + y^2 + z^2 + w^2 = R^2. \tag{1.3}$$

  The metric, expressed in spherical coordinates, from which to derive the Riemann tensor satisfying the condition expressed in Eq. 1.2, results to be, for a unitary radius sphere,

  $$ds^2 = d\psi^2 + \sin^2\psi(d\theta^2 + \sin^2\theta d\phi^2). \tag{1.4}$$

[3] This is a special observer, at rest with respect to surrounding matter. This requisite is necessary since otherwise it would see an anisotropic distribution of velocity and it could select a privileged direction.

[4] It is necessary to underline that the quantities now introduced ($K$, $h_{ab}$, $R_{abcd}$) refer only to the tridimensional space $\Sigma_t$ which can be obtained by spacetime with fixed $t$.

- $K = 0$: this value can be obtained from a tridimensional flat space ($\mathcal{R}^3$) whose metric, expressed in cartesian coordinates, is given by

$$ds^2 = dx^2 + dy^2 + dz^2. \tag{1.5}$$

- $K < 0$: all the negative values of the curvature constant can be obtained from the tridimensional hyperboloids ($\mathcal{H}^3$) defined as surfaces in a four-dimensional space with a Lorentzian signature which satisfy the equation

$$t^2 - x^2 - y^2 - z^2 = R^2. \tag{1.6}$$

  In case of a unitary hyperboloid the metric can be expressed as

$$ds^2 = d\psi^2 + \sinh^2\psi(d\theta^2 + \sin^2\theta d\phi^2). \tag{1.7}$$

The global spacetime metric $g_{ab}$, once isotropy and homogeneity conditions are imposed, can be expressed as

$$g_{ab} = -u_a u_b + h_{ab}(t) \tag{1.8}$$

where for each $t$ the space metric $h_{ab}(t)$ defined on $\Sigma_t$ could be that of a three-sphere (*close Universe*), of an hyperboloid (*open Universe*) or of an Eucledian space (*flat Universe*). The adjectives *close* and *open* refer to the spatial compactness of the described spacetime manifold. For a comoving observer with proper time $\tau$, the *Robertson-Walker spacetime metric* can be expressed as

$$ds^2 = -d\tau^2 + a^2(\tau)\begin{cases} d\psi^2 + \sin^2\psi(d\theta^2 + \sin^2\theta d\phi^2) \\ dx^2 + dy^2 + dz^2 \\ d\psi^2 + \sinh^2\psi(d\theta^2 + \sin^2\theta d\phi^2) \end{cases} \tag{1.9}$$

or alternatively, in a more compact way, as

$$ds^2 = -d\tau^2 + a^2(\tau)\left[\frac{dr^2}{1-kr^2} + r^2(d\theta^2 + \sin^2\theta d\phi^2)\right]. \tag{1.10}$$

where $a(\tau)$ is the cosmic scale factor (which has the dimension of a length), $r$ is a the dimensionless coordinate whose value is contained within the $[0, 1]$ range and $k$ is a parameter associated with the $K$ curvature constant opportunely re-scaled (the conditions $K > 0, K = 0, K < 0$ correspond to $k = +1, k = 0, k = -1$). One should observe that homogeneity and isotropy imply that the spatial metric could be mapped only locally in that of $\mathcal{S}^3, \mathcal{R}^3$ or $\mathcal{H}^3$, while the space properties can globally be very different and present more complex topological defects.

### 1.2.2 The Friedmann Model

The assumptions done in the previous section allow to explicitly express the metric of a Universe satisfying the *cosmological principle*[5]: this metric, besides having three different forms for the three different scenarios, depends on the arbitrary positive function $a(\tau)$. The choice of the stress-energy tensor properties, and hence the selection of a particular matter and energy distribution in the Universe, permit to describe, through Eq. 1.1, the behaviour of $a(\tau)$ and consequently to uniquely define the spacetime geometry.

As first step, one could suppose that the whole energy of the Universe is contained in ordinary matter or it exists as radiation: in this case the identification of the Universe with a perfect fluid would permit to solve, with good approximation, the Einstein's equation. In the case of perfect fluid the stress-energy tensor can be expressed as

$$T_{ab} = \rho u_a u_b + P(g_{ab} + u_a u_b) \tag{1.11}$$

where $\rho$ is the matter or radiation density, $P$ the pressure and $u_a$ the unit fluid four-velocity, tangent to the world lines and hence a timelike vector ($g_{ab}u^a u^b = -1$). One should note that due to the selected form of the perfect fluid as well to the requests on the metric (Robertson-Walker), the "time-space" components of the resulting Einstein's equation have to vanish exactly as those off-diagonal "space-space", while the diagonal "space-space" components reduce to the same equation. As a consequence of the a priori system of 10 equations only 2 equations result linear independent. At this point, considering that

$$G_{ab} = R_{ab} - \frac{1}{2} g_{ab}\mathcal{R} \tag{1.12}$$

it is possible to express Einstein tensor as function of Ricci tensor $R_{ab}$ and of the Ricci scalar $\mathcal{R}$ and so as function of the ordinary Christoffel symbols $\Gamma^a{}_{bc}$ associated with Levi-Civita connection. Once the computation of these symbols (depending only on the spacetime metric) is performed, one can make explicit the "time-time" and "space-space" components of the Ricci tensor, respectively $R_{\tau\tau} = R_{ab}u^a u^b$ and $R_{**} = R_{ab}s^a s^b$ with $s^a$ unit vector, for construction, normal to $u^a$ and spacelike, as

$$R_{\tau\tau} = -3\frac{\ddot{a}}{a} \tag{1.13}$$

[5]With this name the hypothesis of homogeneity and of spacetime previously defined is indicated.

$$R_{**} = \left[\frac{\ddot{a}}{a} + 2\frac{\dot{a}^2}{a^2} + \frac{2k}{a^2}\right] \tag{1.14}$$

and the Ricci scalar

$$\mathcal{R} = 6\left[\frac{\ddot{a}}{a} + \frac{\dot{a}^2}{a^2} + \frac{k}{a^2}\right] \tag{1.15}$$

where $\dot{a} \equiv da/d\tau$ and $\ddot{a} \equiv d^2a/d\tau^2$. Inserting Eq. 1.12 into Eq. 1.1 one obtains, for the consideration made above, the two following linear independent equations

$$G_{\tau\tau} = 8\pi G\rho \tag{1.16}$$

$$G_{**} = 8\pi GP \tag{1.17}$$

with obvious meaning of the nomenclature. Inserting Eq. 1.13, 1.14, 1.15 into Eq. 1.12 and substituting the so obtained expression into Eq. 1.16, 1.17, one obtains for a perfect fluid the expressions

$$\frac{\dot{a}^2}{a^2} + \frac{k}{a^2} = \frac{8\pi G}{3}\rho \tag{1.18}$$

$$2\frac{\ddot{a}}{a} + \frac{\dot{a}^2}{a^2} + \frac{k}{a^2} = -8\pi GP \tag{1.19}$$

known as *Friedmann equations*. The subtraction of these two equations provides

$$3\frac{\ddot{a}}{a} = -4\pi G(\rho + 3P) \tag{1.20}$$

which describes the behaviour of $\ddot{a}$ acceleration as function of the density and pressure of the Universe treated as perfect fluid. From this last equation one obtains that, if $\rho > 0$ and $P \geq 0$, the Universe could not be static: indeed these conditions are sufficient to obtain $\ddot{a} < 0$ and, according to the Friedmann model, the Universe would have always been in expansion ($\dot{a} > 0$) or in contraction ($\dot{a} < 0$). Phisically this means that the distance between two isotropic observers changes with time, but a "centre" of expansion or contraction do not exist; for these observers the distance variation is expressed as function of time by

$$\frac{dR}{d\tau} = \frac{R}{a}\frac{da}{d\tau} = HR \tag{1.21}$$

and so the evolution of the Universe is led by the quantity $H \equiv \dot{a}/a$ called Hubble parameter [6]. Equation 1.18 can be rewritten as function of the new parameter $\Omega$ defined by the following expression

$$\Omega - 1 \equiv \frac{\rho}{\rho_c} - 1 = \frac{k}{H^2R^2} \tag{1.22}$$

[6] This quantity is function of time.

with $\Omega \equiv \rho/\rho_c$ and $\rho_c = 3H^2/8\pi G$ called *critical density*. Since in Eq. 1.22 $H^2R^2 > 0$, the sign of the curvature parameter $k$ is reflected in the sign of $\Omega - 1$ and consequently

$$\begin{aligned} k = +1 &\implies \Omega > 1 \\ k = 0 &\implies \Omega = 1 \\ k = -1 &\implies \Omega < 1. \end{aligned}$$

In the context of the FRW model here presented, it is possible to define the parameter of deceleration of the Universe [7]

$$q_0 = -\frac{\ddot{a}(\tau_0)}{a(\tau_0)H_0^2} \tag{1.23}$$

which can be rewritten through Eq. 1.20 as

$$q_0 = \frac{\Omega}{2}\left(1 + 3\frac{P}{\rho}\right). \tag{1.24}$$

At this point the *Bianchi identity* expressed by

$$\nabla_a T^a_{\ b} = 0, \tag{1.25}$$

where with the symbol $\nabla$ the covariant derivative operator is indicated, can be imposed: it represents a necessary condition that the stress-energy tensor must satisfy so that Eq. 1.1 can be solved. Considering the $0 - 0$ component of the above equation, one obtains

$$\partial_0 \rho - 3\frac{\dot{a}}{a}(\rho + P) = 0 \tag{1.26}$$

which can be rewritten, imposing the perfect fluid equation of state $P = \omega\rho$, as

$$\frac{\dot{\rho}}{\rho} = -3(1 + \omega)\frac{\dot{a}}{a} \tag{1.27}$$

which, once integrated, leads to the relationship

$$\rho \propto a^{-3(1+\omega)}. \tag{1.28}$$

It is evident that the choice of a particular equation of state, and so of a particular model of cosmological fluid, influences heavily the evolution of the Universe, modifying the behaviour of $\rho$ and $q_0$ through Eq. 1.24 and Eq. 1.28.

[7] The subscript 0 indicates that the variables values are calculated at present time.

To make more immediate the following discussion it is convenient to define the quantities

$$\Omega_{lum} \equiv \frac{\rho_{lum}}{\rho_c} \tag{1.29}$$

$$\Omega_M \equiv \frac{\rho_M}{\rho_c} \tag{1.30}$$

$$\Omega_\Lambda \equiv \frac{\rho_\Lambda}{\rho_c} \tag{1.31}$$

where $\Omega_{lum}$, $\Omega_M$ and $\Omega_\Lambda$ refers respectively to cosmic density contributions associated with optically luminous matter, by ordinary matter and radiation and by the vacuum energy. For construction these quantity are connected by the relations

$$\Omega_{tot} = \Omega_\Lambda + \Omega_M \tag{1.32}$$

and

$$\Omega_{lum} \leqslant \Omega_M. \tag{1.33}$$

A first example of fluid is represented by the so called *dust model* or *matter dominated model* ($\Omega_{tot} = \Omega_M = \Omega_{mat}$): if the energy and mass of the Universe were represented only by the visible matter, every galaxy could be considered as a kind of speck of dust (from here the name) with kinetic energy negligible compared to the density of the total energy. In this kind of model the fluid pressure could be considered null ($\omega = 0$) and from Eq. 1.24 and 1.28 one can obtain the conditions

$$\rho \propto a^{-3} \qquad q_0 = \frac{\Omega_{mat,0}}{2}. \tag{1.34}$$

On the contrary, supposing a Universe dominated only by radiation (radiation dominated model with $\Omega_{tot} = \Omega_M = \Omega_{rad}$), represented by the state equation $P = \frac{1}{3}\rho$, one can obtain

$$\rho \propto a^{-4} \qquad q_0 = \Omega_{rad,0}. \tag{1.35}$$

Both these scenarios suggest the idea of a decelerating Universe. What described by Eq. 1.34 and 1.35 can be justified physically by observing the numerical density $n$ of the galaxies decreases with the increasing of the volume ($\propto a^3$); in the dust model the energy density coincides with the density of the galactic rest energy, which is proportional to $n$ and so to $a^{-3}$. Something similar happens for the radiation dominated model in which the energy density

is linked to the numerical density of the photons and to their energy: the first term has behaviour identical to that indicated above ($\propto a^{-3}$), the second one, because of the gravitational redshift, decreases with the increasing of the cosmologiacl scale factor as $a^{-1}$, from which the behaviour indicated by Eq. 1.35 derives.

To these two scenarios which can be defined "classical" a third one, linked to a generalization of Eq. 1.1 can be added. Einstein himself, to guarantee a static Universe as he thought it was, transformed his equation into

$$G_{ab} + \Lambda g_{ab} = 8\pi G T_{ab} \tag{1.36}$$

adding a further term constant and proportional to the metric. This term, rejected later on due to the experimental data which suggested a Universe in espansion, has been then reconsidered by modern cosmologists, but with a different meaning: this factor once reinserted on the right hand side of Eq. 1.1 as

$$G_{ab} = 8\pi G T_{ab} - \Lambda g_{ab} = 8\pi G (T_{ab} + T^{vac}_{ab}) \tag{1.37}$$

behaves like a source term characterized by a stress-tensor

$$T^{vac}_{ab} = -\frac{\Lambda}{8\pi G} g_{ab}, \tag{1.38}$$

curving the spacetime even in absence of ordinary forms of energy/matter ($T_{ab} = 0$)[8]: from here the name of *vacuum energy*. From the mathematical point of view the tensor represented in Eq. 1.38 coincides with that of a perfect fluid with $P = -\rho = -\frac{\Lambda}{8\pi G}$ ($\omega = -1$) and with $\Lambda > 0$. As a consequence together with the matter and radiation dominated models, one can imagined a Universe dominated by the vacuum energy, characterized by $\Omega_\Lambda$. In such condition, recalling Eq. 1.20 and assuming only vacuum energy exists ($P = -\rho = -\frac{\Lambda}{8\pi G}$), one obtains a positive $\ddot{a}/a$, since $\Lambda > 0$, and hence a Universe in accelerated expansion. In general such behaviour can only be obtained, within the FRW model, assuming a perfect fluid with $\omega < -1/3$. One should note that the Friedmann equation (Eq. 1.20) is frequently expressed as

$$\frac{\ddot{a}}{a} = -\frac{4\pi G}{3}(\rho_M + 3P_M) + \frac{\Lambda}{3}. \tag{1.39}$$

where the matter/radiation and the vacuum energy contributions have been explicitly factorized.

[8] In order to reconsider the Newtonian mechanics as limit for weak fields of the relativvistic theory so modified, it is necessary that $\Lambda$ has low values.

At this point it can be interesting to describe the behaviour of $a$ as function of $\tau$ in the three different scenarios. Let's consider the matter dominated model: defining the parameter $\phi$ the three different configurations are represented by [1]

$$\begin{cases} a = \frac{C}{2}(\cosh\phi - 1) \\ t = \frac{C}{2}(\sinh\phi - \phi) \end{cases} \qquad k = -1 \tag{1.40}$$

$$a = \left(\frac{9C}{4}\right)^{\frac{1}{3}} t^{\frac{2}{3}} \qquad k = 0 \tag{1.41}$$

$$\begin{cases} a = \frac{C}{2}(1 - cos\phi) \\ t = \frac{C}{2}(\psi - \sin\phi) \end{cases} \qquad k = +1 \tag{1.42}$$

with $C = \frac{8\pi G}{3}\rho a^3 = cost.$ Similarly in the radiation dominated model one obtaines

$$a = \sqrt{C'}\left[\left(1 + \frac{t}{\sqrt{C'}}\right)^2 - 1\right]^{\frac{1}{2}} \qquad k = -1 \tag{1.43}$$

$$a = (4C^{'})^{\frac{1}{4}} t^{\frac{1}{2}} \qquad k = 0 \tag{1.44}$$

$$a = \sqrt{C'}\left[1 - \left(1 - \frac{t}{\sqrt{C'}}\right)^2\right]^{\frac{1}{2}} \qquad k = +1. \tag{1.45}$$

These behaviours are sketched in Fig. 1.1. It is to observe that in both the scenarios a flat Universe follows the same evolution independently if it is filled with radiation or matter. Similar consideration can be applied in case of open or close Universe. Different is, instead, the behaviour of a vacuum energy dominated Universe (energy characterized by an equation of state with $\omega 1 = -1$). Since only the $\Lambda > 0$ condition has been imposed for construction, only one metric, instead of three, is provided by the Friedmann-Robertson-Walker model. This metric is usually known with the name of De-Sitter and it can be written as

$$ds^2 = -d\tau^2 + e^{2H_\Lambda \tau}[dr^2 + r^2 d\Omega]. \tag{1.46}$$

and, as stressed above, it describes a Universe in accelerated expansion.

The limit cases previously presented are in principle different from the physical reality which is described by their superposition: only the experimental data regarding the different cosmological parameters can allow to determine the dominant contributions of such a superposition. However, it

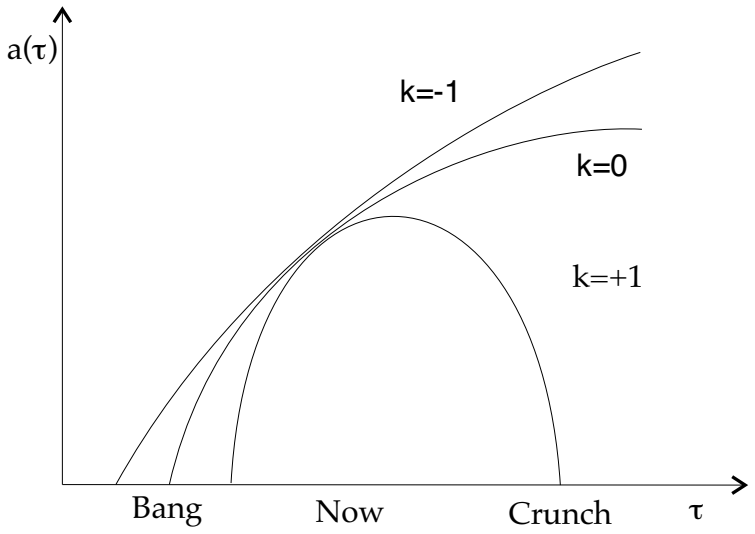


Figure 1.1: Behaviour of $a$ as function of time $\tau$ in a matter and radiation dominated Universe [1].

could be interesting to observe the different behaviours followed by the energy density linked to the single contributions:

$$\begin{aligned} \textit{Radiation Dominated}(p=\tfrac{1}{3}\rho) &\implies \rho \propto a^{-4} \\ \textit{Matter Dominated}(p=0) &\implies \rho \propto a^{-3} \\ \textit{Vacuum Dominated}(p=-\rho) &\implies \rho \propto \textit{cost.} \end{aligned} \tag{1.47}$$

The different behaviours described above let us suppose that the contribution of radiation was dominant in the first minutes of the life of the Universe[9] and that the vacuum term will start to dominate with the increasing of $a$, in the hypothesis that the Universe continues to expand.

## 1.3 The dark matter puzzle

As presented in the previous section, the evolution of the Universe, according to the Friedmann-Robertson-Walker model, is led by the quantity $\Omega_{tot}$,

[9] For this consideration it has been supposed that $\dot{a}(\tau_0) > 0$, that is to say that the positive function $a(\tau)$ is increasing, too: this supposition is confirmed by a lot of experimental data which support the hypothesis of a Universe in expansion.

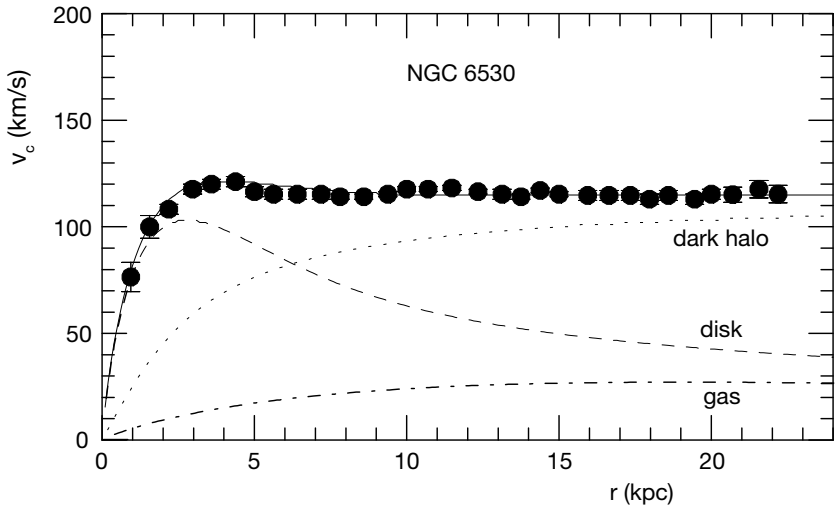


Figure 1.2: Rotation curve of the spiral galaxy NGC 6503 [4, 5]. The lines indicate the contributions from the galactic disk (dotted line), the gas (dot-dashed line) and the dark halo (dashed line), this last necessary to reproduce the observed experimental curve. The solid line stands for the combination of them all.

representing the total amount of energy contained in the spacetime, and by the nature of this energy; the knowledge of the value of this parameter would permit, through Eq. 1.22, to determine the spacetime geometry and so the future behaviour of the Universe. In the last few decades, a lot of experiments have tried to give a solution to this problem but bringing with themselves a lot of questions: a lot of observations in the context of the standard gravitational theory suggest the existence of a non-visible mass on galactic and cosmic scale [2]. According to these data the so called visible mass, the visible mass associated with ordinary matter, would not be sufficient to explain problems such as the dynamics of the galaxies and clusters and, consequently, the present structure of the Universe. From here the necessity of hypothesizing that a large fraction of the total matter of the Universe is not visible and hence *dark*. It is necessary to underline that, in principle, the *dark matter* could have different natures in each of the different studied scenarios (galactic, cluster and cosmic level).

First of all the dark matter problem inside the galaxy has to be considered. The flatness at large radii of rotation curves of spiral galaxies implies a distribution of the mass contained inside them quite different from that described

by their visible mass (see Fig. 1.2). This consideration can be reformulated strictlier by referring, for simplicity, to the Newtonian mechanics: the motion of a mass $m$ which moves with circular velocity $v$ at a distance $r$ from the centre of the galaxy is described by

$$M(r) = v^2 r \tag{1.48}$$

where $M(r)$ represents the mass of the galaxy contained in an ideal sphere with radius $r$. If the total mass of the galaxy $M_{tot}$ were represented only by the visible mass, for values $r > r_{lum}$ it assumes an almost constant value

$$M(r) = M_{tot} \cong M(r_{lum}) \tag{1.49}$$

leading through Eq. 1.48 to a circular velocity $v$ proportional to $r^{-\frac{1}{2}}$ for $r > r_{lum}$. This expected behavior is completely disproved by the experimental data obtained by observing the 21 *cm* emission line of the hydrogen clouds at a great distance from the galactic centre, providing instead a value of $v \approx cost$ (see Fig. 1.2) and suggesting a $M(r) \propto r$ even at large radii. This discrepancy could be wiped out if a not visible matter halo, characterized by density profile $\rho_\chi(r)$ dropping as $r^{-\frac{1}{2}}$ for large radii ($r > r_{vis}$), is supposed[10]. This kind of behaviour is provided by a set of models called *isothermal* describing a system of particles of mass $m_\chi$ interacting only gravitationally and in thermal equilibrium. The simplest of this model, for which spherical symmetry and isotropy are assumed, provides a density profile

$$\rho_\chi(r) \propto \frac{1}{r^2 + a^2} \tag{1.50}$$

where $a$ is called the core radius and it is used to keep finite the dark matter density at small distance from the galactic centre. The above considerations applies to a very large number of spiral galaxies [3] and obviously to the Milky Way, treated in more details in Sec. 1.3.3. Summing up the contributions coming from galaxies, the amount of matter contained in the Universe has been evaluated to be $\Omega_M \approx 0.2\text{-}0.3$ [6]. As stressed before only a small fraction of this quantity is visible ($\Omega_{lum} \approx 4.95 \times 10^{-3}$).

Moving to large scales, evidence for dark matter can be found in cluster of galaxies through gravitational lensing, $X$-rays emission and relative motion of

[10] To provide $M(r) \propto r$ and hence a circular velocity flat at large radii, it is necessary to assume a spherical halo (whose volume increases as $r^3$) with a density profile $\rho_\chi \propto r^{-2}$.

galaxies measurements. As far as the the gravitational dynamics of galaxies within clusters is concerned, measurements on approximately 100 clusters have been performed [7]. Following this approach each galaxy of the cluster is considered as a test mass for deducing the gravitational potential: their dispersion velocities, under the assumption of virialization, suggest that the potential is generated by a total mass higher than the visible one. If the cluster, representing the largest self-gravitating structure in nature, is considered as representative of the Universe, the measurements suggests an $\Omega_M \approx 0.2\text{-}0.4$ [6] once again much more than the cosmological amount of visible matter provided by $\Omega_{lum}$. A similar value can be obtained through $X$-rays measurements: a large amount of ionized gas is always present in cluster leading, through bremsstrahlung processes, to the emission of $X$-rays [6]. The total mass of the cluster, under the assumption of hydrostatic equilibrium, can be expressed as function of the ionized gas temperature and density profiles, intrinsically connected to the $X$-rays luminous density. Following this approach it is possible to express the total mass of the cluster as a function of $X$-rays maps provided by several experiments such as CHANDRA [8] and ROSAT [9]. The results obtained from the independent measurements performed on galactic and higher scales structures seem to be in good agreement, suggesting that the majority of the dark matter is clustered around galaxies and not diffused in the space between them.

Finally, before going on, it is necessary to analyze the role of dark matter on cosmic scale. The theory of Big Bang foresees the existence of the so called Cosmic Microwave Radiation (CMB) associated to photons, whose wavelength has modified due to the Universe expansion, that decoupled from matter approximately when the Universe was $3 \times 10^5\ yr$ old (when recombination occurred). The measurement of the anisotropy of this radiation can be used to extract information about the composition of the Universe (in terms of $\Omega$ parameters) at the moment of decoupling. Through the analysis of the experimental CMB anisotropy power spectrum, performed by several experiments such as BOOMERANG [10], WMAP [11] and MAXIMA [12], one obtains from the position of the first acoustic peak

$$\Omega_{tot} \equiv \Omega_\Lambda + \Omega_M \approx 1 \tag{1.51}$$

corresponding to a flat Universe and from the ratio between the amplitude of the first and second acoustic peak

$$\Omega_B \approx 0.045 \tag{1.52}$$

where $\Omega_B$ represents the component to cosmic density associated with ordinary (baryonic) matter. It is interesting to observe that as far as the cosmic radiation is concerned, its overall contribution leads to $\Omega_{CMB} \approx 4.9 \times 10^{-5}$ obviously negligible if compared to the other nowadays components: the radiation can hence be ruled out in the following considerations concerning the present composition of the Universe. A second fundamental global measurement on cosmological scale has been performed by studying the expansion of the Universe through the use of so-called standard candles, in other words astronomical objects whose luminosity is known: this properties permits to determine the distance of such object by comparing the measured luminosity to the total luminosity. The *supernovae* Ia belongs to this class and a large sample of them has been studied leading to the condition [13, 14]

$$\Omega_\Lambda \approx 1.33\Omega_M + 0.33 \tag{1.53}$$

suggesting a Universe in accelerated expansion dominated by vacuum energy component. As soon as the above mentioned results, provided by very different experimental techniques, are compared an incredible concordancy is obtained, providing the following consistent cosmological scenario characterized by

$$\Omega_\Lambda \approx 0.71 \qquad \Omega_M \approx 0.29 \tag{1.54}$$

leading to the conclusion that, since $\Omega_{lum} \approx 4.95 \times 10^{-3}$ and $\Omega_{rad}$ is negligible, almost the totality of clustered energy (under the form of matter) is constituted by non-visible (dark) matter. A much more striking implication following from Eq. 1.52 is that about 86% of the dark matter has to be non-baryonic and hence it has to be *exotic* matter: in other words it should be represented by a particles with zero baryonic number and neutral, otherwise their direct coupling with photons would make them visible. This result provided by CMB measurement is ulteriorly strengthened by the experimental observations of elements abundance in stars. The comparison between them suggest that the actual measured abundances of elements are very well reproduced if it is assumed that in the early Universe not only Hydrogen was present but also Helium ($^3He$ and $^4He$), Deuterium ($^2H$) and Lithium ($^7Li$)

in opportune ratios. Such primordial presence of light nuclei is foreseen by the Big Bang model and in particular by the so-called primordial nucleosynthesis: according to it, light nuclei should have formed in the first minutes of life of the Universe and their abundance depends on the baryon density $\rho_B$. The measurement of light elements abundance in stars, in particular of Deuterium (for which no astrophysical creation mechanism is known), can be used to uniquely determine the baryonic component $\Omega_B \approx 0.04$-$0.05$ [6] in very good agreement with CMB measurements. The above scenario is also in good agreement with the local measurements concerning dark matter in galaxy and cluster of galaxies.

As far as vacuum energy is concerned, at the moment its nature is completely obscure. From the theoretical point of view several theories have been proposed attributing the above introduced negative pressure term not only to a cosmological constant, and hence to vacuum energy (as treated above), but also to scalar slowly variable fields (quintessence) [15]. In these last cases the $\Omega_\Lambda$ term does not refer to vacuum and hence it is more generally called *dark energy*. Nevertheless, independently from its real nature, it is necessary to observe that due to its negative pressure, this object feels a negative self-gravity and hence, differently from ordinary matter, it tends to be uniformly distributed in all the Universe. As a consequence its contribution within the galaxies has to be considered definitely negligible and hence it could not solve by itself the dark matter puzzle.

As stressed before the majority of dark matter has to be nonbaryonic in order to explain the experimental observations from galactic up to cosmic scale. Nevertheless the comparison between the results from nucleosynthesis and CMB with the observed (optically) luminous matter suggests that some baryonic dark matter should exist. At the moment approximately 10% of the expected total baryon density constitutes the luminous contribution, 40% is represented by ionized gas in the intergalactic space within clusters while the remaining 50% is dark. Several candidates for baryonic dark matter have been proposed and the most significant are represented by cold molecular hydrogen clouds and by the MACHOs class (Massive Compact Halo objects) [6]. As far as $H_2$ clouds are concerned, differently from atomic hydrogen clouds they are not easily detectable since they do not present the characteristic 21 $cm$ emission line and often, according to their temperature, they do not emit any radiation at all [6]. As regards MACHOs, this class contains a large quantity

of astronomical objects whose luminosity is somehow reduced, making them difficult to be detected (dark). Neutron stars, brown/white/red/beige dwarf and black holes belong to this category. Among them the most promising are brown and beige dwarf: these objects are stars with a temperature below the hydrogen fusion threshold. They essentially differ for their allowed masses that should be resplectively lower than 0.11 $M_\odot$ and 0.3 $M_\odot$[11]. Their evolution is essentially characterized by a cooling down process, occurring through the emission of infrared radiation (impossible to be detected).

### 1.3.1 Nonbaryonic candidates

In the previous sections it has been shown that, to justify several experimental observations, one has to assume that dark matter exists and that it is neutral and nonbaryonic, in other words it has to be constituted by a species of elementary particles with zero baryonic number. It is natural to assume, in the framework of Big Bang theory, that this species, like most of the Universe constituents in its early moments, were at thermal equilibrium with the others but, to provide a not negligible abundance and hence to play the requested role at cosmological level ($\Omega_M \approx 0.3$), it is necessary to suppose that this species has already decoupled. If dark matter particles were not relic, that is to say they were still at thermal equilibrium, their present abundance $Y_\chi$ given by [2, 16]

$$Y_\chi \equiv \frac{n_\chi}{s} \approx \left(\frac{m_\chi}{T}\right)^{\frac{3}{2}} e^{-\frac{m_\chi}{T}} \tag{1.55}$$

with $n_\chi$ species $\chi$ numerical density and $s$ entropy density, would be negligible, being the exponential term dominant for small $T$[12]. On the contrary if the decoupling had happened for a temperature $T \approx m_\chi$, the species could present a non negligible relic abundance. Let's consider, for example, a species $\chi$ stable or with an average lifetime higher than the age of the Universe: if this is not the case these particles would already have decayed and hence their abundance would be negligible. In such a condition the reactions which could substantially alterate the number of species would be annihilation and the opposite process

$$\chi\overline{\chi} \rightleftharpoons X\overline{X} \tag{1.56}$$

[11] The symbol $M_\odot$ refers to the sun mass.

[12] The quantity $Y_\chi$ has been introduced to express the particle density in a way independent from the Universe expansion.

where $X$ stands for the different species in which $\chi$ can annihilate. The time evolution of the species density, supposing all the species $X$ in thermal equilibrium with each other[13], is described by the Boltzmann equation in general form

$$\hat{\mathbf{L}}[f] = \hat{\mathbf{C}}[f] \tag{1.57}$$

where $\hat{\mathbf{L}}$ indicates the Liouville operator, $\hat{\mathbf{C}}$ the collision operator which contains the scattering matrixes for the different possible interactions and the distribution function in the phase space $f(p^\mu, x^\mu)$. By expliciting for the RW metric the left operator of Eq. 1.57 one obtains

$$\frac{dn_\chi}{d\tau} + 3\frac{\dot{a}}{a}n_\chi = \frac{1}{(2\pi)^3}\int \hat{\mathbf{C}}\frac{d^3p}{E} \tag{1.58}$$

with $E$ and $p$ respectively energy and moment, and, from the equilibrium conditions,

$$\frac{dn_\chi}{d\tau} + 3Hn_\chi = -\langle\sigma_{\chi\overline{\chi}\to X\overline{X}}|v|\rangle\left[n_\chi^2 - (n_\chi^{eq})^2\right] \tag{1.59}$$

with $n_\chi^{eq}$ numerical density of the $\chi$ species at equilibrium and $\langle\sigma_{\chi\overline{\chi}\to X\overline{X}}|v|\rangle$ thermal average of the product of the velocity for the cross section of each single annihilation section. Summing up on all the channels and introducing the total annihilation cross section $\sigma_A$[14], Eq. 1.59 leads to

$$\frac{dn_\chi}{d\tau} + 3Hn_\chi = -\langle\sigma_A|v|\rangle\left[n_\chi^2 - (n_\chi^{eq})^2\right] \tag{1.60}$$

or, alternatively,

$$\frac{dY_\chi}{dx} = -\frac{x\langle\sigma_A|v|\rangle s}{H(m)}\left[Y_\chi^2 - (Y_\chi^{eq})^2\right] \tag{1.61}$$

with $x \equiv m_\chi/T$ and $H(m_\chi) \equiv x^2H(T)$, where $H(T)$ is the Hubble constant expressed as function of the temperature. The Eq. 1.60 is easy to be interpreted: the term $3Hn_\chi$ represents the Universe expansion, the term proportional to $n_\chi$ is associated with the $\chi$ species annihilation and so to its decreasing, while the term containing $n_\chi^{eq}$ is associated with the $\chi$ species creation $\chi$ through the opposite process. In absence of interactions able to change the numerical density of a species, the density expressed by Eq. 1.60 would evolve as $a^{-3}$ as provided previously by the Friedmann equations. Defining the total

[13] This request coincides with the request that the interactions among the species $X$ are stronger than the interaction with $\chi$.

[14] This term contains also annihilation into final states more general then two-body

annihilation rate $\Gamma_A \equiv n_\chi^{eq}\langle\sigma_A|v|\rangle$, Eq. 1.61 can be re-expressed a

$$\frac{x}{Y_\chi^{eq}}\frac{dY_\chi}{dx} = -\frac{\Gamma_A}{H}\left[\left(\frac{Y_\chi}{Y_\chi^{eq}}\right)^2 - 1\right] \tag{1.62}$$

from which it is evident that the process is dominated by the relationship $\Gamma_A/H$, which compares the annihilation rate with the expansion rate. At this point it is necessary to introduce a clear distinction between extremely relativistic species and the non relativistic ones. According to the kinematical conditions the expression[15]

$$n_\chi = \frac{g}{2\pi^2}\int_{m_\chi}^{\infty}\frac{(E^2 - m_\chi^2)^{\frac{1}{2}}}{e^{\frac{E}{T}} \pm 1}EdE, \tag{1.63}$$

which describes the numerical density at a temperature $T$ of a species of particles with mass $m_\chi$, $g$ internal freedom degrees and zero chemical potential, can be approximated in different ways. In the case the species is relativistic, defined by the condition $T \gg m_\chi$, the limit of Eq. 1.63 would become

$$n_\chi = \frac{g_{eff}}{\pi^2}T^3 \tag{1.64}$$

and so

$$Y_\chi^{eq}(x) = 0.278\frac{g_{eff}}{g_{*s}} \tag{1.65}$$

where $g_{eff} = g$ for bosons, $g_{eff} = 3g/4$ for fermions and [16]

$$g_{*s} = \sum_{i=bosons} g_i\left(\frac{T_i}{T}\right)^3 + \frac{7}{8}\sum_{i=fermions} g_i\left(\frac{T_i}{T}\right)^3 \tag{1.66}$$

where the sum is done only on the relativistic species ($m_i \ll T$). It is evident that $g_{*s}$ is not constant, but it varies with $T$: indeed when temperature decreases the most massive species become non relativistic and their contribution in the sum disappears. The behaviour of $g_{*s}$ is shown in Fig. 1.3 [4]. In the case of a non relativistic species for which $T \ll m_\chi$, Eq. 1.63 would become

$$n_\chi = g\left(\frac{m_\chi T}{2\pi}\right)^{\frac{3}{2}} e^{-\frac{m_\chi}{T}} \tag{1.67}$$

[15]The $\pm$ refers to the case the species is bosonic or fermionic.

[16] In the formula $T_i$ stands for lthe statistic temperatures of each species that, before the decoupling, coincide with $T$.

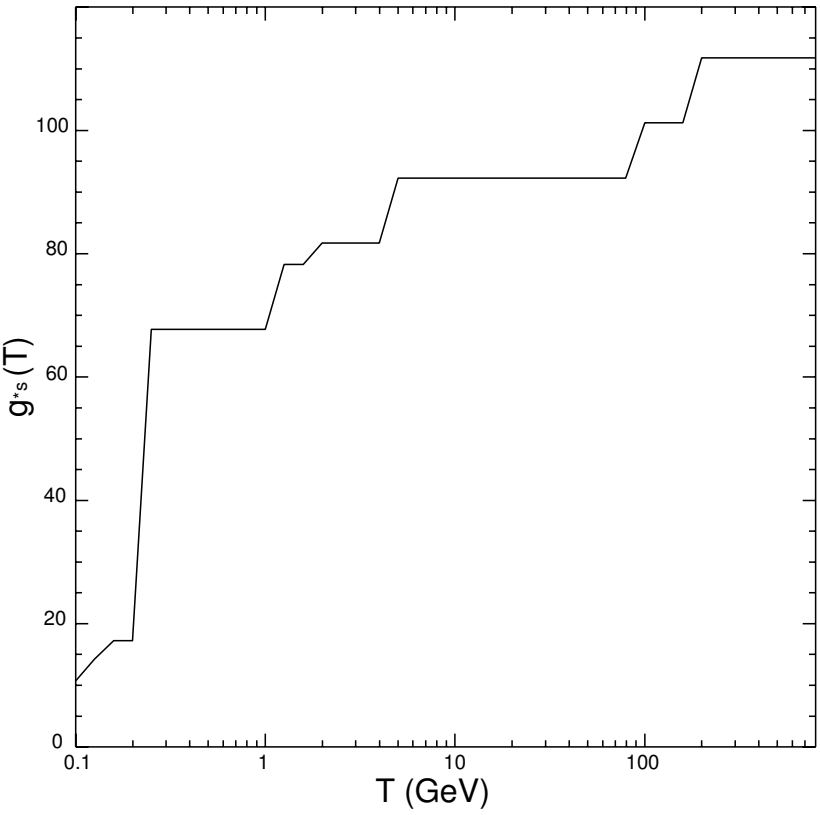


Figure 1.3: The behaviour of $g_{*s}$ as function of the temperature $T$ [4].

from which

$$Y_\chi^{eq}(x) = 0.145 \frac{g}{g_{*s}} x^{\frac{3}{2}} e^{-x}. \tag{1.68}$$

From Eq. 1.64 and 1.67 it follows that $n_\chi^{eq}$ decreases with $T$ and, as a consequence, $\Gamma_A$ decreases too. Let's suppose that the decoupling of a species from the thermal equilibrium occurs at $x = x_f$ ($T = T_f$), when the annihilation rate, decreasing with temperature $T$, reaches the condition $\Gamma_A \approx H$. Although the Boltzmann equation does not admit a general solution, it is possible to define two different regimes of behaviour for the species $\chi$. For $x < x_f$, the species is at equilibrium and $Y_\chi(x) \approx Y_\chi^{eq}(x)$; on the contrary for $x > x_f$, when the decoupling has taken place, $Y_\chi(x) \approx Y_\chi(x_f)$ is obtained. Similar considerations can be made by looking at the behaviour of Eq. 1.60 as function of time $\tau$: for small time, the term containing the Hubble constant ($\propto T^3$) results to be negligible as regards the right hand side member and the numerical density

of the particles follows its equilibrium value ($n_\chi(x) \approx n_\chi^{eq}(x)$). As time passes, on the contrary, the situation reverses and the expansion term starts to dominate: in such conditions, as explained previously, the numerical density $n_\chi(x)$ becomes proportional to $a^{-3}$ leading to a constant numerical density per comoving volume unit ($Y_\chi(x) = cost$). The request of continuity induces to join the two limit solutions and obtain for $x > x_f$ $Y_\chi(x) = Y_\chi(x_f)$. As evident, the numerical density at the moment of decoupling ($Y_\chi(x_f)$ or $n_\chi(x_f)$) plays a crucial role and, as shown by Eq. 1.65 and 1.68, two completely different values of such quantity are expected according to the kinematical conditions of the species at the moment of freeze-out. As a consequence the two different cases of *hot* (relativistic at the moment of decoupling) and *cold* (no more relativistic at the moment of decoupling) dark matter have to be investigated [2].

Let's consider, for example, a hot candidate that, for definition, decouples at $x_f \ll 1$ (when $T \gg m_{chi}$): from Eq. 1.65 it follows that, being $Y_\chi^{eq}$ constant and indipendent of $x_f$, the final value of $Y_\chi$ depends not much on the characteristics of the decoupling. By defining $Y_\chi^\infty \equiv Y_\chi(x \to \infty)$ and supposing constant the entropy per comoving volume unit[17], one obtains

$$Y_\chi^\infty = 0.278 \frac{g_{eff}}{g_{*s}(x_f)} \tag{1.69}$$

from which it can be deduced that the species that decoupled before, presenting a higher $g_{*s}(x_f)$, should show a present abundance lower than those decoupled later (see Fig. 1.4). Remembering the abundance definition of a species and referring it to the present, it is possible to obtain the numerical density of the particles of the species $\chi$ [2]

$$n_{\chi 0} = s_0 Y_\chi^\infty = 2.970 \times 10^3 Y_\chi^\infty cm^{-3} = 825 \left[\frac{g_{eff}}{g_{*s}(x_f)}\right] cm^{-3} \tag{1.70}$$

where $s_0$ indicates the density of the present entropy, from which one can obtain

$$\rho_{\chi 0} = m s_0 Y_\infty = 2.97 \times 10^3 m Y_\chi^\infty cm^{-3} \tag{1.71}$$

and

$$\Omega_{\chi 0} h_0^2 = \rho_{\chi 0} \left(\frac{3H_0^2}{8\pi G h_0^2}\right)^{-1} = 7.83 \times 10^{-2} \left[\frac{g_{eff}}{g_{*s}(x_f)}\right] \frac{m}{eV} \tag{1.72}$$

with the reduced $h_0$ Hubble constant so that $H_0 = 100\ h_0\ km\ s^{-1}\ Mpc^{-1}$.

Let's consider, on the contrary, a species of cold dark matter ($x_f \gg 1$).

[17] If this were not true and $s_0 = \beta s(x_f)$ the result would be $Y_\chi^\infty = Y_\chi^{eq}(x_f)/\beta$.

From Eq. 1.68) it is evident that, due to the explicit dependence of $Y_\chi^{eq}$ from $x_f$, the present abundance of the species $\chi$ is influenced by the specific value taken by $x$ at the moment of decoupling. In order to calculate this value it is necessary to parameterize in partial waves the annihilation cross section. Being $\sigma_0|v| \propto v^p$ with $p = 0$ for the $s$ wave and $p = 2$ for the $p$ wave, and remembering that $\langle v \rangle \propto T^{\frac{1}{2}}$, one obtains $\langle \sigma_0|v| \rangle \propto T^n$ and hence the thermal average of the annihilation cross section can be written as

$$\langle \sigma_0|v| \rangle \equiv \sigma_0 \left( \frac{T}{m_\chi} \right)^n = \sigma_0 x^{-n}. \tag{1.73}$$

Equation 1.61 becomes

$$\frac{dY_\chi}{dx} = -\lambda x^{-n-2} \left[ Y_\chi^2 - (Y_\chi^{eq})^2 \right] \tag{1.74}$$

and, without giving the demonstration, one obtains

$$Y_\chi^\infty = \frac{3.79(n+1)x_f^{n+1}}{(g_{*s}/g_*^{\frac{1}{2}}) m_{pl} m_\chi \sigma_0} \tag{1.75}$$

and

$$x_f = \ln(\gamma) - \left( n + \frac{1}{2} \right) \ln[\ln(\gamma)] \tag{1.76}$$

with $\gamma = 0.038(n+1)(g/g_*^{\frac{1}{2}}) m_{pl} m_\chi \sigma_0$, $\lambda = \lambda(g_{*s}, g_*, m_{pl}, \sigma_0)$ e

$$g_* = \sum_{i=bosoni} g_i \left( \frac{T_i}{T} \right)^4 + \frac{7}{8} \sum_{i=fermioni} g_i \left( \frac{T_i}{T} \right)^4. \tag{1.77}$$

The behaviour followed by the abundance of the $\chi$ species is shown in Fig. 1.4. Similarly to the previous case, for cold dark matter, too, it is possible to express a numerical density

$$n_{\chi 0} = s_0 Y_\chi^\infty = 1.13 \times 10^4 \frac{(n+1)x_f^{n+1}}{(g_{*s}/g_*^{\frac{1}{2}}) m_{pl} m_\chi \sigma_0} cm^{-3} \tag{1.78}$$

and the relative

$$\Omega_{\chi 0} h^2 = 1.07 \times 10^9 \frac{(n+1)x_f^{n+1}}{(g_{*s}/g_*^{\frac{1}{2}}) m_{pl} \sigma_0} GeV^{-1}. \tag{1.79}$$

Although $m_\chi$ does not appear explicitly in Eq. 1.79 it is contained in the definition of $x_f$. From 1.79 it is evident that a species with a small cross

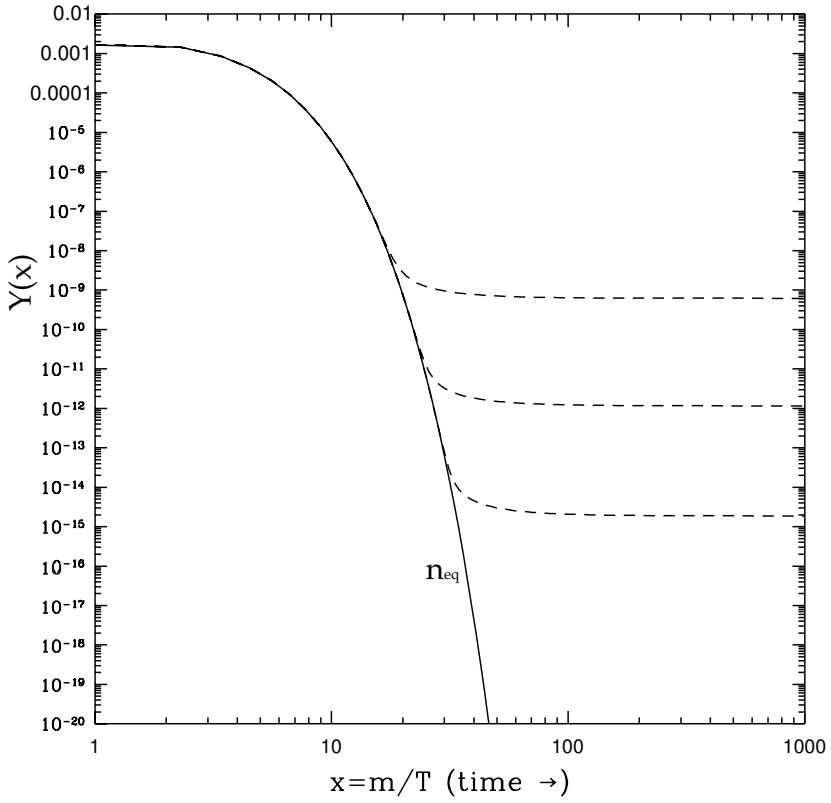


Figure 1.4: Behaviour of cold dark matter abundance before and after decoupling. The three level correspond to three different values of $x_f$. Earlier the freeze-out occurs, higher is the expected present abundance [4].

section would produce a value of $\Omega_{\chi 0}$ higher than one with the same mass but higher annihilation cross section. Unlikely what happens for hot dark matter, in order to draw conclusions regarding the cosmological abundance of a species $\chi$, it is necessary to explicit also the annihilation cross section. To put into evidence the two different behaviours, it is better to consider a species of massive and stable neutrino: as previously explained, the decoupling of a species from the thermal equilibrium happens with a value of $T$ for which the annihilation rate can be compared to the Hubble parameter. So equalizing $H \approx T^2/m_{pl}$ and the annihilation rate of this species $\Gamma = n_\nu \langle \sigma_0 |v| \rangle \approx G_F^2 T^5$ one obtains

$$T_f \approx \left( \frac{1}{G_F^2 m_{pl}} \right)^{\frac{1}{3}} \approx 1 \; MeV. \tag{1.80}$$

Supposing that this species has a mass $m_\nu$ much lower than the temperature $T_f$ ($x_f \ll 1$), that is to say that it is relativistic at the moment of decoupling, one would obtain from Eq. 1.72 [2]

$$\Omega_{\nu 0} h^2 = \frac{m_\nu}{92\ eV}. \tag{1.81}$$

On the contrary, for $m_\nu \gg T_f$, from Eq. 1.79 one obtains

$$\Omega_{\nu 0} h^2 = 3 \left(\frac{m_\nu}{GeV}\right)^{-2} \left[1 + \frac{3 \ln(m_\nu / GeV)}{15}\right]. \tag{1.82}$$

The two different solutions are represented in Fig. 1.5 which indicates the

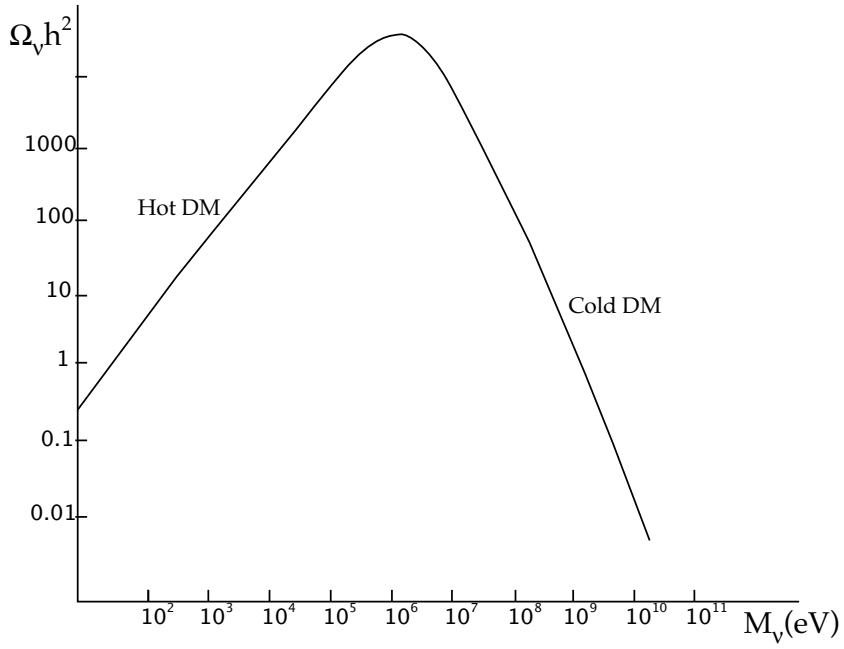


Figure 1.5: Behaviour of $\Omega_\nu$ for an hypothetic massive neutrino as function of its mass [2].

behaviour of the connection region too ($T_f \approx m_\nu$), although only the much higher limits of $m_\nu$ and the much smaller limits of $T_f$. From 1.81 and 1.82 it follows that to produce a $\Omega_\nu = \Omega_M = 0.3$, as requested by the experimental obervations, a hot and stable neutrino should present in principle a mass of the order of few tens of $eV$ while a cold neutrino would have $m_\nu \approx 5\ GeV$. It is evident that this last neutrino, due to its elevated mass, could not be ordinary: indeed the measurements done with LEP exclude a fourth family

with $m_\nu < 45GeV$ and it is clear that none of the three known families can have a so elevated mass.

At this point let's consider a species which interacts weakly. For such a species, by imposing the usual decoupling condition and by giving to the parameters considered values typical of the weak scale, one obtains a decoupling temperature $T_f \approx m_\chi/20$ [4]. Since $x_f \approx 20 \gg 1$, inserting these value into Eq. 1.79 and supposing at first approximation the thermal average of the cross section indipendent from the temperature ($n = 0$), one obtains

$$\Omega_{\chi 0} h^2 \approx \frac{2.2 \times 10^{-10} GeV^{-2}}{\sigma_0} \approx \frac{10^{-38} cm^2}{\sigma_0}. \tag{1.83}$$

From the equation just presented it is evident that a particle with similar properties would show a present abundance not negligible: a typical weak cross section of the order of $10^{-8} GeV^{-2}$ would produce, inserted into Eq. 1.83, an $\Omega_{\chi 0}$ of the order of the unity. A similar nonbaryonic candidate for the cold dark matter is usually called WIMP (Weak Interactive Massive Particle). The WIMPs family contains in itself a large group of stable particles, not relativistic at the decoupling moment, massive ($m_\chi \approx$ *Gev-TeV*) neutral and weakly interacting: the neutrino $m_\chi \approx 5\ GeV$ described previously represents a typical example of WIMP. Due to the experimental limits which seem not to support such a neutrino, a new hypothesis considers that the missing matter is to be attributed to the supersymmetric sector of the elementary particles and in particular to the Lightest Supersymmetric Particle (LSP). The main ingredient needed to provide a natural WIMP candidate in the framework SUSY models is *R-parity* conservation: this last request implies a selection rule on the supersymmetric particles decays, preventing the lightest one to decay to an ordinary particle and hence to be stable and significant in terms of cosmological abundance. A large number of different supersimmetric extensions of the Standard Model (SM) can be imagined: as a consequence even among SUSY theories, the LSP can assume different identities according to the considered model. Nevertheless in most theories, as in the so-called MSSM (Minimal Supersymmetric extension of Standard Model), it coincides with the neutralino, a linear superposition of few supersimmetric particles. As shown in Sec. 2.2, in the context of MSSM, that in the rest of the work will be considered as reference, a large portion of the parameter space allowed region provides for a neutralino abundance significant at a cosmological level [4].

### 1.3.2 Dark matter and galactic structures formation

In the previous section it has been shown that relic nonbaryonic dark matter species can belong to two different classes according to their kinematical conditions at the moment of their decoupling from thermal equilibrium. On the basis of the information provided until now both candidates, although behaving in a completely different way, seem to be able to solve the dark matter puzzle, producing, for certain mass-annihilation cross section couples, the observed $\Omega_M$. One more test has to be performed in order to select the appropriate class of candidates: it is based on the fact that the requested not negligible amount of dark matter has to have played, according to its nature, a different and crucial role during the formation of large scale structures. As shown further on, the comparison between the present structures and those predicted by the two classes of dark matter particles, rules out the hot candidates.

Although the process of the structures formation is not completely understood at the moment, the birth of structures now visible is usually brought back to the presence of matter density fluctuations in a previous age: among the different kinds of density perturbations, the present work will only consider the so called *adiabatic fluctuation*, leaving unaltered the specific entropy inside and outside the perturbation region [18]. The mechanism associated with the fluctuations amplification is essentially ruled by gravity: positive density perturbations, defined by $\Delta\rho/\rho > 0$, with average density matter $\rho$ and exceeding density $\Delta\rho$ produced by the particular fluctuation, induce through gravitational interaction a collapse but, at the same time, the produced mass excess generates a pressure which tends to compensate for the local increase of density. The outlined process typically present a critical amplitude below which the thermal pressure of matter can balance gravitational collapse. Assuming in first approximation that the Universe is static, so it can be approximated to a static gas of mass particles $m$ at temperature $T$, the fluid fluctuations evolution results to be led by the critical quantity [18]

$$l_j = \sqrt{\gamma \frac{\pi k T}{G \rho m}} \tag{1.84}$$

called *Jeans length*: fluctuations on a scale shorter than this length are destined to oscillate, since compensated by pressure, while those on higher scale are amplified leading to a collapse. Together with this typical length a *Jeans*

*mass* $M_j$ can be defined as

$$M_j \propto l_j^3 \rho \propto \rho^{-\frac{1}{2}} T^{\frac{3}{2}}. \tag{1.85}$$

Exactly as before, density perturbation of mass higher than $M_j$ will tend to grow, those lower will continue to oscillate. In the context of adiabatic fluctuations and in the approximation of a static fluid (Universe), the fluctuations with scale greater than $l_j$ would increase exponentially with the passing of time. Extending the calculations done for the case of a fluid in expansion (more appropriate), it is possible to demonstrate that in a matter-dominated Universe every perturbation of amplitude greater than $l_j$ would increase with the passing of time not exponentially but following the power law

$$\frac{\Delta\rho}{\rho} \propto (z+1)^{-1} \tag{1.86}$$

where $z = \frac{a(\tau_0)}{a(\tau_1)} - 1$ has been introduced.

In the above described framework it is meaningful to evaluate the Jeans mass for baryonic fluctuations before and after recombination epoch, occurring approximately at $z_{rec} = 1000$, and representing the moment at which the baryons decoupling from radiation occurred: for $\tau < \tau_{rec}$ $M_j$ is of the order of $10^{16} M_\odot$ while later on it decreases to the is $10^5 M_\odot$. This abrupt drop can be brought back to the enormous decrease in the baryonic pressure as soon as decoupling happens. One should note that the baryonic Jeans mass obtained in the pre-recombination era is even higher than the mass of baryons contained within the horizon at that time and hence all the sub-horizon-sized fluctuations continue to oscillate until recombination is reached: at that moment they can start to grow. From the experimental point of view the amplitude of baryonic density fluctuations at the recombination epoch can be extracted from the anisotropies of the cosmic microwave radiation, obviously extremely sensitive to the matter fluctuations at the moment of its decoupling. The measured temperature anisotropies of the CMR is consistent with baryonic fluctuations $(\Delta\rho/\rho)_b$ at $\tau \approx \tau_{rec}$ too low to justify, through the rescaling law expressed by Eq. 1.86, the structures seen today. As a consequence a Universe composed only of baryonic matter could not exist in the present form. A solution to this problem is provided if, together with ordinary matter, a certain amount of dark matter, not coupled to radiation, is supposed. This last condition permits to the dark matter density fluctuations $(\Delta\rho/\rho)_\chi$, possibly generated during inflation period, to grow undisturbed even for $\tau < \tau_{rec}$: this means

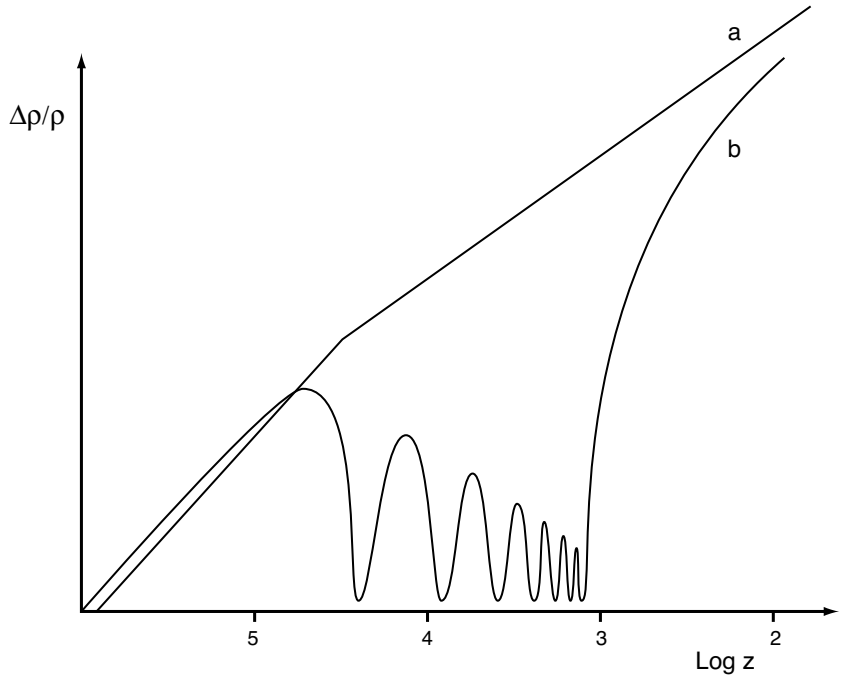


Figure 1.6: Dark matter (solid) and baryonic (dashed) density perturbations growth. Until recombination ($z \approx 1000$) the baryonic perturbations oscillate if their scale is lower than Jeans length (every sub-horizon scale) and they suffer for silk dumping, while dark matter perturbations grow undisturbed. After recombination the baryonic fluctuations are driven by the grown dark matter ones [18].

that for $\tau \approx \tau_{rec}$, the condition $(\Delta\rho/\rho)_\chi > (\Delta\rho/\rho)_b$ may hold and that the decoupled baryonic matter (much more uniformly distributed) falls into the dark matter gravitational potential associated to the amplified fluctuations: as a consequence the baryonic fluctuations growth, instead of following the behaviour of Eq. 1.86, is enhanced by the existing gravitational potential. The described process is summarized in Fig. 1.6 where the leading role of dark matter is evident.

Together with this gravity-pressure balance, determining the oscillation or the growth of a fluctuation, two dissipative damping processes should be considered in order to realistically predict the evolution of fluctuations themselves: they are the *Silk dumping* and the *free streaming*. The *Silk dumping* acts only on fluctuations of baryonic matter density since it afflicts only those species coupled to photons (dark matter is not involved). Roughly speaking

this process consists in the diffusion of photons out of an hyperdense matter region: these photons, interacting through Compton scattering, with free electrons tend to drag them out from the overdense region and these last, through Coulombian attraction, bring with them the protons. This lead to a local reduction of baryonic matter and hence to a dumping of the fluctuation. This process can efficiently occur if the coupling with baryonic matter is strong enough and if photons are free to randomly walk-out from perturbation region. It follows that this process ceases to work when no more free electrons are present and hence in the epoch after recombination. The second conditions implies that this mechanism is efficient if the photon-electron coupling is not too strong to avoid photons diffusion and if the perturbation region is small enough to permit photon diffusion times lower than the Universe expansion typical time. This last observation leads to the definition of a typical critical perturbation mass $M_D$, over which the dumping process is negligible. As far as *free streaming* is concerned, this mechanism afflicts only collisionless particles (such as dark matter) that, since not interacting with the surrounding matter, can flow away from hyperdense to hypodense regions. Obviously this process tends to reduce the amplitude of the matter density fluctuations. The phenomenon strongly depends on the kinematical conditions of the particles and a typical length can be associated to it: for a hot species such length, above which every fluctuation is wiped out, is much higher than that typical for cold candidates. It follows that in a Universe dominated by hot dark matter, small scale structures (such as galaxies) are not directly associated with primordial fluctuations, since small scale dark matter fluctuations, guiding baryonic ones, are efficiently dumped. As a consequence galaxies should be imagined as products of the fragmentation of larger scale structures ("top-down" structure formation) and, according to this model, they should have form very late in the Universe's history. On the other hand, if a cold species is supposed, "bottom-up" structure formation is favored and galaxies start to form earlier. The experimental observations, together with $N$-body simulations, suggest that "bottom-up" structure formation is favored in order to well reproduce the observed present Universe and they evidently rule out the hypothesis of a dominant hot dark matter.

In conclusion the most accepted model, able to reproduce the largest amount of experimental results and to explain the discrepancy between the observed matter density fluctuations and the CMR anisotropies, is the so called

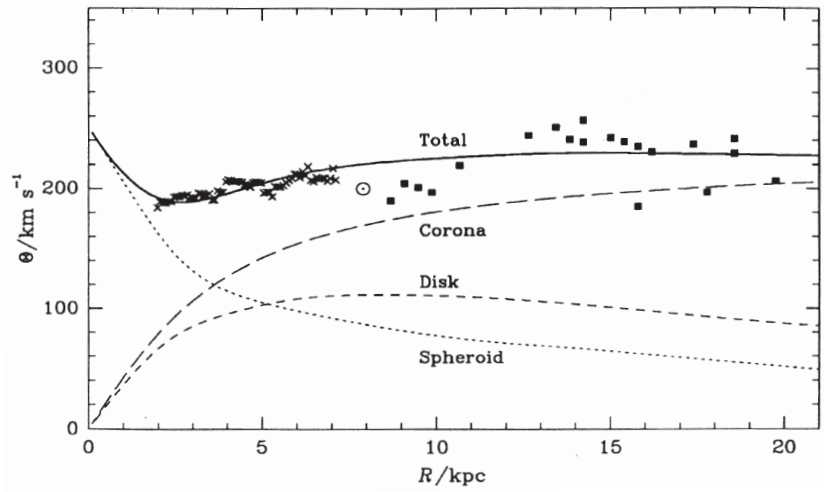


Figure 1.7: Rotation curve for the Milky Way obtained by the means of 21 *cm* emission line observation [19]. The "corona" contribution refers to the dark halo.

ΛCDM (*Cold Dark Matter and* Λ *dark energy*) that assumes a uniformly diffused dark energy component providing $\Omega_\Lambda \approx 0.7$ and nonbaryonic, neutral, relic, weakly interacting and cold dark matter particles (WIMPs) providing $\Omega_M \approx 0.3$.

### 1.3.3 The galactic dark halo and its local density

Before passing to dark matter direct detection it is useful to spend few words on the galactic dark halo of Milky Way (where direct experiments are performed) and on the associated dark matter local density. As it will be clear in next Chap. 2 the interpretation of direct detection experimental results, in terms of neutralino mass and coupling with ordinary matter, strongly depends on the assumed properties of the halo (especially on the neutralinos escaping velocity, on their average velocity and local density).

The Milky Way, like every spiral galaxy, is constituted by the bulge, the disk, the spheroid and, according to rotation curves measurements, this visible matter is immersed within a dark halo, causing its flat bahaviour at high distance from the galactic centre ($R > 7.5$ *kpc*). These rotation curves measurements, as stressed in Sec. 1.3, can be used as evidence for dark matter existence and, if the gravitational contributions coming from the visible components are known, they can be used to infer a possible dark matter distri-

bution. Figure 1.7 shows the galactic rotation curve derived from experimental observations in the radio range [19]. After a rapid increase with the radius, the circular rotation velocity $\Theta(R)$ presents a first maximum around $R \approx 300\ pc$ (not visible in the plot) an then its starts decreasing reaching the minimum value 200 $km/s$ for $R \approx 3\ kpc$. A second maximum $\Theta \approx 230\ km/s$ occurs at about $R = 6\ kpc$ and then, for higher radii, it stabilizes around 220 $km/s$. Unfortunately this kind of measurement, although defining a specific class of halo models, cannot be used to uniquely determine a density profile. Nevertheless the so-called *cored spherical isothermal halo* is often used to reproduce such flat behaviour at high radii. Its profile density, expressed in spherical coordinate centered in the galactic plane centre, is defined by the equation

$$\rho_a(r) = \frac{\Theta_*^2}{4\pi G} \frac{1}{a^2 + r^2} \tag{1.87}$$

where $a$ is the core radius and $\Theta_*$ is a free parameter. The associated rotational curve[18] is hence provided by

$$\Theta_a(R) = \Theta_* \left[1 - \left(\frac{a}{R}\right)\ \arctan\left(\frac{a}{R}\right)\right]^{1/2} \tag{1.88}$$

producing $\Theta_a(R)$ approximately constant for $r \gg a$ ($R \gg a$). The value of the two free parameters of the model, $a$ and $\Theta_*$, can be fixed in order to well reproduce the experimental rotation curve bahaviour. After having estimated the contributions associated to the stellar disk at high radii (dominating this region together with the dark halo), one obtain $\Theta_* \approx 220\ km/s$ and $a \approx 4.8\ kpc$ (see Ref. [6] for a detailed review of the argument). This spherical distribution implies a local dark matter density

$$\rho_0 \equiv \rho_a(R_0) \approx 0.3\ GeV\ c^{-2}\ cm^{-3} \tag{1.89}$$

where $R_0$ is the galactocentric distance of the Sun ($R_0 \approx 8\ kpc$). Results of the same order ($\rho_a(R_0) \approx 0.2 - 0.5\ GeV\ c^{-2}\ cm^{-3}$) are obtained even for different realistic halo models [6]. In the rest of the work Eq. 1.89 will be assumed.

One should note that the introduced isothermal density profile class is consistent with that expected for a halo constituted by collisionless particles

[18] The rotational curves is usually expressed in cylindrical coordinates ($R$, $\phi$, $z$) where $R$ is the distance from the galactic plane centre, $\phi$ is the angular coordinate and $z$ is the distance from the galactic plane. To be consistent a coordinate transformation has to be performed in order to express the rotation curve starting from the halo profile expressed in spherical coordinate. Fortunately $r$ and $R$ in both coordinates systems represent the distance.

interacting only gravitationally and characterized by the phase space distribution function

$$f(\vec{x},\vec{v}) = \frac{\rho_*}{(2\pi\sigma^2)^{3/2}} e^{-\frac{v^2}{2\sigma^2}} e^{\frac{\Psi(r)}{\sigma^2}}. \tag{1.90}$$

where $\Psi(r)$ is the potential. The resulting velocity distribution is a Maxwellian with $v_0$ most probable velocity and $\sigma^2 = \overline{v^2}/3 = v_0^2/2$.

## 1.4 Summary

The most important considerations presented within this chapter concern the nature of dark matter. As shown in Sec. 1.3, the dark matter concept, intended as not visible matter, has to be introduce to explain a large number of astronomical observations from galactic (rotation curve of spiral galaxy) to cosmic scale (CMB anisotropy and standard candles). The consistency of all these measurements, obtained through very different techniques, becomes almost perfect if together with dark matter another new kind of energy, called dark energy, is imagined. This last component whose nature is actually unknown has to present a negative pressure or, in other words, should feel a repulsive gravity. Independently from its nature, as a consequence of this property, this energy is expected to be uniformly diffused in all the Universe and not clustered as dark matter. It follows that, within a galaxy, and in particular within Milky Way, its contribution has to be negligible. The comparison between all the experimental results lead to a scenario in which the Universe is flat ($\Omega_{tot} = 1$) and it is approximately constituted by 70% of dark energy ($\Omega_\Lambda = 0.7$) and 30% of matter ($\Omega_M = 0.3$). The dark energy is responsible for the Universe accelerated expansion. As far as the matter term is concerned, only a small portion of it is represented by visible matter ($\Omega_{lum} \approx 4.95 \times 10^{-3}$) while the remaining is dark. Nucleosynthesis theory together with light nuclei abundance measurements imply that the majority of this dark matter is nonbaryonic (ordinary) and hence it has to be constituted by neutral[19] particles with zero baryonic number. In order to provide a not negligible cosmological abundance dark matter particles have be relic (no more in thermal equilibrium with other species) and, from considerations on structure formation (Sec. 1.3.2) they have to be cold, in other words they should have decoupled from thermal equilibrium when they were no more relativistic

[19] Otherwise they would interact directly with photons becoming visible

(Sec. 1.3.1). To be able to provide a density of the order of the one required to solve dark matter puzzle, a relic neutral cold candidate has to present a typical weak annihilation cross section. This class of particles is usually called WIMPs (Weak Interactive Massive Particles) and among this class, the most promising candidate is represented by the neutralino, the lightests supersymmetric particle of the minimal supersymmetric extension of Standard Model (MSSM). The Milky Way, like every spiral galaxy, is supposed to be immersed within a dark matter halo constituted by WIMPs presenting a maxwellian velocity distribution with respect to the galactocentric reference frame (Sec. 1.3.3).

# Chapter 2

# WIMP Direct detection

## 2.1 General considerations

As stated in the previous chapter several experimental hints, both at galactic or cosmological level, suggest that a large fraction of the matter contained in the Universe is not ordinary and, according to the presented dissertation, this new form of matter has to be stable, nonbaryonic, cold, neutral and weakly interacting in order to justify the data obtained from astronomical and astrophysical observations. Several candidates have been hypothesized to solve this dark matter puzzle, most of which go under the class of WIMPs (Weakly Interacting Massive Particles) since they arise in some extensions of the standard model of electroweak interaction. Inside this group, the most well-motivated candidate is represented by the so-called Lightest Supersymmetric Particle (LSP), whose existence is predicted by a set of SuperSymmetric theories. The most appealing feature of this proposed solution is that the dark matter puzzle could be solved without turning to *ad hoc* models: supersimmetry concept has been introduce in particle physics to cure some Standard Model failures that, in principle, have nothing to do with dark matter.

Assuming that dark matter consists of WIMPs and hence of particles froze out from thermal equilibrium when they were no more relativistic, one should expect that, due to the mutual gravitational interaction, dark matter should have clustered with ordinary matter and hence formed an almost spherical dark halo surrounding the galaxies. This theoretical speculation has been verified for a large number of spiral galaxies for which, for example, the rotation curves have been measured (as described in Sec. 1.3) suggesting the existence

of a dark halo more extended than the visible disk. Although such measurement in the case of the Milky Way is somehow more difficult and it suffers of more uncertainties, since the observer is located inside the galaxy itself, the presence of a halo has been confirmed [19]. Different arguments, concerning mainly the study of galactic clusters dynamic, corroborate the above results (consult Ref. [4, 19] for an overview of the main results). As a consequence, if dark matter exists, it must be present also in the Milky Way to justify the above experimental observations and hence, if it consist, as assumed, of elementary particles, a consistent flux of WIMPs is expected to cross the Earth surface. The WIMPs of the dark halo, although with a very low cross section, should in principle elastically interact with ordinary matter nuclei and induce atomic recoils [20]. The measurement of these induced rare recoils, somehow discriminated from the background, would represent the most satisfactory WIMPs direct detection. A second alternative to WIMPs detection is represented by the so-called indirect detection technique, aimed to observe the products of WIMP annihilation process instead of WIMP-nucleon interactions. Since this annihilation process is guided by the WIMP numerical density ($\propto n_\chi^2$), this interaction is expected to occur more frequently inside astronomical bodies where the gravitational attraction enhances the local dark matter density. For this reason, indirect detection techniques frequently tend to search for anomalous particles production (gamma rays [21], neutrinos [22], anti-matter cosmic rays [23]), considered as product of annihilation, within the Sun, the Earth and the galactic centre.

In the rest of the chapter, direct detection techniques and data interpretation will be presented in detail. To simplify the formalism, those quantities referring to the neutralino will be labeled with the subscript $\chi$, those to nuclei with $N$ and those to nucleon $n$.

## 2.2 Expected nuclear recoils energy spectrum and rate

As suggested by the considerations of Sec. 1.3.1, the WIMPs, if existing, should present a small but finite coupling to ordinary matter. If this is not the case their cosmological abundance would overcome the measured value of the cosmological parameter since, in the early Universe, they would not have efficiently annihilated (see Eq. 1.83). As previously stated, the most

satisfactory proof of WIMPs existence would be represented by the direct detection of ordinary matter nuclear recoils, possibly induced by the elastic reaction

$$\chi + N(A,Z)_{at\ rest} \rightarrow \chi + N(A,Z)_{recoil}. \tag{2.1}$$

with $A$ and $Z$ atomic mass and atomic number of the nucleus $N$. In the centre-of-mass system such scattering, produced by a WIMP of energy $E$ and mass $m_\chi$, would end up into a nuclear recoil of energy

$$E_R = E \cdot r \frac{1-\cos\theta}{2} \tag{2.2}$$

where $\theta$ indicates the scattering angle and $r = 4m_\chi m_N/(m_\chi + m_N)^2$ is a kinematic factor. It follows $0 \leqslant E_R \leqslant Er$. In principle, the detectable differential energy spectrum should be compared to that theoretically predicted in the framework of the selected dark matter model in order to be able to extract physical properties regarding the nature of the WIMPs themselves. These models depend, in general, on several parameters among which the most important are the WIMP coupling with ordinary matter and the WIMP mass. If no signal is found, the experimental data can alternatively be used to put an upper limit on these parameters values.

The WIMP scattering over nuclei is ultimately connected to the neutralino-quark cross section opportunely modified to count for the quarks distribution in nucleons and for the nucleons distribution in nuclei. As far as the WIMPs interaction with quarks and gluons is concerned, its behaviour is essentially provided by the chosen theoretical supersymmetric model: within such framework, the neutralino coupling to all quarks and gluons can be expressed as function of some parameters of the model. Nevertheless one should note that these quantities can assume values within a wide range of possibilities, leading to a wide uncertainty on the WIMP-nucleus cross sections. In order to describe such interactions, the effective supersymmetric Lagrangian should be written down. The WIMP-quark interaction can be expressed as a standard four-fermion interaction and the Lagrangian built up from the particles' currents: the computation is strongly simplified due to the strong not relativistic regime of the WIMPs (since they are cold) and consequently to the small momentum transfer. In this limit the weak propagator factor reduces to a multiplicative constant and of all the possible currents only the scalar ($S$), vector ($V$) and axial-vector ($A$) survive. Assuming the WIMP is the neutralino, and hence a Majorana fermion in the MSSM, the vector current vanishes and of all the

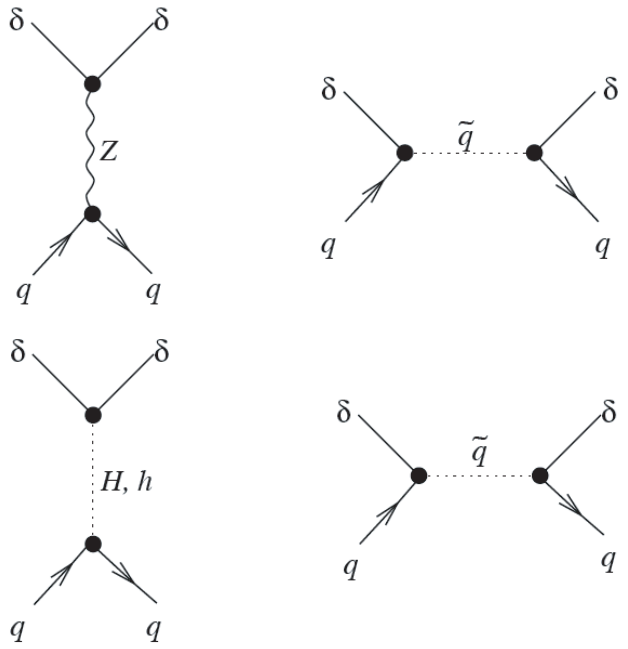


Figure 2.1: Spin-dependent (up) and spin-independent (down) WIMP-quark scattering interactions in MSSM [4].

possible Lorentz scalar combinations of the currents only $S$-$S$ and $A$-$A$ survive. The former does not involve WIMP or quark spins and, for this reason, it is referred as spin-independent interaction while, viceversa, the latter is spin-dependent. The main feynman diagrams at tree-level are summarized in Fig. 2.1 for both interactions. If one-loop level is considered, neutralino-gluon interactions becomes relevant, going to increment only the scalar coupling. For a complete and detailed review of the argument see Ref. [4].

In order to translate the microscopic interactions to WIMP-nucleus cross section, one should define the matrix elements of the quark and gluon operators in nucleon and express the nucleons content within the nucleus. These quantities have to be extracted from scattering experiments data on the basis of some nuclear models. Once again these values are poorly known increasing the uncertainties on WIMP-nucleus cross section. In general the resulting WIMP-nucleus differential cross section can be written down, as function of

the momentum transfer $\vec{q}$, as

$$\frac{d\sigma_{\chi\text{-}N}}{d|\vec{q}|^2} = G_F^2 \frac{C}{v^2} F^2(|\vec{q}|) = \frac{\sigma_0}{4\mu^2 v^2} F^2(|\vec{q}|) \tag{2.3}$$

where $C$ is a dimnesionless factor including all the particle physics model information, $\mu$ is the reduced mass, $F$ is the above mentioned nuclear form factor ($F(0) = 1$), $v$ is the WIMP velocity and $\sigma_0$ is defined as

$$\sigma_0 = \int_0^{4\mu^2 v^2} \frac{d\sigma_{\chi\text{-}N}(q=0)}{d|\vec{q}|^2} d|\vec{q}|^2 = 4G_F^2 \mu^2 C \tag{2.4}$$

and it represents the total cross section in the zero-momentum transfer approximation. Obviously, according to the kind of interaction, the above quantity assumes different expressions. For spin-dependent coupling

$$C_{spin} = \frac{8}{\pi} \Lambda^2 J(J+1) \tag{2.5}$$

and

$$\sigma_{0,spin} = \frac{32}{\pi} G_F^2 \mu^2 \Lambda^2 J(J+1) \tag{2.6}$$

where $J$ is the total angular momentum of the nucleus and $\Lambda^2$ is a quantity function of the spin content of neutrons and protons group in the nucleus. Similarly, in the case of spin-independent interaction one obtains

$$C_{scalar} = \frac{1}{\pi G_F^2} \left[ Z f_p + (A - Z) f_n \right]^2 \tag{2.7}$$

and

$$\sigma_{0,scalar} = \frac{4\mu^2}{\pi} \left[ Z f_p + (A - Z) f_n \right]^2 \tag{2.8}$$

where $f_n$ and $f_p$ are the effective neutralino couplings to neutrons and protons, containing the information connected with the quark distribution within the two nucleons. Assuming that the WIMP interacts in the same way with both nucleons, one obtains $f_n \approx f_p$ [4] leading to $C_{scalar} \propto A^2$ and, for small momentum transfers (for which $F^2(|\vec{q}|) \approx 1$), to a resulting cross section proportional to $A^2$. This coherent enhancement of the cross section will be reduced, as shown further on, by the presence of the nuclear form factor.

On the basis of the above observations it is useful to write down the nuclear recoils differential energy spectrum $dR/dE_R$, providing the recoils rate per unit of mass and per unit of recoil energy $E_R$, as [24]

$$\frac{dR}{dE_R} = R_0 \cdot S(E_R) \cdot F^2(E_R) \cdot I \tag{2.9}$$

where the main ingredients have been factorized in order to decouple the $S(E_R)$ term, counting for the kinematic of the process and the detector response, from the other factors involving the physics of the interactions. Eq. 2.9 has a crucial role in direct detection experiments since it connects the experimental data (represented by the left-hand side) with the theoretically predicted spectrum, opportunely corrected to counts for detector properties. In more details, the right-hand side factors are:

- the spectral function $S(E_R)$: this term contains the basic behaviour of the expected recoil spectrum modified to counts for a series of non trivial corrections. First of all the detector, since at rest with respect to the Earth is moving around the sun while the solar system is moving with respect to the the galactic frame. This fact implies that the WIMP flux through the detector is function of time. The second group of corrections is associated with the detector response and in particular to its energy resolution, to the cut-off effect near the threshold (occurring in presence of the use of coincidence) and to its composition. In principle the detector could be constituted by more than one element, leading to the superposition of different nuclear recoil spectra;

- $R_0$ is the total recoil rate for unit of mass supposing a stationary detector with respect to the galactic centre and assuming an infinite escaping velocity. It strongly depends on the WIMP-nucleus cross section and on WIMP distribution;

- the nuclear form factor $F^2(E_R)$ counting for the finite size of the nucleus;

- the interaction function $I$, used to differ the spin-independent from the spin-dependent interactions, counting for the main differences between Eq. 2.6 and 2.8.

In general, the rate of interactions $R$ for unit mass of target material, due to particles with numerical density $n$ and whose coupling to the matter is ruled by the cross section per nucleus $\sigma_{\chi\text{-}N}$, is given by

$$R = \frac{N_0}{A} \int \sigma_{\chi\text{-}N} \; v \; dn \tag{2.10}$$

where $N_0$ is the Avogadro's number, $A$ the atomic mass of the element composing the target, $v$ the module of the impinging particle velocity and $dn$ the

density of particles with module of the velocity within $d^3v$ about $\vec{v}$. This last term can be expressed as function of the WIMP velocity distribution $f(\vec{x}, \vec{v}, \vec{v}_E; v_{esc})$ as

$$dn = \frac{n_0}{k} f(\vec{x}, \vec{v}, \vec{v}_E; v_{esc}) d^3v \tag{2.11}$$

where $\vec{v}$ is the WIMP velocity relative to the Earth, $\vec{v}_E$ is the Earth velocity with respect to the non rotating galactic halo, $v_{esc}$ is the module of the escape velocity[1], $n_0$ is the mean WIMP numerical density ($\rho_\chi / m_\chi$) and

$$k(v_{esc}) = \int_0^{v_{esc}} v^2 dv \int d\Omega_v f(\vec{x}, \vec{v}, \vec{v}_E; v_{esc}) \tag{2.12}$$

is the normalization constant such that

$$\int_0^{v_{esc}} dn \equiv n_0. \tag{2.13}$$

In order to solve the above equation one should make explicit the velocity distribution of the particles belonging to the dark halo and the dependence of the cross section from the velocity. The former is provided by the assumption, motivated in Sec. 1.3.3, that the halo is well described by an isothermal dark halo and hence, in the galactocentric reference frame, by the maxwellian velocities distribution

$$f(\vec{x}, \vec{v}, \vec{v}_E; v_{esc}) = e^{-(\vec{v}+\vec{v}_E)^2/\vec{v}_0^2} \qquad for\ |\vec{v} + \vec{v}_E| < v_{esc} \tag{2.14}$$

where $v_0 \approx 230\ km\ s^{-1}$ is the most probable velocity and all the constant factors, even that depending on the position, have be included in the normalization $k$ value. The expected value for $v_{esc}$ is equal to $|\vec{v} + \vec{v}_E| \approx 600\ km\ s^{-1}$. As far as the cross section is concerned, as a first step the zero-momentum transfer approximation is considered: the effect of the dependence from the WIMP velocity will be included later on within the nuclear form factor correction. This approximation correspond to $\sigma_{\chi\text{-}N}(|\vec{v} + \vec{v}_E|) = \sigma_0$.

Within the framework of the above discussed assumptions it possible to evaluate the basic event rate and recoil energy spectra in the Earth-centric frame. First one could evaluate the expected rate $R_0$, obtained supposing $v_E = 0$ and $v_{esc} = \infty$, for which the normalization assumes the trivial value $k_0 = (\pi v_0^2)^{3/2}$ and that will be used as reference rate. Its value is obtained

[1] One should note that this cut-off velocity is isotropic with respect to the $\vec{v} + \vec{v}_E$ and not to the velocity with respect to the detector.

from Eq. 2.10 and 2.11 and it is provided by

$$R_0 = \frac{2}{\pi^{1/2}} \frac{N_0}{A} \sigma_0 \; n_0 \; v_0 \tag{2.15}$$

that, expressed in $event\ kg^{-1}d^{-1}$ (total event rate, $tru$) and normalized to the nominal values of $\rho_\chi$ and $v_0$, becomes

$$R_0 = \frac{405}{A \; m_\chi} \left(\frac{\sigma_0}{pb}\right) \left(\frac{\rho_\chi}{0.3 \; GeV \; c^{-2} \; cm^{-3}}\right) \left(\frac{v_0}{230 \; km \; s^{-1}}\right) tru. \tag{2.16}$$

The general value of $R$ defined by eq. 2.10 can hence be expressed, within the zero-momentum transfer approximation, as

$$R = \frac{N_0}{A} \int \sigma_{\chi\text{-}N} \; v \; dn \equiv \frac{N_0}{A} n_0 \langle v \rangle \tag{2.17}$$

and, substituting for $n_0$ through Eq. 2.15, it can be rewritten in the form

$$R(v_E, v_{esc}) = R_0 \frac{\pi^{1/2}}{2} \frac{\langle v \rangle}{v_0} = R_0 \frac{k_0}{k(v_{esc})} \frac{1}{2\pi v_0^4} \int v f(\vec{v} + \vec{v}_E; v_{esc}) d^3v. \tag{2.18}$$

The above equation leads to

$$\frac{R(v_E, v_{esc})}{R_0} = \frac{k_0}{k_1} \left[ \frac{R(v_E, \infty)}{R_0} - \left( \frac{v_{esc}^2}{v_0^2} + \frac{v_E^2}{3 \; v_0^2} + 1 \right) e^{-v_{esc}^2/v_0^2} \right] \tag{2.19}$$

with

$$\frac{R(v_E, \infty)}{R_0} = \frac{1}{2} \left[ \pi^{1/2} \left( \frac{v_E}{v_0} + \frac{v_0}{2 \; v_E} \right) \; \mathrm{erf} \left( \frac{v_E}{v_0} \right) + e^{-v_E^2/v_0^2} \right] \tag{2.20}$$

and

$$k_1 = k_0 \left[ \mathrm{erf} \left( \frac{v_{esc}}{v_0} \right) - \frac{2 \; v_{esc}}{\pi^{1/2} v_0} e^{-v_{esc}^2/v_0^2} \right]. \tag{2.21}$$

The evaluation of Eq. 2.18 for $v_E = 0$ leads to ratio

$$\frac{R(0, v_{esc})}{R_0} = \frac{k_0}{k_1} \left[ 1 - \left( 1 + \frac{v_{esc}^2}{v_0^2} \right) e^{-v_{esc}^2/v_0^2} \right] \tag{2.22}$$

that, for $v_0 = 230 \; km \; s^{-1}$ and $v_{esc} = 600 \; km \; s^{-1}$, is equal to 0.9948 suggesting that the cut-off for $v_{esc}$ has a negligible effect on the total rate.

The above introduced equations, providing the interactions rate as function of the WIMPs halo properties, can be used to obtain the expected differential energy recoils spectrum through the equation

$$\frac{dR}{dE_R} = \int_{E_{min}}^{E_{max}} \frac{1}{Er} dR(E) = \frac{1}{E_0 r} \int_{v_{min}}^{v_{max}} \frac{v_0^2}{v^2} dR(v) \tag{2.23}$$

for which an isotropic scattering is assumed (not depending on $\cos\theta$). In the above equation the quantities $E_0$ indicates the WIMP kinetic energy corresponding to $v = v_0$ while the integration is performed over all that WIMPs energies able to produced a recoil of energy $E_R$. The upper limit is provided by the halo escaping velocity while the lower one is given by $E_{min}(E_R) = E_R/r$, the minimum WIMP kinetic energy required to produce a recoil $E_R$. Differentiating Eq. 2.18 and substituting it in Eq. 2.23, one obtains

$$\frac{dR}{dE_R} = \frac{R_0}{E_0 r}\frac{k_0}{k}\frac{1}{2\pi v_0^2}\int_{v_{min}}^{v_{max}}\frac{1}{v}f(\vec{x},\vec{v},\vec{v}_E;v_{esc})d^3v. \tag{2.24}$$

Substituting for the WIMPs velocities distribution one obtains

$$\frac{dR(v_E,v_{esc})}{dE_R} = \frac{k_0}{k_1}\left[\frac{dR(v_E,\infty)}{dE_R} - \frac{R_0}{E_0 r}e^{-v_{esc}^2/v_0^2}\right]. \tag{2.25}$$

where

$$\frac{dR(v_E,\infty)}{dE_R} = \frac{R_0}{E_0 r}\frac{\sqrt{\pi}}{4}\frac{v_0}{v_E}\left[\mathrm{erf}\left(\frac{v_{min}+v_E}{v_0}\right) - \mathrm{erf}\left(\frac{v_{min}-v_E}{v_0}\right)\right]. \tag{2.26}$$

Assuming the approximation $\vec{v}_E = 0$ Eq. 2.25 reduces to

$$\frac{dR(0,v_{esc})}{dE_R} = \frac{k_0}{k_1}\left[\frac{dR(0,\infty)}{dE_R} - \frac{R_0}{E_0 r}e^{-v_{esc}^2/v_0^2}\right] \tag{2.27}$$

with

$$\frac{dR(0,\infty)}{dE_R} = \frac{R_0}{E_0 r}e^{-\frac{E_R}{E_0 r}}. \tag{2.28}$$

As stressed before, since the value of the escaping velocity is much higher than $v_0$ the effect of the cut-off can be neglected and Eq. 2.26 easier to solve can be used to evaluate the rough behaviour of the differential spectrum: for more precise estimate one has to numerically solve the general Eq. 2.25. In the galactocentric reference frame the velocity Earth velocity $\vec{v}_E$ is provided by

$$\vec{v}_E = \vec{v}_d + \vec{v}_s + \vec{v}_e \tag{2.29}$$

where $\vec{v}_d$ is the galactic disk rotation velocity, $\vec{v}_s$ is the sun proper-velocity (with respect to the disk) measured by relative motion of the nearby stars and $\vec{v}_e$ is the Earth proper-velocity with respect to the solar system frame. Making explicit the terms of the above expression one obtains

$$v_E \approx 244 + 15\cos\left(2\pi\frac{t-152.3}{365.25}\right)\ km\ s^{-1} \tag{2.30}$$

where $t$, expressed in days, is set to zero at $00:00$ $January$ 1: the maximum value of the Earth velocity module occurs the $1^{st}$ of June while the minimum the $1^{st}$ of December. Due to this behaviour, a modulation of the differential energy spectrum as function of time (with period of 1 $year$) is expected. For typical value of $v_0 = 230\ km\ s^{-1}$ and $v_{esc} = 600\ km\ s^{-1}$, the numerical solution of Eq. 2.25 provides the results summarized in Tab. 2.1 for the normalized total rate $R/R_0$: passing from June to December an increment of the low energy part of the spectrum ($E_R < 0.78\ E_0 r$) and a decrease of the high energy ($E_R > 0.78\ E_0 r$) is expected[2]. Obviously these results are just indicative since, as explained before the measured differential spectrum is influenced by nuclear form factor whose effect will be shown later on. Before passing to the other corrections it is useful to observe that for practical use the behaviour described by Eq. 2.26 is well fitted by

$$\frac{dR(v_E, \infty)}{dE_R} = c_1 \frac{R_0}{E_0 r} e^{-c_2 \frac{E_R}{E_0 r}} \tag{2.31}$$

with $c_1$ and $c_2$ constants, depending on the time of the year and having average values $c_1 = 0.751$ and $c_2 = 0.561$.

This theoretical zero-momentum transfer approximation, in order to be compared to an eventually measured recoil spectrum should be modified to count for the finite nucleus dimension and the response of the detector. As far as the former correction is concerned, it can be included within the nuclear form factor $F$ usually expressed as function of the dimensionless variable $qr_N/\hbar$ where $q$ is the module of momentum transfer $\vec{q}$ and $r_N \approx a_N \sqrt[3]{A}$ is the effective nuclear radius. For simplicity $\hbar = 1$ is assumed leading to the dimensionless product

$$qr_N = 6.92 \times 10^{-3} \sqrt{A\ E_R(keV)} (a_N \sqrt[3]{A} + b_N). \tag{2.32}$$

The nuclear form factor is strictly connected with the density distribution $\rho(r)$ of scattering centers within the nucleus being its Fourier transform. In the case of spin-independent interaction, this nucleon distribution is assumed to be equal to the charge distribution in nuclei, obtained by low energy lepton-nucleus measurements. Its rough behaviour, in the case of spin-independent interactions, can be estimated treating the nucleus as a sphere of radius $r_N$ with a uniform density distribution. This approximation leads to more accurate results if a soft-edge is supposed: in this way the discontinuity of $\rho(r)$ for

[2]The value 0.78 is provided by the crossing point of the differential spectra provided by Eq. 2.25 evaluated in June and December

| *Energy Range* | *Normalized total rate* $R/R_0$ | | |
|---|---|---|---|
| $E_R/E_0r$ | *Jun* | *Dec* | *Jun-Dec* |
| 0.0-0.1 | 0.069 | 0.073 | −0.0043 |
| 0.1-0.2 | 0.066 | 0.069 | −0.0035 |
| 0.2-0.3 | 0.063 | 0.066 | −0.0028 |
| 0.3-0.5 | 0.118 | 0.122 | −0.0037 |
| 0.5-0.7 | 0.108 | 0.110 | −0.0016 |
| 0.7-1.0 | 0.144 | 0.144 | 0.0007 |
| 1.0-2.0 | 0.352 | 0.335 | 0.0166 |
| 2.0-3.0 | 0.206 | 0.184 | 0.0220 |
| 3.0-5.0 | 0.179 | 0.148 | 0.0308 |
| 5.0-7.0 | 0.051 | 0.038 | 0.0127 |
| 7.0-10.0 | 0.016 | 0.011 | 0.0050 |
| 0.0-10.0 | 1.374 | 1.302 | 0.0727 (0.1046) |

Table 2.1: Expected annual modulation of the event rate for fixed energy bins. The results are obtained from the numerical integration of Eq. 2.25 in the hypothesis of zero-momentum transfer. In parenthesis it is indicated the value of the total differences between the June and December spectra if the absolute value of the last column is evaluated. The total absolute difference is about 7% of the average normalized total rate if all the spectrum energy range is detected ($E_R/E_0r$ = 0.0-10.0) [24].

$r = r_N$ is removed and the density is assumed to fall to zero within a thin shell of finite thickness $s$. Following the approach described in Ref. [25], the form factor can be expressed as

$$F(qr_N) = 3\frac{j_1(qr_N)}{qr_N}e^{-\frac{(qs)^2}{2}} \tag{2.33}$$

where $j_1$ is the spherical Bessel function of first kind with $n = 1$[3]. The value of $s$ is estimated trying to reproduce, through the approximated Eq. 2.33, the more accurate results obtained from the numerical evaluation of the Fourier

[3]The explicit form of the spherical Bessel function with $n = 1$ is

$$j_1(x) = \frac{\sin x}{x^2} - \frac{\cos x}{x}.$$

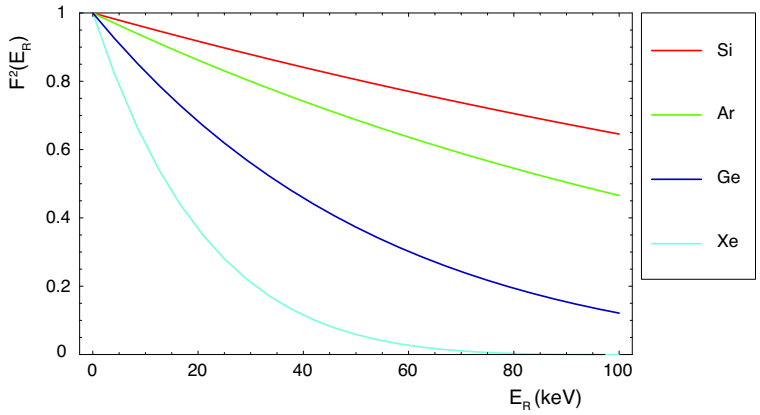


Figure 2.2: Spin-independent nuclear form factors for $Si$ ($A = 28$), $Ar$ ($A = 40$), $Ge$ ($A = 73$) and $Xe$ ($A = 131$) nuclei computed through Eq. 2.33. As the atomic number increases the form factor becomes steeper.

transform relative to a Fermi distribution of scattering centers[4]. A good agreement is obtained for $s \approx 0.9\ fm$ and according to this model $r_N \approx 1.12\sqrt[3]{A}$. The $F^2(E_R)$ behaviour provided by Eq. 2.33 is plotted in Fig. 2.2 for several different targets showing that the higher the nucleus atomic mass the steeper is the corresponding form factor.

As regards of spin-dependent interactions, the usually used form factor (whose computation will not be discussed in this work) is expressed by

$$F^2(qr_N) = \begin{cases} j_0^2(qr_N) & (qr_N < 2.55,\ qr_N > 4.5) \\ 0.047 & (2.55 \leqslant qr_N \leqslant 4.5) \end{cases} \tag{2.34}$$

and $r_N \approx 1.0\sqrt[3]{A}\ fm$. The introduced form factor can be used to count for the finite size of the nucleus and hence to extend the previous results to the non-zero-momentum transfer case as shown in Eq. 2.3. Since $F^2(qr_N)$ is a not increasing function of the momentum transfer, included in the $[0, 1]$ range, the high energy portion of the differential recoils energy spectrum is partially suppressed. For high $A$ nuclei the high energy recoils, those easier to detect, are strongly depleted. This effect somehow tends to absorb the a-priori enhancement of the cross section very rapidly increasing with the atomic mass (see Eq. 2.8).

[4] As stressed before the nuclear form factor represents the Fourier transform of the nucleon distribution inside the nucleus.

Together with these main corrections, in order to properly reproduce the experimental recoil spectrum, one should count for few modifications associated with the detector response. The first is represented by the detection efficiency. In general two particles of different nature, although releasing the same energy within the detector, produce different outputs: this is a well known problem and it could be solved calibrating the detector response with different kind of particles. In particular, since the nuclear recoils are of interest, one could use neutrons scattering data to extract such information: in general these last induce nuclear recoils whose energy spectrum can be used to obtain the proper energy calibration for recoils. This correction could be applied both on the left or right hand side of Eq. 2.9, according to the energy scale used to plot the differential spectrum. If the proper recoil energy scale is used to express the experimental spectrum, there is no need to modify the right hand side. On the other hand, since the majority of the events occurring within the sensitivity window of the detector is associated with electron recoils (mainly produced by $\gamma$ and $\beta$-radioactivity), the so-called electron equivalent energy scale is used and hence the right-hand side terms should be modified to count for the different response of the detector. The different behaviour of the detector is usually represented by the so called *recoil/gamma ratio*, representing the ratio between the energy of a nuclear recoil and an electron generating the same detector output (this value is in general function of the output amplitude). A second correction to the theoretical spectrum should be applied if the detector is built up with a compound target. Obviously in this case the contributions from the two different nuclei have to be decoupled from the global spectrum to obtain two different values of $R_0$. The last couples correction is associated with the not infinite energy resolution of the detector and to the presence of an energy threshold, above which the interactions are detected. The former produces a smearing of the theoretical spectrum and the appropriate corrections have to be evaluated for each detector. The latter introduces a low energy cut in the differential recoils spectrum at $E_R = E_1$. By the light of this last modification, always present in any experiment, the expected detected recoils rate can hence be expressed, through integration of Eq. 2.31 opportunely modified to count for the nuclear form factor $F_A^2(E_R)$,

as

$$R(E_1, E_2) = \int_{E_1}^{E_2} \frac{dR(v_E, \infty)}{dE_R} F_A^2(E_R)\ dE_R = \int_{E_1}^{E_2} c_1 \frac{R_0}{E_0 r} e^{-c_2 \frac{E_R}{E_0 r}} F_A^2(E_R)\ dE_R \tag{2.35}$$

where the upper limit $E_R = E_2$ has been introduced too. Obviously this energy threshold plays a crucial role especially in those experiments with high $A$ nuclei. For this kind of target the steep form factor, lowering the "end-point" of the recoil spectrum, coupled with a high energy threshold could in principle strongly reduce the portion of detected spectrum and, as a consequence, the total detectable rate. The quantity $R(E_1, E_2)$, although measured in *event* $kg^{-1}d^{-1}$, is often referred in *iru* (integrated rate unit) instead of *tru*. This convention is aimed to stress the difference between the rough total rate $R_0$, expressed in *tru*, and a rate obtained from a partial integral of the differential spectrum, as in Eq. 2.35 case.

In the framework of the introduced formalism it is possible to partially compare, at least for spin-independent interactions, the results obtained with different targets. This is achieved by evaluating WIMP-nucleon cross section instead of WIMP-nucleus one. Once assumed an equal neutralino coupling to proton and the neutron ($f_n \approx f_p$), the two cross sections $\sigma_0$ (zero-momentum transfer approximation) and $\sigma_{\chi\text{-}n}$ are connected by

$$\sigma_0 = \sigma_{\chi\text{-}n} \frac{\mu_N^2}{\mu_n^2} A^2 \tag{2.36}$$

where $\sigma_{\chi\text{-}n}$ has been obtained evaluating Eq. 2.8 for a single nucleon (A=1, $\mu = \mu_n$). This last quantity, for the typical involved energies, is not function of the momentum transfer since in this range the nucleon is seen as point-like by the WIMP. In other words, $\sigma_{\chi\text{-}n}$ is the exact total WIMP-nucleon cross section and not the zero-momentum transfer approximation (differently from $\sigma_0$) and it represents the best way to compare results obtained with different targets. The allowed region of this $\sigma_{\chi-n}$-$m_\chi$ parameters space is plotted in Fig. 2.3 for spin-independent interaction in the general MSSM [26]. This region, encompassing many orders of magnitude, is essentially constrained by collider bounds, by the request that the neutralino presents a not negligible cosmological abundance and by indirect limits from measurements of rare processes (such as flavor-changing neutral-current interactions) [4] and of the

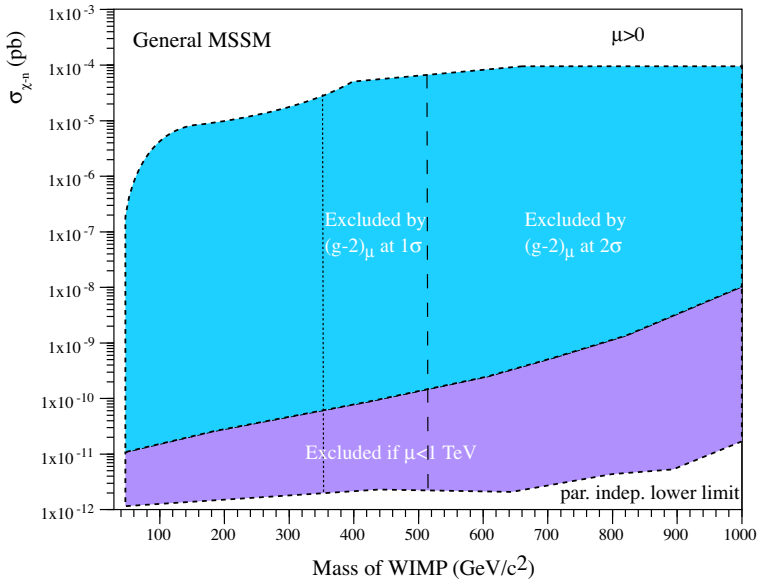


Figure 2.3: Ranges of spin-independent neutralino-nucleon cross section vs. neutralino mass. The colored region is obtained within the general MSSM by imposing collider bounds, a not negligible cosmological neutralino abundance ($0.1 < \Omega_\chi h^2 < 0.2$), by the indirect limits from measurements of $BR(b \to s\gamma)$ [4] and by the requests $\mu > 0$ (Higgs/higgsino mass parameter). The violet region below the dashed line is excluded if one imposes the constraint $\mu < 1\ TeV$. The ranges of $m_\chi$, defined by the two vertical lines, are excluded at 1 $\sigma$ and 2 $\sigma$ $C.L.$ by the discrepancy between the experimental value of the anomalous magnetic moments of muons $(g_\mu - 2)/2$ and the Standard Model prediction [26]. If the discrepancy is interpreted in terms of SUSY, the experimental results of $(g_\mu - 2)/2$ implies $\mu > 0$ [26].

anomalous magnetic moment of the moun[5] [26]. As shown in the next section, only a small portion of the allowed region has been investigated until now by the running experiments and to be able to spam as much as possible the allowed cross section range, very large detectors mass has to be reached.

## 2.3 Direct detection experimental techniques

In order to gain an appropriate sensitivity to WIMP interactions, producing rare and low energy recoils, and to spam a large portion of the allowed

[5]The presence of a SUSY sector will produce additional contributions to standard model predictions constrained at some level by the experimental precision measurements.

region in the above described $\sigma_{\chi\text{-}n}$-$m_\chi$ parameters space, a direct detection experiment has to present some key-features concerning the energy threshold, the target mass, the counting time and the background to WIMP signals.

As far as the energy threshold is concerned such value $E_1$, introduced in Eq. 2.35, has to be as low as possible in order to be sensitive to a larger portion of the expected recoil spectrum roughly falling as an exponential (see Eq. 2.31). Obviously at the same time the upper value $E_2$ has to be as large as possible but in general its value is set to be higher than the expected "end-point" of the recoils spectrum once form factors are introduced. Together with an increase in the total event rate, a lowering of the threshold would consequently enhance the rate annual modulation effect since the difference between June and December recoils spectra increases in the low energy region as shown in Tab. 2.1.

The second important characteristic that a WIMPs detector should present concerns the target mass and the counting time. These two aspects are strictly connected since they both has to be as large as possible in order to provide a large enough statistic for the detection of these rare events. Obviously, since a reasonable experiment lifetime is somehow limited to few years a great increase in the sensitivity is obtained by enlarging the detector mass.

The last and more crucial way to gain sensitivity for direct detection experiment is provided by an effective reduction of the background. The energy window of interest, roughly up to 100 $keV$ of recoils energy, is in general dominated by a substantial background mainly due to events associated with natural radioactivity. This background events are primarily produced by those particles, electromagnetically interacting within the detector and associated to the presence of $\alpha$, $\gamma$, $X$[6] and $\beta$-emitters contained in the materials that compose or surround the detector itself. The second source is represented by neutrons, produced by natural radioactivity or cosmic rays interactions, able to induce nuclear recoils perfectly mimicking a WIMP elastic interaction. For this reason, as a first step, it is mandatory to work in underground laboratory and to recur to the typical precautions for rare events experiments, like material selection (strict requests on radiopurity) and the use of $\gamma$ and eventually neutron shielding. Different treatments of the surviving background can be thought according to the different experimental used techniques.

[6]Both $X$-rays and $\gamma$-emitters induce the emission of a photon finally ending up into an electron recoil.

A first experimental method, followed by a first-generation of WIMPs detectors, consists in the direct detection of all those events releasing an amount of energy contained in the detection window, without discriminating the WIMP candidate signals (nuclear recoils events) from the surviving background events associated with electrons recoils and neutron induced events. A second technique is represented by the so-called dual detection modality experiments that, differently from the previous category, provide a discrimination method to partially reject the surviving background due to electron recoils. This technique, obviously paired to the event energy measurement, can be used to ulteriorly reduce the background and hence to improve in principle the sensitivity of the detector. Usually such discrimination is associated to the fact that electron recoils (due to $\gamma$, $X$ or $\beta$-emission) present an energy loss per unit length ($dE/dx$) different from that associated with nuclear recoils: in general this fact leads to a different ionization density that, according to the various techniques, implies a different output of the experimental apparatus. The discrimination method are generally not infallible and at some level (in the sense of number of background events) starts to fail, leading to electron recoil events wrongly labeled as nuclear recoils. Nevertheless an effective reduction of the background can be achieved applying this modality. An in between method is represented by the search for an annual modulation of the observed events energy spectrum. Following this technique, although only the event energy is measured, a consistent fraction of the background can be rejected, looking only at a particular modulation of the spectrum (few percents of the total WIMP rate). This technique, although promising, implies an incredible stability of the system not easily obtainable.

The experiments performing the first two mentioned techniques can in principle detect the WIMPs by observing a differential recoil spectrum (roughly exponentially falling) above a background after having shown that the features of such spectrum are not compatible with the studied background (note that if the second technique is applied a much more reduced background is measured). In this case the experiment could provide a confidence region in the $\sigma_{\chi\text{-}n}$-$m_\chi$ parameters space representing all those models predicting a WIMPs rate compatible with the results. On the other hand, if such energy spectrum is not observed above the background, the experiment provides an upper limit in parameter space, rejecting with a certain confidence level those models providing an interaction rate higher than the background one. In this case, once

reached a high enough background statistic (aimed to reduce the statistical errors), the sensitivity of the experiment cannot be ulteriorly improved by increasing the mass or the counting time. Following this approach the background rate represents the maximum sensitivity level reachable by a detector and hence, during the projection of an experiment, its estimate plays a crucial role together with the evaluation of the expected WIMP recoils rate. If the background behaviour is known, by the use of independent measurements or simulations, the fitted background spectrum can be subtracted from the measured spectrum. In the same way, if the failure of the discrimination technique has been measured at some level, the expected fake nuclear recoils background (due to misreconstruction) can be subtracted from the measured spectrum, to improve the experiment sensitivity. In this case this last quantity is expected to increase as $(\sqrt{MT})^{-1}$ where $MT$ represent the total exposure, given by the mass and counting time product (for a detailed description of this argument see Ref. [27]).

To avoid misunderstandings it is useful to stress that a detector response is in general function of the nature of the interacting particle. This often leads, as stressed in Sec. 2.2, to a different detection efficiency or, in other words, to a different detector output for a nuclear recoil and an electron recoil (eventually generated by a $\gamma$-interaction) of the same energy. This different behaviour is in general summarized by measuring the so called *recoil/$\gamma$ ratio*, frequently improperly called as *quenching factor*[7]. This quantity, depending onto the target and the applied detection technique, is in general lower than unity: this means that the detection threshold applied to the output signal correspond in general to different threshold energies, higher for nuclear recoils than for electron recoils. This effect is responsible for the raise in the dark matter detectors threshold, usually providing very low energy threshold for electron-recoil events. The *recoil/$\gamma$ ratio* ($RC/\gamma$) is in general function of the energy and it should be known in order to attribute the opportune energy scale to nuclear recoils. Since the detector are typically calibrated recurring to $\gamma$-sources, the thresholds and the energy scales are often given in term of *keV e.e.*, *keV* electron equivalent.

[7] In the rest of the work this quantity will be referred as *recoil/$\gamma$ ratio* while the term *quenching factor* will be used to describe a different quantity defined in Sec. 3.2.3.1

### 2.3.1 Experiments review

The nature of WIMPs makes their detection a hard challenge for experimentalists since, assuming the standard properties for WIMP maxwellian distribution, a typical WIMP masses range $20 - 200\ GeV$ and typical atomic masses for the target nuclei lower than $A = 200$, they should induced tiny nuclear recoil depositing energies roughly up to 100 $keV$ with a rate lower than 1 $tru$. A higher WIMP mass, although increasing the average recoils energy, will end up into a lower interaction rate[8]. Due to this low interaction rate the experiment should reduce as much as possible the background. For this reason they have to run deep underground to avoid the high rate interactions induced by cosmic-rays. A variety of different experimental techniques have been developed in order to be sensitive to such tiny energy depositions. As stressed before the main direct detection experiments can be divided into two large families: single and double detection modality.

Independently from which category they belong, the direct detection experiments are based essentially on three different detection principles (eventually coupled) that are essentially based on

- *ionization detection*: a particle interacting inside the detector target produces a certain amount of free electron-ion couples (liquid or gaseous target) or alternatively of electron-hole pairs (crystals) that can be detected through the means of a collecting drift field and of a detector device sensitive to charge. This kind of measurements is always characterized by $RC/\gamma$ values quite different from unity;

- *scintillation detection*: a particle interacting within a scintillating target induces the emission of light produced by the de-excitation of excited atoms. Such light signal can be detected by the means of opportune light sensitive devices like photomultipliers. Typically used scintillator are $NaI(Tl)$ and $Xe$, respectively presenting $recoil/\gamma\ ratios$ for the scintillation signals of the order of 0.3 for $Na$, 0.09 for $I$ and 0.2 for $Xe$;

- *phonon (heat) detection*: this technique includes all the cryogenic detectors (cooled down to temperature of the order of $few\ mK$) and it is based on the fact that the detector heat capacity is so low that even

[8]Since the local dark matter density has been measured, a higher WIMP mass will correspond to a lower WIMP numeric density.

a tiny energy deposition induces an increase of its temperature. For this kind of detection technique $RC/\gamma = 1$. This aspect leads to two different considerations: on the one hand this technique offers the lowest energy threshold (nuclear recoils of $few\ keV$), on the other it does not intrinsically provide a way to discriminate and reject background events. Furthermore the required low working temperatures bring with them several critical technical difficulties.

A large number of experiments performing one or more of the above detection techniques has been proposed throughout the years. As far as the single modality is concerned, those experiments belonging to this category have to work in really ultra-low background conditions since they cannot provide background rejection. Each event, detected inside the acceptance window, is simply accepted as good WIMP candidate and characterized by the corresponding measured energy. This class contains the pure cryogenic detector CREEST I [28] and the ionization detector HDMS [29]. CREEST I (Cryogenic Rare Event Search using Superconducting Thermometers) is a cryogenic bolometer using sapphire crystals as absorbers operating at 15 $mK$. This technique provides a threshold energy on nuclear recoils of the order of $500 - 600\ eV$, much lower than the minimum thresholds offered by the other experimental methods. This low threshold makes unique this kind of detector, sensitive to very low WIMP masses ($m_\chi < 20\ GeV\ c^{-2}$) although such region has been almost ruled out by accelerator physics. Moreover the reduced target mass (262 $g$) limit the experimental sensitivity. As regards of HDMS (Heidelberg Dark Matter Search), it is built by two high purity ionization germanium detectors: 200 $g$ p-type Ge target detector surrounded by a 2 $kg$ n-type Ge used as veto and hence partially reducing the electron recoils background. The declared threshold is around 2 $keV$ *e.e.* and $RC/\gamma \approx 0.16(E_R)^{0.18}$ for ionization in Germanium.

As far as the double modality is concerned, this category includes all those experiments able to couple to energy measurement a discrimination method to efficiently reject electrons recoils, representing a dominant background. Among the experiments belonging to this class the most significant results have been provided by CDMS (Soudan) [30], EDELWEISS [31] and ZEPLIN I [32]. The Cryogenic Dark Matter Search collaboration has developed a ionization/phonon technique. It uses a set of Ge (each 250 $g$) and Si (each 100 $g$) ZIP ($Z$-dependent Ionization and Phonon) detectors, cooled to

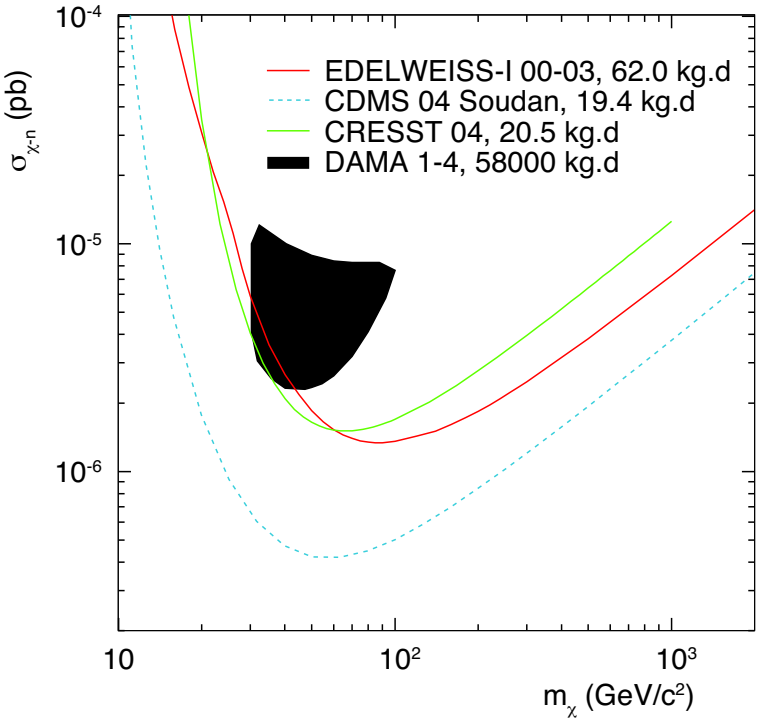


Figure 2.4: 90% C.L. limits (open curves) for spin-independent interactions obtained by CDMS (Soudan) [30], EDELWEISS [31] and CREEST II prototype [36]. The closed curve delimits the DAMA 1-4 $3\sigma$ C.L. allowed region [35].

temperatures $< 50\ mK$. Simultaneous measurement of ionization and phonon signals in the Ge and Si detectors allows an efficient rejection of the remaining gamma and beta backgrounds. While the phonon signal present, as stressed above, $RC/\gamma = 1$, the ionization signal from recoils are "quenched" and hence this second readout channel can be used to discriminate the nature of the particle. The recoil energy threshold is 10 $keV$. EDELWEISS (Experience pour DEtecter Les WIMPs En Site Souterrain) experiment makes use of three 320 $g$ cryogenic Germanium detector: as the CDMS experiment it presents both the ionization and heat readout channels for particle discrimination and it provides a threshold of 20 $keV$ *e.e.*. These two experiments, after a net exposure of 19.4 $kg\ d$ (CDMS) and 62.0 $kg\ d$ (EDELWEISS) of Ge, provides the sharpest constraints so far on WIMP spin-independent cross section, generating, in the usual model dependent $\sigma_{\chi\text{-}n}$-$m_\chi$ parameters space, the 90% C.L. upper limit of Fig. 2.4.

In between the two classes of experiment the DAMA (DArk MAtter) [33] experiment is positioned. It is constituted by nine 9.7 $kg$ highly radiopure $NaI(Tl)$ detector encapsulated inside radiopure $Cu$ housing, providing a threshold at 2 $keV$ $e.e.$. Although only the scintillation light is detected, a signal shape discrimination can be performed at some reasonable level and hence the energy evaluation can be coupled with a discrimination method. The low background and the large achieved detector mass permits to study the annual modulations of the differential spectrum of those scintillation events falling into the energy acceptance window. After seven annual cycles for a total exposure of $1.1 \times 10^5$ $kg$ $d$, the DAMA collaboration claims to have observed, at 6.3 $\sigma$ C.L., an effect which satisfies all the peculiarities of the annual modulation signature. This annual fluctuation in the background rates occurs near threshold, in the 2-6 $keV$ $e.e.$ region (approximately corresponding to the nuclear recoils energy 22-66 $keV$ if the interaction is assumed to occur on $I$ nuclei) where the pulse shape discrimination starts to fail [34]. The observed modulation amplitude is equal to $(0.02 \pm 0.0032)$ $cpd$ $kg^{-1}$ $keV^{-1}$. As soon as the standard spin-independent model described in Sec. 2.2 is assumed, the DAMA evidence region of Fig. 2.4 is obtained[9]. As evident from Fig. 2.4, in the framework of the above described "standard" spin-independent interaction model, the results from EDELWEISS excludes at a 90% C.L. the central value of the signal reported by DAMA while CDMS (Soudan) excludes, at a 90% C.L., the whole DAMA 3 $\sigma$ region [35]. One should note that the DAMA results has not yet beeing excluded or confirmed and that the involved collaborations are still debating on the obtained results [33].

Together with the above mentioned experiments, a large number of mixed technique detectors has been proposed throughout the years most of which are still in R&D phase. The CREEST collaboration has proposed an upgrade to CREEST II [36], in which 33 $CaWO_4$ crystals (300 $g$ each) are used as target and the standard phonon detection is coupled to a scintillation light measurement, providing a discrimination method with a declared efficiency better than 99% for nuclear recoils energies above 15 $keV$. Meanwhile the DAMA collaboration has upgraded to a 250 $kg$ $NaI(Tl)$ detector [37], called LIBRA (Large sodium Iodine Bulk for RAre processes), that is in measurement from March 2003. As in the previous experiment, an annual modulation is searched as signature for WIMP detection. Another mixed technique, common to a lot of

[9]Note that the evidence region of the plot refers only to an exposure of 58000 $kg$ $d$.

new generation experiments, is the simultaneous measurement of scintillation and ionization induced by an interaction within a Liquid Xenon target. This strategy is followed by the family of ZEPLIN experiments [38, 39]. A different technique has been proposed by the XMASS (Xenon neutrino MASS detector) collaboration [40], proposing to build up a self-shielding Liquid Xenon detector (800 $kg$) readout by an array of phototubes.

## 2.4 Argon as proposed WIMP target: the WARP programme

As stressed above an ideal WIMP direct detector should present a huge mass, a detection threshold as low as possible and a highly efficient reduction of the background, obtained through the means of both shielding and particle discrimination technique. Obviously the choice of the target should be based also on the expected event rate, critically dependent onto the target material: in the standard model, presented in Sec. 2.2,the cross section enhances with the atomic mass due to coherent effects while a coherence loss is caused by the nuclear form factor, becoming steeper as the atomic mass increases. After having considered all these aspects the WARP (WIMP ARgon Programme) collaboration has proposed to develop a detector for dark matter search based on liquid argon technology, opportunely modified to provide an efficient particle discrimination technique [41]. This technology seems to be really promising since ultra-pure liquid Argon technology is already well supported industrially, it has a low cost and it is fully operational: this lead to the possibility of realizing very large size detector. The proposed detection method is based onto the simultaneous measurement of scintillation light and ionization produced by a particle interaction in a liquid argon volume, on the top of which a gaseous argon volume is located. The prompt UV scintillation light is detected by a set of photomultipliers while, by the means of an electrical field, the produced ionization electrons are drifted toward the liquid-gas interface, extracted into the gaseous region where, through opportunely set electric fields, they are accelerated inducing the emission of electroluminescence: this luminous signal, called secondary scintillation, is proportional to the amount of drifted ionization electrons and it can be detected by the same array of phototubes. The ratio between the primary and the secondary scintillation signal is function of the amount of excitation and ionization produced by the primary ionizing

particle and, as shown is Sec. 4.1.2.3, their simultaneous measurement can be used to discriminate the nature of the particle and to effectively distinguish nuclear from electron recoils. Once discriminated the nature of the interaction, the primary scintillation amplitude can be used to determine the energy released to the medium: the $recoil/\gamma\ ratio$ has been measured by the means of a dedicated test (see Sec. 4.1.2.3), providing a $RC/\gamma(E_R) \approx 0.3$ in the energy range of interest. This discrimination technique can be paired to a signal shape discrimination (see Sec. 4.2.2.2), leading to very efficient background events rejection power. This proposed technique has been deeply investigated by the means of a 2.3 $l$ detector prototype and it is widely described in Chap. 3 and 4. On the basis of the obtained results, as a first step the collaboration proposes the realization of a 100 $l$ sensitive volume detector (see Chap. 5 for details). Assuming a very reasonable detection threshold of 20 $photoelectrons$ and the estimated photoelectrons yield of 0.67 $phe/keV$, the minimum detectable nuclear recoil energy can be set around 30 $keV$ ($\approx$ 10 $keV$ $e.e.$), significantly improvable by increasing the photoelectrons yield (through optimization of phototubes efficiency or increasing the performance of UV light collection). One should note that for too low threshold the expected background produce by elastic scattering of neutrinos becomes not negligible.

Apart from the technology performance, the Argon as target for WIMPs interactions has been investigated within the framework of the standard spin-independent model illustrated in Sec. 2.2. As an example the argon recoils differential spectrum induced by a flux of WIMPs, with different mass values and coupling with nucleon of the order of $10^{-5}$ $pb$ (belonging to the DAMA allowed region), is reported in Fig. 2.5. This typical spectrum is obtained by multiplying Eq. 2.31 for the argon nuclear form factor displayed in Fig. 2.2 (typical values of $\rho_\chi$ and $v_0$ have been assumed): in these conditions a total rate of approximately 1.4 $tru$ along the whole spectrum is expected. As stressed before the presence of a detection threshold will in general reduce this rate. More generally the potentially observable recoils integrated rate, assuming the conservative detection limit $E_1 = 30$ $keV$ and $E_2 = 100$ $keV$ (see Chap. 5), is indicated in the form of iso-events rate curves in the $\sigma_{\chi\text{-}n}$-$m_\chi$ parameters space of Fig. 2.6. These curves have been obtained by evaluating the contour lines of $R(E_1, E_2)$ defined by Eq. 2.35 and considered as a func-

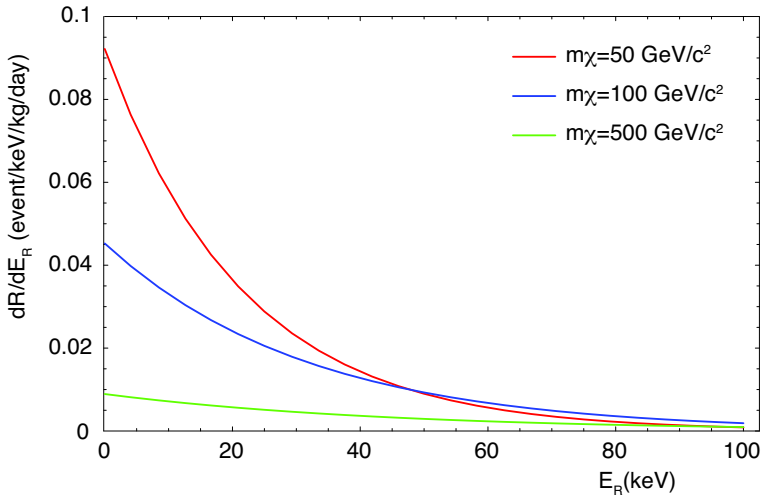


Figure 2.5: Argon recoils differential spectrum for $\sigma_{\chi\text{-}n} \approx 10^{-5}$ $pb$ and different values of $m_\chi$ (50-100-500 $GeV\ c^{-2}$). The spectrum includes the spin-independent nuclear form factor correction shown in Fig. 2.2.

tion of $\sigma_{\chi\text{-}n}$ and $m_\chi$[10]. Incidentally the argon nuclei possess zero nuclear spin making the target sensitive only to spin-independent interactions, simplifying the interpretation of a possibly observed signal. One should note that, in the case of argon target, the whole allowed region of Fig. 2.3 can be spanned if sensitivity of the order of $10^{-7} iru$ are reached (see Fig. 2.6). The estimate of the projected sensitivity for the 100 $l$ detector, directly obtainable by the above iso-rate curves, is left at the end of Chap. 5 (Sec. 5.3), after the description of the apparatus and a rough estimate of the background.

The present work describes the main results obtained by the means of a small WARP prototype, used to evaluate the performance of the proposed background rejection technique, where the signatures of a hypothetical WIMP in Argon has been simulated by the use of neutrons sources. The final chapter is dedicated to the proposed 100 $l$ detector and to its estimated performance.

[10]Equation 2.35 depends on the WIMP-nucleon cross section through the definition of $R_0$. The explicit dependence of this quantity from $\sigma_{\chi\text{-}n}$ can be obtained by combining Eq. 2.16 with Eq. 2.36.

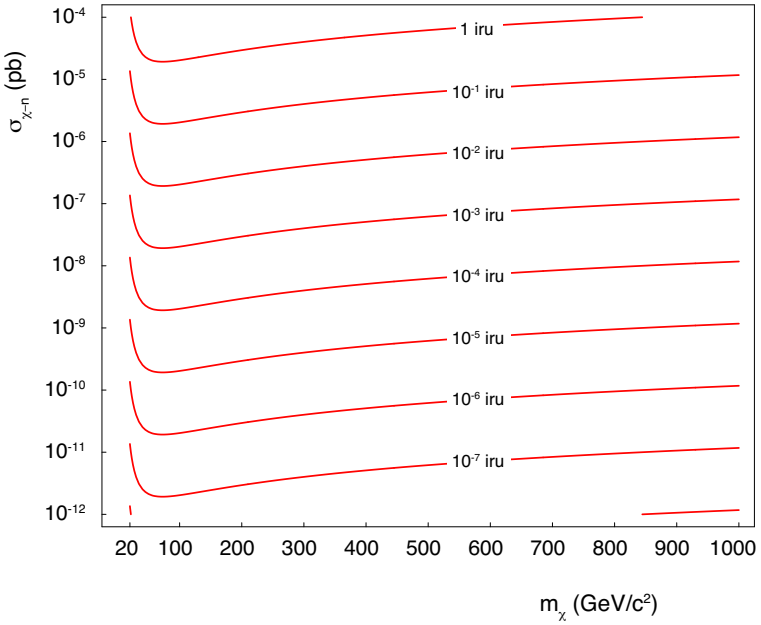


Figure 2.6: Iso-rate curves, expressed in *iru* ($event\ kg^{-1}\ d^{-1}$), as function of WIMP mass and WIMP-nucleon cross section for an Argon ($A = 40$) target with a detection threshold of $E_R = 30\ keV$. The curves are obtained from the numerical solution of Eq. 2.35 with $E_1 = 30\ keV$ and $E_2 = 100\ keV$. As far as the model parameters are concerned, the following values have been assumed: $v_0 = 230\ km\ s^{-1}$, $\rho_\chi = 0.3\ GeV\ c^{-2}\ cm^{-3}$ and for $c_1$ and $c_2$ their average values.

## 2.5 Summary

If dark matter exists and if it constituted by WIMPs, intended as neutralinos, one should expect that although with a very low cross section they should interact elastically with ordinary matter nuclei through their coupling with quarks. As a consequence a large number of experimental efforts are in the direction of directly detecting these induced nuclear recoils that, according to the theoretical predictions, should be distributed roughly as a negative exponential in the approximate energy range $0 \div 100\ keV$ (Sec. 2.2). Due to the rare nature of WIMP interactions, approximately leading, for typical WIMP masses up to $200\ GeV$, to a rate lower (even much lower) than $1\ ev\ kg^{-1}\ d^{-1}$, this energy window is generally strongly dominated by electromagnetic interactions within the detector associated with natural radioactivity. A second and most dangerous source of background is represented by neutrons able to elas-

tically interact with target nuclei inducing, like WIMPs, nuclear recoils. As a consequence direct detection experiments have to reduce as much as possible these otherwise dominant backgrounds, recurring to the typical precautions for rare events experiments: they have to run in underground laboratory (to reduce cosmic rays interactions), using shielding and applying material selection (strict requests on radiopurity).

Supposing that a detector is sensitive to recoils of energy $E_R$ included in the range $E_1 \div E_2$, the total observable recoils rate, assuming a spin-independent interaction, can be expressed by Eq. 2.35

$$R(E_1, E_2) = \int_{E_1}^{E_2} c_1 \frac{R_0}{E_0 r} e^{-c_2 \frac{E_R}{E_0 r}} F_A^2(E_R)\ dE_R$$

where $R_0$ contains the dependency from the unknown WIMP mass and cross section with nucleus and where $F(E_R)$ is the nucleus spin-independent form factor. As explained in Sec. 2.2, while $R_0$ increases with the atomic mass $A$ of the target nuclei, the form factor tends to become more steeper for high $A$, strongly depleting the high energy part of the recoil spectrum. The above equation depends also on the values $c_1$ and $c_2$ that are function of time with a period of 1 $year$. Due to the motion of the Earth around the Sun, the WIMP flux, in a reference system at rest with respect to the Earth, is annually modulated producing a spectrum slowly varying with time and a modulation in the recoils rate $R(E_1, E_2)$. Such modulation, to be consistent with the theoretical expectations, has to satisfy several requests making it quite a strong signature for WIMPs detection.

From an experimental point of view two different direct detection approaches have been followed: they are the so-called, single and dual detection modalities. In the first case every event releasing an amount of energy contained in the detection window is considered as a good signal: no discrimination on the nature of the events (nuclear recoil or electromagnetic interaction) is applied and just an energy measurement is performed (by the means of scintillation or ionization or phonon detection). Those experiments belonging to this class usually present very strict requests on radiopurity. These requests may be eventually slightly released if the dual detection method is applied. Following this last approach two different kind of measurements (scintillation-ionization or scintillation-phonon or ionization-phonon) are performed simultaneously and their combination is used to efficiently discriminate the nature of the interacting particles: in this way it is possible to separate within the

detection window, nuclear recoils from the radioactive background, leading to a higher experimental sensitivity. The experiments performing these two techniques can in principle detect the WIMPs by observing a differential recoil spectrum (roughly exponentially falling) above a background after having shown that the features of such spectrum are not compatible with the studied background. As explained before, a second WIMP signature is represented by an annual modulation in the total rate of interactions satisfying a set of conditions provided by the theory.

In general a competitive dark matter direct detection experiment should provide a huge mass, a detection threshold as low as possible and a highly efficient reduction of the background, both obtained through the means of shielding and particle discrimination technique. The combination of these features increases the sensitivity of the experiment, making it able to spam a large portion of the neutralino allowed region (Fig. 2.3). The WARP (WIMP ARgon Programme) collaboration has proposed to develop a WIMP detector based on liquid argon technology, opportunely modified to provide an efficient particle discrimination technique based on scintillation-ionization measurements. This technology seems to be really promising since ultra-pure liquid Argon technology is already well supported industrially, it has a low cost and it is fully operational: this lead to the possibility of realizing very large size detector. As shown in Chap. 4 also the rejection technique is very performing leading to the possibility to be sensitive to very low WIMP induced recoils rates.

# Chapter 3

# Liquid Argon Technology

## 3.1 Introduction

As previously pointed out, due to the small interaction cross section that makes WIMP-nucleus scattering a very rare event, large masses detectors are favorable in order to spam as much as possible the *minimal SUSY* allowed region of the standard $m_\chi$-$\sigma_{n-\chi}$ plot of Fig. 2.3. In order to provide the requested high sensitivity, new generation dark matter detectors should present also a highly efficient background discrimination technique since nuclear recoils of typical energy $0 \div 100\ keV$, possibly induced by WIMPs interactions, should be discriminated from the more consistent background associated with $\gamma$-particles and electrons.

From this point of view the cryogenic noble liquids technology (Ar and Xe) is one of the most promising techniques: as pointed out by the *ICARUS* collaboration already in 1993 [42], the simultaneous measurement of scintillation and ionization produced in noble liquids by an impinging particle permits to discriminate its nature. Furthermore this technique has the potentiality to be extended to multi-ton sensitive volumes.

The WARP (*W*imp *AR*gon *P*rogramme) collaboration has focused on argon since its technology is already fully operational [43], well supported at industrial level and it has low costs, providing at the same time a sensitivity similar to xenon for a reasonable energy threshold ($E_R > 30\ keV$), as shown in Chap. 2. For this aim the concept of liquid argon TPC detector has been modified to foresee a gaseous phase volume at thermal equilibrium with the liquid one and a different readout technique - light instead of charge is

detected. An interaction in a sensitive volume of liquid argon produces excitation and ionization leading, in presence of an opportune electric field, to the prompt emission of scintillation light and to the drift of a fraction of ionization electrons towards the gaseous region placed on the top of it. Once reached the interface the electrons are extracted to gas and accelerated in a high electric field region in order to induce proportional light emission. The detector is then read out by some light-sensitive device, in this case photomultipliers, detecting both the prompt scintillation signal and the delayed proportional one, the latter delayed by the drift time of electrons in liquid argon. The ratio between the two luminous signals strongly depends on the nature and on the kinematical conditions of the ionizing particles. This technique involving the use of a double phase system is necessary in order to be able to amplify tiny ionization signals.

In the following sections argon technology will be presented and discussed. Particular attention will be given to its general properties (scintillation light, electron-ion production and their recombination), to free electrons extraction through liquid-gas interface and light multiplication processes, the latter playing a crucial role for the proposed double phase technique.

## 3.2 Particles interaction in Argon

The choice of liquid argon for this kind of application is well documented in literature. In the condensed state it provides a high density and, when excited, its atoms decay quite fast ($\tau_s \approx 6\ ns$ and $\tau_t \approx 1500\ ns$) if compared to the typical required drift times (several tens of $\mu s$) with a high scintillation yield. Its high electron mobility, the high dielectric rigidity and the possibility to remove through opportune filters the electronegative impurities to a level of less than 1 *ppb* ($O_2$ equival.) make this medium excellent for TPC like applications requiring electrons drift (see Sec. 3.2.5). The main properties of argon are summarized on Tab. 3.1.

A particle interaction in liquid argon induces, through the mechanism of atomic excitation and ionization, the emission of a narrow band luminescence UV photons. Once an electric field is applied, part of the initially produced ionization can be collected and, in principle, the ratio between the collected light and charge could be used to discriminate the nature and the kinematical condition of the primary impinging particle. As shown in the next sections

| *Parameter* | *Value* |
|---|---|
| Z | 18 |
| A | 40 |
| Boiling point @ 1.02 *bar abs*, $T_f$ | 87.2 $K$ |
| Dielectric rigidity | 100 $kV/cm$ |
| GAr dielectric constant, $\epsilon_g$ | 1 |
| LAr dielectric constant, $\epsilon_l$ | 1.5 |
| $\mu_l$ | $\approx 500 cm^2 s^{-1} V^{-1}$[44, 45] |
| $W'_{g,\beta}$ | 26.4 $eV$[46] |
| $W'_{l,\beta}$ | 23.6 $eV$[46] |
| First ionization potential, $I$ | 15.7 $eV$ |
| Liquid argon energy gap, $\overline{E}_{gap}$ | 14.3 $eV$[46] |
| Rayleigh scattering length, $\lambda_0$ | 90.0 $cm$ |
| Scintillation light wavelength $\lambda$ | 128 $nm$[47] |

Table 3.1: The table summarizes the values of some quantities for argon. LAr and GAr, exactly as the subscripts $l$ and $g$, stand for liquid and gaseous argon. $\mu_l$ is the electron mobility measured in liquid argon at fields up to 100 $V/cm$. $W^{g,\beta}$ and $W^{l,\beta}$ are the average energy losses per electron-ion pair production for minimum ionizing particles.

the process leading to scintillation emission is strictly connected with the ones concerning ionization. This last process could be factorized into two separated mechanisms happening at different times. They are:

- *the mechanism of production of the electron-ion pairs*: the energy of an interacting particle is dissipated into the medium according to its nature and kinematic conditions. Ionization from slow ions ($\beta \approx 0.01$), for example, is not successfully described by the classic Bethe-Bloch formula since electronic collisions are suppressed and energy losses are mainly due to energy transfer to screened nuclei. This fact translates into an average number of pairs per unit energy loss significantly different from that of particles for which Bethe-Bloch formula does not break [48];

- *the recombination process*: the initially produced ion-electron couples tend to recombine under the effect of mutual Coulomb attraction, according to their ionization density and to the presence of eventually

applied external electric fields. Once again the process strongly depends on the nature and kinetic energy of the particle.

For this reason before describing the luminescence phenomenon in argon, it should be useful to deepen the description of the above processes.

### 3.2.1 Electron-ion pairs production in argon

As pointed out before the mechanism of primary electron-ion pairs production strongly depends on the way the impinging particle dissipates its energy into the medium. The behaviour of heavy particles (heavier than electrons) such as protons, muons, pions, $\alpha$-particles and light nuclei, with velocity ranging from relativistic region down to $\beta \approx 0.1$, is successfully explained by the famous Bethe-Bloch formula (with density effect and shell corrections): the energy is released to the medium essentially through inelastic scattering on atomic electrons inducing ionization. Outside that energy range some of the assumptions of Bethe-Bloch are not yet valid: in the velocity regime $0.01 < \beta < 0.1$ no valid theory has been proposed and effects, associated with different interactions, start to dominate (electron capture by heavy nuclei) [48]. For even lower $\beta$ (less than 0.01), in particular for ion velocities smaller than the ones of atomic electrons ($v_0 = e^2/\hbar = 2.2 \times 10^8\ cm/s$), the energy losses are essentially transferred to atoms *in toto* and inelastic collisions with atomic electrons stop occurring. In this case ionization still happens but with a low efficiency. A successful explanation of the mechanism of energy transfer to screened nuclei has been provided by Lindhard [49].

Differently from heavier particles, electron energy transfer through collisions with atomic electrons could not be explained by standard Bethe-Bloch essentially due to its small mass (the assumption that impinging particle remains undeflected during collision with atomic electrons fails) and to the fact that the two interacting particles are now indistinguishable. Although these aspects, the Bethe-Bloch formula can be corrected to fit electrons behaviour since the basic mechanisms of collision loss are still valid.

As found in literature the mean energy loss for $e^-$-$Ar^+$ pair production, although in principle function of the nature and velocity of the interacting particle, has the same value for all particles releasing their energy to the medium essentially through collisions to atomic electrons: its value is $W_{g,\beta} = 26.4\ eV$ in argon gas and $W_{l,\beta} = 23.6\ eV$ in liquid argon [46]. According to the ex-

perimental measurements carried out in argon gas by Jesse, these values are obtained even for $\alpha$-particles of typical energy $few\ MeV$ ($\beta \approx 0.06$) [50]. Completely different values, as suggested by the Lindhard theory, have been measured in the case of slow ions in argon gas [51, 52]: a set of data is reported on Tab. 3.2. Since slow ions ($v < v_0$) ionization efficiency is much lower than that of fast particles, their average energy loss per pair formation is much larger than the one measured for minimum ionizing particles. As clearly shown on Tab. 3.2 the measured $W_{g,R}(E_R)$ increases as the impinging ion velocity decreases. One should note that $Ar^+$ and $Ar^{++}$ ions of energy $E_R \approx 50\ keV$ produce essentially the same amount of ionization.

Lindhard theory conceptually divides the impinging particle energy loss $E$ into two parts, $\overline{\nu}$ and $\overline{\eta}$: $\overline{\nu}$ stands for the average energy ultimately released directly to atomic motion while $\overline{\eta}$ represents the average energy ultimately given to the electrons of the medium. The two introduced contributions could be considered quite well separated: slow atoms, recoiling after the interaction with the impinging particle, are not able to effectively excite electrons and, viceversa, the energy given to electrons can be transferred back to atoms only extremely slowly. This observation leads to the equation

$$E = \overline{\eta} + \overline{\nu}. \tag{3.1}$$

The energy loss given due to inelastic interaction with the atomic electrons can be expressed as [53]

$$\overline{\eta}(E) = N_i \overline{E}_i + N_{ex} \overline{E}_{ex} + N_i \overline{\epsilon}_{se} \tag{3.2}$$

where $N_i$ is the number of electron-ion pairs ultimately produced with an average energy expenditure $\overline{E}_i$, $N_{ex}$ the number of argon excited atoms at an average energy expenditure $\overline{E}_{ex}$ and $\overline{\epsilon}_{se}$ the average kinetic energy of the sub-excitation electrons (electrons whose energy, lower than excitation potential, goes into heat). All these quantities should be computed only at the end of the global process, when primary and secondary ionization electrons have reduced their energy to a value below $E_i$ and $E_{ex}$ and they are no more able to excite or ionize: at the same time they should be evaluated before recombination eventually occurs. *In practice recombination effects should be computed separately on the number of electron-ion pairs provided by Lindhard theory.* One should note that in the noble gases the average energy loss per ionizing collision $\overline{E}_i$ exceeds the ionization potential value $I$ since part of the ionization energy

| *Particle* | $E_R$ $(keV)$ | $v_0/v$ | $W_{g,R}$ $(eV)$ | $\overline{N}_i$ $(pairs)$ |
|---|---|---|---|---|
| $H^+$ | 50.00 | 0.704 | 26.8±0.2 | 1868.0±9.5 |
| $He^+$ | 25.19 | 1.986 | 29.6±4.5 | 850.3±15.1 |
| | 50.06 | 1.408 | 28.8±0.4 | 1740.6±19.6 |
| $C^+$ | 25.16 | 3.441 | 55.0±0.7 | 457.2±5.3 |
| | 50.01 | 2.441 | 43.8±0.5 | 1142.6±11.4 |
| $N^+$ | 24.97 | 3.734 | 62.2±0.8 | 401.4±5.0 |
| | 50.00 | 2.638 | 47.4±0.4 | 1054.9±6.2 |
| $Ar^+$ | 24.90 | 6.320 | 90.9±1.6 | 273.9±4.8 |
| | 30.97 | 5.670 | 84.5±0.8 | 366.5±3.3 |
| | 37.38 | 5.154 | 78.9±1.1 | 473.9±6.2 |
| | 37.39 | 5.154 | 80.2±0.6 | 466.0±2.8 |
| | 37.49 | 5.152 | 80.3±0.8 | 466.8±4.2 |
| | 41.95 | 4.866 | 79.2±0.9 | 529.7±5.6 |
| | 49.97 | 4.458 | 77.4±0.7 | 645.6±5.6 |
| $Ar^{++}$ | 49.84 | 4.464 | 76.1±0.9 | 654.9±7.4 |
| | 61.97 | 4.004 | 71.9±0.6 | 861.6±6.4 |
| | 74.68 | 3.647 | 68.7±0.7 | 1087.7±10.7 |
| | 74.71 | 3.646 | 69.3±0.8 | 1078.1±12.0 |
| | 83.87 | 3.441 | 67.3±0.7 | 1246.7±11.3 |
| | 100.01 | 3.151 | 65.0±0.5 | 1538.6±8.9 |

Table 3.2: The table shows a set of experimental data concerning the ionization induced by low energy ions in argon gas [51]. For each particle the kinetic energy $E_R$, the velocity with respect to $v_0$, the average number of measured ion-electron couples $\overline{N}_i$ and the deduced average effective energy loss per electron-ion pairs production is indicated.

goes into excited ions and multiply charged ions [53]. Moving to the liquid condensed state the ionization potential loses its role in this context and it should be substituted by the band-gap energy $\overline{E}_{gap}$: a band structure similar to the one for the solid state is usually assumed [46]. In the case of argon this implies the replacement of $I = 15.7\ eV$ with $\overline{E}_{gap} = 14.3\ eV$, leading to different values of $E_i$ and $E_{ex}$ and finally to the measured $W_{l,\beta} = 23.6\ eV$ lower than $W_{g,\beta}$.

The estimate of the introduced variables could be in general quite complex

since the equations governing their behaviour are functions of several parameters among which the involved differential cross sections. The general situation could be sketched as follows: one particle, with mass number $A_1$ ($M_1$) and atomic number $Z_1$, releases an energy $E$ into a medium constituted by one atomic species with mass number $A_2$ ($M_2$) and atomic number $Z_2$. Since at moderate energy ($> 100\ eV$) the behaviour of the atomic electronic clouds could be described with statistical methods, a Thomas-Fermi like approach has been used by Lindhard to simplify the description of the phenomenon. The evaluation of $\overline{\eta}$ and $\overline{\nu}$ involves the so called electronic and nuclear stopping power per atom, respectively $S_e(E)$ and $S_n(E)$, representing the mean energy released per unit length and per atom to electronic and nuclear motion. For low velocities the $S_n(E)$ could be approximated by the constant value $S_n^0$ given by

$$S_n(E) \approx S_n^0 = \frac{\pi^2}{2.7183} \frac{e^2 a_0 Z_1 Z_2 M_1}{Z^{1/3}(M_1 + M_2)} \qquad for\ v < 0.015 v_0 Z^{2/3} \tag{3.3}$$

with $Z = (Z_1^{2/3} + Z_2^{2/3})^{-2/3}$ and $a_0$ is the Bohr's radius. Almost in the same velocity range, the electronic stopping power is proportional to the velocity of the impinging particle and it can be approximated as

$$S_e(N) \approx 8\pi e^2 a_0 \frac{Z_1^{7/6} Z_2}{Z} \cdot \frac{v}{v_0} \qquad for\ v < v_1 \approx v_0 Z_1^{2/3}. \tag{3.4}$$

To simplify the formulation it is useful to introduce the so called *dimensionless energy* $\epsilon$ and *range* $\rho$ defined as

$$\epsilon = E \frac{a\ M_2}{Z_1 Z_2 e^2 (M_1 + M_2)} \tag{3.5}$$

$$\rho = R \cdot \frac{4\pi a^2 N_2\ M_2 M_1}{(M_1 + M_2)^2} \tag{3.6}$$

where $a = 0.8853\ a_0 \cdot Z^{-1/3}$, $N_2$ is the number of atoms per unit volume and $R$ is the range. The competition between the two different kind of energy losses can be schematically approached looking at the dimensionless stopping power $d\epsilon/d\rho$ as function of $\sqrt{\epsilon}$ (proportional to the particle velocity). The dimensionless partner of the stopping power can be obtained by equations 3.5 and 3.6 and it is given by

$$\frac{d\epsilon}{d\rho} = S \cdot \frac{M_1 + M_2}{4\pi e^2 a\ Z_1 Z_2 M_1} \tag{3.7}$$

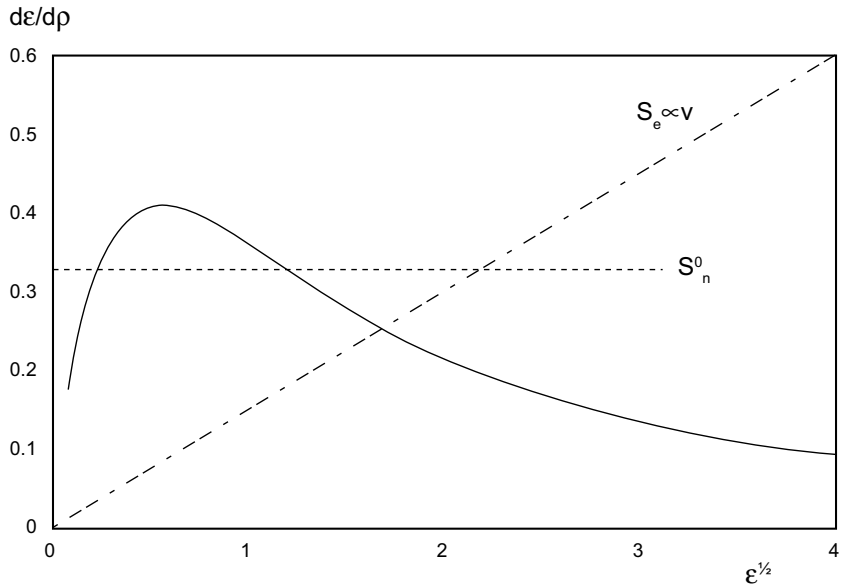


Figure 3.1: Stopping power expressed as function of the dimensionless variables. The solid line represents the behaviour of the numerically computed nuclear stopping power $(d\epsilon/d\rho)_n$ assuming a Thomas-Fermi description of screened nuclei (see footnote 1). The dotted line represents the approximation of assuming such stopping power as constant while the dotted-dashed line describes the behaviour of the electronic stopping power $(d\epsilon/d\rho)_e = k \cdot \epsilon^{1/2}$ where $\epsilon^{1/2}$ is proportional to the impinging particle velocity and $k = 0.15$ [49].

where $S$ is the total stopping power per unit length and per atom. In this new dimensionless variables space, plotted in Fig. 3.1, the condition $S_n(E) = S_n^0$ and Eq. 3.4 translate respectively into $(d\epsilon/d\rho)_n = 0.327$ and $(d\epsilon/d\rho)_e = k \cdot \epsilon^{1/2}$ where $k$, although function of the involved parameters, is often within the range $0.10 < k < 0.20$. In this approximation it is obvious that the two curves cross each over at a particular value of the dimensionless energy referred as $\epsilon_c$: for a typical value of $k = 0.15$ the dimensionless velocity corresponding to this critical point is $\sqrt{\epsilon_c} = 4.75$. As partially shown in Fig. 3.1, three different regimes of the phenomenon are naturally suggested by the behaviour of nuclear and electron dimensionless stopping power. They are

- *Region* I ($0 < E \lesssim E_c(\epsilon_c)$): in this region the nuclear stopping power is dominant even if $S_n$ is not approximated as a constant;
- *Region* II ($E_c(\epsilon_c)E \lesssim E_1(\epsilon_1)$): the upper bound of this region is mainly

defined by $v_1$ value that determines, as explained above (see Eq. 3.4), the region of proportionality between electronic stopping power and particle velocity. This corresponds to $\epsilon_1 \approx 10^3$. In this energy region the energy loss due to electronic collision starts to dominate and the ratio $S_e/S_n$ rapidly increases: $S_e$ reaches a maximum for $v \approx v_1$.

- *Region* III ($E \gtrsim E_1(\epsilon_1)$): in this region electronic stopping power, after having reach its maximum for $v \approx v_1$, starts decreasing and gradually it approaches Bethe-Bloch. The ratio $S_e/S_n$, although still increasing, tends to saturate and it reaches a value of the order of $4 \times 10^3$.

For region I and II, in which Eq. 3.4 is a good approximation of the electronic stopping power, and for $Z_1 = Z_2$ (for example a nuclear recoil in a medium) the Lindhard model, without loosing generality, reduces the description of the energy loss to following integral equation for $\overline{\nu}$

$$k \cdot \epsilon^{1/2} \cdot \overline{\nu}'(\epsilon) = \int_0^{\epsilon^2} \frac{dt}{2t^{3/2}} \cdot f(t^{1/2}) \left\{ \overline{\nu}\left(\epsilon - \frac{t}{\epsilon}\right) - \overline{\nu}(\epsilon) + \overline{\nu}\left(\frac{t}{\epsilon}\right) \right\} \qquad (3.8)$$

where $t = \epsilon^2 \cdot \sin^2 \frac{\theta}{2}$ is proportional to the energy transfer and $f$ is a universal numerically computed function describing the scattering once assumed a Thomas-Fermi like interaction potential.[1] It should be noted that the previous equation depends only on $k$ and $\epsilon$. Obviously the knowledge of $\overline{\nu}(\epsilon)$ implies the knowledge of $\overline{\eta}(\epsilon)$ since for definition $\epsilon = \overline{\nu}(\epsilon) + \overline{\eta}(\epsilon)$. The integral Eq. 3.8 has been obtained by summing up energy losses due to electronic collisions produced by the impinging particle, by the scattered atoms and by the excited electrons: in the sum each term has been weighted with the average probability of occurrence of each individual process (given by the corresponding differential cross section). To compute the equation two more conditions have

[1] The electrostatic interaction potential produced by a nucleus screened by the electron cloud can be described as

$$V(r) = \frac{Z_1 Z_2 e^2}{r} \cdot \phi_0\left(\frac{r}{a}\right)$$

where $r$ is the distance between the probing charge and the centre of the positive charge distribution and $\phi_0(x)$ is the Fermi function for a single Thomas-Fermi atom. The resulting differential cross section between two atoms for non-relativistic energies can be approximated as

$$d\sigma = \pi a^2 \frac{dt}{2t^{3/2}} f(t^{1/2})$$

where $f$ is a universal function computed numerically starting from Fermi function. Its behaviour for high energy and not too small angles approaches the standard Rutherford cross section.

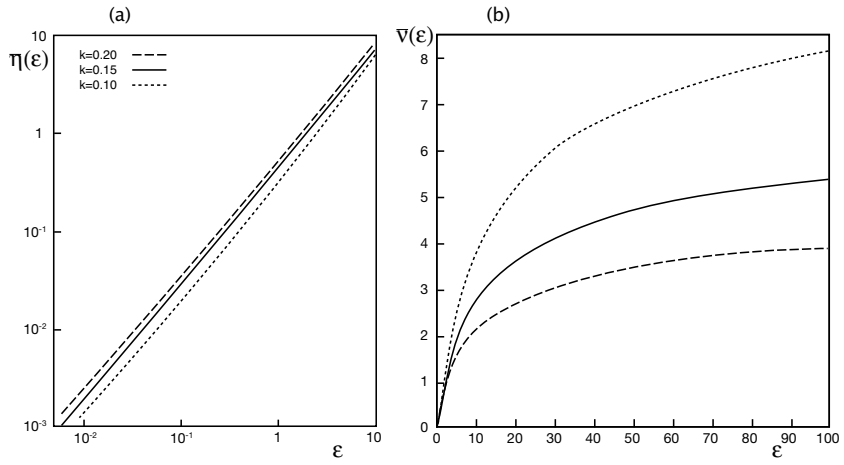


Figure 3.2: Figure *a* and *b* shows the numerical solutions of Eq. 3.10, for various values of $k$, expressed in terms of $\overline{\eta}(\epsilon)$, in the low energy region, and $\overline{\nu}(\epsilon)$, in the intermediate energy region [49].

been assumed. The first request is that energy transfer to electrons is small if compared with the impinging particle energy. This assumption is valid since, as stated before, the theory is not interested in explaining the energy loss for very low energy. The second request is that nuclear and electronic collisions can be decoupled: once again the observation that only a negligible part of electronic excitation occurs at small impact parameters, where nuclear collisions play a role, justifies the assumptions. A numerical solution of Eq. 3.10 has been computed by Lindhard for fixed values of $k$: the results are plotted in Fig. 3.2 for the low and intermediate energy intervals.

Since the final goal of the present work is the description of the behaviour of argon recoils of low energy (energy region I and II) in argon, the conditions $Z_1 = Z_2 = 18$ and $A_1 = A_2 = 40$ can be imposed to simplify the above introduced formulas leading to

$$\epsilon = 11.5\ Z_1^{-\frac{7}{3}} \cdot \left(\frac{E_R}{1\ keV}\right) = 0.014 \cdot \left(\frac{E_R}{1\ keV}\right) \tag{3.9}$$

and $k = 0.133\ Z_1^{2/3} A_1^{2/3} = 0.15$. The corresponding energy boundaries of region I and II ($k = 0.15$) become $E_c \approx 340\ keV$ and $E_1 \approx 50\ MeV$, the latter abundantly far away from the region of interest. These considerations imply that Eq. 3.10 can be used to describe appropriately the ionization induced by argon recoil of low energy. The behaviour of $\overline{\nu}$ for argon recoils in argon is

then efficiently described by the solution with $k = 0.15$ plotted in Fig. 3.2. Such solution, in the energy range $0.1 < \epsilon < 2.0$ (corresponding to 1 $keV \lesssim E \lesssim 140$ $keV$), is well fitted by the following function

$$\overline{\eta}(\epsilon) \approx A \cdot \epsilon^{\alpha} \qquad with\ \alpha = 1.171\ and\ A = 0.421. \tag{3.10}$$

The corresponding value of $\overline{\nu}(\epsilon)$ is obtained from the above equation recalling that $\epsilon = \overline{\nu}(\epsilon) + \overline{\eta}(\epsilon)$. In this energy range and according to the introduced parametrization, the fraction of energy loss spent for electronic collisions, often called *nuclear quenching factor* (see Sec. 3.2.3.1), can be described recalling the above equation as

$$q_{nc} = \frac{\overline{\eta}(E_R)}{E_R} = \frac{\overline{\eta}(\epsilon)}{\overline{\eta}(\epsilon) + \overline{\nu}(\epsilon)} \approx A_I \cdot \left(\frac{E_R}{1\ keV}\right)^{\alpha_I} \tag{3.11}$$

where $E_R$ is the kinetic energy of the argon nuclear recoil, $\alpha_I = \alpha - 1 = 0.171$ and $A_I = 0.203$.

To avoid misunderstandings due to different definitions found in literature of the quantity experimentally measured, it should be useful, at this point, to write them down in the case of a nuclear recoil and of a relativistic particle both interacting in argon gas. As suggested by the results from several experiments [53, 50] conductedin argon gas at low pressure[2], the average number of electron-ion pairs produced by relativistic electrons, or even $\alpha$-particles (5.298 $MeV$), is roughly proportional to their released energy. Such constant of proportionality, derived from the experimental data, is often defined as the average energy expended for $e^{-}$-$Ar^{+}$ pair production and in argon gas its value is [53]

$$W_{g,\beta} = \frac{E}{\overline{N}_i} = 26.4\ eV \qquad (for\ argon\ gas). \tag{3.12}$$

In the case of nuclear recoils of low energy the situation is more complex since, as experimentally shown, the average pair number is not proportional to the recoil energy loss. Such effect could be understood by observing that for these particles the average energy spent for atomic collision is not negligible and hence the average number of produced couple should be proportional not to

[2]One should note that in argon gas at low pressure, as the one used in the mentioned experiments, the effect of recombination is strongly suppressed, even at low electric fields, and that the measured value of collected pairs $\overline{N}_i$, is essentially equal to the average number of pairs initially produced and given by Lindhard theory.

the total energy but only to the energy ultimately given to electrons. This translates into

$$\overline{N}_i = \frac{\overline{\eta}(E_R)}{W'_{g,R}} \tag{3.13}$$

where $W'_{g,R}$ is the proportionality constant typical of the medium and of the kind of particle. According to this definition $W'_{g,R}$ is independent from the energy loss. Since from the experimental side the measurable quantities are essentially the global energy loss $E_R$ and the number of pairs, it should be helpful to introduce, as in the previous case, a kind of *effective energy loss per pair production*, function of the energy loss and given by

$$W_{g,R}(E_R) \equiv \frac{E_R}{\overline{N}_i} = \frac{\overline{\eta}(E_R) + \overline{\nu}(E_R)}{\overline{\eta}(E_R)/W'_{g,R}} = W'_{g,R} \cdot \frac{\overline{\eta}(E_R) + \overline{\nu}(E_R)}{\overline{\eta}(E_R)} \tag{3.14}$$

that for $1\ keV \lesssim E_R \lesssim 140\ keV$, recalling Eq. 3.11, becomes

$$W_{g,R}(E_R) = \frac{W'_{g,R}}{A_I \left(\frac{E_R}{1\ keV}\right)^{\alpha_I}}. \tag{3.15}$$

It should be noted that for relativistic particles $W'_{g,\beta} \equiv W_{g,\beta}(E) = 26.4\ eV$ since $E \approx \overline{\eta}(E)$: for this reason the differentiation of the two quantities becomes superfluous.

To compare the experimental results by Phipps *et al.* shown on Tab. 3.2 to the theoretical prediction of Lindhard model, the value of the $W'_{g,R}$ should be known. As a first approximation one can suppose that $W'_{g,R} = W'_{g,\beta} = 26.4\ eV$ (note that this does not mean that $W_{g,R} = W_{g,\beta} = 26.4\ eV$)[3]: in other words

[3]Throughout the section different definitions concerning the average energy for pair production have been introduced. They are

- $\overline{E}_i$: it is defined as the *average energy loss per ionizing collisions*. This average energy counts for the fact that some ionized atoms can be excited or double charged and for this reason $\overline{E}_i > I$ where I is the ionization potential;
- $W'_{particle}$: it is defined as the ratio between the *energy spent into electronic collisions* and the number of produced couples $N_i$. This average energy differs from the previous one since it counts for the fact that the energy loss given to atomic electrons goes not only into ionization but also into excitation and sub-excitation electrons kinetic energy as explained by Eq. 3.2. Its value is not function of the impinging particle energy and $W'_{beta} > \overline{E}_i > I$;
- $W_{particle}(E)$: this value is defined as the ratio between the *global energy* loss and the number of ion pairs $N_i$. This value for slow particles is higher than $W'_{beta}$ since it counts for the fact that only a fraction of the energy loss is spent for electron

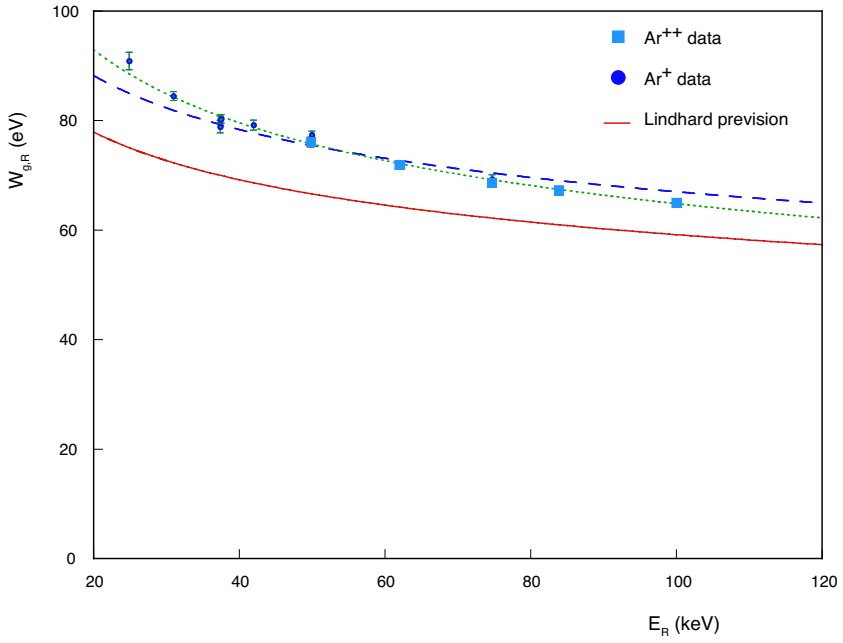


Figure 3.3: Experimental points of the energy loss $W_{g,R}$ required to produce a ion-electron pair for slow argon ions in low pressure argon gas [51]. The prediction of the Lindhard model (red line) are also shown: it seems to underestimate the quantity. Two different fits have been executed on experimental data. See the text for more details.

the mean energy expended to produce an electron-ion pair is assumed to be independent from the nature of the impinging particle although the effective average energy loss differs in the two cases. According to this hypothesis the different amounts of couples produced, per unit energy loss, by a relativistic electron and by a nuclear recoil are only due to the two different fractions of the global energy loss given to electrons of the medium. As previously stated the comparison can be meaningful only in the hypothesis that experimental data are not suffering for ionization losses (the authors of the considered work estimate the recombination effect to be less than 2% studying the ionization curves as function of the applied electric field for different argon gas pressure [51]). The theoretical prediction of $W_{g,R}$ obtained by Eq. 3.15 (assuming

collisions. In general this quantity, differently from $W'_{particle}$ depends on the energy of the interacting particle and represents the average energy loss for ionization pair production.

$W'_{g,R} = W'_{g,\beta} = 26.4\ eV$) and the results from Phipps *et al.* work are plotted together in Fig. 3.3: as evident the theoretical prediction seems to underestimate it although the general behaviour seems well described. The discordancy should be caused by a wrong estimate of $W'_{g,R}$ or by a low accuracy of the model itself. To rule out the first hypothesis a fit to the experimental data with the functional form 3.15 provided by the model ($\alpha_I = 0.171$ and $A_I = 0.203$), leaving the $W'_{g,R}$ parameter free to run, has been executed. As shown in Fig. 3.3 (dashed blue line) the results of this fit provides $W'_{g,R} = 30.1\ eV$ but the data are not well described due to the wrong slope. For this reason the inaccuracy should be attributed to the model itself. A second fit with the same functional form suggested by the theory but leaving $\alpha_I$ and $A_I$ free and assuming $W'_{g,R} = W'_{g,\beta} = 26.4\ eV$ has been performed. An excellent agreement as evident from figure 3.3 (dotted green line) is provided for $\alpha_I = 0.224$ and $A_I = 0.145$.

The results of the previous fit can be used to extrapolate the value $W_{l,R}(E_R)$ for argon recoils in liquid argon: the only parameter of Lindhard theory that changes its value from gas to liquid medium is the $W'_{g,R}$. For liquid argon $W'_{l,\beta} = 23.6\ eV$ has been measured by several authors [46, 54]. According to this observation the mean number of ion pairs produced by an argon recoil in liquid argon can be expressed as

$$\overline{N}_i(E_R) = \frac{E_R}{W_{l,R}(E_R)} = \frac{A_I E_R}{W'_{l,R}} \left(\frac{E_R}{1\ keV}\right)^{\alpha_I} \approx 6 \cdot \left(\frac{E_R}{1\ keV}\right)^{\alpha_I+1}. \qquad (3.16)$$

with $\alpha_I = 0.224$: this parametrization will be used later on for a comparison with the experimental data of this work. In this context also the range of low energy argon recoils in argon should be useful. Figure 3.4 shows the range values for low velocity argon ions in argon gas at standard pressure and temperature conditions [52]: according to the data a 50 $keV$ argon recoil is brought to rest within approximately 175 $mum$ leading to an average stopping power of about 1.6 $keV/(\mu gr/cm^2)$. As reference this average stopping power should be compared to measured one for a 5.5 $MeV$ $\alpha$-particles and to 1 $MeV$ electron respectively equal to 0.73 $keV/(\mu gr/cm^2)$ and $1.6 \times 10^{-3}$ $keV/(\mu gr/cm^2)$ [55].

### 3.2.2 Ionization recombination process in liquid argon

As shown in the previous section the interaction of a particle in a noble gas detector produces, according to its properties, a certain amount of ioniza-

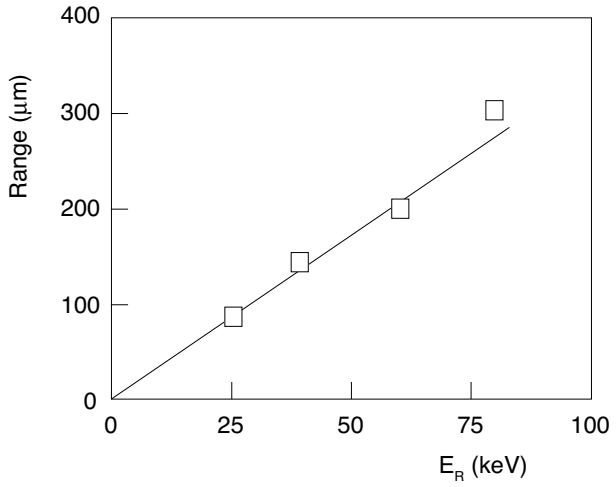


Figure 3.4: Range values at STP of low-energy heavy ions in Ar gas [52].

tion electron-ion pairs. Obviously after being created the electron and ion can recombine. Their recombination process has been widely studied throughout the years and a large variety of measurements has been conducted [56, 64]. According to these results the recombination process is strongly dependent on external applied electric field strength, on the nature and on the kinematical properties of the ionizing particle that, through its $dE/dx$, can affect the ionization density. From a theoretical point of view, two classes of models have been proposed: the so-called *geminate theory* and *columnar-like theory* [59, 60, 61]. The former assumes that each electron-ion pair is spatially separated from the others. On the other hand, the latter describes the process under the assumption that an electron could recombine even with an ion different from its parent one. According to the physical properties of the medium (especially on its density) one approach should be more appropriate than the other.

In the following description of the proposed models it is supposed that an impinging particle interacts in a gaseous or liquid volume where an electric field of strength $\mathcal{E}_d$ is applied. A charge detector is placed at the end of the drift volume (with respect to the drifting electrons direction). According to several model-dependent parameters, the effect of recombination can be described through a relationship between the initially produced electronic charge (proportional to the number of electrons and ions initially produced) and the

collected charge $Q$ (proportional to the collected number of electrons escaping from recombination). In all these models the effect of electron capture by electronegative impurities, eventually contained in the medium, has been discharged.

The first geminate model has been developed by Onsager [60]. It refers to the interaction between two ions. This model treats all the ions pairs as independent. In other words it assumes that the couples are spatially separated and that the two ions interact through an infinite range Coulomb force. On this basis the theory evaluates the probability that a pair of ions, of initial given separation $r_0$, recombine: such quantity is obviously function of the applied field that influences mutual electrostatic attraction. For electron-ion recombination and for low electric field ($\mathcal{E}_d \ll \mathcal{E}_{kT}$) the predicted behaviour of collected charge as function of the drift field is well approximated by [56]

$$Q(\mathcal{E}_d) = Q_0 \left(1 + \frac{\mathcal{E}_d}{\mathcal{E}_{kT}}\right) e^{-\frac{r_{kT}}{r_0}} \qquad with\ \mathcal{E}_{kT} = \frac{2\epsilon k^2 T^2}{e^3} \tag{3.17}$$

where $r_0$ is the thermalization length and $r_{kT} = e^2/\epsilon_r kT$, called Onsager length, represents the distance between electrons and ions for which the electrostatic potential energy equals the electron thermal energy $(3/2)kT$. For liquid argon at $T = 87.2\ K$ the parameters assume the values $r_{kT} = 89.6\ nm$ and $\mathcal{E}_{kT} = 1.58\ kV/cm$ [56]. The value of $r_0$ is not provided by the model itself and it is used as free parameter to fit the data. The experimental data collected by Scalettar *et al.* in liquid argon with a $^{113}Sn$ electrons source are plotted in Fig. 3.5 together with the fit from Onsager model. Even at low field ($\mathcal{E}_d \approx 0.3\ kV/cm$), where the applied approximation is evidently justified, the functional behaviour described in Eq. 3.17 is in strong disagreement with the experimental data. Such discrepancy should be caused by the fact that the assumption of an infinite range Coulomb attraction does not fit the argon liquid case: due to its high polarization coefficient the induced argon dipoles around the ions tend to reduce the effective potential falling off more rapidly than $1/r$ [61].

A completely different approach has been used by Jaffé in his so-called columnar model [59] for which electron-ion pairs are not independent and an electron could recombine both with its parent ion or with another ion produced along the ionization track. The electron and ion recombination rate

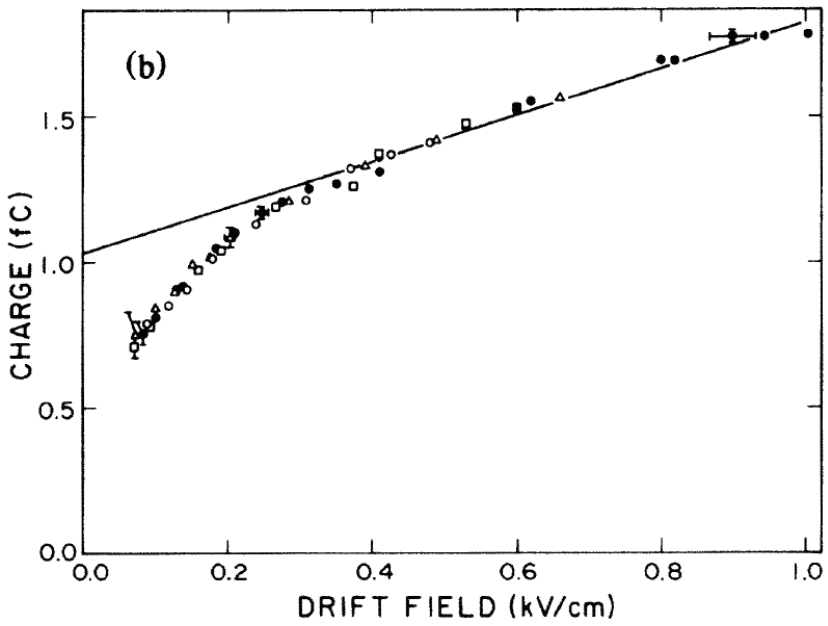


Figure 3.5: The total collected charge as function of the applied electric field is plotted for $^{113}Sn$ conversion electrons in liquid argon [56]. The fit of Onsager model is plotted too. A strong discrepancy in the behaviour at low field can be observed. For field intensity higher than the shown scale the approximation of Eq. 3.17 is no longer valid.

can be in general described through the diffusion equations

$$\begin{aligned} \frac{\partial N_+}{\partial t} &= -\mu_+(\mathcal{E}_d \cdot \nabla N_+) + d_+(\nabla^2 N_+) - \alpha N_- N_+ \\ \frac{\partial N_-}{\partial t} &= \mu_-(\mathcal{E}_d \cdot \nabla N_-) + d_-(\nabla^2 N_-) - \alpha N_- N_+ \end{aligned} \tag{3.18}$$

where $N_+$ and $N_-$ is respectively the ions and electrons charge distribution, $\mu_+$ and $\mu_-$ their mobility, $d_+$ and $d_-$ their diffusion coefficients, $\alpha$ the recombination coefficient (assumed independent from the ion densities). In these equations the effect of electrostatic interaction has been absorbed in the last phenomenological term counting directly for recombination. Their solution is well known for $\alpha = 0$ (zero recombination) for which the two equations become decoupled. On the basis of this observation Jaffé computes the system solution treating the recombination term with perturbative technique in the particular case of $\mu_+ = \mu_- = \mu$, $d_+ = d_- = d$ and assuming an initial charge distribution similar to a column around the ionization track. From here the

name columnar theory. It should be noted that this approach, although correct for gas, fails in the liquid case where the strong recombination cannot be considered as a perturbation. The obtained solution can be expressed as

$$Q = \frac{Q_0}{1 + F(\mathcal{E}_d)} \tag{3.19}$$

where $F(\mathcal{E}_d)$ is a complex function of the field that for high enough field strength ($10 \div 500\ kV/cm$) can be approximated with

$$F(\mathcal{E}_d) = \frac{\alpha N_0}{4\sqrt{2\pi} b \cdot \mu \mathcal{E}_d} \tag{3.20}$$

where $N_0 = N_-(t = 0) = N_+(t = 0)$ and $b$ is a constant. Kramers pointed out that the perturbative technique is unreliable since the diffusion term, in presence of the electric field, becomes smaller than drift and recombination terms. He solved the system 3.18 neglecting the diffusion term and considering it, later on, as a perturbation [56]. The final predicted behaviour for high fields traces the Jaffé approximations.

One should note that both the previous techniques assume an equal drift velocity for electrons and ions ($\mu_+ \mathcal{E}_d = \mu_- \mathcal{E}_d = \mu \mathcal{E}_d$): this assumption is obviously too rough for liquid argon since $Ar^+$ ion mobility is several order of magnitude lower than electron mobility in liquid argon [61]. This observation together with the smallness of the diffusion term in presence of electric field (few *mm* per *meter* of drift in liquid argon) has been used by J. Thomas and D. A. Imel to reduce the system 3.18, in the case of liquid argon, into

$$\begin{aligned} \frac{\partial N_+}{\partial t} &= -\alpha N_- N_+ \\ \frac{\partial N_-}{\partial t} &= \mu_- \mathcal{E}_d \frac{\partial N_-}{\partial z} - \alpha N_- N_+ \end{aligned} \tag{3.21}$$

where $\mathcal{E}_d$ has been assumed parallel to the $\mathbf{z}$ direction and the drift term for ions has been neglected. Differently from the previous model the columnar boundary conditions are here substituted by a uniform distribution of electron-ion pairs within a box of dimensions $a$ (at $t = 0$ the box contains $N_0$ ions and electrons). Each pair is considered as in the Onsager model as independent: in other words the proposed *box model* is a geminate theory although the mathematical approach is similar to the one introduced by Jaffé columnar theory [61]. According to this model the dependence of the recombination on the external electric field is expressed by

$$Q(\mathcal{E}_d) = \frac{Q_0}{\xi} \ln(1 + \xi) \qquad with\ \xi = \frac{N_0 \alpha}{4a^2 \mu_- \mathcal{E}_d}. \tag{3.22}$$

Since the value of the $\xi$ is not provided by the theory itself, it is usually treated as a free parameter of the model to be fitted to the experimental data. Apart from its absolute value, it should be noted that the predicted recombination functional form, for high field, is essentially equal to the asymptotic formula by Jaffé.

A modification of their box model has been suggested by Thomas and Imel themselves [62] on the basis of the observation that the ionization density induced by an impinging particle increases its value along the track ($dE/dx$ increases during the slowing down process). Hence they propose a *double density box model* where $\xi_1$ describes the minimum ionizing section of the track and $\xi_0$ the high density final section. This fact is obviously true also for each $\delta$-ray (ionization electrons enough energetic to ionize) produced by the primary ionizing particle. They define essentially two threshold energies $E_1$ and $E_2$ for describing $\delta$-ray ionization. Those $\delta$-rays with energy below $E_1$ produce too few ionization pair and therefore their induced ionization density is low. High energy $\delta$-rays $E_1 < E_\delta < E_2$ produce only high ionization density. Finally $\delta$-rays with $E_\delta > E_2$ have both minimum ionizing sector (along which they spend the majority of their energy) and a high ionization density blob at the end. Once defined the distribution $N(E, E_\delta)$, giving for an energy deposition $E$ the number of emitted $\delta$-rays of energy $E_\delta$, the global effect of recombination can be computed. Such distribution can be obtained for primary ionizing relativistic electrons recalling Rutherford scattering cross section (for details see [62]). The computation leads to a very simple formula

$$Q(\mathcal{E}_d) = Q_0 \left[ a \frac{\ln(1+\xi_0)}{\xi_0} + (1-a) \frac{\ln(1+\xi_1)}{\xi_1} \right] \tag{3.23}$$

where $a$ is a complex formula of the selected $E_1$ and $E_2$. As in previous single density model the value of $\xi_0$ and $\xi_1$ are obtained by fitting the data. Although more realistic than its predecessor this model presents a limitation: the assumption of a geminate-like recombination is not well motivated in liquid argon since the mean distance between two ionization sites in liquid argon is not too different from the Onsager radius ($\approx 1000$ $\mathring{A}$) [63]. Consequently the pairs can hardly be considered independent.

As suggested from the previous dissertation none of the proposed recombination models is completely satisfying. Experimental data obtained in liquid argon with a $^{113}Sn$ conversion electrons source (364 $keV$), a $^{241}Am$ $\alpha$ source (5.64 $MeV$)[56] and a $^{207}Bi$ electron source (1 $MeV$) [57] are plot-

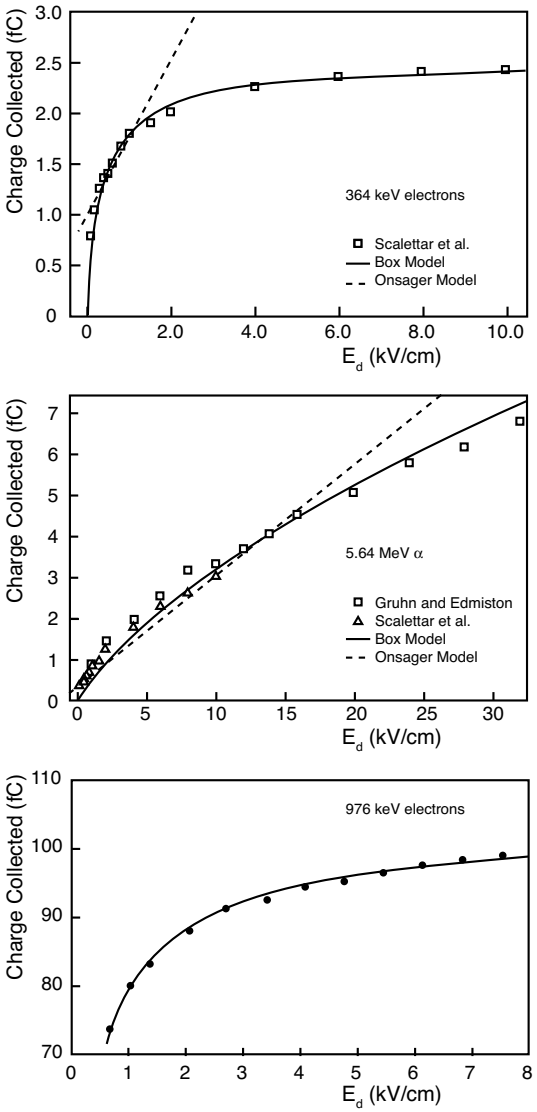


Figure 3.6: The total collected charge as function of the electric field is plotted for $^{113}Sn$ conversion electrons (up), $^{241}Am$ $\alpha$ (middle) and $^{207}Bi$ 1 $MeV$ electrons in liquid argon. The figure shows also the fit obtained with the functional forms from Onsager model [60] and box model [61], for the first two plot plots, and from double density box model for the last [57]. See text for details.

ted in Fig. 3.6. The box model fits and Onsager theory fits are also reported. Although, as described before, the box model assumptions are not correct, the resulting $Q/Q_0$ behaviour as function of the electric field is well

fitted up to 10 $kV/cm$ by the functional forms described in equations 3.23 and 3.23. The result of the fit provides $\xi\mathcal{E}_d = 0.84\ kV/cm$ for 364 $keV$ electrons, $\xi\mathcal{E}_d = 470\ kV/cm$ for 5.64 $MeV$ $\alpha$-particles and $\xi_0\mathcal{E}_d = 2.9\ kV/cm$ and $\xi_1\mathcal{E}_d = 0.28\ kV/cm$ for 1 $MeV$ electrons.

Another interesting approach to recombination is provided by the study of scintillation light. As shown in the next section scintillation and recombination processes are deeply connected, and hence measurements of the particle induced emitted light are useful to gain knowledge on the complex recombination phenomenon.

### 3.2.3 Scintillation light emission in liquid argon

An interaction in argon produces, as stated before, both atomic excitation and ionization, leading to a narrow band 128 $nm$ luminescence emission [65, 63, 66, 67]. As experimentally measured the scintillation light is constituted by two different components: the so-called *recombination luminescence* and *self-trapped exciton luminescence (excitation luminescence).*

The *recombination luminescence* in the UV range originates from the following processes [65]

$$\begin{gathered} Ar^+ + Ar \rightarrow Ar_2^+ r \\ e^-_{hot} + collisions \rightarrow e^-_{th} \\ Ar_2^+ + e^-_{th} \rightarrow Ar^{**} + Ar \\ Ar^{**} \rightarrow Ar^* + heat\ (non\ radiative\ transition) \\ Ar^* + Ar \rightarrow Ar_2^* \\ Ar_2^* \rightarrow Ar + Ar + h\nu\ (UV) \end{gathered} \tag{3.24}$$

In the previous processes the symbol $Ar$ stands for an argon atom, $Ar^+$ for an atomic ion, $Ar^*$ for an excited atom, $Ar^{**}$ for a highly excited atom, $Ar_2^+$ for a molecular ion, $Ar_2^*$ for an excited molecule, $e_{hot}$ for a sub-excitation electron and $e_{th}$ for a thermalized electron. As suggested by the name this process is essentially driven by the presence of a free electron-ion pair. on the other hand the *excitation luminescence* produced by a simpler process [65]

$$\begin{gathered} Ar^* + Ar \rightarrow Ar_2^* \\ Ar_2^* \rightarrow Ar + Ar + h\nu\ (UV) \end{gathered} \tag{3.25}$$

is prompted by the presence of the excited argon atom. Both processes, ending up with the same radiative reaction, induce the emission of a 128 $nm$ UV

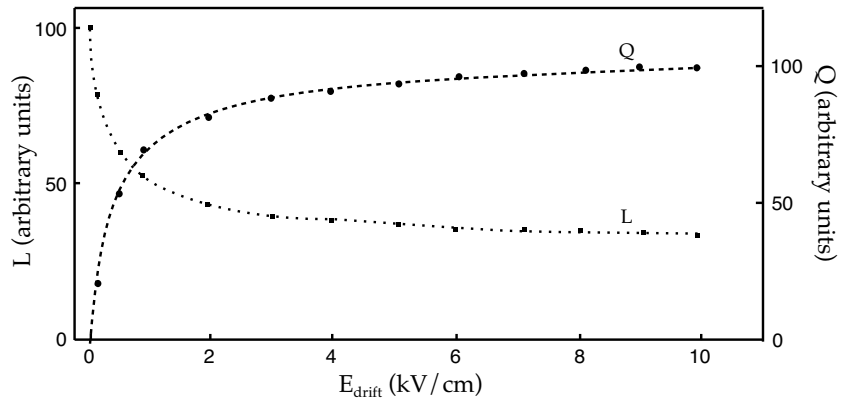


Figure 3.7: The graph shows the behaviour of the luminescence light intensity and of the collected charge as function of the electric field strength. The $y$ axis scales are expressed in arbitrary unit. The left scale refers to luminescence intensity: the value 100 is set for the total light collected at $E_d = 0\ kV/cm$. The right scale refers to wire collected charge and the value 100 is set for the initially produced charge $Q_0$. About 30% of the light produced at zero field seems to be uninfluenced by the application of the electric field, most likely representing the excitation component of the luminescence [65]. The data refer to 1 $MeV$ primary electrons.

photon ($E \approx 9.7\ eV$). The analysis of the light emission spectrum shows that atomic de-excitation photon emission by $Ar^*$ is strongly suppressed: in average, the $Ar^*$ atom captures an $Ar$ atom and forms a $Ar_2^*$ bound state before atomic de-excitation occurs. Nevertheless several lines, probably associated with atomic transitions, have been observed in the infrared region $[0.7 \div 1.8\mu m]$ [68].

As explained in the previous section, the presence of an external electric field can strongly influence recombination process and hence recombination luminescence in liquid argon. The application of such a drift field has been used by the experimentalists to decouple the two light components and to measure their relative intensities referred respectively as $L_{ex}$ for excitation and $L_i$ for recombination [65]: the used experimental setup consists of a parallel plate ionization chamber readout by a photomultiplier and a system of wire to collect eventually drifted charges. Figures 3.7 and 3.8 show the collected light behaviour as function of the applied field and of the collected charge for signals by $^{207}Bi$ internal conversion electrons (1 $Mev$). The collected light reaches its maximum at zero field and it starts decreasing as soon as the applied field

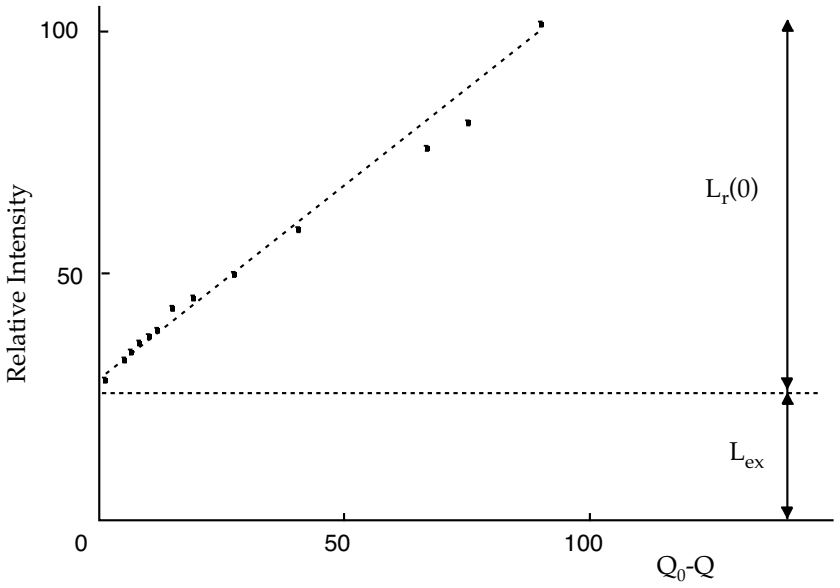


Figure 3.8: The graph shows the proportionality between the not-collected charge $Q - Q_0$ and the luminescence light intensity as function of the applied electric field. The deduced contributions at zero field are indicated on the right [65].

increases and electron-ion recombination is therefore somewhat suppressed: in this particular case (1 $MeV$ electrons) at fields strength of the order of 10 $kV/cm$ only 33% of the light survives. Observing that at this field 95% of $Q_0$ is collected, the relative intensity of luminescence components at zero field is

$$\frac{L_{ex}}{L_i(0)} \approx 0.43. \tag{3.26}$$

The result shown above could be considered reliable only for minimum ionizing particles in liquid argon (like 1 $Mev$ electrons) since, as shown before, the recombination process strongly depends on the nature of the ionizing particle.

The measured scintillation light decay curves for liquid argon are plotted in Fig. 3.9 [63]. They have been obtained in two opposite field conditions in order to decouple excitation from recombination luminescence: a first set of measurements has been performed at high electric field in order to push to zero the recombination component. A second set has been conducted at zero electric field, measuring the total scintillation light and subtracting the previously measured contribution from excitation. The experimental results show for both excitation and recombination components the presence of two differ-

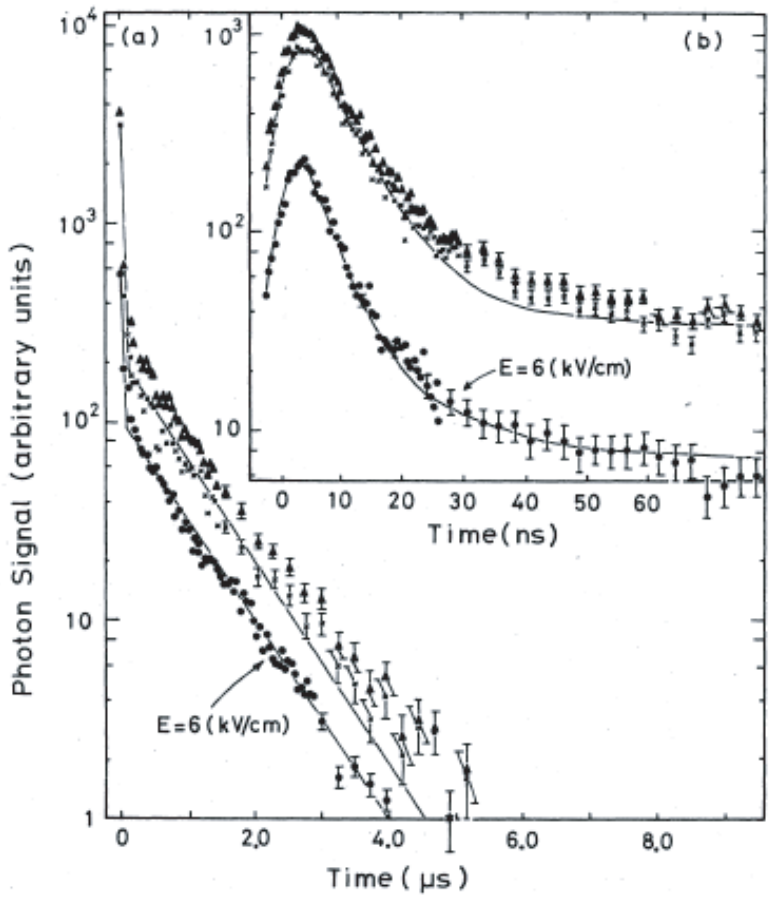


Figure 3.9: Scintillation decay curves in liquid argon are plotted. The experimental results show for both excitation (obtained at 6 $kV/cm$) and recombination components the presence of two different contributions, one characterized by a $\tau_s \approx 6\ ns$ decay time and one by a $\tau_t \approx 1500\ ns$ decay time [63].

ent contributions, one characterized by a $\tau_s \approx 6\ ns$ decay time and one by a $\tau_t \approx 1500\ ns$ decay time. The presence of the fast and slow components seems to be associated with $Ar_2^*$ molecular transition to fundamental dissociate state $^1\Sigma_g^+$ respectively from excited molecular states $^1\Sigma_u^+$ (singlet) e $^3\Sigma_u^+$ (triplet). This last transition is in principle forbidden by the selection rule $\Delta S = 0$ of the Russel-Sauders formalism but it should be noted that such notation is no longer adequate for argon atoms.

#### 3.2.3.1 Scintillation reduction: quenching and escaping electrons processes

After this general introduction it should be useful to recall Eq. 3.2 in order to define the quantities frequently used to describe the scintillation process. According to this equation, assuming no light reduction effects (neither *quenching* nor *escaping electrons*) and the emission of a single $UV$ photon for each $Ar_2^*$ de-excitation, the maximum number of emitted photons by a particle releasing to the medium an energy $E$ can be expressed, at zero electric field, as

$$N_{ph} = N_i + N_{ex} = N_i \left(1 + \frac{N_{ex}}{N_i}\right) = \frac{E}{W'_{l,\beta}} \left(1 + \frac{N_{ex}}{N_i}\right) = \frac{E}{W'_{l,ph}} \tag{3.27}$$

where the *intrinsic* mean energy for photon production in liquid argon

$$W'_{l,ph} = \frac{W'_{l,\beta}}{(1 + N_{ex}/N_i)} \tag{3.28}$$

has been introduced. Since $W'_{l,\beta}$ is equal to 23.6 $eV$ and the measured value of $N_{ex}/N_i \approx 0.21$ [65][4], $W'_{l,ph}$ has been estimated to be 19.5 $eV$ [69]. This $W'_{l,ph}$-value provides the maximum theoretical scintillation yield $dL/dE$ (scintillation intensity for unit absorbed energy) and, as suggested by a set of experiments [69], it is appropriate only for relativistic heavy ions from $Ne$ ($A = 20$) to $La$ ($A = 139$). These experimental data, obtained at zero electric field, are summarized in Fig. 3.10 that shows the scintillation yield as function of the so-called $LET$ (Linear Energy Transfer). This last quantity represents the average energy loss rate along a particle path (obtained dividing the energy loss for the particle range). For particles other than the above mentioned ions the measured scintillation suppression can be explained introducing the concept of *electron escaping* and *quenching* and it leads to an effective average energy loss $W_{l,ph}$ higher than the intrinsic $W'_{l,ph}$. The two previous effects essentially occur in two different regions of the $LET$ scale. Electron escaping is dominant in the low $LET$ region: it occurs for relativistic electrons and light ions and it is generated by the fact that, at zero drift field, a large fraction of electrons do not recombine for long time (of the order of *few ms*), due to the large thermalization radius (larger than the Onsager radius). This recombination time is several orders of magnitude higher than the time-window normally used, in

[4]

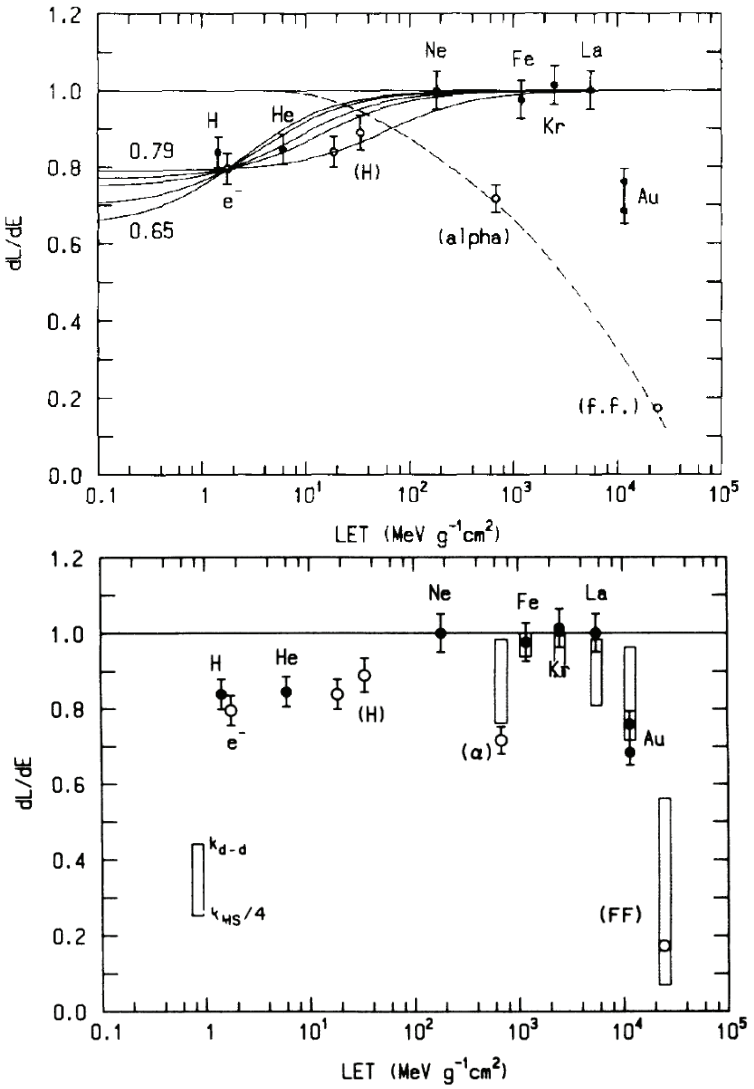


Figure 3.10: The relative scintillation yield per unit energy deposition as function of the *LET* in liquid argon [69]. The particles used are listed on Tab. 3.3. Circles show experimental results with error bars. Filled circles indicate relativistic ions. In the upper graph the solid lines, describing the escaping electrons process, are drawn by fitting the curves from Eq. 3.33 to the experimental point of 0.976 $MeV$ $e^-$ for five different values of $\Theta_0$. The best fit is obtained for $\Theta_0 = 0.75$. In the lower graph the theoretical calculation by Hitachi *et al.*, relative to quenching process in the high LET region, are reported (box) [70].

the experiments, to detect luminescence: this leads to a global decrease in the detected scintillation yield. To describe the process phenomenologically, the total yield at zero drift field can be expressed as the sum of three components

$$\frac{dL}{dE} = \left(\frac{dL}{dE}\right)_{ex} + \left(\frac{dL}{dE}\right)_{gem} + \left(\frac{dL}{dE}\right)_{col} \tag{3.29}$$

respectively representing the light produced by de-excitation, by electrons recombining with their parent ions and by electrons recombining with other ions. The first two terms should, in principle, not depend on the $LET$ (their constant sum will be referred as $\Theta_0$) while the third, counting for recombination between electrons and ions of the column, should be influenced by the mean distance between two different ionization pairs and hence on the $dE/dx$ of the particle. To express this dependence it is useful to define the number of recombination photons per unit length emitted during the observation time $\tau$ as

$$\left(\frac{dL}{dx}\right)_{col} = A \cdot \int_0^{\tau} dt \left(\frac{\partial n_-}{\partial t}\right) = \frac{A n_0^2 \alpha \tau}{1 + n_0 \alpha \tau} \tag{3.30}$$

where $n_-$ is the electron density, $n_0$ its value at $t = 0$ and $A$ is the area of the transversal section of the ionization column [69]. To solve the above integral, it has been assumed that the recombination process of electrons is governed by the second equation of system 3.21 with $\mathcal{E}_d = 0$. Assuming that the initial electron density is proportional to the stopping power, $n_0 = K(dE/dx)$, the previous equation becomes

$$\left(\frac{dL}{dx}\right)_{col} = \frac{A \cdot K \cdot C}{1 + K\frac{dE}{dx}} \left(\frac{dE}{dx}\right)^2 \tag{3.31}$$

with $C = K\tau\alpha$ and it leads to

$$\left(\frac{dL}{dE}\right)_{col} = \frac{A \cdot K \cdot C}{1 + K\frac{dE}{dx}} \left(\frac{dE}{dx}\right). \tag{3.32}$$

The previous function is a monotone increasing function of the stopping power and, for large $LET$, its value tends to $AK$. The global scintillation yield at zero field described in Eq. 3.29 can hence be rewritten as

$$\frac{dL}{dE} = \frac{A \cdot K \cdot C}{1 + K\frac{dE}{dx}} \left(\frac{dE}{dx}\right) + \Theta_0. \tag{3.33}$$

The involved parameters values can be obtained by fitting this function on low $LET$ data of figure 3.10, requiring that $\Theta_0 + AK = 1$. The experimental

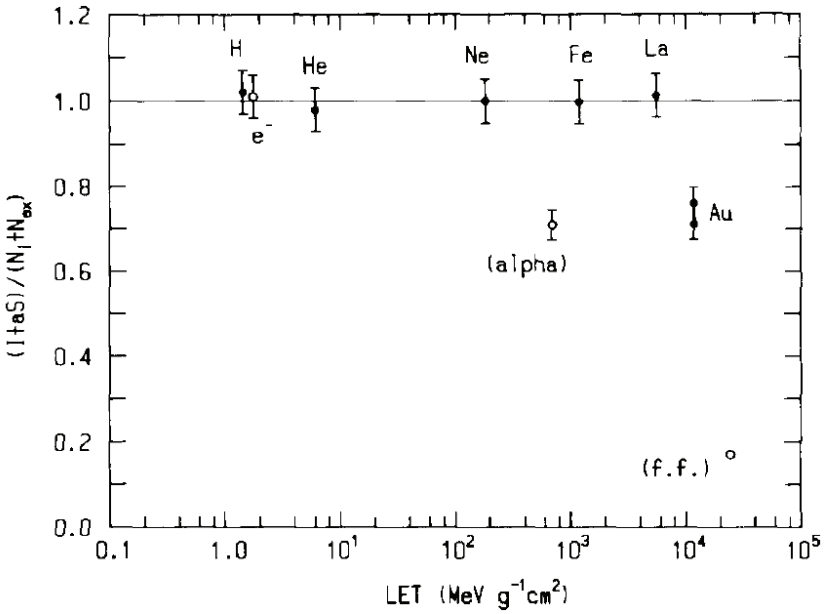


Figure 3.11: *LET* dependence of the ratio $Q + aS/N_{ex} + N_i$ in liquid argon for a variety of particles. Particles presenting a value lower than unit are suffering for quenching [69].

behaviour is well reproduced by the fit shown in Fig. 3.10. It should be noted that, as soon as a drift field is applied, these escaping electrons are collected. This has been deduced looking at the quantity $Q + aS$, representing the sum of the collected charge and scintillation intensity ($a$ is a normalization factor): if no quenching occurs, its value should be equal to $N_{ex} + N_i$. With no field applied, $Q = 0$ and due to escaping electrons the ratio $aS/(N_{ex} + N_i)$ differs from unity. As soon as the drift field is turned on, such ratio reaches the unity value suggesting that the escaping electrons are collected [69]. This is clearly shown in Fig. 3.11 where the value of the ratio is plotted as function of the *LET* for $\mathcal{E}_d \neq 0$. In this conditions, low *LET* particles suffering at zero field for electron escaping behaves like relativistic ions while, as before, $\alpha$-particles and fission fragments produce a lower amount of scintillation. The process responsible for this loss is called *quenching* and it is mainly due to the high ionization density.

As suggested by the experimental data of figure 3.10, the quenching process, affecting high *LET* particles, cannot be considered just a function of the energy loss density otherwise $Fe$, $Kr$ and $La$ relativistic ions should have

presented a quenching factor greater than one measured for $\alpha$-particles. According to a theoretical model developed by Hitachi and his collaborators [70], the above mechanism should be affected also by the details of the track, such as radial distribution. The proposed mechanism [70] possibly leading to scintillation quenching is[5]

$$Ar^* + Ar^* \rightarrow Ar + Ar + e^-. \tag{3.34}$$

and its rate depends on the $Ar^*$ excitons density. Since excitons are produced by both self-trapped and recombination luminescence mechanisms (see processes of equations 3.24 and 3.25), both components will suffer from this quenching phenomenon. Following the approach suggested by Hitachi, the highly ionizing particle track should be divided into two regions: the *core* and the *penumbra*. The first represents the inner region of the track where a large amount of the energy is deposited: it is mainly constituted by the primary particle energy loss but also a part of energy can be released in this region by $\delta$-rays. The penumbra represents the surrounding region where the energy loss deposition is mainly due to interactions of $\delta$-rays enough energetic to penetrate the core volume. The two regions are essentially discriminated on the basis of the energy deposition density, higher in the core than in the penumbra: for a heavy ion the two deposited energy densities are respectively of the order of $10^{-1}$ $ev/\mathring{A}$ and $10^{-4}$ $ev/\mathring{A}$. Due to this great gap, the luminous quenching process 3.34 for heavy ions and $\alpha$ is assumed to occur only in the high density core region. For fission fragments due to the high ionization density (higher than the one of other particles) the quenching effect occurs both in core and penumbra that practically are melted. Figure 3.12 provides a sketch of the track structure indicating the evaluated dimensions for $\alpha$, fission fragments and heavy $Au$ ions tracks. The global energy $\eta_S$ spent for scintillation can then be expressed (for particles other than fission fragment) as

$$\eta_S(E) = q_{el}\overline{\eta}(E) = q_c\eta_c(E) + \eta_p(E) \qquad with\ \overline{\eta}(E) = \eta_c(E) + \eta_p(E) \tag{3.35}$$

where $\overline{\eta}(E)$ is the fraction of energy loss given to electrons (see Sec. 3.2.1), $\overline{\eta}_c$ and $\overline{\eta}_p$ are the energy losses in the core and in the penumbra, $q_{el}$ is the

[5]The experimental observations suggest that the process responsible for quenching should occur at early stage before the $Ar_2^*$ is formed otherwise decay constant values should be affected by the process, differently from what has been measured for $\alpha$-particles, fission fragments and relativistic electrons for which the decay constants have similar values. For this reason the hypothesis that quenching is due to an interaction between $^3\Sigma_u^+$ and $^1\Sigma_u^+$ $Ar_2^*$ states should be discharged.

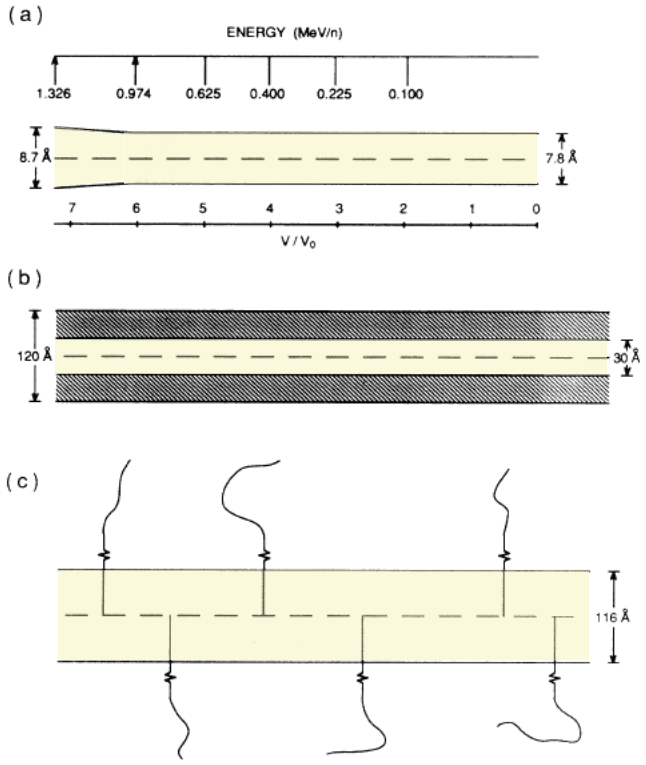


Figure 3.12: The core and the penumbra structure for heavy-ion tracks in LAr: a) $\alpha$-particle, b) fission fragment and c) $Au$ ions. The core is the yellow region. For $\alpha$-particles the penumbra is a disjointed collection of emergent $\delta$-rays (not shown). These are $\approx 200-2000\,eV$ in energy ejected nearly perpendicular to the track and they have a typical $LET$ slightly lower than the primary particle. For fission fragments the $\delta$-rays coalesce to form a quasi-continuous penumbra although the energy density is less than that in the core. For $Au$ ions, the induced $\delta$-rays have energy $\approx 2000\,eV$; these are ejected perpendicularly to the track with negligible stopping or scattering with the core. Their mean ranges are 2000 $\mathring{A}$, their $LET$'s are orders of magnitude lower than that of the primary particle and they overlap little. The wavy lines indicate breaks in the $\delta$-rays path [70].

overall luminous quenching factor (if no quenching occurs $q_{el} = 1$) and $q_c$ is the quenching occurring in the core. The quantity $q_c$ represents the fraction of energy in the core that survives quenching (if $q_c = 1$ then $q_{el} = 1$).

The proposed model can be used to evaluate the size of the core (expressed as the radius $r_c$ of the cylinder) and compute the value of $\overline{\eta}_c/\overline{\eta}$. On the basis of this value the exciton initial density $N_\Xi(t = 0)$ is estimated for the different

| *Particle* | $r_c$ ($\mathring{A}$) | $\overline{\eta}_c/\overline{\eta}$ |
|---|---|---|
| 1.33 $MeV/n$ $\alpha$ from $^{210}Po$ | 4 | 0.72 |
| 1.51 $MeV/n$ $\alpha$ from $^{212}Bi$ | 4 | 0.71 |
| 1.53 $MeV/n$ $\alpha$ from $^{252}Cf$ | 4 | 0.71 |
| 2.20 $MeV/n$ $\alpha$ from $^{212}Po$ | 4 | 0.69 |
| 0.98 $MeV/n$ FF from $^{252}Cf$ | 15 | 0.76 |
| 0.56 $MeV/n$ FF from $^{252}Cf$ | 15 | 0.80 |
| 1.04 $GeV/n$ H ion* | 59 | 0.5 |
| 1.04 $GeV/n$ He ion* | 59 | 0.5 |
| 631 $MeV/n$ Ne ion* | 54 | 0.5 |
| 1.35 $GeV/n$ Ne ion* | 62 | 0.5 |
| 705 $MeV/n$ Fe ion* | 55 | 0.5 |
| 730 $MeV/n$ Kr ion* | 55 | 0.5 |
| 1.08 $GeV/n$ La ion* | 60 | 0.5 |
| 870 $MeV/n$ Au ion* | 57 | 0.5 |

Table 3.3: Computed values of the key quantities for Hitachi quenching model [70]. The symbol * refers to relativistic particles ($\beta > 0.75$)

particles: to stress the different details of the tracks, from $\alpha$, fission fragment and relativistic heavy ions, the profile of the initial excitons distribution inside the core is plotted on figure 3.12. The corresponding $q_c$ value is defined as ratio between the number of self-trapped excitons $A_2^*$ per unit length for $t \to \infty$ over the initial number of excitons $Ar_*$ per unit length.[6] The estimated values for the different particles of the key quantities are shown on Tab. 3.3 and the predicted relative $dL/dE$ as function of the $LET$ are indicated in Fig. 3.10. The theory justifies the relative different behaviour of the particles: the absolute normalization is given by assuming that the $dL/dE$ is maximum for $Fe$ and $Kr$ ions.

As evident from figure 3.13 $\alpha$-particles, although characterized by a $LET$ lower than that of $La$ ions, presents a higher excitons density leading to a higher quenching effect with respect to relativistic ions. Considering the rel-

[6] the number of surviving self-trapped excitons $A_2^*$ per unit length corresponds to the number of emitted VUV photons per unit length and it is determined by the biexcitonic quenching rate function of the exciton density.

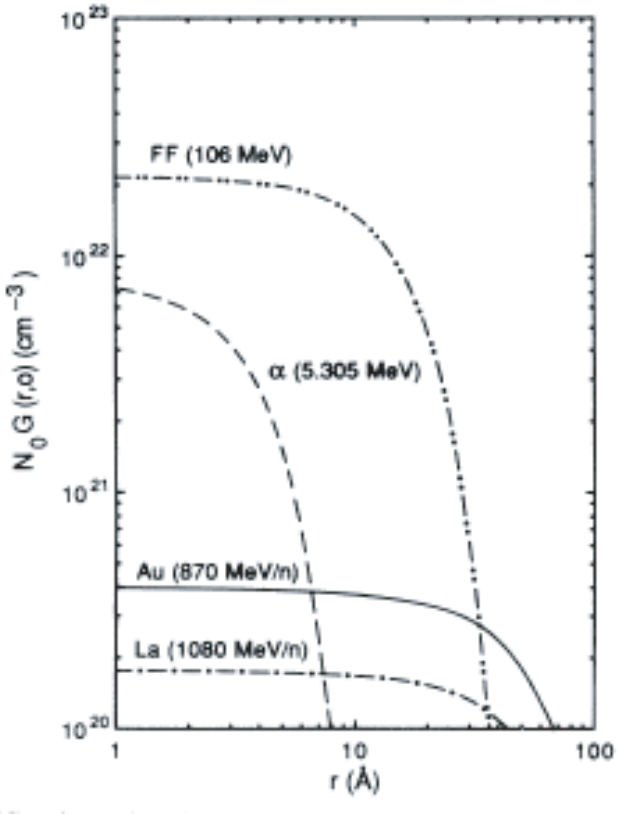


Figure 3.13: The initial distribution of excited species in the track core produced in liquid argon by $\alpha$-particles, fission fragments, $Au$ and $La$ ions [70].

ativistic ions data, one should note that, since the track radii remain almost constant ($\approx 50 - 60$ $\AA$), the excitons density depends essentially on the $LET$ and the $q_{el}$ value decreases as the ion $LET$ increases: this is the reason for which $Au$ ions are more quenched than $Ne$ ions [70].

All the considerations until here have been carried ahead assuming that no drift field was applied. As shown in Fig. 3.11 quenching effects still survive with electric field turned on. A graph analogous to the one shown in Fig. 3.7, describing the behaviour of scintillation and ionization for relativistic electrons, has been plotted for fission fragments and $\alpha$-particles (affected by quenching) on figure 3.14 [71]. Differently from what occurs for minimum ionizing particles, the scintillation intensity increases with the field for intermediate field strength (up to 2 $kV/cm$), at least for $\alpha$-particles: the simultaneous measurement of light and charge, shown in figure 3.14, suggests that the

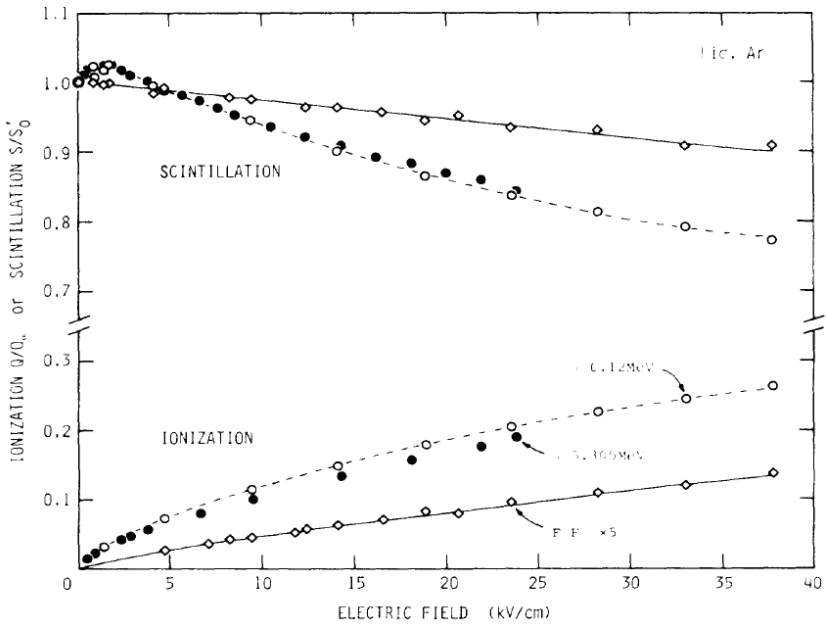


Figure 3.14: Variation of the scintillation and ionization as function of the applied drift field for $\alpha$-particles and fission fragments in LAr [71]

scintillation increase does not occur at the expense of ionization (that for intermediate fields is increasing too). Consequently it can be only attributed to a reduction of the quenching process. This behaviour can be explained in the context of the previous model. The application of a drift field can help part of the ionization electrons to shift out from the track core and hence, the atomic excitons (produced through recombination process described in Eq. 3.24) are formed in a less dense region, leading to a reduced quenching effect. This fact is apparently not occurring for fission fragment (see picture 3.14) since evidently external electric field cannot significantly influence the high density charge distribution.

It should be noted that the determination of the energy of a particle through its induced luminescence should, in principle, consider that both nuclear and electron quenching can occur. The first is essentially determined by the fact that low velocity particles dissipate a large fraction of their energy through atomic collisions instead of giving it to electrons: the second quantity responds for the fact that, according to the density and structure of ionization track part, a different amount of energy goes into scintillation. The

| *Particle* | $q_{el}$ | $q_{nc}$ | $W_{l,ph}$ $(eV)$ |
|---|---|---|---|
| $\alpha$ | 0.71 | $\approx 1.0$ | 27.5 |
| Relativistic $e^-$ | 0.77 | $\approx 1.0$ | 25.1 |
| Relativistic heavy ions (up to $La$) | 1.0 | $\approx 1.0$ | 19.5 |
| FF form $^{252}Cf$ | 0.17 | $\approx 1.0$ | 114.7 |
| Au | 0.70 | $\approx 1.0$ | 27.8 |

Table 3.4: Measured quenching factors (nuclear and electronic) and average energy loss for UV photon production for some kinds of particles. The data refer to zero field [64, 70].

.

global quenching factor to be considered in scintillation measurements is then provided by Eq. 3.35 and 3.11 leading to

$$\eta_S(E) = q_{el} \cdot \overline{\eta}(E) = q_{el} \cdot q_{nc}(E) \cdot E = q_{tot} \cdot E \tag{3.36}$$

where the parameter $q_{tot}(E) = q_{nc}(E) \cdot q_{el}$ has been introduced and where the use of $q_{el}$ has been extended also to describe scintillation loss due to escaping electrons [72]. The previous equation can be used to express the effective energy loss for photon emission as function of the particle global energy loss according to

$$\overline{N}_{ph} = \frac{\eta_S(E)}{W'_{l,ph}(E)} = \frac{q_{tot}(E) \cdot E}{W'_{l,ph}(E)} = \frac{E}{W_{l,ph}} \qquad with\ W_{l,ph} = \frac{W'_{l,ph}(E)}{q_{tot}(E)}. \tag{3.37}$$

Since $q_{tot} \leqslant 1$, the average energy loss for VUV photon emission is higher than the one for relativistic ions up to $La$: they have been used as reference since, for them, $q_{nc} \approx 1$ (relativistic) and $q_{el} = 1$ (no quenching occurs). This subdivision becomes important only for low velocity heavy particles, like low energy nuclear recoils, for which the nuclear quenching factor differs from unity due to the different energy loss processes (see Sec. 3.2.1). Apart from them, the scintillation reduction is essentially affected only by electronic quenching. Table 3.4 reports the $W_{l,ph}$ value for different particles. It should be noted that, as stated above, the $q_{el}$ parameter is in general function of the applied electric field too.

For nuclear recoils it is expected that most produced $\delta$-rays are not enough energetic to penetrate the core of the track: for this reason an undifferentiated

core and penumbra region is created ($\eta(E) = \eta_c(E)$) as in the case of fission fragments [73]. Due to the similar electronic stopping power deduced by range measurements, the radial distribution of excited species for nuclear recoils tracks should be similar to that of $\alpha$-particles tracks cores leading to $q_{el,R} \approx q_{c,\alpha} = 0.6$[7].

#### 3.2.3.2 Effect of ionization on the time dependence of luminescence

As briefly described before, the scintillation light induced by an interaction in liquid argon presents two different components characterized by the two different decay constants $\tau_s \approx 6\ ns$ and $\tau_t \approx 1.5\ \mu s$. Their emission have been attributed respectively to the transitions from the first singlet molecular excited state $^1\Sigma_u^+$ and from the triplet $^3\Sigma_u^+$ to ground state. According to the results found in literature, these decay constants are not function of the energy loss density ($LET$) and they assume similar values for particle of different nature (see Fig. 3.15) [74]. Their relative intensity $I_s/I_t$ (singlet/triplet), on the other hand, strongly depends on the $LET$ as shown by the experimental data summarized on Tab. 3.5. It has been observed that for high $LET$ the singlet component intensity increases at expense of the triplet one. As suggested in the work by Hitachi *et al.*, several mechanisms can be imagined to describe the observed behaviour: the most plausible seems to be the one concerning superelastic collisions with thermal electrons [74]. According to this explanation, the ionization electrons after being thermalized, can collide, before recombination, with singlet state and induce a single-to-triplet transition. The probability of this process is somewhat connected with the recombination time in liquid argon that, as obvious, is function of the ionization density. Such process is hence evidently favored for low ionizing particles (low $LET$ region), for which recombination is slower: in this case the initially produced number of singlet states is more effectively reduced. This mechanism can qualitatively explain the $I_s/I_t$ as function of the $LET$. This phenomenon has been observed in liquid xenon too. The results are reported on Tab. 3.5. All the measurements have been conducted with zero drift field applied.

[7] The value $q_{c,\alpha} = 0.6$ is obtained from

$$\frac{\eta_S(E)}{\overline{\eta}(E)} = q_{el,\alpha} = q_{c,\alpha}\frac{\eta_c(E)}{\overline{\eta}(E)} + \frac{\eta_{p,\alpha}(E)}{\overline{\eta}(E)}$$

assuming $q_{el,\alpha} = 0.71$ (see Tab. 3.4) and the ratios $\eta_c(E)/\overline{\eta}(E) \approx 0.72$ and $\eta_{p,\alpha}(E)/\overline{\eta}(E) = 0.28$ [70].

| *Particle* | $\tau_s$ $(ns)$ | $\tau_t$ $(ns)$ | $I_s/I_t$ |
|---|---|---|---|
| *Argon* | | | |
| Relativistic $e^-$ | $6 \pm 2$ | $1590 \pm 100$ | 0.3 |
| $\alpha$ | $7.1 \pm 1.0$ | $1660 \pm 100$ | 1.3 |
| FF form $^{252}Cf$ | $6.8 \pm 1.0$ | $1550 \pm 100$ | 3 |
| *Xenon* | | | |
| $\alpha$ | $4.3 \pm 0.6$ | $22 \pm 1.5$ | $0.45 \pm 0.07$ |
| FF form $^{252}Cf$ | $4.3 \pm 0.5$ | $21 \pm 2$ | $1.6 \pm 0.2$ |

Table 3.5: Decay constants for singlet and triplet components of scintillation light and their relative intensities for LAr (upper part) and LXe (lower part)[74].

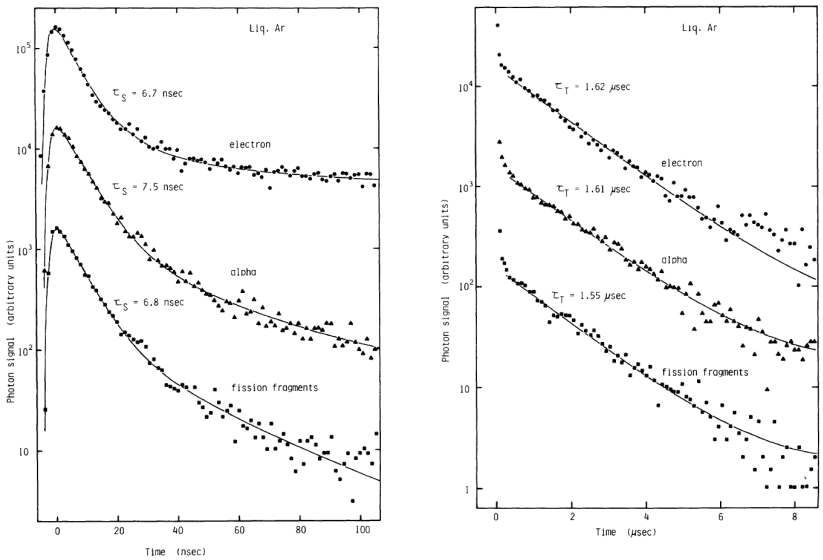


Figure 3.15: Decay curves obtained, at zero field applied, with electrons, $\alpha$-particles and fission fragment in LAr [74]. The fast (right) and slow (slow) components are plotted.

### 3.2.4 Xenon doped Argon: general behaviour

The global effect on scintillation light emission produced by the presence of Xe impurities inside liquid argon ($LAr + Xe$) has been investigated in literature [75, 76]. According to these works the xenon (whose scintillation properties are listed in table 3.5), if diluted in opportune concentrations, behaves

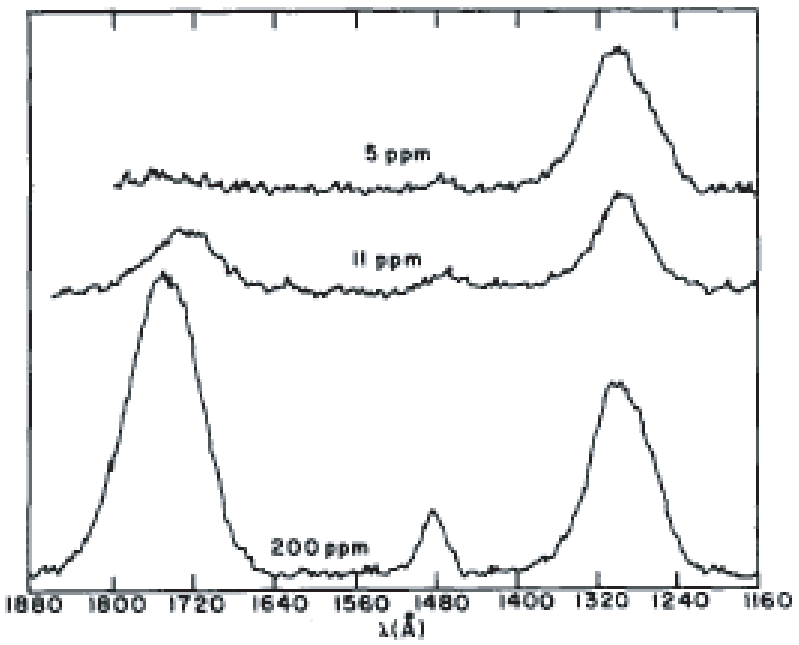


Figure 3.16: Emission spectra of xenon-doped liquid argon at 87.2 $K$ [75].

like a wavelength shifter from pure LAr 128 $nm$ to 175 $nm$ light. As suggested by the experimental data two different processes should be responsible for this behaviour. The first can be outlined as

$$\begin{aligned} Ar_2^* &\rightarrow Ar + Ar + h\nu_1 \\ h\nu_1 + Xe &\rightarrow Xe^* \\ Xe^* + Xe &\rightarrow Xe_2^* \\ Xe_2^* &\rightarrow Xe + Xe + h\nu_2 \end{aligned} \tag{3.38}$$

where $\nu_1$ and $\nu_2$ corresponding to 128 $nm$ and 175 $nm$ photons. This mechanism occurs after photon emission by the argon molecular exciton ($\tau_s \approx 6$ $ns$ and $\tau_t \approx 1500$ $ns$) has occurred and hence, since the time scales for the last three processes are negligible, compared to the slow component decay time involved in the first radiative reaction, the time behaviour of the resulting 175 $nm$ light is almost equal to the one followed by the ordinary LAr scintillation light. This effect becomes visible for xenon mass concentration $[Xe] \approx 10$ $ppm$. As soon as the xenon concentration increases and reaches

| *[Xe]* % | $\tau_t$ $(ns)$ |
|---|---|
| $\approx 0.01$ | $\approx 1500$ |
| 0.980 | $121 \pm 7$ |
| 4.880 | $37 \pm 3$ |
| 9.970 | $40 \pm 3$ |

Table 3.6: Measured scintillation decay constant (slow component) as function of xenon mass concentration [76].

$[Xe] \approx 1\%$ the non-radiative mechanism

$$\begin{aligned} Ar_2^* + Xe &\rightarrow Ar + Ar + Xe^* \\ Xe^* + Xe &\rightarrow Xe_2^* \\ Xe_2^* &\rightarrow Xe + Xe + h\nu_2 \end{aligned} \tag{3.39}$$

starts to dominate and the time behaviour of the scintillation light starts to modify. Since the first reaction in Eq. 3.39 is much faster than the last one, the luminescence emission is now determined by the decay time constant of the $Xe_2^*$ molecular exciton.

The effect of xenon is qualitatively shown in Fig. 3.16 by the measured $LAr + Xe$ emission spectra for various values of $[Xe]$. The measured decay constant values are reported on Tab. 3.6 for the slow component: it is evident that for $[Xe] \geqslant 1\%$ the scintillation response becomes much faster than the one from pure liquid argon and that with $[Xe] = 4.880\%$ and $[Xe] = 9.970\%$ similar results are obtained. This observation suggests that the mixing saturation is reached around $[Xe] \approx 5\%$.

Together with the scintillation time dependence also ionization yield has been investigated [77] and, as shown in Fig. 3.17, the experimental results suggest that the ionization yield increases with the xenon concentration, at least in the concentration range $0 \leqslant [Xe] \leqslant 2.0\%$. Although no precise results are presented, according to the authors of reference [76] also scintillation yield does not evidently decrease passing from pure to doped argon. As shown by these works, the $LAr + Xe$ mixture is really promising since it offers a behaviour similar to the one of xenon (higher wavelength, faster time response, etc.) but, obviously, at a cheaper price (only few ppb of xenon are used).

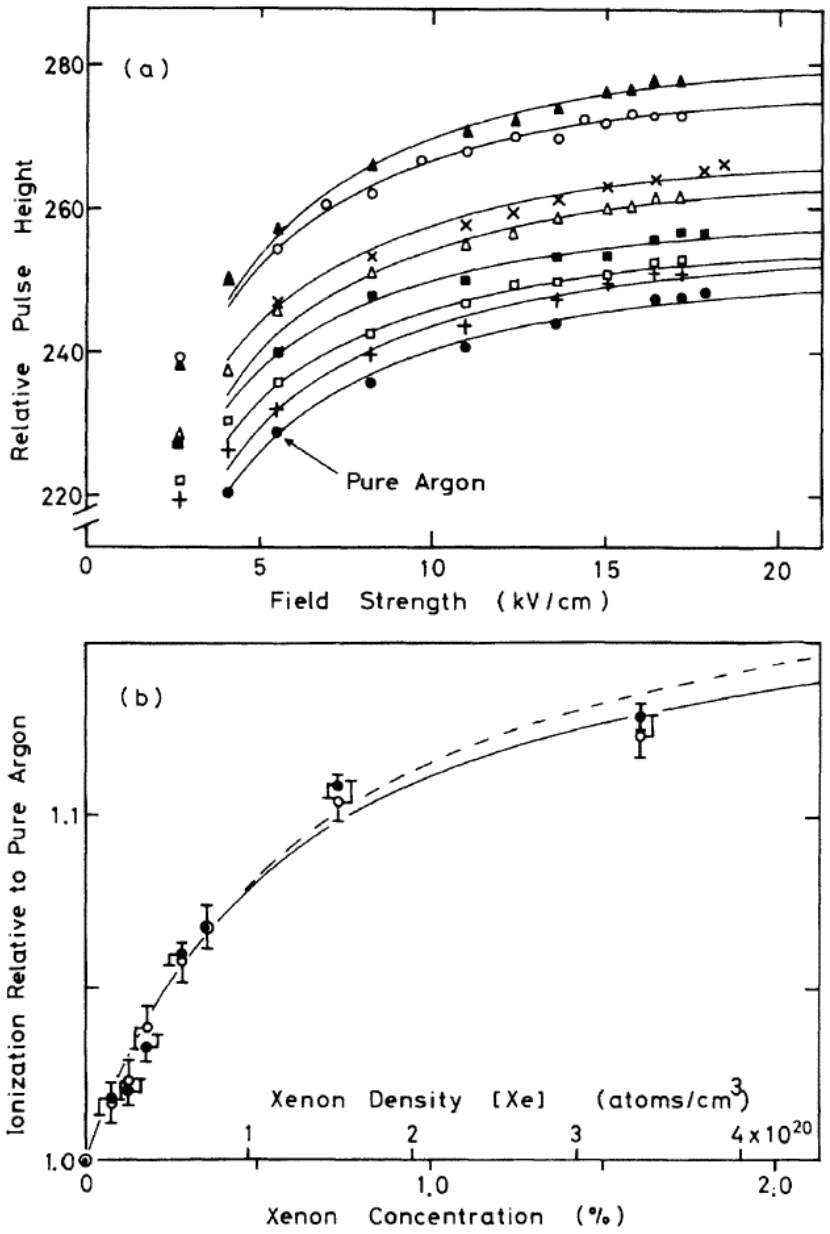


Figure 3.17: Relative ionization yield in LAr+Xe mixture as function of xenon concentration. The measurements refer to [Xe] equal to (from bottom to top) 0.08%, 0.12%, 0.18%, 0.28%, 0.37%, 0.73% and 1.6% [77].

| *Impurity* | $K_i(l\ mole^{-1}\ s^{-1})$ |
|---|---|
| $O_2$ | $5.5 \times 10^{10}$ |
| $H_2O$ | $\approx 10^7$ |
| $CO_2$ | $\approx 10^7$ |

Table 3.7: $K$ values for the reactions of Eq. 3.40 in LAr. It should be noted that capture process induced by $O_2$ impurities is $10^3$ times more effective than the others [43].

### 3.2.5 Electronegative impurities electrons attachment

For TPC-like applications, concerning electrons drifting along a liquid argon volume, another aspect not yet presented should be investigated. As stressed in the previous chapters, the ionization electrons survived recombination could eventually suffer, during their drift, from electronegative impurities attachment, according to LAr purity. The main electronegative impurities surviving the argon distillation process are oxygen, water and carbon dioxide that capture free electrons through reactions

$$\begin{aligned} O_2 + e^- &\rightarrow O_2^- \\ H_2O + e^- &\rightarrow H_2O^- \\ CO_2 + e^- &\rightarrow CO_2^-. \end{aligned} \tag{3.40}$$

A rate $K_i$, directly obtained from the relative computed cross section can be associated to each of the above reactions: this quantity is evidently function of the applied electric field since the capture cross section depends on electron velocity. The $K_i$ values for $\mathcal{E}_d = 1\ kV/cm$ are reported on Tab. 3.7. On this basis, assuming $t = 0$ as the start time of the drift, the capture process can be described through

$$\begin{cases} \frac{dN_e(t)}{dt} = -\left[\sum_i K_i N_i(t)\right] N_e(t) \\ \\ \sum_i \left[N_i(0) - N_i(t)\right] = N_e(0) - N_e(t) \end{cases} \tag{3.41}$$

where $N_i(t)$ represents the numeric density of impurities and $N_e(t)$ the electrons one, both seen as function of the time $t$. Since the $N_i(t)$ is usually several orders of magnitude lower than $N_e(t)$, its value should be considered, in first

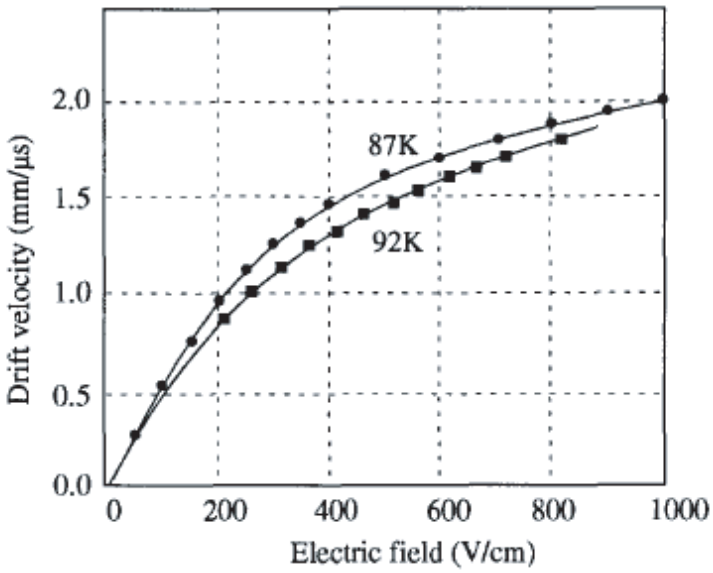


Figure 3.18: Electron drift velocity as function of the applied drift field in LAr [80].

approximation, as constant and the system 3.41 reduces to

$$\frac{dN_e(t)}{dt} = -\left[\sum_i K_i N_i\right] N_e(t) \tag{3.42}$$

leading to the solution

$$N_e(t) = N_e(0)\exp\left(-\frac{t}{\tau_l}\right) \tag{3.43}$$

with $\tau_l = (\sum_i K_i N_i)^{-1}$. This last quantity is called *lifetime* and it represents the time after which the number of survived electrons reduces by a factor $1/e$. Obviously a more pure argon guarantees a higher lifetime. The impurity attachment process is often described by the so called attenuation length $\lambda$: its value can be obtained through equation $\lambda = v_d\tau_l$ where $v_d$ is the electron drift velocity whose dependence on the electric field is plotted in Fig. 3.18. At 1 $kV/cm$ the K value for $O_2$ is $5.5 \times 10^{10}\ l \cdot mol^{-1} \cdot s^{-1}$ and hence a lifetime of the order of 3 $ms$ can be achieved with an argon purity of the order of 0.1 *ppb* of $O_2$ *equiv.*[8]: since at that field the drift velocity is 2 $mm/\mu s$ this leads to an attenuation length of about 6 $m$.

[8]The total impurities concentration is often expressed in $O^2$ *equiv.*. This value can be obtained from equation $N_{O_2} = K_i N_i / K_{O_2}$ and represents the amount of $O_2$ impurities that can mimic the effect due to $N_i$ impurities.

## 3.3 Double-phase implementation of the standard liquid argon technology

As suggested in the previous sections the scintillation and ionization mechanism in liquid argon strongly depend on the nature and on the kinematic conditions of the primary ionizing particle. This means that, in principle, the simultaneous measurement of luminescence light and ionization charge, collected through the application of an electric drift field, can be used to discriminate the nature and the energy of the impinging particle. The major limit of this technique has to be found in the not too low ionization detection threshold: tiny energy depositions produce, in average, few ionization electrons that, in absence of an amplification mechanism, are detectable only with very expensive low-noise amplifiers. Charge and light proportional amplifications, although observed in the gas phase and already used in several proportional scintillation counter, are not occurring in liquid argon, at least in a reliable proportional regime [84]. Such a limitation can be overcome realizing a double-phase detector where ionization electrons are extracted from liquid and light- or charge-multiplied in the gaseous phase [85]. This solution provides the advantage of the liquid argon phase, mainly a high density and a high scintillation yield, together with the possibility of amplifying the ionization signal, leading to a global improved detection efficiency. In the following sections the extraction and electroluminescence in gas processes are presented.

### 3.3.1 Electrons extraction through liquid-gas interface

The excess electrons extraction has been studied for a variety of non-polar dielectrics [83]. Particular attention has been given to their transmission from liquid to vapor phase in the case of condensed noble gas, characterized by a high electron mobility [82, 85, 81, 84]. According to these works the extraction process strongly depends on the value $V_0$, representing of the minimum energy of the conduction band in liquid. This value, that can assume positive or negative values, describes the interaction between quasi-free electrons and the liquid itself. In the case of argon its value has been measured to be $V_0 = -0.2\ eV$: assuming that in the argon vapor the electron energy level (at zero field applied) is closed to the vacuum level, $V_0$ represents also the energy gap between the conduction band in liquid and the vapor phase. The potential energy of an electron, at a distance $x$ from the interface and in presence of an

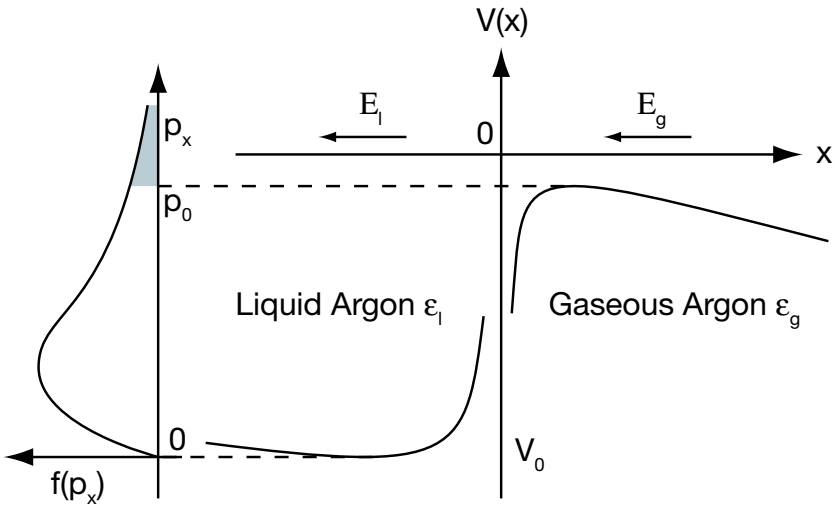


Figure 3.19: Potential distribution near the interface of condensed non-polar dielectrics at equilibrium with their vapor phase. Although not in scale, an indicative momentum distribution is reported on the left [84].

electric field normal to the surface, could be expressed as

$$V_l(x) = V_0 - e\mathcal{E}_l x + A_l, \qquad for\ x < 0\ (liquid) \tag{3.44}$$

and

$$V_v(x) = -e\mathcal{E}_v x + A_v, \qquad for\ x > 0\ (vapor) \tag{3.45}$$

where $\mathcal{E}_l$ and $\mathcal{E}_v$ are the electric fields in liquid and vapor and $A_v$ and $A_l$ have been obtained applying the so-called Schottky model [81]. This model essentially describes the barrier effect as an interaction between the electron and its dielectric image. According to it $A_v$ and $A_l$ can be expressed as

$$A_{l,v} = -\frac{e^2(\epsilon_l - \epsilon_v)}{4\epsilon_{l,v}(\epsilon_l + \epsilon_v)} \frac{1}{(x + \beta\frac{x}{|x|})} \tag{3.46}$$

where $\epsilon_l$ and $\epsilon_v$ are the dielectric constants and $\beta$ represents the physical thickness of the interface (few inter-atomic distances). This last quantity has been inserted to avoid divergences for $x \to 0$ and it becomes important for distances of the order of the liquid-vapor boundary thickness. According to the experimental data from Gushchin *et al.*, show in Fig. 3.20, the quasi-free ionization electrons, under the effect of a drift field are effectively extracted and they can be emitted in the vapor phase as "hot" or "thermal" electrons. In the first

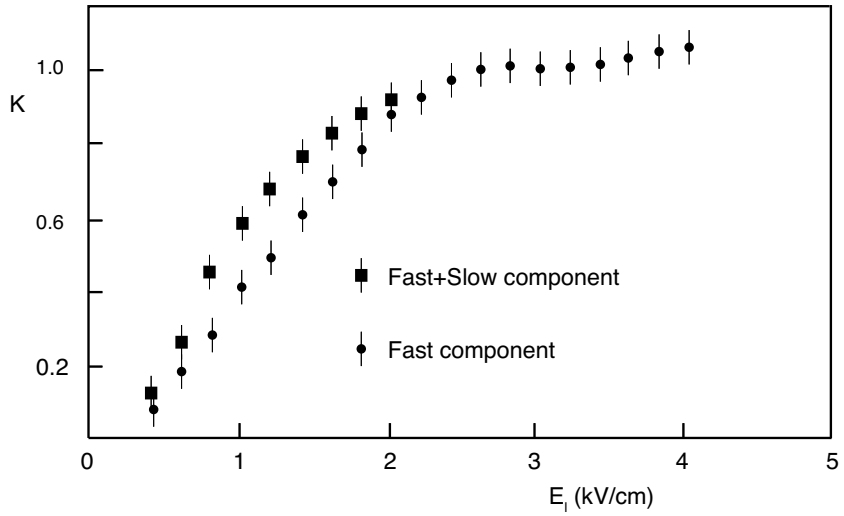


Figure 3.20: Behaviour of electrons extraction efficiency as function of the electric field strength in liquid argon [81].

case the extraction is very fast: within 0.1 $\mu s$ the totality of hot electrons is emitted. In the second case, thermal electrons are extracted at longer time and, as shown below, their typical emission time is critically determined by the applied electric field.

A model has been developed to describe the presented experimental data. According to it, a drifting ionization electron, once reached the interface, could follow two different destinies: it could overcome the barrier or be backscattered to liquid. The different behaviour is essentially determined by its kinematic condition: if its momentum projection along $x$ direction $p_x$ is higher than $p_0 \approx (2m_e|V_0|)^{1/2}$, it is able to reach the vapor phase, otherwise, if its momentum is lower than $p_0$, it is reflected by the potential back to liquid. The directly emitted electrons represent the so called "hot" electrons since they possess a mean energy (provided by the drift field) that is much higher than thermal energy $kT$. These electrons are emitted very fastly ($t_f < 0.1$ $\mu s$) and they constitute the observed fast component. Clearly this component increases with the electric field strength: a higher field provides a higher average value of the electron velocity distribution and hence the tail with $p_x > p_0$ is more populated.

On the other hand, the unemitted electrons are thermalized through several collisions with the medium ($\approx 1$ $ps$ in liquid argon) and they have the

possibility to be emitted, in a second time, as thermal electrons. Once again, although cooled down, their emission can occur only if $p_x > p_0$ and, if this last condition is not satisfied, they are backscattered: for average extraction time much greater than relaxation time of the momentum distribution, the above described process can be considered as stationary. In other words this means that the momentum distribution function $f(p)$ is not distorted by the electrons emission, that tends to depopulate the high momentum tail of $f(p)$. In such stationary condition the emission process can be described through

$$N(t) = N_0 e^{-\frac{t}{t_e}} \tag{3.47}$$

where $N(t)$ is the number of thermal electrons under the interface at a time $t$ and $t_e$ is the characteristic extraction time for the slow process. If the electrons lifetime in liquid phase is not very high (see Sec. 3.2.5), electronegative attachment could cause the capture of this electrons cloud waiting to be extracted. In this case Eq. 3.47 should be extended as

$$N(t) = N_0 e^{-t\left(\frac{1}{t_e}+\frac{1}{\tau_l}\right)}. \tag{3.48}$$

The total number of emitted electrons within a time $t$ is then obtained by integrating the emission rate $(dN(t)/dt)$ as

$$N_e(t) = \int_0^t dt' \left(\frac{N(t)}{t_e}\right) = N_0 \frac{\tau_l}{t_e + \tau_l}\left[1 - e^{-\frac{t_e+\tau_l}{t_e \tau_l} t}\right]. \tag{3.49}$$

leading to an emission probability for thermal electrons

$$K = \frac{N_e(\infty)}{N_0} = \frac{1}{1 + \frac{t_e}{\tau_l}}. \tag{3.50}$$

The value of $t_e$, representing the main parameter of the model, strongly depends on the barrier height, on temperature and on the electric field. In absence of electric field the spontaneous emission from liquid argon at 87.2 $K$ is strongly suppressed since the potential barrier $V_0$ is much higher than the mean thermal energy $kT$ of the free electrons. The application of an electric field enhances the emission process: as a first effect, it tends to populate the high energy tail of the drifting electron distribution, increasing the number and the energy of hot emitted electrons. As shown in Fig. 3.20 for fields strength approximately below $\mathcal{E}_c = 0.2\ kV/cm$ no fast extraction has been observed: this means that only at field strengths of the order of $\mathcal{E}_c$, the high

momentum tale of the velocity distribution effectively overcomes the $p_0$ value. As a second effect, the electric field reduces the effective barrier energy at the interface (given by the difference of Eq. 3.44 and 3.45), shortening the extraction time $t_e$ typical of the slow component. As shown in Fig. 3.19 the measured dependence of $t_e$ on the applied field is well described by a $1/\mathcal{E}_l$ behaviour for fields strength up to 0.5 $kV/cm$. For fields of the order of $2.5 - 3.0$ $kV/cm$ the measured slow component disappears and all drifting electrons have, in average, enough energy to directly overcome the barrier and being emitted in vapor as hot electrons.

### 3.3.2 Proportional light emission in noble gases

The processes generated by free electrons drifting in noble gases have been widely studied in literature for their application to proportional counters [88, 87]. Under the effect of an opportune drift field, the free electrons can receive enough energy between two successive collisions to be able to excite or even ionize the gaseous medium, leading to electroluminescence (electron-induced photon emission) and charge multiplication. These processes can be used to amplify the initial drifting charge and, from the point of view of the above described double-phase detector, they make possible to detect few ionization electrons, produced by a tiny energy deposition into the liquid and then extracted into the gas phase. In the following paragraphs the electron drift process in gas will be considered from the point of view of the emitted light since the proposed WARP detection technique is based on electroluminescence. For detailed description of charge multiplication processes in gas see reference [86].

If the electrons are accelerated by a high enough electric field $\mathcal{E}$, they can induce, through atomic collisions, the formation of $Ar*$ excitons that induce the emission of a 128 $nm$ photons, following the reaction already presented for liquid argon and passing through $Ar*_2$. This mechanism has been deeply studied using the so called GPSC (Gas Proportional Scintillation Chamber). Such gas detectors are usually characterized by a drift low field region, delimited by a cathode and by a grid $g1$, where the primary ionization phenomenon occurs. The resulting free electrons cloud is drifted towards a high field region, delimited by two grids $g1$ and $g2$, where they are accelerated applying a voltage $V_{g1textrm-g2}$. The field intensity between the two grids could be considered almost uniform in the central region, while it increases as soon as the

drifting electrons reaches the volume surrounding the wires: in this region the field goes approximatively like $1/r$ (where r is the electron distance from the wire) and it reaches a maximum value $E_w$ for $r \to r_w$ [87]. As stated above, the electroluminescence mechanism is a threshold process, since it occurs only when the field provides to electrons an average kinetic energy high enough to induce excitation: this occurs for $\mathcal{E} > \mathcal{E}_s$. Experimentally such value can be evaluated by measuring the minimum value $V_{g1textrm-g2,s}$ of the applied voltage at which electroluminescence is observed at a given gas pressure $p$. In such conditions the maximum value $\mathcal{E}_s$ of the electric field, corresponding to the region near the wires, can be computed. This value represents the minimum electric field for which secondary scintillation emission is observed. Such complex evaluation is necessary to remove from the experimental results the clear dependence from the setup geometry (geometry of the grids). A second threshold effect is expected for higher electric fields: this is produced when drifting electrons start inducing ionization ($\mathcal{E} > \mathcal{E}_m$). In the region between excitation and ionization thresholds ($\mathcal{E}_s < \mathcal{E} < \mathcal{E}_m$) the electroluminescence mechanism should proceed linearly, since the energy of the drifting electrons is dissipated through the emission of photons which do not participates further in the process. Once ionization threshold is reached primary electrons start producing ionization electrons and these last, accelerated by the field, may themselves induce ionization and excitation. A procedure, similar to the one described above, should be executed to extract the value $\mathcal{E}_m$ from the experimental data. It should be noted that although threshold value can be effectively decoupled from the geometry layout the behaviour of the gain curve cannot.

As far as photon-multiplication in argon is concerned, all the experimental data have been acquired at room temperature: in this condition it has been observed that the process depends only on the value of the so-called reduced field given by the ratio $\mathcal{E}/p$ where $p$ is the GAr pressure. The experimental data are plotted in Fig. 3.21 giving the relative amplitude of the detected light signals (for a fixed amount of ionization) as function of the applied reduced field: as expected, the two threshold effects are observed respectively at $\mathcal{E}_s/p \approx 0.7\ V\ cm^{-1}Torr^{-1}$ and $\mathcal{E}/p \approx 3.7\ V\ cm^{-1}Torr^{-1}$ [88]. If no temperature induced effects are assumed, these data correspond, after density rescaling, to a $\mathcal{E}_s \approx 1.7\ kV/cm$ and $\mathcal{E}_s \approx 9\ kV/cm$ in the case of argon vapor at 87.2 $K$ and 1 $atm$ (typical condition of a double-phase argon

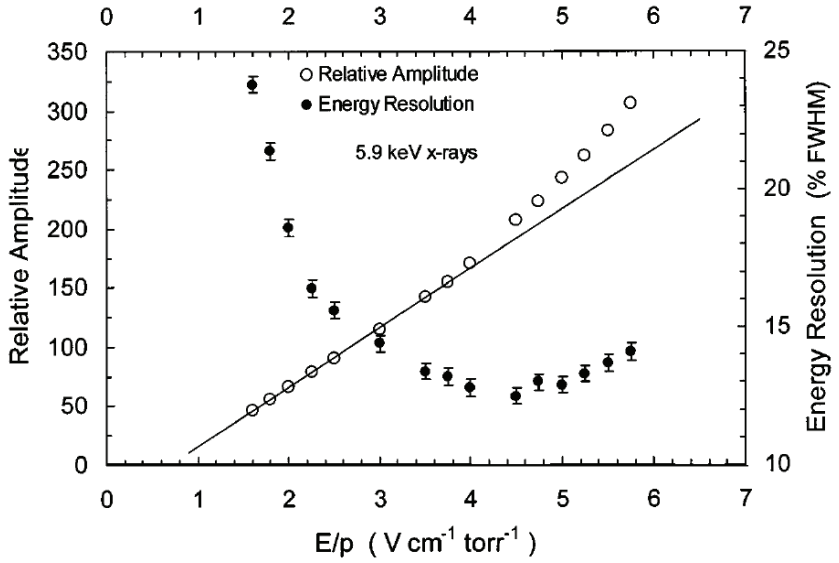


Figure 3.21: Light pulse amplitude as function of the reduced electric field for a fixed ionization in GAr produced by a 5.9 $keV$ $X$-rays source. The deduced threshold reduced fields are $\mathcal{E}_s/p \approx 0.7\ V\ cm^{-1}Torr^{-1}$ and $\mathcal{E}/p \approx 3.7\ V\ cm^{-1}Torr^{-1}$ [88].

detector). Although no direct measurement has been performed in the above double-phase-like conditions, these results should be treated just as indicative since temperature effects should occur, as suggested by the electron avalanche measurement at low temperature in GAr [89]. According to these data acquired at equal $\mathcal{E}_s/\rho$, where $\rho$ is the gas density, the measured amplification gain, instead of remaining constant, decreases of a factor 2-3 when shifting from room temperature down to 150 $K$. The data concerning secondary light emission in argon vapor, obtained with the double phase WARP prototype, will be shown in next chapter.

## 3.4 Summary

In this chapter liquid argon technology has been presented in details giving particular attention to the ionization and scintillation processes induced by an impinging particle. An interaction in the medium produces excitation ($Ar^*$) and ionization pairs ($Ar^+$-$e^-$). If no electrical field is applied, all the pairs recombine leading through a series of reactions to the excited molecule $Ar_2^*$ that can be produced into two different states (singlet and triplet): the

same final state is produced starting from $Ar^*$ excited atom. As a consequence both components (excitation and ionization) lead to the emission of UV scintillation light (128 $nm$) produced by the de-excitation of the molecular excitons $Ar_2^*$ (Sec. 3.2.3). This de-excitation process present two clearly separated decay constants associated to the two different states of the excited molecule, the singlet with $\tau_s \approx 6\ ns$ and the triplet with $\tau_t \approx 1500\ ns$. In general the presence of an electric field will tend to suppress the scintillation light since, according to the local ionization density, a fraction of electrons will escape recombination with argon ions. These ionization electrons, once avoided recombination, can be collected and hence the scintillation signal can be coupled to a ionization signal if an opportune electric field is applied.

The observed amount of ionization, collected far away from the interaction site, is the result of two opposite process: the mechanism of production of the electron-ion pairs and the recombination process. The first is strongly dependent on the nature of the interacting particles: while for minimum ionizing particles it is in general well described by Bethe-Bloch formula, this treatment evidently fails for slow ($\beta \approx 0.01$) nuclear recoils since their energy dissipation occurs through energy transfer to screened nuclei of the medium more than through collision with atomic electrons (Sec. 3.2.1). For this kind of particles (that are of interests since WIMP can be detected through induced nuclear recoils) a model has been developed by Lindhard in which the two different energy loss channels are separately treated. The ultimate result provided by this theory is represented by the expected effective energy loss per pair production $W(E)$ that is in general function of the kinetic energy of the recoil. Although this model tends to underestimate this quantity, it seems to well describe its behaviour. In the case of gaseous argon (for which recombination is negligible) one obtains experimentally $W_{g,\beta}(E) = 26.4\ eV$ for minimum ionizing particles and $W_{g,R}(E_R)$ included in the range $90 \div 70\ eV$ for argon recoils of $20 \div 100\ keV$. In other words a recoil produces a number of pair for unit of energy loss that is approximately 2-3 times lower than that produced by minimum particles. These data can be used to estimate the expected recoil behaviour in liquid argon as soon as it is observed that the effective energy loss for minimum particles in liquid is $W_{l,\beta}(E) = 23.6\ eV$, leading to a scaling of $W_{l,R}(E_R)$ according Eq. 3.16. Obviously in liquid argon, due to the higher density, the initially produced electron-ion pairs (obtained by dividing the energy of the particle for the above mentioned average energy loss for pair

production) suffers for recombination, function of the applied electric field and of the ionization density, that tends to reduce the amount of observed ionization electrons. Several models have been developed to describe such complex process all of them involving the diffusion Eq. 3.18 and different assumptions: although these models cannot be used to predict the effect of recombination, they provide the opportune functional form to execute fits on the experimental data. In particular the Box and Double Box Model of Thomas and Imel can be used to well reproduce $\alpha$-particle and 1 $MeV$ electrons recombination process as function of the electric field (Sec. 3.2.2).

As stressed before, together with ionization signal, scintillation light is produced by an interaction. This quantity, besides being function of the electric field, heavily depends on the nature of the particle and, in particular, on its ionization density and on the ionization track structure. It has been demonstrated that the maximum photon yield is produced by relativistic ions with masses up to $La$ (A=139) for which the average energy for photon production is $W'_{l,ph} \approx 19.5\ eV$. This quantity is assumed as reference and a luminous quenching factor $q_{tot}$ is used to describe the increase of such average energy according to the nature of the particle and to its kinematical conditions. The quenching factor can be essentially factorized into two components: the first is called *nuclear quenching* $q_{nc}$ and it is used to express the fraction of energy going into collisions with atomic electrons of the medium. This quantity is equal to unity if all the energy is dissipated through this channel (minimum ionizing particles) while it assumes lower values if dissipation through energy transfer to screened nuclei occurs, as in the case on nuclear recoils (as explained before). The second factor is called *electronic quenching* $q_{el}$ and it expresses the fraction of energy transfered to electronic collision going into photon emission. It is equal to unity for relativistic ions while for other particles it assumes lower values. Two main processes cause this decrease. In the low LET region (e.g. 1 $MeV$ primary electrons) the *escaping electron process* occurs: due to the reduced ionization density produced by the interacting primary particle the recombination typical time are sometimes too long if compared to the typical integration times. As a consequence, within the detection window only a fraction of the produced light is observed resulting into an effective reduction of the scintillation light. In the high LET region, the high ionization density favors the occurring of the *quenching reaction* of Eq. 3.40 that tends to reduce the number of radiative de-exciting $Ar^*$, leading

to a global decrease of scintillation light. A model developed by Hitachi and his collaborators seems to well reproduce the experimental data on the bases of the track structure and ionization density (3.2.3.1). The above described quenching process is extremely important since within a liquid argon detector the same amount of detected scintillation light will correspond to a different energy release according to the nature of the the interacting particle. The nature of the impinging particle will also influence the time dependence of the scintillation signal influencing the relative intensities of singlet and triplet decays.

In the second section of the chapter the double phase implementation of the liquid argon TPC technology is described. As shown in the next chapter this method will be used to provide the simultaneous measurement of scintillation and ionization, leading to a very efficient technique for the discrimination of nuclear recoils (possibly produced by WIMPs) from the $\gamma$-like background. Particular attention has been given to electrons extraction from liquid to gaseous phase and to production of electroluminescence light in the gaseous region. As far as extraction is concerned it has been shown by several works on this topic that extraction occurs and that, if fields of the order of 2.5 kV/cm are applied in the liquid phase, approximately the totality of the free ionization charges is extracted to the gaseous phase with typical times lower than 0.1 $\mu s$ (Sec. 3.3.1). As regards electroluminescence, several experimental works have shown that the acceleration of free electrons in a gaseous argon region leads to the emission of scintillation light as soon as a certain electric field intensity is reached (Sec. 3.3.2). According to the applied field and to the density of the gas, the electrons can acquire enough kinetic energy to induce the excitation of the gas itself. If higher fields are applied and ionization threshold is overcome, the proportional process loses it linearity entering in an avalanche regime. This two properties have been studied in details by the means of a small double phase argon chamber and the results will be presented in next chapter.

# Chapter 4

# WARP R.&D. experimental results

As stated in the introductory chapters, noble gases double-phase technology provides the possibility to simultaneously measure the excitation and ionization induced by an interacting particle even if the amount of charge, surviving recombination, consists of few free electron-ion pairs. If opportune fields conditions are provided, the prompt primary scintillation light (characteristic of standard scintillation chambers) is followed by the secondary scintillation light, due to electroluminescence in gas and associated with ionization electrons drifted toward interface, extracted and photon-multiplied in a high field region. The amount of secondary light is proportional to the initial accelerated charge (see Sec. 3.3.2) and, if the event is localized (not a long track), it is delayed, with respect to the primary emission, of the average time spent by the electrons cloud to reach the interface and to be extracted. Primary and secondary light could be readout through a photomultiplier and the recorded delay can be used to determine the event position along the drift direction (see Sec. 4.1.1.4).

The proposed technique would permit the discrimination of the impinging particle on the basis of the measured ratio between the primary and secondary scintillation light intensity and, due to the low ionization threshold, it could be in principle used even for tiny energy deposition produced by nuclear recoils, generating few ionization electrons. According to the quantities introduced in Sec. 3.2.1, a 40 $keV$ nuclear recoil should produce an average amount of 550 *ionization electrons* of which only a small fraction ($few\ units$) is ex-

pected to survive recombination.

To verify the proposed technique, a small double-phase argon chamber has been realized and several tests have been carried out (phase I). At the end of this stage and supported by the obtained results, the prototype has been refurbished and installed at the underground National Laboratory of Gran Sasso (LNGS) to study its behaviour in a low background environment (phase II): particular attention has been given to the argon intrinsic radioactivity.

## 4.1 WARP Prototype 2.3 *l*: phase I

In order to verify the basic hypothesis associated with the proposed argon recoils detection and discrimination, several tests have been carried out with a small double-phase argon prototype, realized by modifying a chamber previously used to detect scintillation light in coincidence with ionizing tracks. The prototype has been used to study the electrons extraction process and the electroluminescence mechanism in argon vapor at 87.2 $K$. Both phenomena, although independently measured, have never been applied together in argon before, at least according to author's knowledge. After these technical measurements, the chamber has been exposed both to $\gamma$ and neutrons sources, in order to study its different response to different kinds of ionizing particles, such as electrons recoils (induced by $\gamma$-particles Compton scattering) and nuclear recoils (produced by the elastic scattering of neutrons over nuclei). According to the electric fields configuration the chamber can work as a standard scintillation chamber (only primary scintillation is produced) or as an enhanced chamber with extraction and proportional multiplication turned on (events are characterized by double light signals). In the first condition the *photoelectrons yield* have been measured for the different sources: this quantity, assuming different values according to the nature of the ionizing particle, provides the average number of *photoelectrons* produced per energy unit released in the medium and it is used to calibrate with the opportune energetic scale the detected scintillation events (once determined the nature of the impinging particle). As stressed in Sec. 2.2 and 3.2.3.1, particles of different nature and energy might produce the same luminous output, due to the different quenching processes: it follows that, as an example, electron and nuclear recoils have to be characterized by two different photoelectrons yields, whose ratio provides the *recoil*/$\gamma$ *ratio* described in Sec. 2.2. On the other

hand, the second and enhanced chamber configuration has been used to verify the proposed detection and discrimination techniques resulted, at the end of the tests, adequate for efficiently detect and discriminate argon recoils.

### 4.1.1 Experimental Set-up

The test prototype is basically an argon double-phase drift chamber, opportunely modified to guarantee electron extraction and electroluminescence. The liquid drift volume is delimited by a stainless steel circular cathode ($\varnothing = 200\ mm$) and by a system of shaping field stainless steel race tracks providing a high field uniformity. A set of three grids, 4 $mm$ pitched and spinned with 150 $\mu m$ thick wires, is placed at the top of the drift region: the lower one ($g1$) is used to close the drift field and it is placed just below the liquid-gas interface. Such geometry defines a total drift length of almost 75 $mm$ and a drift cylindrical volume of 2.3 $l$. The middle grid ($g2$) is positioned at 7.5 $mm$ from the lower grid, just above the the liquid-gas boundary. If an opportune power supply is applied, the $g1$-$g2$ system could provide the extraction of free drifted electron from the liquid to the gaseous phase. The upper grid $g3$, completely contained in the gas phase together with $g2$, is used to favor the proportional scintillation light process. An 8 $inch$ photomultiplier (PMT) positioned in the gaseous phase at 40 $mm$ from the upper grid detects primary and proportional scintillation light. To provide a higher collection efficiency, the surface delimiting the active volume, constituted by the drift region and by the gaseous region facing the PMT photocathode, has been completely covered by a reflective and shifting coating (see Sec. 4.1.1.2). For calibration purpose the cathode is projected to possibly accommodate a $PEEK^{TM}$ support positioning a radioactive source in the middle of the drift volume (35 $mm$ from the cathode). The previously described system is fully contained in a stainless steel vacuum tight cylindrical container. The main geometric characteristics of the detector are summarized in Tab. 4.1 and Fig. 4.1.

Since the gaseous and liquid argon phases have to coexist in the described drift chamber, the whole container is cooled down to 87.2 $K$ (argon boiling point @ 1.02 $bar\ abs$) by placing it in an external liquid argon bath. This set-up ensures, in the inner container, a constant absolute pressure equal to the external pressure (see Sec. 4.1.1.1). The chamber is filled injecting ultra-purified liquid argon (0.1 $ppb\ O_2\ equiv.$): such a level of impurities is achieved by the use of $Oxisorb^{TM}$ and $Hydrosorb^{TM}$ filters (see Sec. 4.1.1.1). Since the

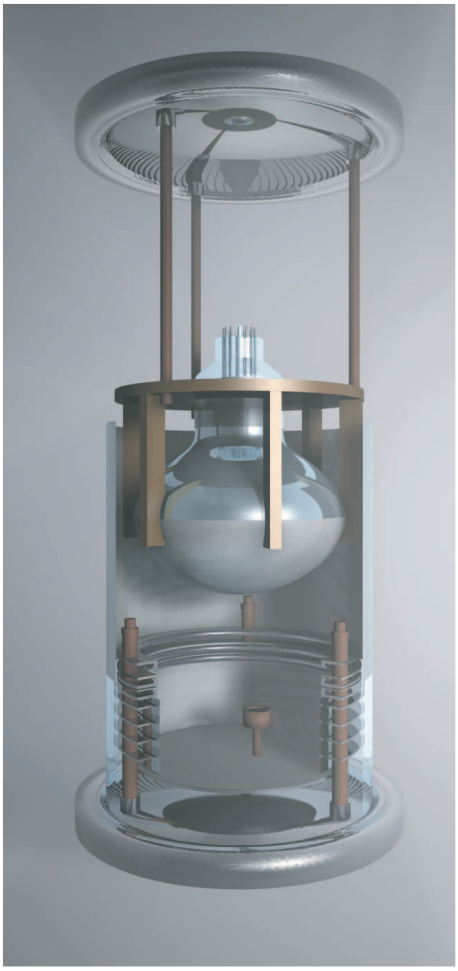

Figure 4.1: Tridimensional view of the chamber inner volume. See details in the text.

total drift length is quite short, no recirculation system has been implemented: lifetime degradation has essentially no appreciable effects on the drift process at least in the $15 \div 20$ days following the filling procedure (typical requested time for a single set of measurements).

As mentioned before, in order to correctly extract the drifted free electrons, the liquid-gas interface has to be positioned between the two lowest grids with a precision of almost 0.5 $mm$ (see Sec. 4.1.1.1). For this reason the filling procedure is monitored by two different kinds of level sensors: one based on the dependency of resistivity from the temperature, the other on the different

| *Quantity* | *Value* |
|---|---|
| Cathode diameter | 200 $mm$ |
| Race tracks inner diameter | 200 $mm$ |
| Drift lenght | 75 $mm$ |
| Drift volume | 2.3 $l$ |
| Distance $g1$-$g2$ | 10 $mm$ |
| Distance $g2$-$g3$ | 7.5 $mm$ |
| Distance $g3 - PMT$ | 40 $mm$ |
| LAr Container diameter | 250 $mm$ |
| LAr Container height | 600 $mm$ |

Table 4.1: Geometric parameters of the 2.3 $l$ chamber. See also Fig. 4.1.

permittivity for liquid and in gaseous argon.

#### 4.1.1.1 Cryogenic and purification system

The gas-liquid phase co-existence in argon is well described in the phase-diagram of Fig. 4.2. As stated above the level of liquid should be maintained constant in time to provide a uniformity in the extraction process: for this reason the system should be kept at a constant temperature. The easiest way to provide such uniformity is to cool down the chamber into an open LAr bath: since the bath is open, its boiling point depends on the external atmospheric pressure and hence, since in the measurement site $P_{ext} = 1.02\ bar\ abs$, the external bath temperature is $T_b = 87.2\ K$ (see Fig. 4.2). In this way, if the chamber walls provide a good heat transmittance and if the chamber itself exchanges heat only with the bath (heat from cables is negligible), the system is kept at a constant temperature of $T_{int} = T_b = 87.2\ K$ and at a constant vapor pressure equal to external pressure ($P_{int} = P_{ext} = 1.02\ bar\ abs$)[1]. As shown in Fig. 4.3 the chamber is inserted in an external dewar containing liquid argon,

[1]If for some reason the internal pressure decreases (corresponding to a raising of the liquid level), the boiling temperature decreases of a certain amount $\delta T$ ($T_b - \delta T$) according to the phase diagram: in this condition the liquid near the walls, exchanging heat with them that are maintained at $T_b$, feels a temperature above the boiling point and hence it tends to evaporate. This causes a lowering of the level and bringing the system at the initial equilibrium conditions. A similar effect is obtained also in the case of a decrease of the level. The system is self-maintaining.

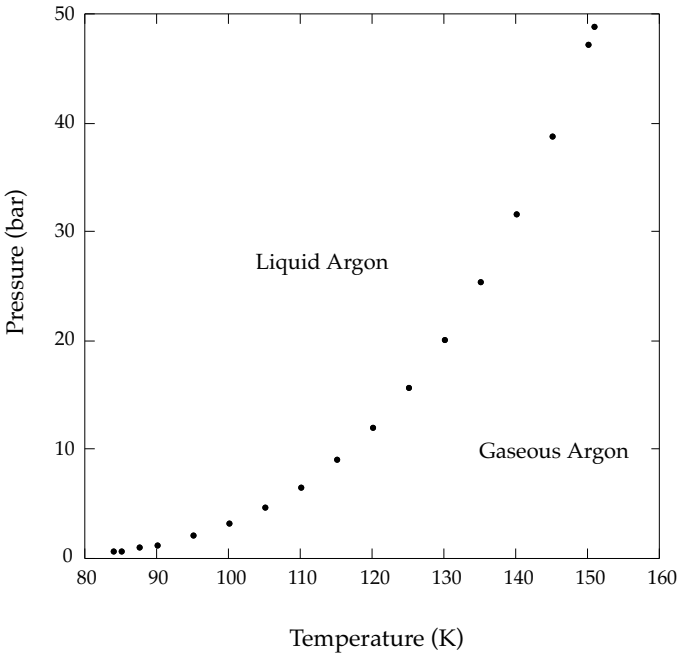


Figure 4.2: The phase diagram shows the vapor pressure curve in argon. Obviously it extends up to argon critical temperature (150.87 $K$) above which the gas cannot be liquified [90].

periodically refilled in order to maintain the prototype completely submerged. Before cooling down starts, the chamber is evacuated through the use of a turbomolecular vacuum pump and an internal pressure of $few\ 10^{-4}\ mbar$ is reached: this operation is necessary to avoid a low argon electronegative purity. Once the evacuated chamber has thermalized with the external bath, purified gaseous argon is injected. Since the chamber is filled through argon gas liquefaction, the filling process is quite slow and essentially dominated by the working pressure: through the use of several sensors the level position is continuously monitored and the procedure stops when the liquid level overcome $g1$ grid.

Following the standard purification system developed by the ICARUS collaboration [43], ultra-pure commercial $Ar$ 60, with a nominal impurities concentration of 0.1 $ppm\ O_2\ equiv.$, passes through $Hydrosorb^{TM}$ and $Oxisorb^{TM}$ cartridges before being injected in the drift chamber. The $Hydrosorb^{TM}$ is a mechanical molecular sieve constituted by crystalline aluminum-silicates form-

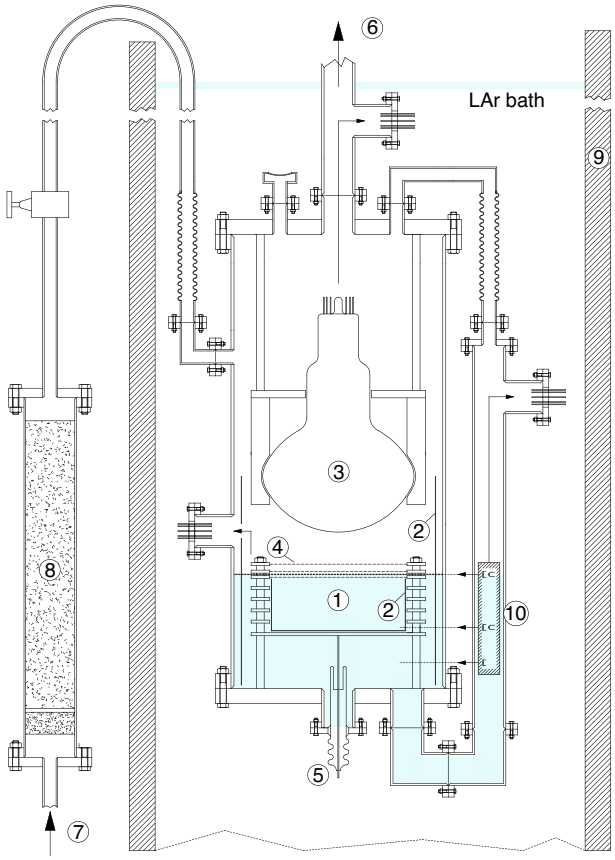


Figure 4.3: Layout of the experimental set-up. In light blue is indicated the LAr region inside the chamber. The chamber is completely submerged inside a LAr external bath. (1) Drift volume; (2) Reflective layer; (3) PMT; (4) Grids; (5) HV supply feed-through; (6) to vacuum pump and pressure sensors; (7) LAr injection; (8) Hydrosorb$^{TM}$/Oxysorb$^{TM}$ filter; (9) External dewar; (10) Level meters.

ing a precise array of cavities whose average dimensions depend on the elements constituting the lattice. The filter efficiently stops all the molecules with an effective dimension higher than the cavities dimensions. Since Ar atoms have an average diameter of 2-3 $\mathring{A}$, a filter with 4 $\mathring{A}$ cavities is frequently used. Molecules with a smaller dimension are able to enter the sieve but, if polar, they are trapped by the attraction due to the positive ions of the lattice, usually facing the cavity itself. Small non-polar molecules overcome

the filter[2]. $H_2O$ and $CO_2$ molecules are efficiently removed by the filter. $O_2$ molecules, since smaller than the sieve diameter and non-polar, survives the $Hydrosorb^{TM}$ cartridge: for this reason this filter is followed (along the filling direction) by the chemical getter $Oxisorb^{TM}$. This last one is essentially constituted by a silica gel impregnated with chromic oxide that absorbs oxygen molecules through reaction

$$2Cr + 3O_2 \rightarrow 2CrO_3. \tag{4.1}$$

The use of this double filter produces a decrease of about a factor 1000 on the impurity concentration of industrially produced argon, leading to a level of 0.1 *ppb* $O_2$ *equiv.* and providing a lifetime of $few\ ms$ (see Sec. 3.2.5). The obtained initial lifetime is obviously several order of magnitude higher than the required one since the whole 7.5 *cm* drift region is covered by drifting electrons in about 40 $\mu s$ (if $\mathcal{E}_d = 1\ kV/cm$). Since no recirculation is applied (due to the small dimension of the chamber), the initially provided lifetime degrades in time due to the out-gassing process: the plastic porose materials tend to release electronegative impurities initially trapped inside of them. The slope of lifetime decrease is obviously function of the out-gassing surfaces and of the liquid argon volume.

As stated above the filling procedure is continuously monitored through two different kinds of level sensors, placed at different position along the drift region. The first is based on the principle that the resistance increases with the temperature: the passage of current in a resistor induces an increase in its temperature and, due to the different heat dissipation occurring in liquid and in gas, the resulting equilibrium temperature within the resistor assumes different values in the two phases. When a high enough voltage is applied to a resistor, in such a way that this heating effect is significant, the resulting resistance assumes higher value in gas than in liquid where the heat is more effeciently dissipated. The used commercially produce silicon resistor behaviour is plotted in Fig. 4.4. The precision of this level meter is essentially determined by the physical dimension of the resistor itself ($\approx 1\ mm$)[3]. The second set of level meters is based on the different dielectric rigidity of liquid and va-

[2]The molecular filter should be periodically activated. This operation is provided by heating the cartridge at 350 $^\circ C$ under vacuum: it is necessary to free the positive ions from the polar attached molecules.

[3]The resistor can actually dissipate heat also if it is not completely submerged in LAr and hence its resistance could change its value even if it is just touched by the LAr.

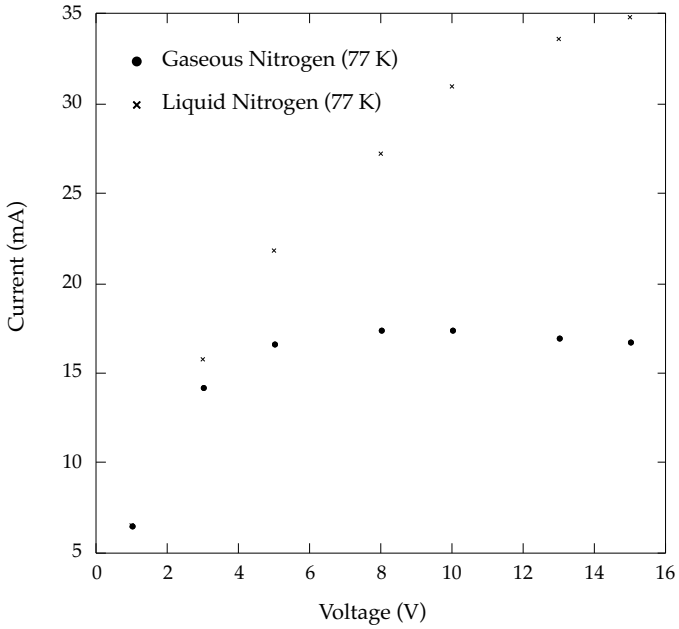


Figure 4.4: Silicon resistor behaviour in liquid and gaseous nitrogen. At the working voltage of 12 $V$, the measured current passes from 16 $mA$ in gas to 36 $mA$ in liquid.

por argon. The custom produced sensor is constituted by a metal nail facing a conductor plate 0.5 $mm$ distant: an opportune voltage is applied between them. The induced electric field is high enough to accelerate loose charges and induce breakdown effects (generating a discharge) in the vapor phase, but not in liquid one. As soon as the liquid submerges the plate the discharge stops occurring. This level meter provides a precision of 0.5 $mm$. These two different techniques allow the positioning of the level within $\approx 0.5$ $mm$.

#### 4.1.1.2 Photomultiplier and light collection

The scintillation UV light produced by an interaction in liquid argon is not easily detectable by a photomultiplier. Two are the major problems, one concerning the behaviour of the PMT at such low temperature (87.2 $K$) and the other associated with the very low wavelength (128 $nm$) of the luminescence light, completely absorbed by the standard borosilicate glass used in PMT windows.

According to the nature of their photocathodes, the photomultipliers response, as function of the temperature, can follow different behaviours as

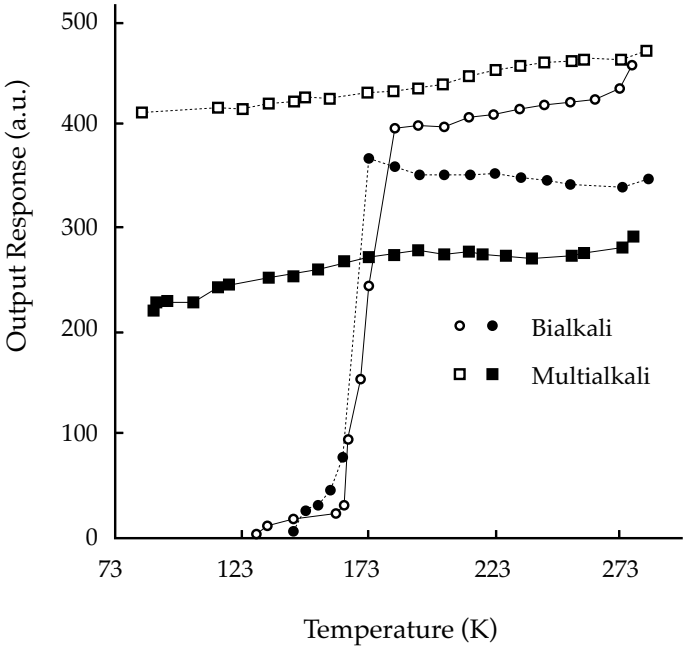


Figure 4.5: Phototubes output dependence from the working temperature. According to the nature of their photocathodes, the phototubes present very different behaviour. Bialkali photocathode photomultipliers show an abrupt drop of the response around 170 $K$ [91].

shown in Fig. 4.5 [91]. For PMTs with bialkali photocathodes an abrupt decrease is observed as soon as the temperature reaches typical cryogenic values. On the other hand, when multialkali photocathodes are used, the photomultipliers response does not present rapid drops. The two behaviours can be explained recalling the different resistivity dependence from the temperature for multi and bialkali materials. At typical cryogenic temperatures, the resistivity of bialkali is about $10^6$ times higher than that of multialkali materials. In other words, once reached a critical temperature, the emission of a large number of photoelectrons by the photocathode, produced by an important light flux, induces a local voltage decrease not efficiently neutralized, in short times, by the supplied charge, due to the high photocathodic resistivity. Since it is a local effect, the photomultiplier response strongly depends on the light flux. The recovery time is obviously function of the dimension and hence of the capacitance of the photocathode itself. This problem can be avoided by evaporating the bialkali photocathode onto a thin conductor layer ($\approx 50$ $\mathring{A}$ of

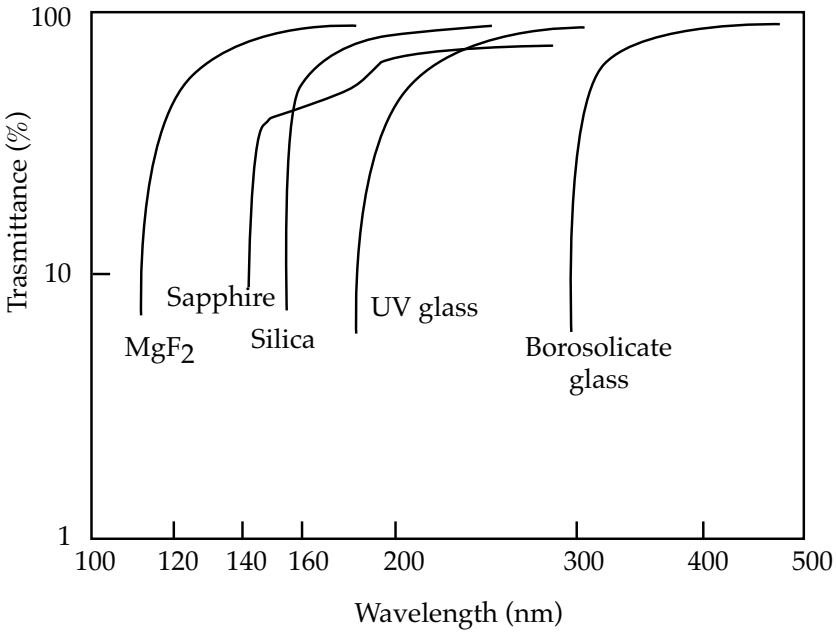


Figure 4.6: PMT windows transmittance as function of the incident light wavelength. Several glasses and crystals are compared. The data refers to 1 $mm$ thick window [93].

$Pt$) [96]. Such conducting under-layer has to be thick enough to guarantee an efficient and fast charge redistribution and, at the same time, thin enough to reduce as much as possible the impinging photon absorption. Nevertheless one should note that, during cooling down procedure, a global gain decrease has been observed in literature [96], both for multialkali and bialkali with the platinum under-layer phototubes. As shown in Fig. 4.5 in the case of multialkali, this decrease is smooth and does not present abrupt drops. For this reason, in order to maintain an almost constant phototube response, its power supply should be increased with time during cooling down.

The second great difficulty afflicting UV scintillation light detection by the means of photomultipliers is represented by the low wavelength of the emitted photons and by the reduced transmittance of ordinary PMTs windows at such wavelengths, as shown in Fig. 4.6. In the specific case of pure liquid argon luminescence light (peaked around 128 $nm$), only $MgF_2$ windows present a transmittance value sensitively different from zero. This material, besides its high cost, presents bad mechanical characteristics at low temperature due to its fragility.Moreover, in order to provide a high detection efficiency, the in-

| | |
|---|---|
| Length and diameter | 293 $mm$ / 203 $mm$ |
| Cathode size | 190 $mm$ |
| Spectral response | 300500 $nm$ |
| Cathode type | $K_2CsSb$ *on Pt layer* |
| Dynodes | $12LF\ CsSb$ |
| SER peak-to-valley | 2 |
| Risetime and FWHM | 5 $ns$ / 8 $ns$ |
| Maximum gain | $5 \times 10^7$ |
| Quantum efficiency (blue) | $\approx 20\%$ |
| HV supply for $10^7$ gain | 1200 $V$ |

Table 4.2: Nominal characteristic of the *Electron Tubes* $9357FLA$ photomultiplier [96].

ner surfaces of the chamber should be covered by a high performance diffusive layer (see Fig. 4.1), increasing the amount of light reaching the PMT and making more homogeneous the detector response[4]. This layer, since covering the drift volume, should be dielectric in order to avoid electric field modifications. Once again, no commercial materials present high enough diffusive properties for 128 $nm$ incident light.

The above described drawbacks could be solved by the use of wavelength shifters, shifting the pure LAr 128 $nm$ light into a wavelength region for which PMT transmittance is considerable and high reflecting layers exist. Several options have been investigated in literature [92, 94, 95]. The solution, applied during phase I of the 2.3 *liters* detector, foresees the use of *Tetraphenylbutadiene* (TPB). This powder substance is used as shifter, absorbing the pure LAr 128 $nm$ light and reemitting it with a broad peak centered around 438 $nm$ (visible range) [94]. A TPB layer is coated onto the photomultiplier borosilicate glass window (*Electron Tubes* $9357FLA$, see Tab. 4.2)[5]: its thickness should be optimized to increase as much as possible the conversion efficiency and, at the same time, to reduce auto-absorption effects. This layer can be evaporated under vacuum conditions, airbrushed or through doping of the substrate [94]. The optimum has been obtained for 200 $\mu g\ cm^{-2}$ [92]. The quantum efficiency,

[4]If only the direct light was detected the response of the chamber would depend on the event position. Such dependence is removed if all the produced light is detected.

[5]The borosilicate glass presents a 100% transmittance for visible light.

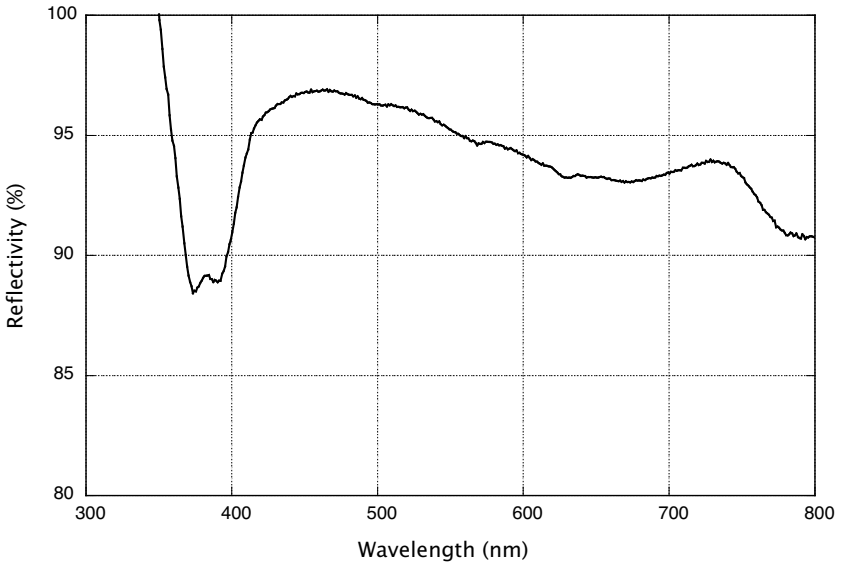


Figure 4.7: Measured reflectivity for the $VM2000 + TPB$ system as function of the impinging light wavelength. Its values before and after cooling down are plotted. Several different solutions ($Barium\ Sulfate + TPB$, $Magnesium\ Oxide + TPB$, $PTFE + TPB$) have been investigated and the most performing ($VM2000 + TPB$) has been selected.

as function of the coated amount of TPB, has been measured for a PMT with photocathode and window properties identical to the one installed but different dimensions (flat 30 $mm$ diameter Electron Tubes photomultiplier) [92]. The results suggest an average quantum efficiency around 9% for 128 $nm$ incident light to be compared with the 20% on visible light. A rough estimate, assuming an isotropic light re-emission by the TPB, leads to the an average correspondence of 1 $\gamma(vis.)$ each 1 $\gamma(128\ nm)$. Since as shown in Ref. [95] the conversion efficiency by TPB is of the order of 80% for wavelength down to 160 $nm$, this means that, in average, when conversion occurs more than one visible photon is emitted (otherwise the measured ratio 1/1 is not motivated). In this configuration the reflective layer is constituted by $VM2000^{TM}$ plastic mirror[6] (specular reflectivity $\approx 99\%$) glued on $Mylar^{TM}$ substratum: the whole is coated with TPB exactly as for the photomultiplier.

According to the described set-up, the UV light is shifted as soon as it touches the PMT window or the diffusive layer: the resulting emitted visible

[6]Produced by $3M\ WorldWide$.

light (centered at 438 $nm$) is then reflected by the $VM2000 + TPB$ system until it is absorbed or detected by the PMT. The measured diffusive layer reflectivity[7], in the visible range, is about 95%, a high enough value to provide a good light collection. The experimental results are shown in Fig. 4.7. According to the used geometry the reflector and the PMT window cover 85% of the inner volume total surface.

#### 4.1.1.3 Fields configuration and grid transparency

Different configurations of the electric fields have been applied to the chamber, according to the kind of the carried out test. The choice of the power supplies is essentially determined by the necessity of avoiding high voltages in the gaseous phase (due to discharge problems) and by the request of total electronic transparency of $g1$ and $g2$ grids.

In order to provide, in the argon volume, regions with significantly different electric fields strengths and, at the same time, to efficiently screen them each other, a system of grids differently power supplied has been used. As previously explained the role of $g1$ and $g2$ is respectively to close the drift volume and to provide a high field region near the interface to favor electrons extraction. The electrons emitted in the gas phase are then accelerated in the region between $g2$ and $g3$ and eventually collected by the upper grid. To improve as much as possible the efficiency detection of the ionization signal, no ionization loss should occur: in other words, the intermediate grids should provide a high electron transparency otherwise, part of the ionization electrons is collected before it reaches the multiplication region. The grid transparency is well described by the Bunemann law [97] expressing the grid transparency as a function of the uniform electric field in front of and behind it with respect to the electrons drift direction, respectively $\mathcal{E}_1$ and $\mathcal{E}_2$[8]. The transparency has been computed by Bunemann assuming that the electrons diffuse along the field lines of force and hence that the fraction of surviving electrons is equal to the fraction of lines by-passing the grid. This assumption is justified both in liquid argon and in argon gas (at the working pressure). The computation has been executed for a parallel wires grid with a pitch equal to $d$ and a wire radius equal to $r$: the geometrical parameter used in the theory is $\rho = \frac{2\pi r}{d}$. According to the model results, the fraction of lines by-passing the grid is

[7]The measured reflectivity includes both diffusive and specular components.

[8]This are the value of the fields far from the wires, where it can be considered uniform

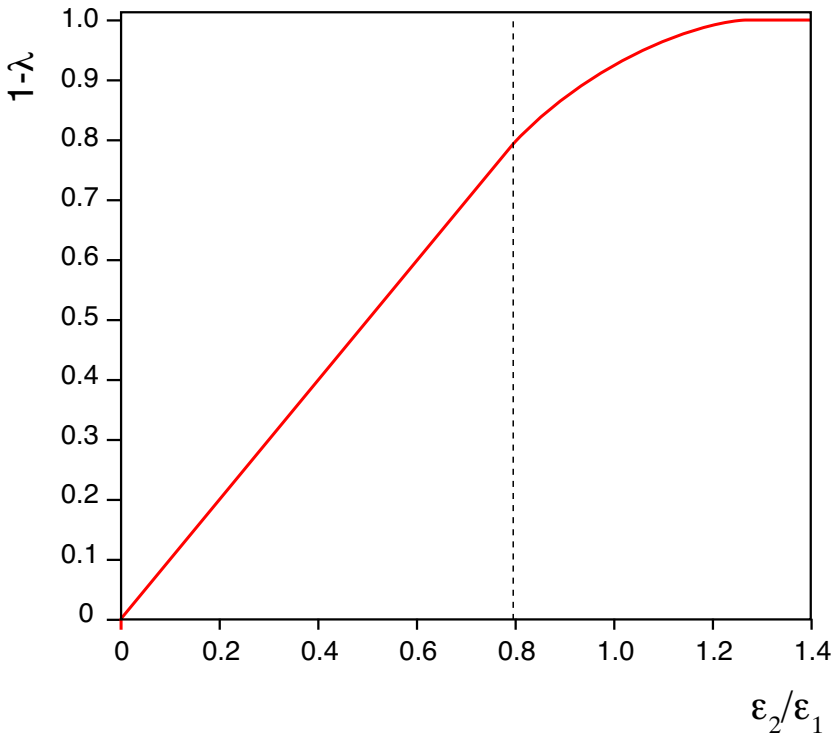


Figure 4.8: Grid transparency as function of the field ratio for $\rho = 0.1178$. The upper limit for total transparency is $\mathcal{E}_2/\mathcal{E}_1 = 1.27$ and the lower limit $\mathcal{E}_2/\mathcal{E}_1 = 0.789$.

given by [97]

$$1-\lambda = 1 - \frac{\mathcal{E}_2 - \mathcal{E}_1}{\pi \mathcal{E}_1}\left\{\sqrt{\left(\frac{\mathcal{E}_1+\mathcal{E}_2}{\mathcal{E}_2-\mathcal{E}_1}\rho\right)^2 - 1} - \arccos\left(\frac{\mathcal{E}_2-\mathcal{E}_1}{\mathcal{E}_1+\mathcal{E}_2}\frac{1}{\rho}\right)\right\} \tag{4.2}$$

for value of fields such that

$$\frac{1-\rho}{1+\rho} < \frac{\mathcal{E}_2}{\mathcal{E}_1} < \frac{1+\rho}{1-\rho}. \tag{4.3}$$

For a fields ratio greater than the above upper limit, all the lines of force by-pass the grids and total transparency is obtained

$$1-\lambda = 1 \qquad for\ \frac{\mathcal{E}_2}{\mathcal{E}_1} > \frac{1+\rho}{1-\rho} \tag{4.4}$$

On the other hand, for fields in front of the grid stronger than those behind of it and such that

$$\frac{\mathcal{E}_2}{\mathcal{E}_1} < \frac{1-\rho}{1+\rho} \tag{4.5}$$

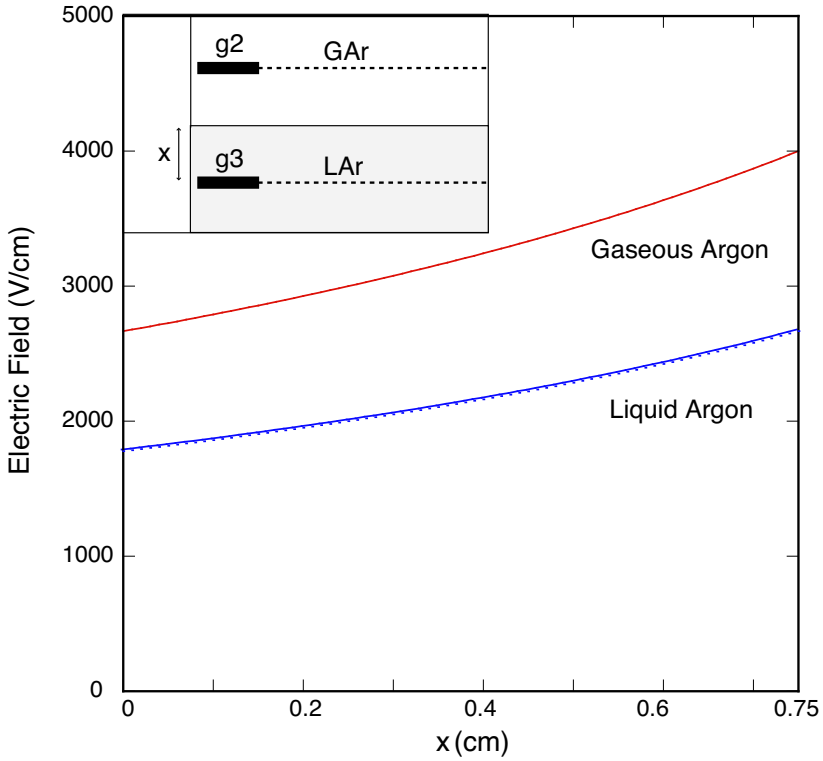


Figure 4.9: behaviour of the electric fields strength in liquid and gaseous argon for an applied voltage of 2 $kV$ between $g1$ and $g2$ grids (d=0.75 $cm$). In the small box the geometrical configuration is sketched.

all the "difference" between $\mathcal{E}_1$ and $\mathcal{E}_2$ is collected by the grid leading to[9]

$$1 - \lambda = \frac{\mathcal{E}_2}{\mathcal{E}_1}. \tag{4.6}$$

The computed grid transparency as function of $\mathcal{E}_2/\mathcal{E}_1$ ratio is plotted in Fig. 4.8 for the grids used in the chamber ($r = 75\ \mu m$, $d = 4\ mm$ and hence $\rho = 0.1178$). As expected, for opposite directions electric fields all the electrons are collected by the grid.

Another important aspect, that should be stressed to avoid misunderstandings, concerns the electric fields value in the extraction region. Due to the different permittivities of the two phases, the electric field in this region is not uniform: a free charge in liquid feels a lower field than one in the gaseous

[9]Since $\mathcal{E}_2 < \mathcal{E}_1$ the density of lines of force is higher in front of the grid than behind the grid and hence the "surplus" lines per unit surface are collected.

phase. The problem could be solved in general, simplifying the situation to the case of a capacitor filled by two different dielectrics characterized by the permittivities $\epsilon_l$ and $\epsilon_g$: the used geometry is sketched in Fig. 4.9. Supposing that voltage $V$ is applied between the plates and that the interface level is position at $x$, the value of the electric fields could be obtained imposing

$$V = V_g + V_l \tag{4.7}$$

and the boundary condition that, at the interface, the normal component of the $\overline{\mathbf{D}}$ field is conserved

$$\frac{V_l}{x}\epsilon_l = \frac{V_g}{d-x}\epsilon_g \tag{4.8}$$

leading to

$$\mathcal{E}_g(x) = \frac{V_g}{d-x} = \frac{V}{x(\epsilon_g/\epsilon_l - 1) + d} = \mathcal{E}_0 \frac{1}{(x/d)(\epsilon_g/\epsilon_l - 1) + 1} \tag{4.9}$$

$$\mathcal{E}_l(x) = \frac{V_l}{x} = \frac{V}{x(1 - \epsilon_l/\epsilon_g) + d(\epsilon_l/\epsilon_g)} = \mathcal{E}_0 \frac{1}{(x/d)(1 - \epsilon_l/\epsilon_g) + (\epsilon_l/\epsilon_g)} \tag{4.10}$$

where $\mathcal{E}_0 = V/d$ (the field produced when only one dielectric fill the whole region) has been introduced. The behaviour of $\mathcal{E}_g(x)$ and $\mathcal{E}_l(x)$ for a fixed value of $V$ is shown in Fig. 4.9. Since in the real case the two plates are represented by two grids, the Eq. 4.9 and 4.10 should be referred to the value of the electric fields far from the wires, where they can be considered uniform.

To provide the possibility of testing a variety of different fields configurations the two upper grids are independently power supplied with standard Novalec 8174 HV Module. In this way the extraction process is decoupled from the multiplication one. For what concerns the drift field, its uniformity is provided by the means of standard race-tracks: each ring is connected to the upper one through a cryogenic ceramic resistor $R \approx 50\ M\Omega$. The race-tracks chain is connected to the cathode and, on the other side, to the lower grid $g1$. Both $g1$ and the cathode ($k$) are independently power supplied respectively using a Novalec 8174 HV Module and an Heizinger HNC. In the rest of the work, the symbols $\mathcal{E}_d$, $\mathcal{E}_{e,l}$, $\mathcal{E}_{e,g}$ and $\mathcal{E}_m$ will refer respectively to the drift field, to the extraction field in liquid, to the field in the gas region of the extraction volume and to the multiplication field: they are the value assumed by the fields far enough from the grids. These values are respectively determined by the applied voltage $V_{k\text{-}g1}$, $V_{g1\text{-}g2}$ and $V_{g2\text{-}g3}$.

In order to use the chamber as a pure scintillation counter, extraction and

multiplication have to be avoided since only the primary scintillation should be produced: in this case the total collection by grid $g1$ is requested. This can be achieved providing $\mathcal{E}_{e,l}$ opposite to $\mathcal{E}_d$ for which all the lines of force are collected by the grids and none of the drifted electrons is emitted into vapor phase. To avoid multiplication of electron due to ionization in the gas region the multiplication field is turned off. On the other hand, to use the chamber as a double-phase detector, a completely different configuration has to be applied. To reduce electrons loss before multiplication region, total transparency is required for $g1$ and $g2$ together with total extraction. The first two requests are satisfied if $\mathcal{E}_{e,l}/\mathcal{E}_d > 1.27$ and $\mathcal{E}_m/\mathcal{E}_{e,g} > 1.27$ (see Fig. 4.7). To provide total extraction a field $\mathcal{E}_{e,l} \approx 2.5\text{-}3.0\ kV/cm$ should be applied (see Sec. 3.3.1). Eventually, to favor the collection of the electrons by the last grid a reverse configuration for the photomultiplier has been chosen: a negative voltage is provided to the photocathode while the anode is grounded. In this way all the lines of force should close onto the last grid and not on the photocathode. As stated above, due to breakdown problems, these conditions sometimes are not satisfiable and configurations without total transparency have to be used.

Although the Bunemann approach is quite satisfying, the drift chamber has been simulated by the means of *Garfield* software [100]: for the used grids configuration the results are in a good agreement with the Bunemann approximation.

#### 4.1.1.4 Signal description and data acquisition system

To properly describe the data acquisition systems it should be useful to outline the light signals formation and their characteristics (for a more detailed description of the signal see Sec. 4.1.2.3). An interaction in the drift volume produces a ionization track whose length depends on the characteristic of the ionizing particle: as stressed before, this leads to the emission of prompt UV photons with decay constants $\tau_s \approx 6ns$ and $\tau_t \approx 1.5\mu s$. In other word within $few\ \mu s$ the primary scintillation emission process is almost completed. According to the applied drift field the electrons, escaped from recombination, are drifted towards the liquid-gas interface, extracted and photon-multiplied in the gaseous phase: the ensemble of all these emitted secondary UV photons is called proportional light signal (see Fig. 4.10). A photomultiplier, facing the multiplication region, detects both the direct and the reflected light (by the diffusive layer surrounding the sensitive volume) produced as primary and sec-

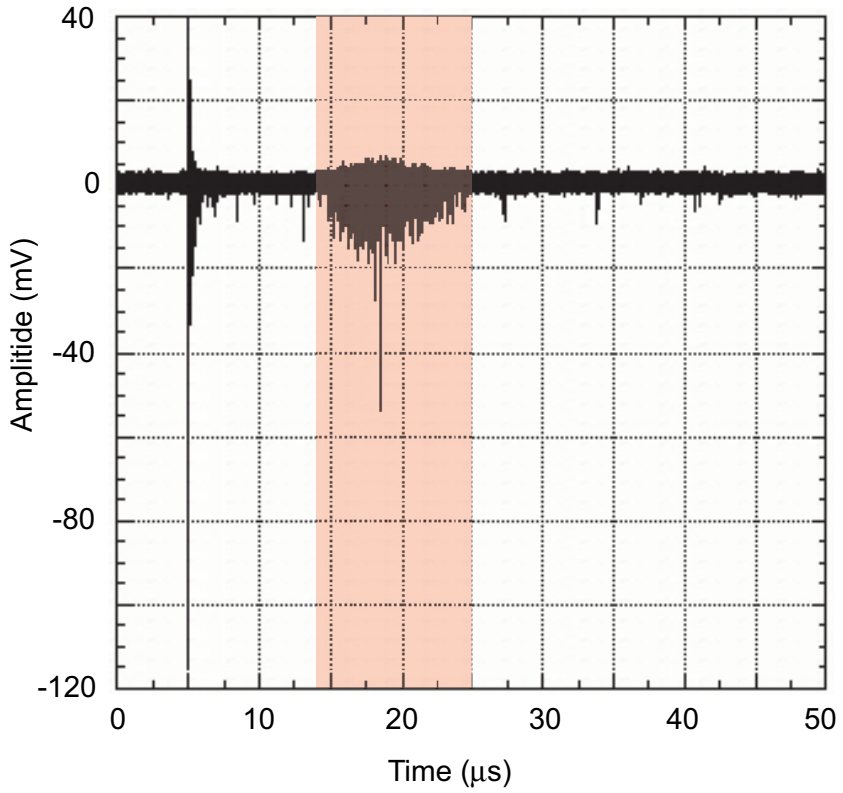


Figure 4.10: Typical PMT signal detected in the double phase chamber. The first peak is primary scintillation while the train of small pulses constitutes the proportional scintillation.

ondary scintillation. Differently from what occurs for primary light emission, the duration of the proportional light pulses train is function of the length and orientation of the track produced in the liquid (see Fig. 4.10): it assumes very different values according to the kind of ionization event. The time separation $\Delta\tau$ between the primary signal and the barycenter of the proportional signal is equal to the mean time spent by the ionization electrons cloud to drift from the interaction point to the multiplication region: obviously this quantity is meaningful for localizing events in which the ionization electrons cloud is almost contained a small volume (compared to the chamber drift volume). In this case (point-like events), the delay provides information about the space distance between the interface and the interaction point along the $z$ drift axis. On the other hand, for extended tracks, like the ones typically produced by muons and crossing from top-to-bottom the whole chamber, its value cannot

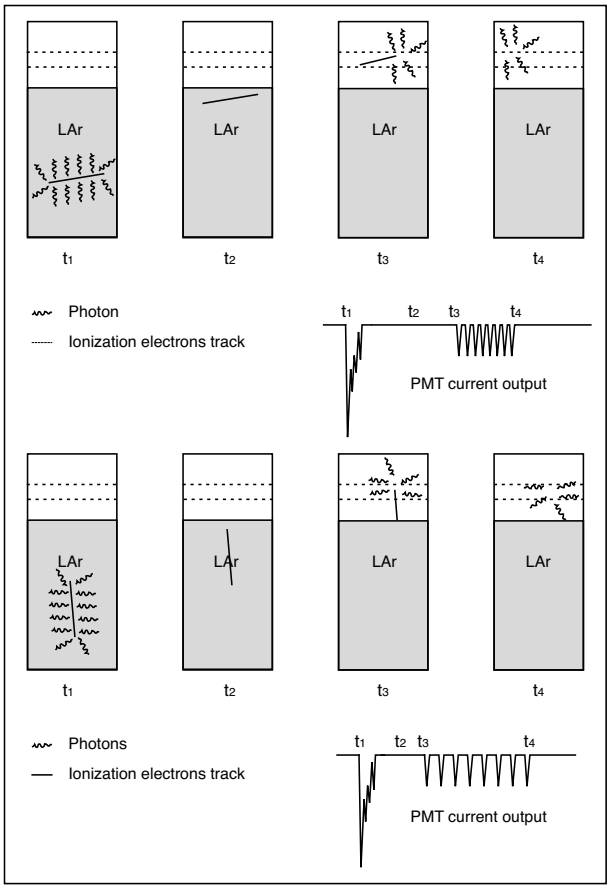


Figure 4.11: Signal formation for two differently oriented tracks (not point-like): one parallel to the drift direction and another almost perpendicular to it. At the instant $t_1$ the interaction in the sensitive volume occurs: a prompt bunch of photons is emitted (primary light). At the instant $t_2$ the electrons, produced by the interaction, are drifting towards the interface and no light is produced. At instant $t_3$ the first electrons reaches the multiplication region and they induce the emission of light. At instant $t_4$ the last electrons are collected by the final grids and no more photons are produced. According to the orientation of the track and to its length, the secondary signals train duration changes. For two tracks ideally constituted by the same amount of ionization electrons, $t_4$-$t_3$ of the parallel track is shorter than that of perpendicular one.

be used to properly describe the ionization event: in this case primary light is immediately followed by a train of secondary emitted photons that lasts for the total drift time. A sketch of the formation of the signal for differently

oriented tracks is shown in Fig. 4.11.

The meaningful physical information that can be extracted from the PMT output signal, represented by its anodic current, can be listed as:

1. The number of primary scintillation photoelectrons $N1$, in first approximation proportional to the charge subtended by the primary scintillation signal;

2. The number of secondary scintillation photoelectrons $N2$, proportional to the charge subtended by the totality the secondary pulses;

3. The primary signal duration;

4. The primary signal pulse-shape (see Sec. 4.2.2.2);

5. The proportional signal duration;

6. The delay time $\Delta\tau$ between the primary and the proportional light barycenter.

Assuming a high reflectivity of the diffusive layer, that makes the chamber response spatially homogeneous, the ratio $N2/N1$ can be used to determine, in a fixed field configuration, the nature of the ionizing particle: different particles produce different amounts of ionization and excitation and the number of primary photoelectrons $N1$ can be used to determine, after particle discrimination, its energy.

Since, as stated above, the number of photoelectrons associated with primary and electroluminescence signals is the meaningful quantity, the PMT output signal is sent to a Canberra 2005 inverting charge preamplifier with a leading edge of 15 $ns$, a fall time of 50 $\mu s$ and a charge sensitivity of 4.5 $mV/pC$ or 22.7 $mV/pC$. The anodic current from the photomultiplier is hence integrated and a voltage signal, proportional to the subtended charge, is provided. A typical pre-amplified signal is shown in Fig. 4.12. Two separated peaks form in correspondence with the primary scintillation and the proportional light signals. In its linearity range, the amplitude of the Canberra output is proportional, for fast signals, to the number of photoelectrons constituting the input signal. For slow signals (like the train of secondary photoelectrons) due to the limited preamplifier fall time ($\approx 50$ $\mu s$) the amplitude should be

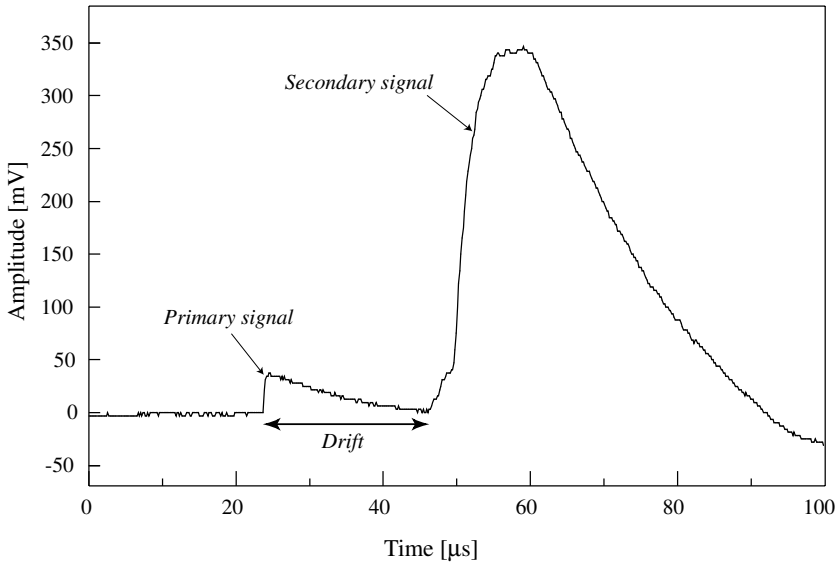


Figure 4.12: Typical phototubes preamplified signal, obtained by integrating a current signal similar to that of Fig. 4.10. As shown later, this signal topology is typical of the $\gamma$-like events.

corrected to be proportional to the input charge[10]. In the rest of the work, $S1$ and $S2$ will refer respectively to the corrected amplitude of the primary and secondary scintillation peaks. The shown $S2$ data should be considered, if not explicitly declared, as corrected for lifetime degradation too, obviously afflicting the $S2$ amplitude according to the interaction position along the $z$ axis.

The delay $\Delta\tau$ between $S1$ and the start of $S2$ is essentially determined by several, in principle independent contributions (since electrons pass through regions with different and independent electric fields). They are

- the time $\tau_d$ spent by ionization electrons, nearest to the interface[11], to drift toward the grid $g1$. It can be modified changing $\mathcal{E}_d$ and its maximum value is provided by $\tau_d^{max} = v_d(\mathcal{E}_d) \cdot 7.5\ cm$;

[10] If a secondary signal is constituted by a long train of pulses, the pre-amplifier output ideally associated with the first pulses starts to significantly decay while other signals are still arriving. As a consequence, the maximum amplitude of the output signal is no more proportional to the total number of photoelectrons. This effect would vanish if longer fall time pre-amplifiers were used. Nevertheless, knowing the duration of the signal, it is possible to correct the $S2$ amplitude to count for this effect.

[11] This specification is essential for extended tracks.

- the time $\tau_{g1\text{-}e}$ expended to reach the interface from $g1$, influenced by $\mathcal{E}_{e,l}$;
- the electrons extraction time $\tau_e$ function of $\mathcal{E}_{e,l}$ and $\mathcal{E}_{e,g}$ (see Sec. 3.3.1);
- the time $\tau_{e\text{-}g2}$ spent by extracted electrons to reach $g2$ from the liquid-gas interface. It depends on $\mathcal{E}_{e,g}$;
- the drift time $\tau_m$ spent by electrons, in the multiplication region, until an electric field, high enough to produce electroluminescence ($> \mathcal{E}_s$), is met. If secondary light production occurs just near the wires, this time depends on the $\mathcal{E}_m$ (the value of the electric field in the uniform region far from the grids). If $\mathcal{E}_m > \mathcal{E}_s$ the production starts as soon as the electrons reach the region $g2$-$g3$ and $\tau_m = 0$.

Obviously these time intervals, apart from $\tau_d$, are in practice equal for all signals, since their sum represents the global time spent by an electron to reach, from the end of the drift volume ($g1$), the region where electroluminescence occurs. While, at the working voltage, $\tau_e$ and $\tau_m$ are almost negligible (see Sec. 4.1.2.2), the contributions $\tau_{g1\text{-}e}$ and $\tau_{e\text{-}g2}$ should be considered since of the order of $few\ \mu s$ (comparable to short drift times). The order of magnitude of $\tau_{g1\text{-}e}$ and $\tau_{e\text{-}g2}$ is determined by the average electron drift velocity at fields of the order of $few\ kV/cm$ ($few\ mm/\mu s$). The global delay can then be expressed as $\Delta\tau = \tau_d + \tau_{const}$ (with $\tau_{const} \approx few\ \mu s$) and hence, in the rest of the work, the delay and the drift time will be indifferently used since they both contain the same information concerning the event distribution along $z$ direction.

The durations of the two signals in the PMT anodic output essentially correspond, after preamplifier integration, to the risetime of the primary and secondary peaks, called $\tau_{r1}$ and $\tau_{r2}$ (see Fig. 4.12). Typical risetime for primary signal in pure liquid argon is few $\mu s$ (determined by the longest de-excitation decay time). The quantity $\tau_{r2}$ is function both of the geometry and of the applied field and it represents the time interval between the first electrons start producing light and the last one (of the lower part of the track) is collected by the grid $g3$. For point-like events and $\mathcal{E}_m > \mathcal{E}_s$ the risetime is equal to the time spent by the electrons to cover the multiplication region (assuming electroluminescence occurs all along the electron drift). If, on the contrary, the multiplication field is above threshold only near the wires, the risetime $\tau_{r2}$

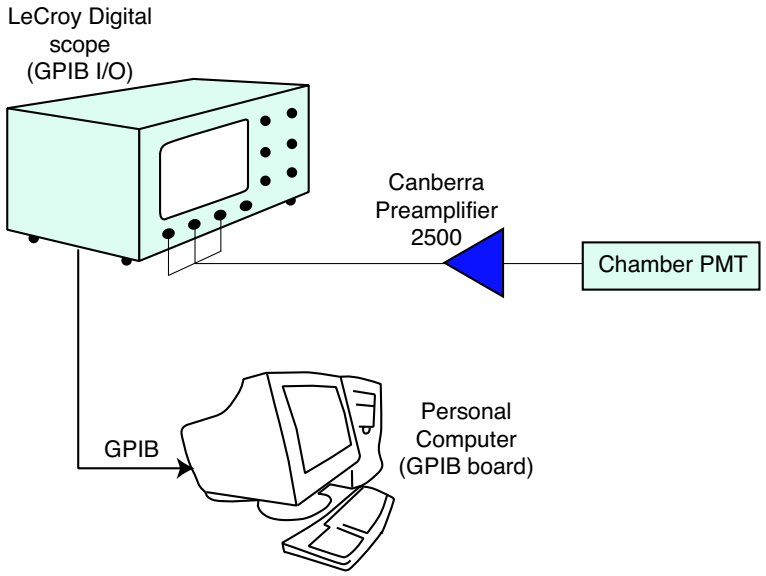


Figure 4.13: The PMT anode signal is preamplified and formed by the means of a shaping amplifier with variable gain. The signals amplitude is recorded by the means of an ORTEC Multichannel Analyzer board installed onto a personal computer.

of a localized event is equal to $\tau_{m\text{-}g3}$, the time spent by the electron to drift in the region where electroluminescence occurs (shorter than the time required to cover the nominal $g2$-$g3$ distance).

On the basis of the previous observations, it is possible to evaluate the width of a time interval completely containing the double signal produced by a ionization event in the liquid region: this quantity plays a crucial role in the data acquisition (DAQ) system since it influences the width of the buffer recorded once a trigger is provided. Its value is approximately given by

$$\tau_{tot} = \tau_d^{max} + \tau_{const} + \tau_{g2\text{-}g3} \tag{4.11}$$

representing the global time spent by an electron drifting from the cathode level to the collection $g3$ grid. At the working voltage $\tau_{tot}$ is of the order of 50 $\mu s$.

Since the chamber has been used both as a traditional scintillation counter or as an enhanced double-phase detector, two different data acquisition systems have been realized. The first configuration has been essentially used to evaluate the detection efficiency of the chamber and to execute a series of energy calibrations with different radioactive sources. For this kind of ap-

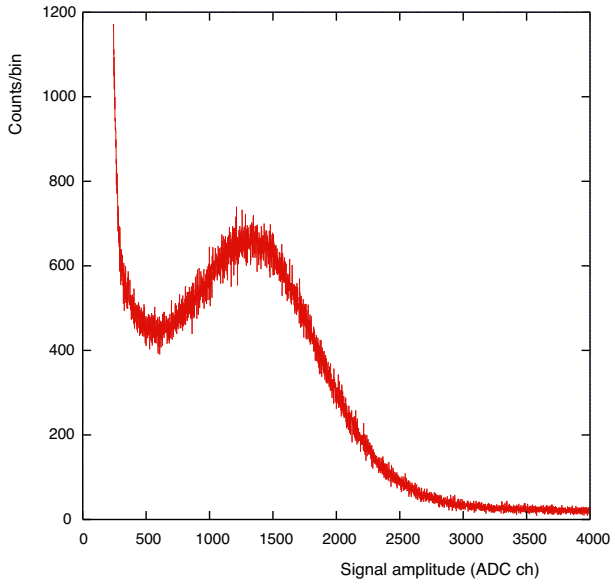


Figure 4.14: The SER distribution is usually measured by illuminting the phototubes through a photodiode or a lamp connected to an optical fiber, in such a way to induce at maximum the emission of one photoelectron. Another way, leading to a similar results in terms of *phe/ADC ch*, is based on the phototube noise distribution. Due to the very low work function of the photocathode materials, the thermionic emission has a finite probability of occurring and it is not negligible even at 87.2 $K$ [93]. From the measured distribution the single electron response can be deduced.

plication the spectrum of the primary light is studied and the production of proportional light has to be suppressed. In other words the meaningful information is just contained in the spectrum of the primary signal amplitude expressed in photoelectrons. To acquire these data, the DAQ system shown in Fig. 4.13 has been used. The anodic signals from the PMT are sent the charge preamplifier and then shaped at 6 $\mu s$ through an *ORTEC 570* amplifier (the shaping time interval should be large enough to fully contain all the produced primary light whose slow component has a characteristic decay constant of 1.5 $\mu s$). The output amplitude distribution is recorded by means of a multichannel analizer (providing *counts/ADC ch*). According to the selected amplification value, this chain can be used to measure at different scales the primary scintillation spectrum. The calibration factor *phe/ADC ch* is needed to express the primary spectrum in photoelectrons: such value has been obtained by measuring the response of the PMT to single photoelectrons (SER)

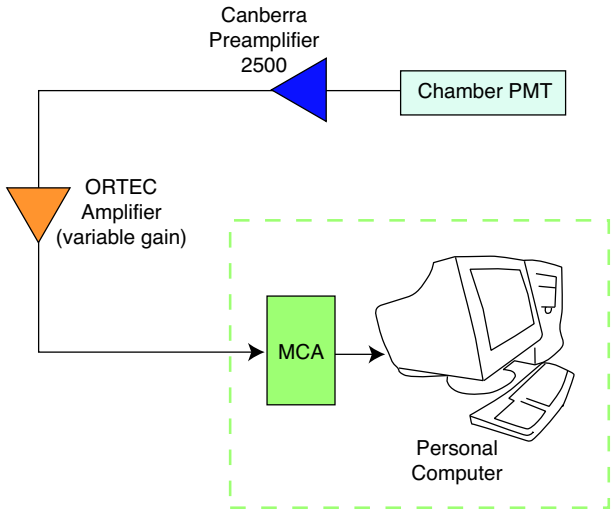


Figure 4.15: Double signals acquisition system. The phototube anodic current signal is preamplified by the means of a Canberra Model 2005 charge amplifier and sent to a digital scope where it is split onto three channels. The oscilloscope self trigger is set onto the high gain channel. Each time a trigger occurs, the data are transferred to a personal computer through GPIB interface.

with the same chain. In other words a SER charge distribution is acquired before each primary light measurement. Obviously to be sensitive to these small amplitude signals a high gain for the amplifier should be used. A typical SER distribution is plotted in Fig. 4.14. The peak position is used to evaluate the average *phe/ADC ch* factor[12]. This factor is function of the PMT gain (voltage applied) and of the preamplifier and amplifier gains.

As soon as the extraction and multiplication fields are turned on, the light detected by the photomultipliers becomes a superposition of scintillation and electroluminescence signals and hence light spectrum, acquired with the above acquisition systems, becomes useless. At the same time the single electron response is not actually affected by the presence of proportional light: this is due to the fact that all the secondary scintillation signals have amplitudes, in average, higher than the amplitude range where the SER is measured. Consequently, as in previous case, the SER is evaluated before each double signals

[12]Since SER distribution and source spectra are acquired with different gains of the electronic chain, this last has been calibrated in order to rescale the *phe/ADC ch* to the appropriate value in each scale.

data acquisition, since the gain of the PMT change in time due to cooling down processes (see Sec. 4.1.1.2). For double signal acquisition the DAQ system sketched in Fig. 4.15 has been used. The Canberra output is splitted and sent to the channels of a digital scope (Lecroy LC534AM) with a sampling rate of 25 $MHz$ and a 8 $bit$ dynamical range. The input impedance of the oscilloscope channels are set to 1 $M\Omega$ providing an almost correct splitting. Different vertical scales have been applied to face the different dynamical ranges of the primary and secondary peaks and to provide an appropriate vertical resolution for both of them. In the standard configuration, the oscilloscope internal trigger is used and set on the highest gain channel in order to trigger on low amplitude primary signals (see Sec. 4.1.2.3 for more precise details). The performed trigger is defined by $max(S1, S2) > threshold$. Since often the secondary signal is significantly higher than the primary one, the trigger could occur on secondary peak instead of primary (when primary is below threshold). For this reason the trigger delay has been positioned in the middle of an acquisition window of 200 $\mu s$: in this way even the longest double signal ($\approx 50$ $\mu s$ as shown above) is fully contained in the window for events triggered on primary or secondary peak. The limited dynamical range of the digitizer is saturated by a fraction of the acquired data. This saturation effect could occur both on $S1$ or $S2$. In the first case the saturation effect is sharp. A less clean cut is observed on secondary signal amplitude since it often occurs on the tail of primary signal: in this case the saturated amplitude is the sum of $S2$ signal and the amplitude of the $S1$ tail at the $S2$ arrival time. The digitized pulse shapes are transferred through a $GPIB$ *board* to a personal computer and recorded in a storage device for offline analyses. The value of the measured SER is associated with each data acquisition in order to be able to express the $S1$ and $S2$ amplitude in terms of photoelectrons. The above described DAQ system has been slightly modified during the measurement with the neutron gun generator (see Sec. 4.1.2.3): in this case, the signal provided by the neutron gun itself, synchronous to neutrons bunch, has been used as an external trigger for the digital scope in order to acquire light events most likely due to neutron interactions.

### 4.1.2 Experimental results

The WARP prototype has been calibrated with a set of different radioactive sources. Light efficiency collection, extraction and multiplication processes

have been deeply investigated by the means of a $^{109}Cd$ source placed in the middle of the drift chamber through a dielectric support. The discrimination technique has been studied by comparing the detector response, in term of primary and secondary signal, for $\gamma$-particles, minimum ionizing particles, $\alpha$-particles and nuclear recoils induced by elastic scattering with neutrons. Some tests have been executed both in pure and xenon-doped liquid argon.

Before going into deeper details, it should be useful to briefly comment on the photon and neutron interaction in liquid argon. Figure 4.16 shows the interaction length for photons as function of their energy: at low energies (up to 30-40 $keV$), the photoelectric effect dominates, while at high energies Compton scattering takes over. The two cross section are almost comparable around 70 $keV$ and they both induce the emission of an electron: in the case of photoelectric effect, the electron is emitted with an energy close to the initial photon energy and the difference is represented by the initial bound energy of the emitted electron (for K-shell $E_b \approx 3\ keV$). For Compton scattering, the electron recoil energy follows the well known distribution predicted by *Klein-Nishina* cross section reaching a maximum at

$$E_e^{max} = h\nu - \frac{h\nu}{1 + 2h\nu/m_0c^2} \tag{4.12}$$

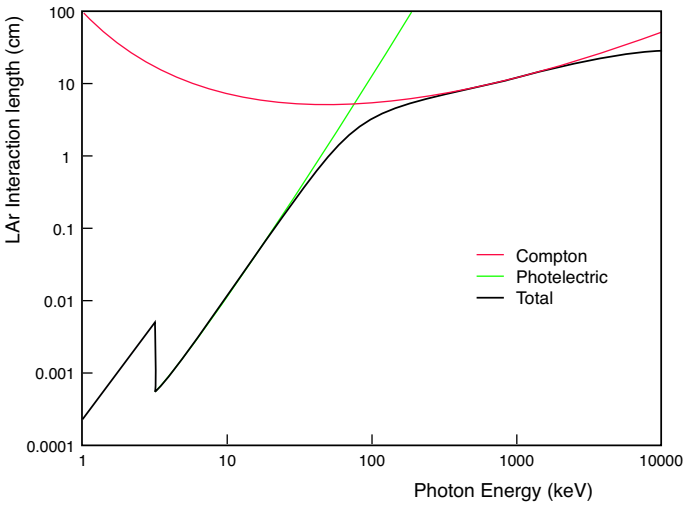


Figure 4.16: Average interaction length for photons interactions in liquid argon as function of photon energy. For higher energies (3-4 $MeV$) the pair-production starts to become important.

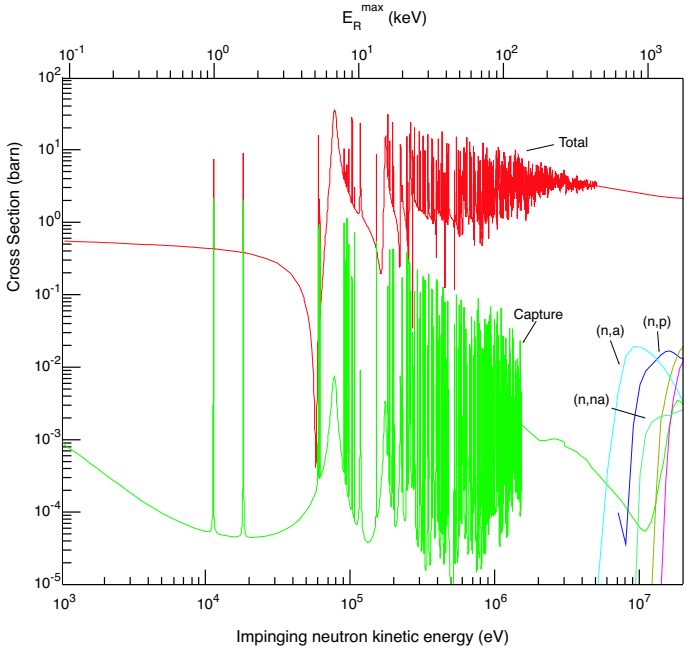


Figure 4.17: Cross sections for *n-Ar* interactions. The elastic contribution is given by the difference between the total cross section and the inelastic ones [99].

where $h\nu$ is the impinging photon energy and $m_0c^2$ is the electron rest mass energy. Above a $few\ MeV$, pair production (not shown in Fig. 4.16 ) becomes relevant. On the other hand in Fig. 4.17 the neutron cross sections in natural Argon is shown. The elastic cross section is dominant for neutrons energies up to 40 $keV$ and in the $MeV$ region.

#### 4.1.2.1 Evaluation of light collection efficiency

In order to measure the response to low energy electrons a $^{109}Cd$ source, mounted on a $PEEK^{TM}$ support (see Sec. 4.1.1), has been positioned approximately in the middle of the drift volume: it emits $X$- and $\gamma$-rays and conversion electrons (see Tab. 4.3). Due to the source thickness (0.07 $mm$), conversion electrons are emitted with a continuous spectrum up to the maximum energy displayed in the Tab. 4.3. $X$-rays are converted within $few\ mm$ (see Fig. 4.16) from the source by photoelectric absorption. The 88 $keV$ $\gamma$-rays have a mean free path in LAr of about 3.3 $cm$: at this energy about 70% of the photons undergoes Compton scattering, emitting electrons with maxi-

| *Particle* | *Energy* ($keV$) | *B.R.* | M.F.P. in LAr |
|---|---|---|---|
| Conversion El. | 63 | 0.41 | $range \approx 60\ \mu m$ |
| Conversion El. | 84 | 0.45 | $range \approx 100\ \mu m$ |
| Conversion El. | 87 | 0.09 | $range \approx 100\ \mu m$ |
| $X$-rays | $20 - 25$ | 1.0 | $< 1\ mm$ |
| $\gamma$-rays | 88 | 0.036 | $\approx 3.3\ cm$ |

Table 4.3: Characteristics of the $^{109}Cd$ source used for detector calibration of (total activity 2200 $Bq$). The last column represents the mean free path in liquid argon of the emitted particle. The $X$-rays spectrum shows prominent lines at 21.99 $keV$ $(28,9\%)$, 22.16 $keV$ (54.5%) and 24.93 $keV$ (13.7%) leading to the emission of electrons of energy 19-25 $keV$. The lower energy limit is provided by subtracting to the photon energy the maximum bound energy $E_b \approx 3\ keV$ (K-shell). The 88 $keV$ $\gamma$'s lead to the emission of 85-88 $keV$ electrons.

mum energy $E_e^{max} \approx 23\ keV$ (Eq. 4.12), while the remaining 30% induces the emission of electrons through photoelectric effects. The range of the emitted electrons, from $X$- and $\gamma$-rays, is of the order of $few\ tenth\ of\ mm$ [55]: both ionization events can be considered as point-like.

For these measurements the chamber has been used like a pure scintillation counter and the primary light spectrum has been acquired in the two conditions $\mathcal{E}_d = 0$ and $\mathcal{E}_d = 1\ kV/cm$. The data have been acquired by the means of a multichannel analyzer, following the DAQ chain illustrated in Sec. 4.1.1.4. The resulting scintillation light distribution associated with the $^{109}Cd$ source is plotted in Fig. 4.18. It is the superposition of

- a photoelectric peak from 20-25 $keV$ $X$-rays (electrons energy 19-25 $keV$);
- a continuum from conversion electrons up to 87 $keV$;
- a continuum distribution due to 88 $keV$ $\gamma$-rays Compton scattering with Compton edge at 23 $keV$, smeared by the limited resolution;
- a photoelectric peak at 88 $keV$ from $\gamma$-rays (electrons energy 85-88 $keV$).

Another important aspect should be consider to clearly understand the measured spectrum. The ionization induced by $X$-ray, exactly as the one from conversion electrons, occurs within $few\ mm$ from the source support, that obviously absorbs the fraction of light impinging over it. According to the

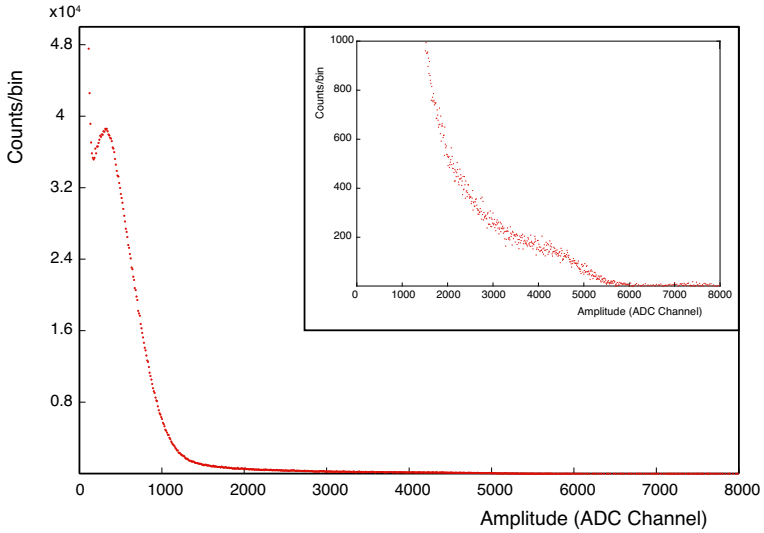


Figure 4.18: Primary scintillation spectrum in presence of $^{109}Cd$. From the calibration provided by SER measurements, 16.5 *ADC channels* correspond to 1 *phe*. The photoelectric peak from $X$-rays is centered around channel 320 of the ADC (0.88 $phe/keV$). This yield should be corrected for light collection problem associated with $X-rays$ interactions. The photoelectron peak from 88 $keV$ $\gamma$ (small box) is centered around channel 4100 (2.9 $phe/keV$).

performed simulation, for these interactions, in average, more than half of the produced light is absorbed by the support. On the other hand, due to a higher mean interaction length, $\gamma$-rays interact at a relatively large distance from the source and where this screening effect is negligible. Looking at the spectrum, a photoelectric peak associated with $X$-rays, superposed to the continuum spectrum from conversion electrons and from $\gamma$-ray Compton scattering, is clearly identified. The photoelectron peak from the 88 $keV$ $\gamma$-rays is clearly distinguishable too. The Compton edge and the conversion electrons spectrum are strongly superimposed and no characteristic points are recognizable. Since no corrections should be applied, the most meaningful feature is represented by the $\gamma$-rays photoelectron peak: its average value is position around channel 4100 of the multichannel corrisponding, after SER caibration, to 248.5 *phe* and leading to a photoelectrons yield of about $\Gamma(\mathcal{E}_d = 0) = 2.9$ $phe/keV$ for electrons recoils of energy about 86.5 $keV$ (85-88 $keV$). This value is obviously function of the experimental set-up (reflectivity of the diffusive layer and photo-cathodic coverage) and of the ionizing particle scintillation yield: the

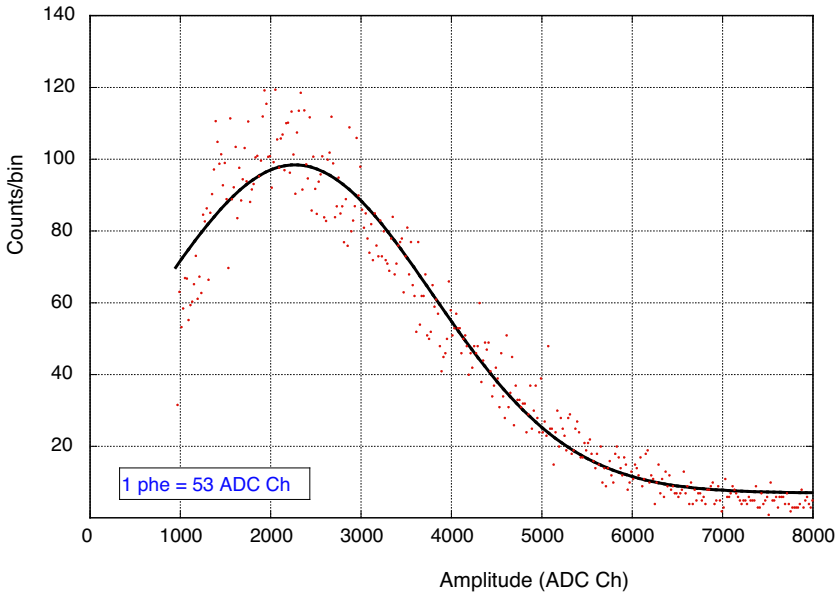


Figure 4.19: Primary scintillation spectrum for xenon-doped argon. It is zoomed on $X$-rays photoelectric peak.

latter, as explained in chapter 3, depends on the applied drift field and on the particle nature and kinematic conditions. A similar evaluation for $\Gamma(\mathcal{E}_d = 0)$ is obtained from the $X$-ray peak once correction due to light collection is applied.

The same measurement has been performed with xenon-doped LAr. The presence of xenon, in opportune concentrations, can be used to efficiently shift the proper wavelength in LAr (128 $nm$) to the characteristic emission line at 175 $nm$ of LXe. The used $\approx 500$ $ppm$ concentration is high enough to provide wavelength shifting but, at the same time, it is lower enough to leave untouched the scintillation light production. This means that, the 128 $nm$ light is firstly produced and then converted and no other radiative mechanism dominates: in other words, in pure and slightly doped liquid argon ($[Xe] < 1\%$) the average number of emitted photons is almost equal for equal interactions (for details see Sec. 3.2.4). This observation is meaningful since, a possibly measured variation of photoelectrons yield has hence to be attributed only to the different optical properties of the reflective layer for the two different wavelengths and not to a variation of the amount of produced light (see Sec. 4.1.1.2). The

experimental results, on Fig. 4.19, shows an almost doubled $X$-rays photoelectric peak with respect to pure liquid argon (the peak position was at 41 $phe$, while in pure LAr we obtained at 20 $phe$). The resulting photoelectrons yield is $\Gamma(\mathcal{E}_d = 0) = 5.9\ phe/keV$. This is most likely due to a higher conversion efficiency of the TPB wavelength shifter coated on the inner surfaces.

As soon as the drift field is activated the scintillation signal decreases as expected for electrons, as widely explained in the previous chapter (see Sec. 3.2.3). At an electric field of 1 $kV/cm$ the photoelectric peaks position reduces of a factor 0.82 providing the yield $\Gamma(1\ kV/cm) = 2.3\ phe/keV$. The ratio 0.82 is significantly different from the 0.5 measured for 1 $MeV$. This fact should be traced back to the very different kinematical conditions: passing from a relativistic electron (LET$\approx 1.69\ MeV/g/cm^2$) to a 22 $keV$ electron ($19-25\ keV$), the LET increases of about a factor 10 ($13.5\ MeV/g/cm^2$) [55]. The higher ionization density is hence less affected by the external electric field and less electrons escapes from recombination.

#### 4.1.2.2 Analysis of extraction and multiplication data

To verify the effect of extraction and multiplication fields, a first acquisition of the PMT signals in presence of the $^{109}Cd$ source has been exe-

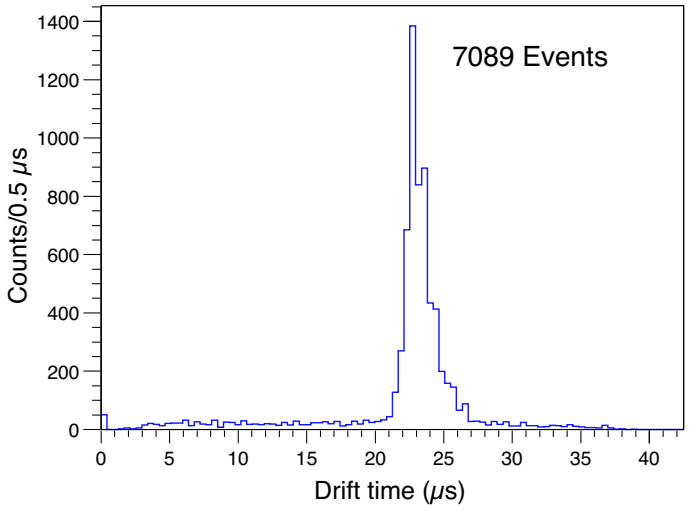


Figure 4.20: Drift time distribution for events recorded in presence of $^{109}Cd$ source. The distribution presents a clear peak in corrispondence to the source position inside the drift region around 22 $\mu < \tau_d < 25\ \mu s$.

cuted through the DAQ system shown in Fig. 4.15, with $\mathcal{E}_d = 1\ kV/cm$ and $\mathcal{E}_m = \mathcal{E}_{e,l} = \mathcal{E}_{e,g} = 0$ (in this condition neither extraction nor electroluminescence should occur). The offline analysis has shown that all the events present only the primary peak. Only a small percentage of the recorded events presents two peaks, but both characterized by the fast risetime ($few\ \mu s$ as shown in Sec. 4.1.1.4): this kind of events is compatible with a double interaction occurring in the same acquisition window and producing two uncorrelated primary scintillation signals. As soon as extraction and multiplication fields are turned on, a secondary peak appears together with the primary one, with risetimes longer than that measured for primary scintillation: obviously it is associated with electroluminescence in gaseous phase. To study in details the signal shape and the extraction and multiplication phenomena a set of data has been acquired with the internal $X$-ray source applying $\mathcal{E}_d = 1\ kV/cm$, $\mathcal{E}_{e,l} = 2.14\ kV/cm$, $\mathcal{E}_{e,g} = 3.2\ kV/cm$ and $\mathcal{E}_m = 2.5\ kV/cm$. This source has the important advantage of inducing the emission of energy peaked electrons ($22\ keV$) produced within $few\ mm$ from the source support, in the middle of the drift volume: in other words it generates point-like events, peaked in energy and easily selectable. This kind of events indeed, since occurring in a fixed position of the chamber, can be easily selected by looking at the events drift time distribution displayed in Fig. 4.20. As expected, it extends up to a maximum value representing the time spent by an electron produced near the cathode to reach the multiplication region[13]: above a relatively uniform flat background (mostly due to natural radioactivity and cosmic rays) it shows a prominent peak centered around $\tau_d = 23.5\ \mu s$ corresponding to the source location. The request $22\ \mu < \tau_d < 25\ \mu s$ is applied to obtain a high purity $^{109}Cd$ sample.

The first check has been performed on signals risetimes. The measured average primary and secondary signal risetimes, $\tau_{r1}$ and $\tau_{r2}$, for the selected point-like events are shown in histograms of Fig. 4.21. As expected the primary and electroluminescence signals are characterized by different values of risetime. Signal $S1$ is characterized by $\tau_{r1} \approx 1\ \mu s$: it is evidently dominated by the scintillation slow component (decay time of the order of $1.5\ \mu s$). For what concerns the secondary signal $\tau_{r2} \approx 11\ \mu s$ has been measured. This results confirms the hypothesis that, with the used fields values, the electroluminescence occurs all along the path of electrons in the multiplication region and

[13] For a fixed $1\ kV/cm$ drift field, $\tau_d^{max} \approx 38\ \mu s$.

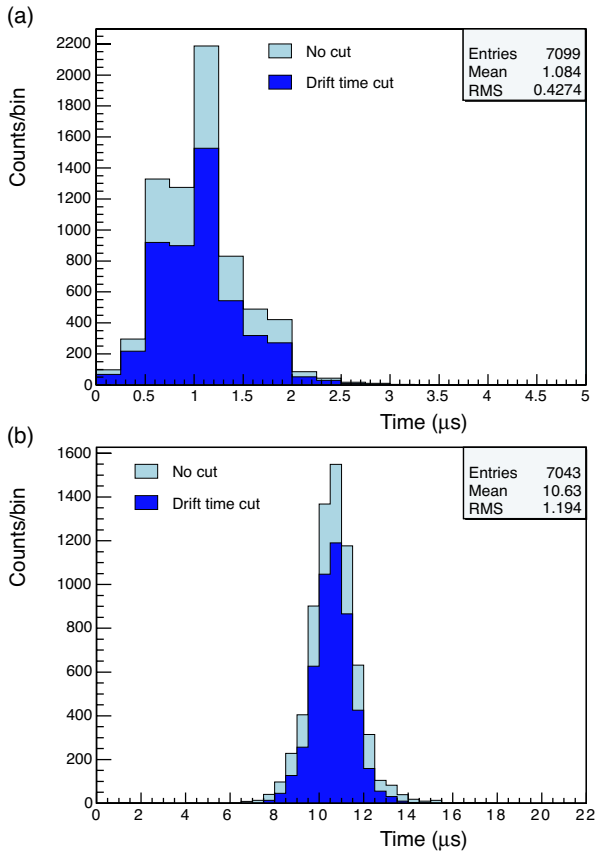


Figure 4.21: Primary (a) and secondary (b) risetime distribution for double signal events. The effect of a cut on drift time, aimed to select events produced near the source and hence most likely point-like, is also shown. The data have been acquired with $\mathcal{E}_d = 1\ kV/cm$, $\mathcal{E}_{e,l} = 2.14\ kV/cm$, $\mathcal{E}_{e,g} = 3.2\ kV/cm$ and $\mathcal{E}_m = 2.5\ kV/cm$.

not only near the wires. The observed time interval is indeed almost equal to the expected time needed by the electrons to cross the multiplication region (for this fields the electron drift velocity in GAr is around $1-2\ mm/\mu s$). With reference to the introduced parameter of Sec. 4.1.1.4, this consideration leads to a value $\tau_m = 0$.

Once verified the presence of proportional light and its main characteristics, a set of technical tests has been performed at fixed drift field $\mathcal{E}_d = 1\ kV/cm$. To decouple the extraction from multiplication mechanism several sets of data have been acquired for fixed $\mathcal{E}_m$ and variable extraction field. This is provided by changing the applied voltage $V_{g1\text{-}g2}$ and leaving untouched $V_{k\text{-}g1}$

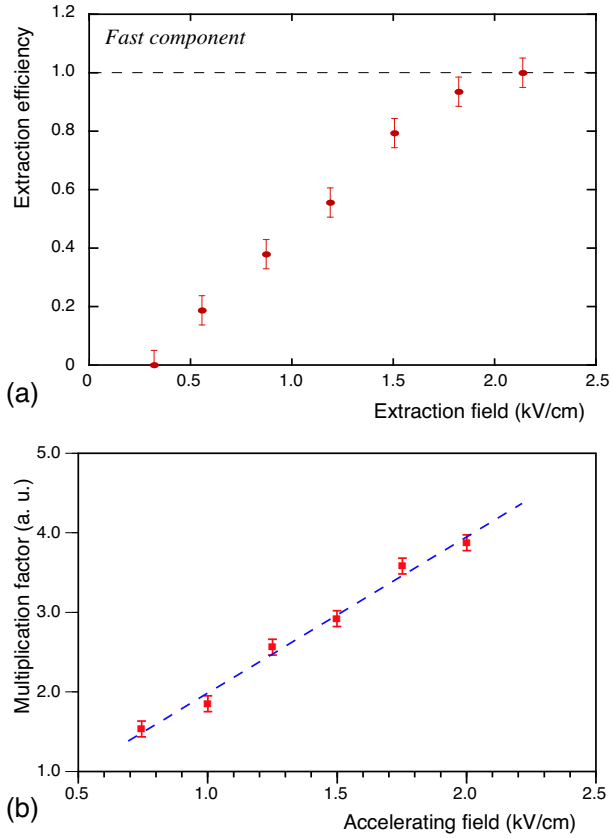


Figure 4.22: (a) Measured extraction efficiency as function of the electric field in liquid phase $\mathcal{E}_{e,l}$. (b) Multiplication factor as function of $\mathcal{E}_m$.

and $V_{g2\text{-}g3}$. Obviously, as shown in Sec. 4.1.1.4, different values of $V_{g1\text{-}g2}$ imply different values of $g1$ and $g2$ grids transparency, respectively determined by the ratios $\mathcal{E}_{e,l}/\mathcal{E}_d$ and $\mathcal{E}_m/\mathcal{E}_{e,g}$. For each data set the average value of $S2$, opportunely corrected for grid transparency, has been evaluated. Since $S2$ is function of the extraction and of the fixed multiplication and since the amount of ionization is almost constant (peaked energy distribution), the behaviour of secondary amplitude can be used to study the extraction efficiency as function of the extraction field in liquid argon. The results are plotted in Fig. 4.22. The slope of the extraction efficiency is equal to the one measured in Ref. [81] and presented in Sec. 3.3.1. A shift along the horizontal axis is observed. This effect could be traced back to a different definition of the electric field plotted in the graph: in one case the real field in the liquid (this work) and, in the

other, the nominal field between two grids, given by the $V/d$ ratio and corresponding to the field in presence of an homogeneous dielectric medium. This observation is suggested by the fact that in Ref. [81] no clear description of the computed field in liquid argon is provided. As shown in Fig. 4.22 total extraction occurs for $\mathcal{E}_{e,l} \approx 2.1\ kV/cm$ (corresponding to $V_{g1-g1} \approx 2.0\ kV$).

With a similar strategy the role of multiplication field has been investigated. Data have been acquired for fixed extraction field (equal to full extraction value) and varying $\mathcal{E}_m$. The results, corrected for $g2$ grid transparency, are plotted 4.22. They are strongly dependent on the grids geometrical properties (wire diameters and pitch) and hence the obtained behaviour cannot be extended to different grids layout. One should observe that even in the gaseous gap of the extraction region, near the wires, electroluminescence can occur: this effect has been counted both for extraction and multiplication measurements.

#### 4.1.2.3 Particle discrimination based on $S2/S1$

The proposed particle discrimination technique is based, as previously stated, on the simultaneous measurement of primary scintillation and proportional light associated with an interaction in the medium. The response of the chamber to $X$-rays, $\gamma$- and $\alpha$-particles and nuclear recoils has been investigated. In order to arrive to a suitable criterion able to efficiently separate the signatures of low energy electrons from the one of nuclear recoils, the correlation between $S2$ and $S1$ has been studied. In principle, both signals, namely the scintillation signal from the liquid and the secondary light produced by the electron emission (from the liquid to the gas and the subsequent scintillation) should be proportional to each other, but with a proportionality factor which depends on the effects of recombination.

| | *Voltage* $(kV)$ | *Field* $(kV/cm)$ |
|---|---|---|
| $V_{k\text{-}g1}$ | $-7.5$ | 1.0 |
| $V_{g1\text{-}g2}$ | 2.0 | 3.2 $(gas)$; 2.1 $(liq)$ |
| $V_{g2\text{-}g3}$ | 2.5 | 2.5 |
| $V_{PMT-g3}$ | $-2.8$ | $-0.7$ |

Table 4.4: Power supply scheme.

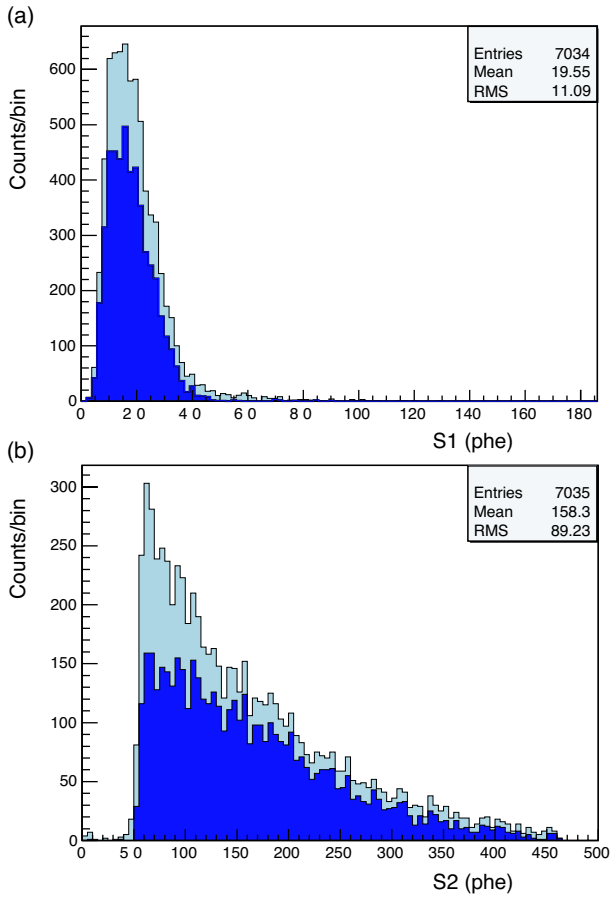


Figure 4.23: Primary (a) and secondary (b) signal amplitude distributions. The effect of the drift time cut is shown.

### Detector response to $X$-rays

Double signals acquisition has been performed in presence of the $^{109}Cd$ source placed inside the chamber. The field conditions are $\mathcal{E}_d = 1\ kV/cm$, $\mathcal{E}_{e,l} = 2.14\ kV/cm$, $\mathcal{E}_{e,g} = 3.2\ kV/cm$ and $\mathcal{E}_m = 2.5\ kV/cm$: this configuration is a compromise between discharge problems and the request of a high extraction and multiplication efficiency. The voltage set is summarized in Tab. 4.4. About 10000 of the digitalized PMT signals have been visually scanned. The signals characterized by multiple events, where more than one primary peak was recognized, have been rejected together with the ones where two separated peaks where not reconstructable: top-to-bottom crossing muons have been, for example, excluded since primary and secondary signals are not time

separated. After the selection, 7035 events with proper double peaks, compatible to $S1$ and $S2$ risetimes, survive. Primary and secondary signal amplitude distributions are plotted in Fig. 4.23 for a trigger threshold of the order of 50 *phe*, with and without drift time cuts aimed to select events associated to the source as explained in Sec. 4.1.2.2. The relative scatter plot is shown in Fig. 4.24 again before and after drift time cuts. The mentioned drift time cut cleans up considerably the correlation, removing the diffused background, which is not source associated. The very few events outside the correlation band are compatible with residual background flat in the drift time, indicating a diffuse origin. As for light efficiency measurements, the detected $S1$ for events occurring near the source has to be corrected in order to reproduce the right amount of initially produced light. The strong correlation between $S1$ and $S2$ is clearly evident and a ratio $S2/S1 \gg 1$ is observed. One should note, in order to compare these results to data obtained with different set-up, that at the working electric fields, summarized in Tab. 4.4, total electronic transparency is not provided for grid $g2$: the measured $S2$ signal is hence reduced by a factor 0.78 given by the electric fields ratio as shown in Fig. 4.8.

Having a look at the width of $S1$ and $S2$ distribution of Fig. 4.23, one should note that $S2$ is much more unresolved. According to author's opinion this systematic effect could be produced by the un-uniformity of the multiplication fields as it follows. Electroluminescence production occurs both along the multiplication region and near the collection wires of $g3$: due to this reason a two equal localized ionization cloud, produced for example by two equal point-like events, can induce the emission of a different amount of proportional light according to their positions in the plane normal to the drift direction. If, from one hand, they generate the same average amount of photons along the path in the uniform field region, as soon as the collection grid region is reached the two clouds, following different line of force, can cover different path length before being collected by the wires. In the specific, a cloud perfectly below the wire is immediately captured on the contrary of one occurring in between two wires. This great difference is essentially generated by the fact that the grid $g3$ is used in collection mode and lines of force could greatly differ one from the other. To reduce this effect a slightly modified grids set-up has been used in the successive sets of measurements.

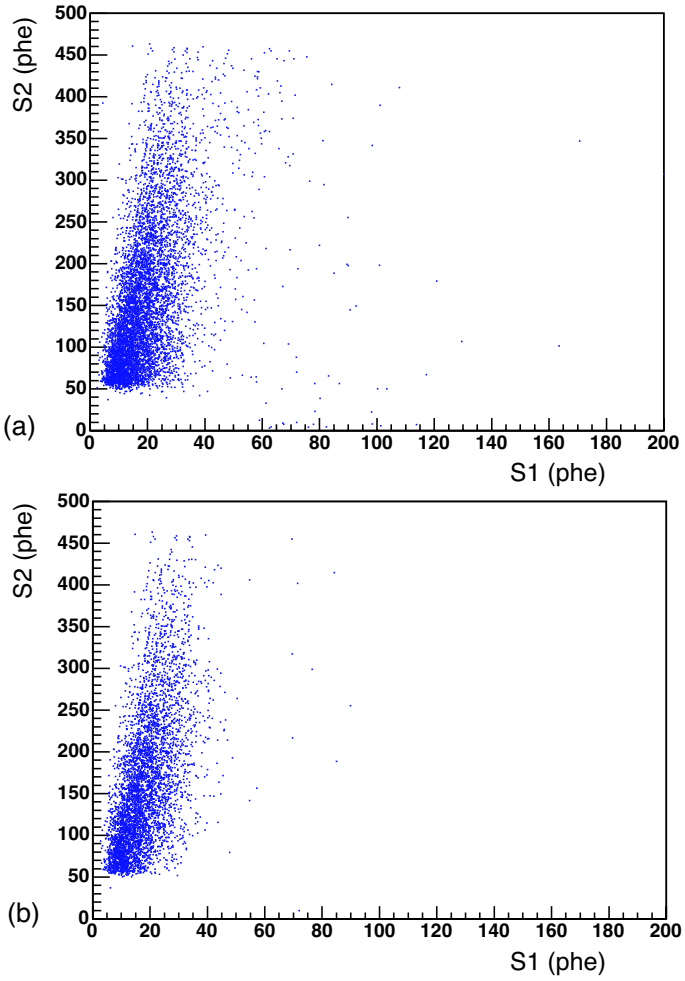


Figure 4.24: $S2$ *vs.* $S1$ scatter plots (where each point represents a double event) before (a) and after (b) drift time cut. The trigger occurs for events for which $max(S1, S2) > 50$ *phe*. As evident, for the majority of events the trigger occurs on $S2$.

### Detector response to nuclear recoils

As already pointed out, fast neutrons interacting elastically with the Argon of the detector can be used to generate recoils in the energy range close to the one foreseen for a *WIMP* signal. Therefore the chamber has been exposed both to the pulsed beam from a $D-T$ 14 $MeV$ neutrons generator and to an *Am-Be* neutrons source, with a continuum in the interval $2 \div 6$ $MeV$.

The measurement of the differential angular cross section of 14 $MeV$

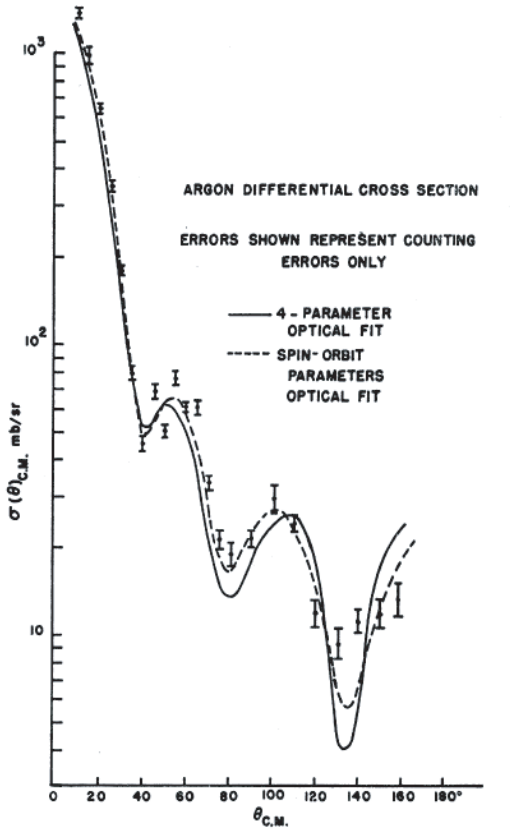


Figure 4.25: Experimental differential cross section, in the centre of mass frame, for $n$-$Ar$ elastic scattering. It is strongly peaked in the forward direction. The solid curve is the optical-model prediction [98].

neutrons elastically scattered from Argon is reported in the literature [98]. The angular distribution as a function of the centre of mass angle is strongly peaked in the forward direction and rapidly falling with marked diffraction dips, as shown in Fig. 4.25. It is well fitted with an Optical Model with empirical parameters. Such a differential angular cross can be converted to a recoil spectrum distribution as function of the recoil energy in laboratory frame, $d\sigma/dE_R$. Both measured values and Optical Model fit are shown in Fig. 4.26. Sharp forward peaking implies small recoil energies in the laboratory frame. Although the maximum recoil energy corresponding to backward scattering is $E_R = 1350\ keV$, the useful recoil spectrum is limited to about 200 $keV$. The finite nuclear radius and the corresponding nuclear form factors associ-

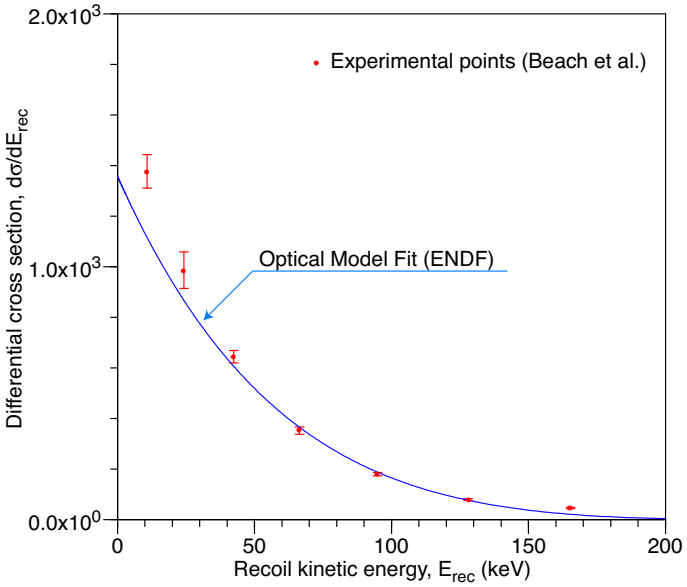


Figure 4.26: Expected nuclear recoils energy distribution for 14 $MeV$ neutrons elastically scattered on Argon. The data are obtained by re-elaborating the experimental differential cross section of Fig. 4.25. The solid line is the optical-model prediction [98].

ated with neutron scattering bring about suppression effects which are quite comparable to those already mentioned for the electroweak, WIMP related, form factors. Reactions other than elastic, such as $(n, n')$, $(n, \gamma)$, $(n, p)$ etc., which represent at 14 $MeV$ as much as one half of the total cross section (see Fig. 4.17), do not contribute appreciably in the energy deposition range of interest. In addition, a wide spectrum of $\gamma$-rays is expected, due to interaction of the neutrons with materials in the environment, primarily the steel walls of the chamber: they may contribute to a general, diffused background.

The Neutron Generator Genie 16 has been used to provide a triggered neutron source [101]. Neutrons are primarily produced through the reaction $D + T \rightarrow 4He + n$. The energy distribution is a peaked line with a mean energy of 14.076 $MeV$ and $\sigma = 0.238$ $MeV$. The gun generates a neutron bunch every 200 $\mu s$ in a narrow time window of 20 $\mu s$: each bunch contains, on average, 2000 neutrons mainly concentrated around the end of the time window. The chamber has been positioned at a distance of about 200 $cm$ from the gun corresponding to a flux of 20 $neutrons\ cm^{-1}\ s^{-1}$, namely 1 neutron impinging over the active volume every 2 $bunches$. This distance has been selected

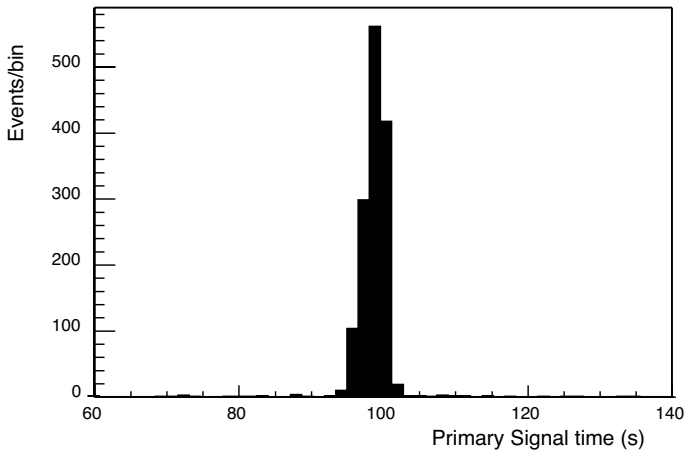


Figure 4.27: Time correlation of signal $S1$ with the time mark from the neutrons generator.

to reduce pile-up effects (multiple interaction in the same acquired window). The $D$-$T$ generator provides a signal output in coincidence with the neutron bunch and hence the time acquisition of the detector is externally triggered in synchronously with the neutron bunch.

The data have been acquired with the standard DAQ line, slightly modified to foreseen the external trigger (see Sec. 4.1.1.4). The fields conditions are equal to the ones of the previous run: $\mathcal{E}_d = 1\ kV/cm$, $\mathcal{E}_{e,l} = 2.14\ kV/cm$, $\mathcal{E}_{e,g} = 3.2\ kV/cm$ and $\mathcal{E}_m = 2.5\ kV/cm$. The time distribution of the prompt scintillation light $S1$ is tightly correlated with the pulse from the neutron generator (used as trigger), as shown in Fig. 4.27: once again, a cut based on this time distribution ensures of the correct origin of the events. The fraction of out of timing events is negligible, indicating a negligible background from events not directly associated with the neutron beam. In particular the background due to natural radioactivity and noise from the photomultiplier are completely eliminated by the coincidence requirement. The secondary pulse $S2$, whenever present, exhibits a rather flat drift time distribution, corresponding to a practically uniform illumination of the liquid argon drift volume. The resulting $S1$ *vs.* $S2$ scatter plot is shown in Fig. 4.28. Besides the emergence of an events population, which has the same characteristics of the $\gamma$-ray signature seen with $^{109}Cd$, a cluster of events (about 30%), absent in the $\gamma$-source case (see Fig. 4.24 and Fig. 4.31), populate a region characterised by a smaller

signal $S2$ when compared to $S1$: in the rest of the work we will refer to the region with $S2 < 20$ *phe* and $S1 < 150$ *phe* as the *neutrons* or the *nuclear recoils region*. A typical double signal belonging to this class in displayed, as example, in Fig. 4.29. A fraction of these events have a significant $S1$ signal, but no $S2$ signal, implying the absence of secondary electrons. Such kind of events has been detected also during acquisition with $^{109}Cd$ source but in a less percentage. This single peaked events could be associated both to interactions in the PMT or to neutron-like events with no ionization electrons surviving recombination. A diffused background in the $S1$-$S2$ plot, most likely related to residual inelastic events ($(n,\gamma)$, $(n,n')$ etc.), appears too.

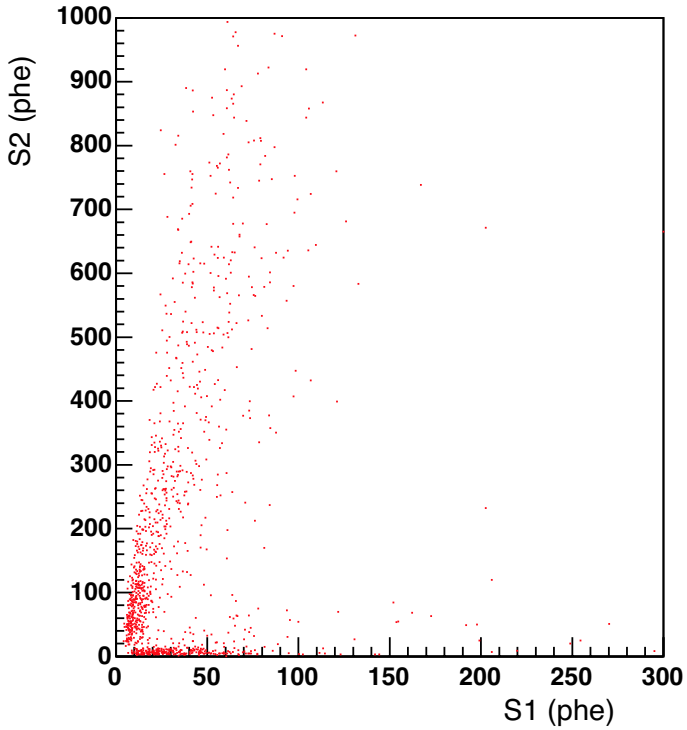


Figure 4.28: $S2$ *vs.* $S1$ scatter plot for events acquired in presence of the neutron generator. Two distinguishable bands are recognizable: one similar to that observed with the $^{109}Cd$ source and hence most likely due to electron conversions of $\gamma$-rays; the other emerging just in presence of the neutrons source and hence attributable to the nuclear recoils they should induce. This last population presents a behavior similar to that theoretically expected ($S2$ signal strongly suppressed if compared to that measured for $\gamma$-like events).

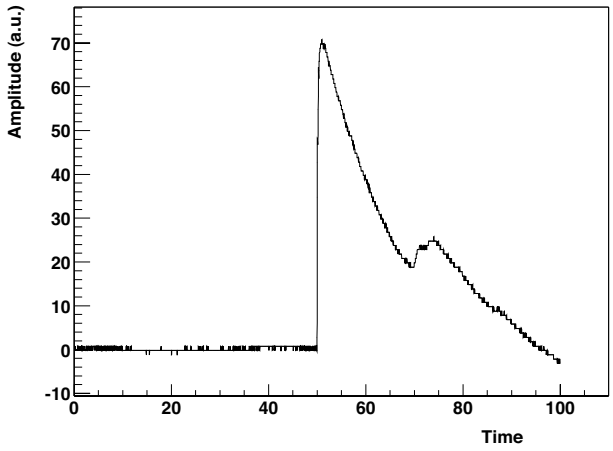


Figure 4.29: Typical signal associated with a recoil event. The S2 is strongly suppressed if compared to $\gamma$-like signal of Fig. fig:signal.int.

As evident from Fig. 4.24 and 4.28 the behaviour of nuclear recoils and gamma induced ionization events is quite different. This difference is much more evident if the scatter plot is evaluated in the $S2/S1$ *vs*. $S1$ space: as an example Fig. 4.30 displays this plot for neutron gun and $Am - Be$ data. As stated above these data are characterized by the coexistence of gamma-like and nuclear recoils events since the neutron source generates both particles. In both cases these two populations are clearly distinguishable: the upper band is associated with $\gamma$-induced events and characterized by a ratio $S2/S1 \approx 10$. On the other hand, $S2/S1 < 1$ region is populated by nuclear recoils events: the few diffused events are probably related to residual inelastic events from neutron-argon interaction. This result is ulteriorly confirmed by comparing the neutron data with the measurements conducted, in the same fields conditions, without neutron sources (neutron gun nor *Am-Be*): the scatter plot extracted by these last data is displayed in Fig. 4.31. As expected the nuclear recoils region empties while the $\gamma$-induced events, this time due to natural radioactivity, is still there. The few surviving events in the $S2/S1 < 1$ region are compatible with the expected rate due to neutrons from natural radioactivity[14]. One should note that, for $S1 \gtrsim 50$, the upper part of $\gamma$ band starts to be cut due to saturation effects associated with the reduced dynamical range of

[14]These data have been acquired in the same room where the neutron gun is usually in function: a highly contaminated environment.

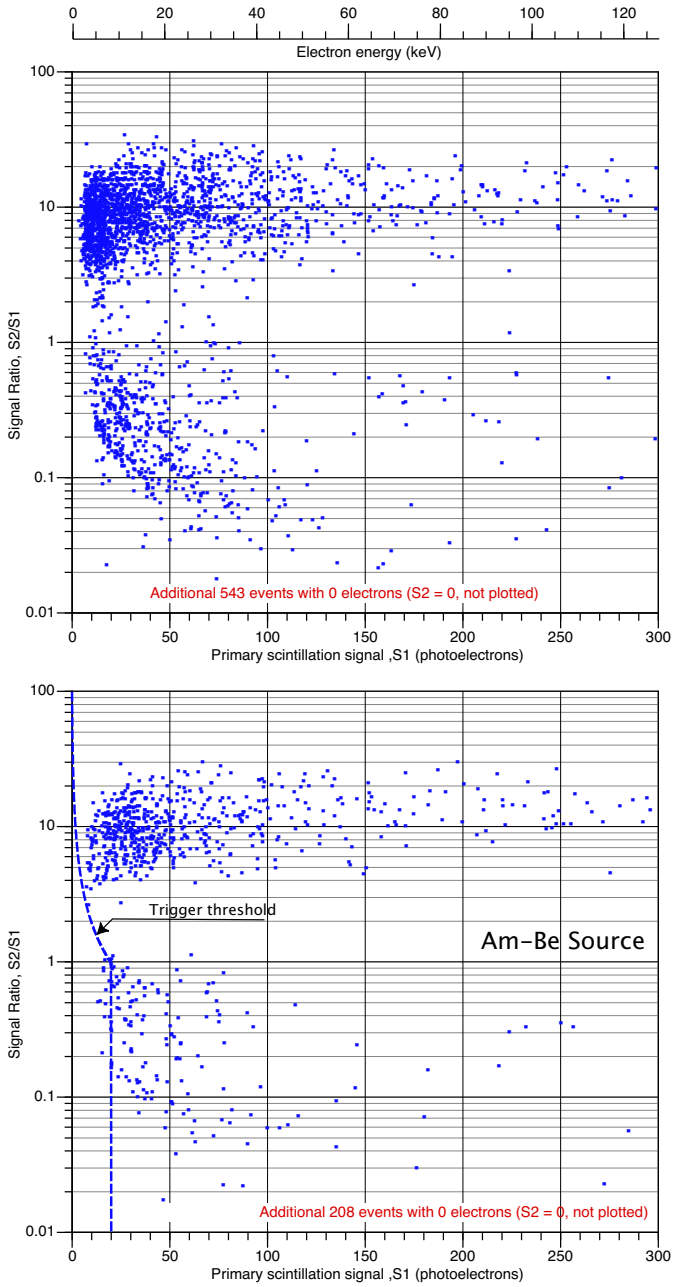


Figure 4.30: Ratio $S2/S1$ *vs.* $S1$ scatter plot for all valid events (double peak with appropriate rise-times) acquired with the neutron gun (up) and Am-Be neutron source (down). The separation between $\gamma$-rays and neutron induced events is clearly evident.

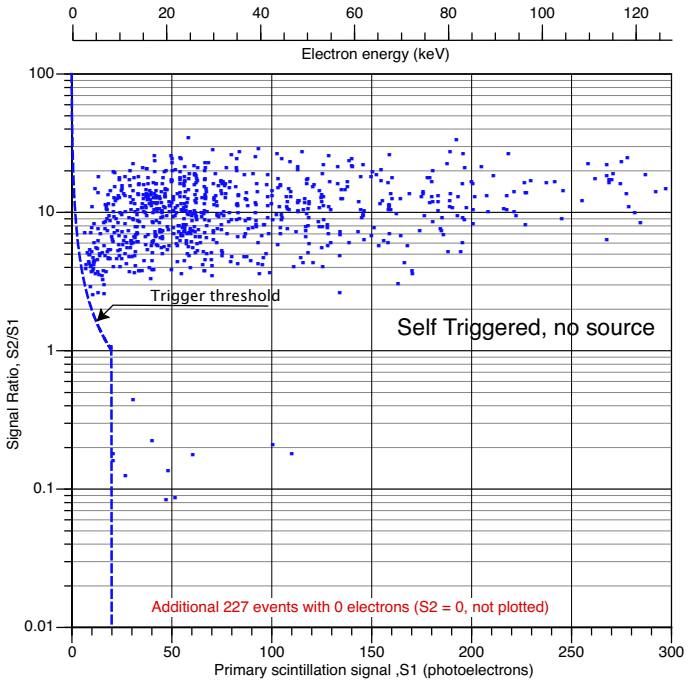


Figure 4.31: Ratio $S2/S1$ *vs.* $S1$ scatter plot for all valid events recorded without sources. A small number of neutrons are recorded, compatibly with expected room background.

the oscilloscope digitizer and already explained in Sec. 4.1.1.4. For low energy deposition, where the saturation is not occurring, the $S2/S1$ ratio for $\gamma$-like events tends to decrease: this effect is expected since, for low energies electrons the escaping-electrons effect becomes less efficient and the scintillation light is less quenched. At the same time, due to a an increase of ionization density, if compared to the one produced by a relativistic electron, a higher recombination is expected leading to a global decrease of $S2$ signal.

As in the $^{109}Cd$ source measurement the width of the secondary amplitude distribution seem dominated by systematic effect instead of statistical fluctuations, mainly due to collection on $g3$. The problem has been solved in the following sets of measurement changing the grid set-up.

Once determined the region associated with nuclear recoils, the primary light spectrum for the selected events has been investigated: this distribution is obtained projecting the neutron region scatter plot over the $S1$ axis. For this analysis the cut over the primary amplitude has been extended up to

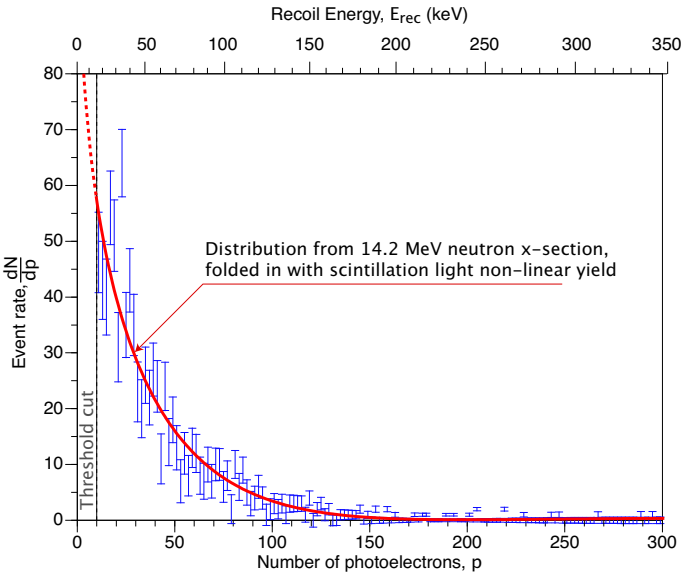


Figure 4.32: Experimental photoelectrons distribution of events, acquired in presence of the neutrons generator and belonging to the nuclear recoils region. The continuous line $dN/dp$ is derived from the recoils distribution of elastic scattering $dN/dE_R$ (Fig. 4.26) multiplied by the response of the scintillation process $dE_R/dp$ for recoils, with a multiplicative correction resulting from a best fit procedure of these data.

$S1 < 300$ *phe* while the cut on secondary signal is left unaltered. The results are shown in Fig. 4.32 where the event distribution, $dN/dp$ is plotted as a function of the $S1$ amplitude expressed in number of photoelectrons $p$. This quantity is strictly connected to the recoil energy distribution $dN/dE_R$, obtained from Fig. 4.26, through equation

$$\frac{dN}{dp} = \frac{dE_R}{dp}\frac{dN}{dE_R}. \tag{4.13}$$

At zero drift field, the number of collected photoelectrons for a given energy loss $E$ can be parameterised as

$$p(E) = (\Gamma' q_{tot}(E)) \cdot \chi \cdot E \tag{4.14}$$

where $\Gamma'$, expressed in $photons/keV$, is the scintillation yield at zero electric field for a relativistic ions, $q_{tot}(E_R)$ is the total quenching factor and $\chi$ is the conversion factor $phe/photons$ function of the geometry and reflectivity of the chamber and hence constant for a fixed set-up. As explained in detail in

Sec. 3.2.3.1, the scintillation yield assumes its maximum value in liquid argon for relativistic heavy ions with masses up to the $La$ one whose average energy loss for UV photon emission assumes the minimum value $W'_{l,ph} = 19.5\ eV$. For this reason the relativistic ion scintillation yield is conventionally used as reference and the yield obtained for a specific particle is expressed by defining a reduction factor called quenching factor, characteristic of the particle and of its specific LET whose value is contained in the $[0, 1]$ range. Although the parameter $\chi$ is not known the product $\Gamma = \Gamma' \cdot \chi$ can be directly obtained by the measurement conducted with $^{109}Cd$ source. At zero field, an electron of energy $E = 20\ keV$ (from the photoelectron peak), is characterized by a scintillation yield equal to $2.9\ phe/keV$: as evaluated at the end of Sec. 4.1.2.1, such a particle has a $LET \approx 13.5\ MeV/g/cm^2$ and a quenching factor due to escaping electron at zero field $q_{el} = 0.91$. Since for an electron of this energy the $q_{nc} = 1$[15], the global quenching factor is $q_{tot}(20\ keV) = q_{el}q_{nc} = 0.91$ (see Sec. 3.2.3.1). The above observations can be used to extrapolate the photelectron yield $\Gamma$ for heavy relativistic ions (in the used chamber): they lead to $\Gamma = 3.2\ phe/keV$. Equation 4.14 could hence be rewritten as

$$p(E) = (\Gamma' q_{tot}(E)) \cdot \chi \cdot E = (\Gamma q_{tot}(E)) \cdot E = \left(3.2 \frac{phe}{keV}\right) q_{tot}(E) \cdot E \quad (4.15)$$

The introduces formalism could be extended also in presence of an electric field using, as in the previous case, the scintillation yield of relativistic ions at zero field as reference value. Once again the decrease in scintillation light is incorporated in the quenching factor, now function of the field too. The number of photoelectrons produced by a nuclear recoil in presence of a field $\mathcal{E}_d$ is hence formally given by

$$p(E_R) = \Gamma q_{tot}(E_R, \mathcal{E}_d) \cdot E_R = \Gamma q_{el}(E_R, \mathcal{E}_d) \cdot q_{nc}(E_R) \cdot E_R \quad (4.16)$$

where $q_{nc}$ describes the fraction of energy loss given to atomic electrons, hence independent from the field while $q_{el}$ describes the scintillation quenching due to high ionization density effects (see Sec. 3.2.3.1). The value of nuclear quenching factor has been evaluated for argon recoils in Sec. 3.2.1 providing

$$q_{nc}(E_R) \approx A_I \cdot \left(\frac{E_R}{1\ keV}\right)^{\alpha_I} \quad (4.17)$$

with $\alpha_I = 0.224$ and $A_I = 0.145$. This behaviour has been obtained fitting the experimental data by Phipps *et al.* with a Lindhard-like function as shown in

[15] The energy is still dissipated by interaction with atomic electrons.

Sec. 3.2.1. Equation 4.17 leads for a 65 $keV$ nuclear recoil to $q_{nc} \approx 0.37$. This evaluation, as stressed in Sec. 3.2.1, is valid up to approximately 140 $keV$ after which the used approximation of Lindhard solution (displayed in Eq. 3.10) is no more proper.

For $\mathcal{E}_d = 1\ kV/cm$, as for the acquired data, Eq. 4.17 can be used to express the expected $dE_R/dp$ as

$$\frac{dE_R}{dp} = \frac{1}{\Gamma q_{nc}(E_R) q_{el}(E_R, 1\ kV/cm)} =$$

$$= \frac{1}{\Gamma q_{el}(E_R, 1\ kV/cm) \cdot A_I \left(\frac{E_R}{1\ keV}\right)^{\alpha_I}} = \frac{1}{A_S \left(\frac{E_R}{1\ keV}\right)^{\alpha_I}} \tag{4.18}$$

where the parameter $A_S(E_R, 1\ kV/cm) = \Gamma \cdot q_{el}(E_R, 1\ kV/cm) \cdot A_I$ has been introduced: as a first approximation an electronic quenching factor almost constant in the energetic range of interest is assumed leading to $A_S(E_R, 1\ kV/cm) \equiv A_S(1\ kV/cm)$. The above function could be used to fit, through Eq. 4.13, the scintillation spectrum of Fig. 4.32 starting from the expected recoil energy distribution $dN/dE_R$. This last quantity is obtained from the distribution $d\sigma/dE_R$ of Fig. 4.26 once evaluated the neutron flux and the time duration of data acquisition. The fit provides a value of $A_S = 0.25\ phe/keV$ corresponding, for a 65 $keV$ nuclear recoil, to a photoelectrons yield of about 0.63 $phe/keV$. The relationship between the recoil energy and the number of photoelectrons, expressed by Eq. 4.16, can hence be rewritten as

$$p(E_R) = A_S \left(\frac{E_R}{1\ keV}\right)^{\alpha_I} \cdot E_R = A_S \cdot 1\ keV \cdot \left(\frac{E_R}{1\ keV}\right)^{1+\alpha_I} =$$

$$= 0.25\ phe \left(\frac{E_R}{1\ keV}\right)^{1.224}. \tag{4.19}$$

The result is affected by an overall error of about 10%: it is mainly generated by the systematic error due to $dN/dE_R$ uncertainties. The data are still well fitted by the above function also for $E_R > 140\ keV$. The obtained argon recoil photoelectrons yield has to be compared to the measured yield for 20 $keV$ electrons with $\mathcal{E}_d = 1\ kV/cm$ equal to 2.3 $phe/keV$. The obtained spectrum, as stressed before, is obtained by selecting all those double peaked events belonging to the nuclear recoils region. Since the experimental spectrum is well reproduced by the theoretically expected function, it seems obvious to assume that the majority of the nuclear recoils events, within the range of

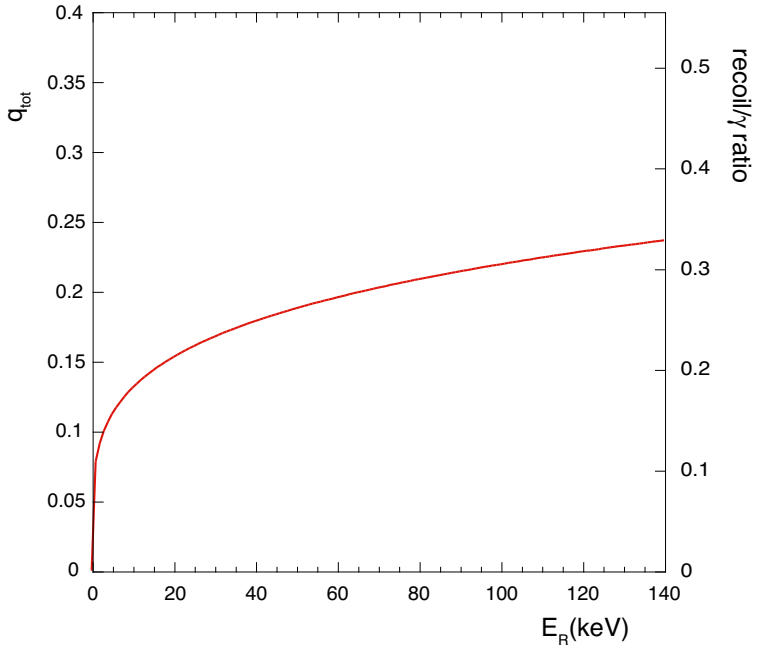


Figure 4.33: Measured light reduction for nuclear recoils, due to quenching, expressed as standard scintillation quenching factor, referred to deduced relativistic ions photoelectrons yield at zero field (3.2 $phe/keV$), or as $recoil/\gamma$ ratio, referred to the measured photoelectrons yield for 20 $keV$ $X$-rays (2.3 $phe/keV$) at 1 $keV/cm$.

interest, has associated a detectable, although tiny, ionization signal. If this is not the case a not observed (not uniform) deformation of the spectrum should occur.

From the executed fit it is possible to extract the behaviour of $q_{tot}$, shown in Fig. 4.33. The left vertical scale refers to the standard quenching factor $q_{tot}$, defined as the decrease of light with respect to relativistic ions: on the other hand, the right vertical scale refers to the so called $recoil/\gamma$ ratio (see Sec. 2.2), expressing in this case, the light reduction if the measured 20 $keV$ $\gamma$ at 1 $kV/cm$ is assumed as reference (2.3 $phe/keV$). While the first implies the estimate of the light yield of a relativistic ion (deduced, as previously shown, from $\gamma$-rays data), the second is just the ratio between the two measured photoelectrons yields. As shown in Fig. 4.33, the total quenching factor value for a 65 $keV$ recoil is about $q_{tot} \approx 0.20$ providing, since $q_{nc} \approx 0.37$, an argon recoils electronic quenching factor $q_{el}(1\ kV/cm) \approx 0.5$. This result is almost in agreement with some theoretical evaluation made by Hitachi [72] according

to which, the argon recoil $q_{el}(0)$ should be of the same order of the $q_c(0)$, the electronic quenching occurring in the core of an $\alpha$-particle track, and hence, at zero drift field, around 0.6 (for details see Sec. 3.2.3.1). The effect of 1 $kV/cm$ field on the quenching process is almost negligible for heavy ionizing particles, as shown in Sec. 3.2.3.1, and hence the last theoretical observation can be extended also in presence of field (if it is not too intense).

Data have also been collected with an *Am-Be* neutron source of lower neutron energy, which has provided a good confirmation of the results obtained with the neutron generator populating the same region attributed to nuclear recoils.

**Detector response to $\gamma$ and $\alpha$-particles**

After slightly modifying the chamber to reduce discharge problems in the gaseous phase and permitting the use of higher multiplication fields, a new set of measurements has been performed without sources, just triggering on cosmic rays events and natural radioactivity induced events. The distance between $g2$ and $g3$ has been increased to 2 $cm$: as stated before only linear multiplication (not the one occurring near wires) is considered. A different and, as shown by the measurements results, less performing reflective layer has been installed. Differently from the above measurements, where low energy deposition where analyzed, the PMT power supply, the Canberra 2005 gain and the oscilloscope scales have been set to acquire, without saturation, the high energy part of the scatter plot: the internal trigger of the scope is used to select events with $max(S1 : S2) > 50$ $phe$. The measurements have been conducted for different sets of electric fields. For $\mathcal{E}_d = 1$ $kV/cm$, $\mathcal{E}_{e,l} = 2.14$ $kV/cm$, $\mathcal{E}_{e,g} = 3.2$ $kV/cm$ and $\mathcal{E}_m = 3.5$ $kV/cm$, the obtained scatter plot is shown in Fig. 4.34. Looking at it, different populations are easily recognizable:

- a population associated with events with $S1 <\lesssim 800$ $phe$ and a broadly distributed $S2/S1 \approx 10.9$: these events are produced by $\gamma$-like interactions;

- a region characterized by few diffuse events most probably due to high energy photons and cosmic rays and hence not point-like;

- a bunch of saturated signals positioned along a curve approximately described by the condition $S1 + S2 = const$: they clearly represent the

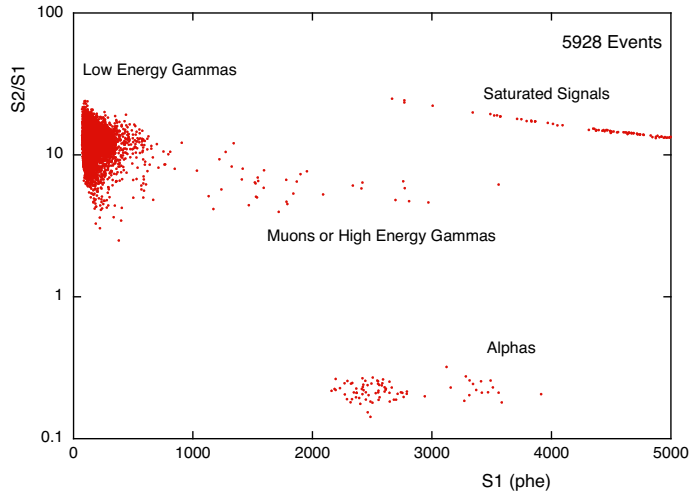


Figure 4.34: Ratio $S2/S1$ *vs.* $S1$ scatter plot for high energy events acquired without sources. See text for details.

high energy events, mostly due to cosmic rays, saturating the oscilloscope dynamical range (see Sec. 4.1.1.4);

- two clusters placed in the very high energy part of the plot characterized by ratio centered around $S2/S1 \approx 0.194$ most likely due to $\alpha$-decays in the sensitive volume (see further on for explanation).

A detailed analysis of the primary scintillation behaviour as function of the applied electric drift for events belonging to the last population has suggested that these events are mainly due to $\alpha$-decays in the sensitive volume. Experimentally it has been observed that an increase in the applied drift field (up to $\mathcal{E}_d = 1\ kV/cm$) does not significantly alter the measured average scintillation yield of this cluster, differently from what occurs for $\gamma$-like ionizations, significantly decreasing. This behaviour agrees with the $\alpha$-particles hypothesis since, as widely explained in the previous chapter, these events are characterized by a so high ionization density that fields of the order of the used one, are not enough to significantly alter the recombination process. As a consequence, while for relativistic electrons the ratio $S2/S1$ grows with the value of $\mathcal{E}_d$, since the field reduces recombination[16], in the case of $\alpha$-decays, $S2/S1$ is essentially constant, since fields of the order of 1 $kV/cm$ are not high enough to

[16]The presence of the field is used to collect ionization electrons and avoid their recombination with $Ar^+$ ions: the higher is the field the more recombination is reduced. The

affect recombination process and scintillation quenching (see Fig. 3.14). The experimental data are consistent with the characteristic decay chain resulting from a small $^{222}Rn$ contamination in the freshly produced Argon. The $^{222}_{86}Rn$ chain is

$$^{222}_{86}Rn \rightarrow {}^{218}_{84}Po + \alpha + 5.49\ MeV \quad (3.82\ d)$$

$$^{218}_{84}Po \rightarrow {}^{218}_{82}Pb + \alpha + 6.00\ MeV \quad (3.11\ m) \tag{4.20}$$

$$^{218}_{82}Pb \rightarrow {}^{214}_{83}Bi + \beta^- + < 250 > \ keV \quad (27\ m) \tag{4.21}$$

$$^{214}_{83}Bi \rightarrow {}^{214}_{84}Po + \beta^- + < 1508 > \ keV \quad (19.9\ m) \tag{4.22}$$

$$^{214}_{84}Po \rightarrow {}^{210}_{82}Pb + \alpha + 7.686\ MeV \quad (163\ \mu s) \tag{4.23}$$

$$^{210}_{82}Pb \rightarrow 22.3y. \tag{4.24}$$

The events in the cluster follow the expected time dependence of the decay chain (3.82 $d$): as experimentally measured this population almost disappears within few days. The lower $S1$ cluster is associated with 5.49 $MeV$ and 6.00 $MeV$ $\alpha$-particles while the higher to 7.686 $MeV$. The relative position is consistent with the emitted $\alpha$'s energies ratio. The above hypothesis of a $^{222}Rn$ contamination in liquid argon is ulteriorly confirmed by the drift time distribution of these events: they are distributed along the whole drift volume and hence associated with something diffused in the sensitive region.

Due to their spatial homogeneity and to their peaked energy spectrum, $\alpha$-events are ideal for calibration purposes and for studying the response of the experimental apparatus (5.49 $MeV$ and 6.00 $MeV$ $\alpha$-cluster is considered). As a first measurements primary and secondary light distributions have been investigated: they are displayed in Fig. 4.35. This results should be compared to the one previously obtained with the $^{109}Cd$ source (Fig. 4.23). In both cases the $S2$ distribution is dominated by systematic effects associated with the intrinsic resolution of the instrument and prevailing onto the expected statistical fluctuations: on the other hand, it is evident that the instrumental resolution observed during this second set of measurements is definitely higher than the one measured in the $^{109}Cd$ run. These results suggest, as supposed in Sec. 4.1.2.3, that the measured $S2$ distribution, in the $X$-ray measurements, was affected by electric field disuniformity near the collection wires. The performed modification of the chamber has evidently led to a global improvement

global effect is a reduction of $S1$, since less ionization electrons recombines leading to photon emission, and an increase of the number of collected ionization electron and hence of $S2$.

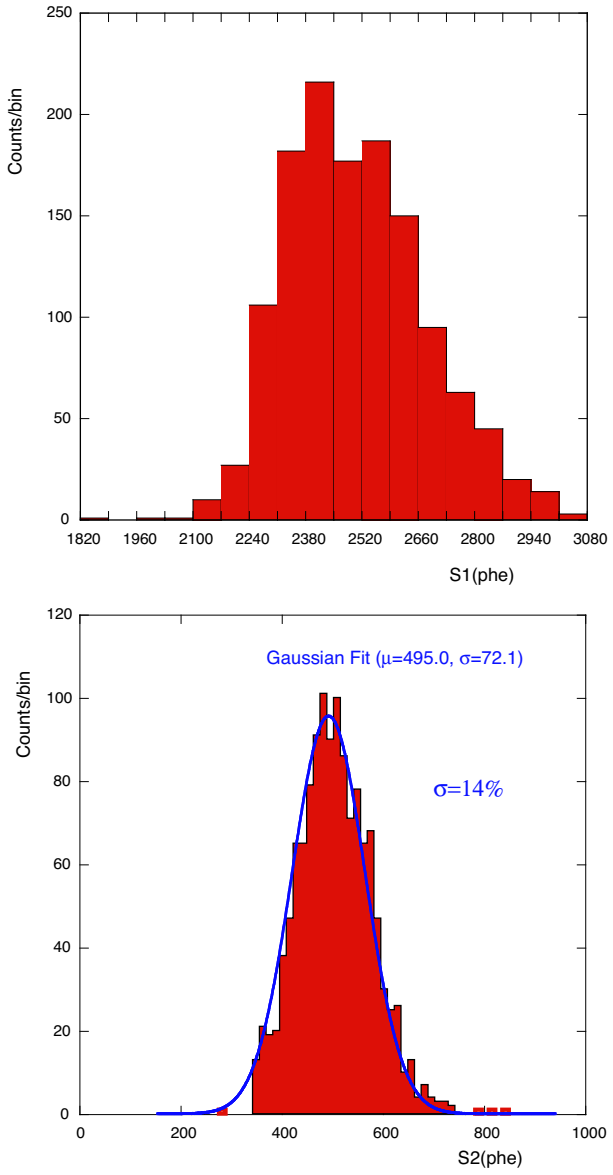


Figure 4.35: Primary and secondary signal amplitude distributions for $\alpha$-particles population.

in the detector response, become more uniform, and, assuming a gaussian behaviour, a relative width $\sigma_{r,S2} = 14\%$ has been measured (to be compared to the expected 4% due for statistical fluctuations). Supposing that the measured $\sigma_{r,S2}$ is independent from $S2$ amplitude (but just associated with the instruments performance), one should expect that with this new set-up the

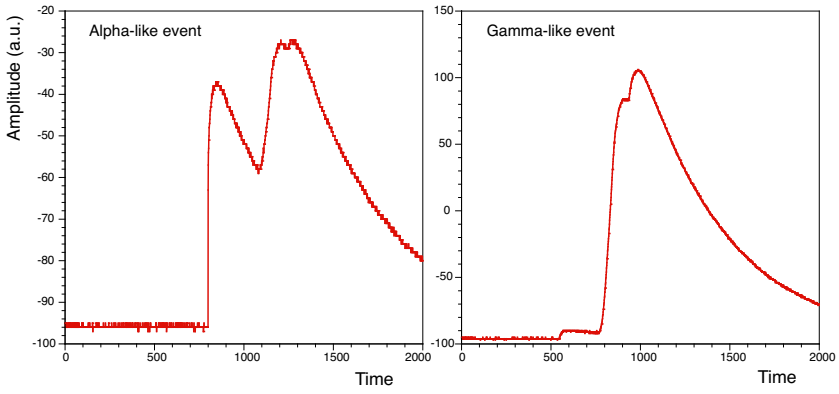


Figure 4.36: The two different events present three peaks. The first two are the known $S1$ and $S2$ while the third one is associated with electrons collection with the new grid set-up. On the left a pulse trace for an $\alpha$-event. The event is characterized by a large $S1$ followed by a tiny $S2$. On the right the pulse trace typical of $\gamma$-like events. A very tiny $S1$ pulse is followed by a huge $S2$ signal.

$S2$ distribution, in the few photoelectrons region, is dominated by the more prevailing statistical error.

The separation between low energy $\gamma$ and $\alpha$-particles according to the proposed $S2/S1$ criterion has been investigated too. Two typical signals, representative of the populations, are shown in Fig. 4.36. The two events are completely different: this difference is much more evident if the scatter plot of Fig. 4.31 is projected over the $S2/S1$-axis. The resulting distribution shows a net separation between the two families, as displayed in Fig. 4.37, and a suppression factor of the order of 60/1 is measured. As expected the secondary signal for $\alpha$'s is strongly suppressed due to the high ionization density enhancing recombination effects and, at the applied multiplication field, $S2/S1$ is less than unity. The observed suppression factor is in good agreement with the expected behaviour. According to the results presented in the previous chapter, an $\alpha$-particle with a kinetic energy of 5.75 $MeV$ should produce, in liquid argon, an average number of ionization electrons equal to 243644 *electrons* (assuming that all the energy is dissipated for atomic electron interactions and the measured average energy loss per pair production $W'_{l,\beta} = 23.6\ eV$). Due to recombination process only a fraction of these ionization electrons survives. This fraction, as function of the applied drift field, has

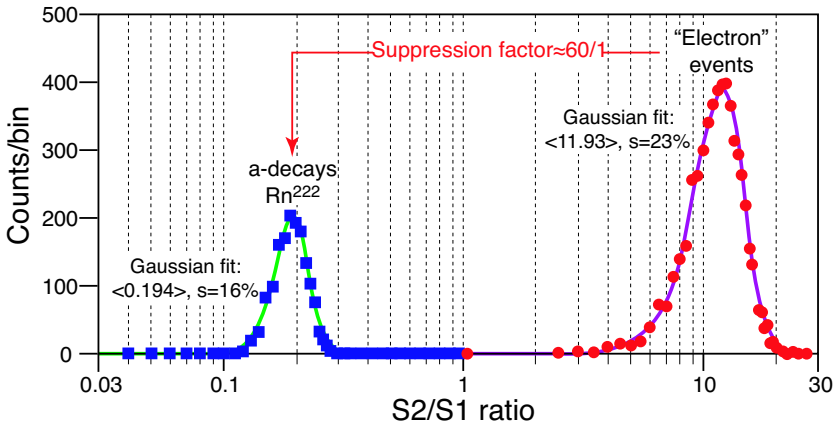


Figure 4.37: Histogram of the distribution of events, plotted as a function of the ratio between the secondary light produced by electrons extracted into the gas and the primary scintillation produced in the liquid, $S2/S1$. Events are produced by spontaneous decays in the detector. A clear separation in two peaks is observed. While the first peak (red) is due to general background produced by relativistic particles ($\gamma$-like), the second peak (blue) is due to $\alpha$-decays of a small, time dependent contamination of $^{222}Rn$. This last family of signals, which presents a sharp peak in $S1$ corresponding to an energy of 5.49 $MeV$, progressively disappears when the liquid is aging, with a characteristic half-life of 3.82 *days*. Because of the very strong recombination for these events, the secondary signal $S2$ is strongly depressed with respect to $S1$. Data are well represented by Gaussian fits of width in agreement with the expected resolutions. Note the remarkable separation between the two populations.

been measured in Ref. [56][17]. At the working drift field of 1 $kV/cm$ approximately 5284 *electrons* ($n_{e,\alpha}$) survive recombination. At the same time the number of UV emitted photons, at zero drift field, is about 209091 *photons*, assuming the average effective energy loss for photon emission $W_{l,ph} = 27.5$ computed in Sec. 3.2.3.1. The presence of the electric field leaves almost unaltered this number ($n_{ph,\alpha} = 209091$ *phtonos*). A similar computation can be executed, referring to Sec. 3.2.3.1, for relativistic electrons (as reference a 976 $keV$ electron is assumed). An electron of this energy provides, in average,

[17]The recombination for alpha has been directly obtained by the 1 kV/cm experimental point of Ref. [56]. The previously introduced fit, provided by the box model of Thomas and Imel (see Sec. 3.2.2) and described by formula 3.22 with $\xi\mathcal{E}_d = 470$ $kV/cm$, tends to underestimate the recombination parameter in this low field region. From the data only the 2.1% of the produced electrons survives recombination.

41355 ionization electrons and, at $\mathcal{E}_d = 1\ kV/cm$, about the 77% survives ($n_{e,\gamma} = 31843\ electrons$). The amount of photons is provided, at zero field, by the value of Tab. 3.4, leading to 38884 *photons*. At the working drift field this value decreases of about 50% as shown in Fig. 3.7. A total amount of $n_{ph,\gamma} = 19442\ photons$ is expected. Since $S1$ is proportional to the number of primary photons and $S2$ to the number of ionization electrons surviving recombination the suppression factor can be computed as

$$\frac{(S2/S1)_\gamma}{(S2/S1)_\alpha} \approx \frac{n_{e,\gamma}/n_{ph,\gamma}}{n_{e,\alpha}/n_{ph,\alpha}} = 64.5. \tag{4.25}$$

The obtained value refers to the expected ratio between $\alpha$-particles and 1 $MeV$ electrons and obviously this value tends to decrease if less energetic electrons are considered, due to the enhancement of the recombination process, depleting the $S2$ component. The average $S2/S1 \approx 10.9$ of the $\gamma$-like population shown in Fig. 4.37 is well represented by the 1 $MeV$ electrons (contained in the high energy tail) and hence the suppression factor (evaluated on the average $S2/S1$ of the two populations) should be well represented by the measured $(S2/S1)_\gamma/(S2/S1)_\alpha$. An excellent agreement is observed between the theoretical prediction of Eq. 4.25 and the measured suppression factor 60/1 shown in Fig. 4.37.

The previous measurements and computations have been performed for different values of the multiplication uniform field (high enough to provide a total electronic transparency of the grid), leaving unaltered the other electric fields. The results are plotted in the graph of Fig. 4.38, showing the behaviour of $S2/S1$ ratio as function of the applied multiplication field for both $\gamma$ and $\alpha$ families. The suppression factor, as expected, does not depend onto the applied multiplication field, affecting only the electroluminescence gain, a technical parameter equal for all events.

Due to the refurbishing of the chamber, multiplication fields higher than the ones obtained before have been reached. For this reason multiplication gain behaviour of Fig. 4.22 ($\mathcal{E}_m \approx 0 \div 2.0\ kV/cm$) should be updated with the new results displayed in Fig. 4.39 ($\mathcal{E}_m \approx 3.5 \div 5.0\ kV/cm$). These data are obtained looking at the behaviour of $\alpha$-family and considering that the $S2/S1$ can be expressed, assuming total grid transparency, as

$$\frac{S2(\mathcal{E}_m)}{S1} = \frac{n_{e,\alpha} \cdot \rho(\mathcal{E}_m) \cdot \kappa_g}{n_{ph,\alpha} \cdot \kappa_l} \tag{4.26}$$

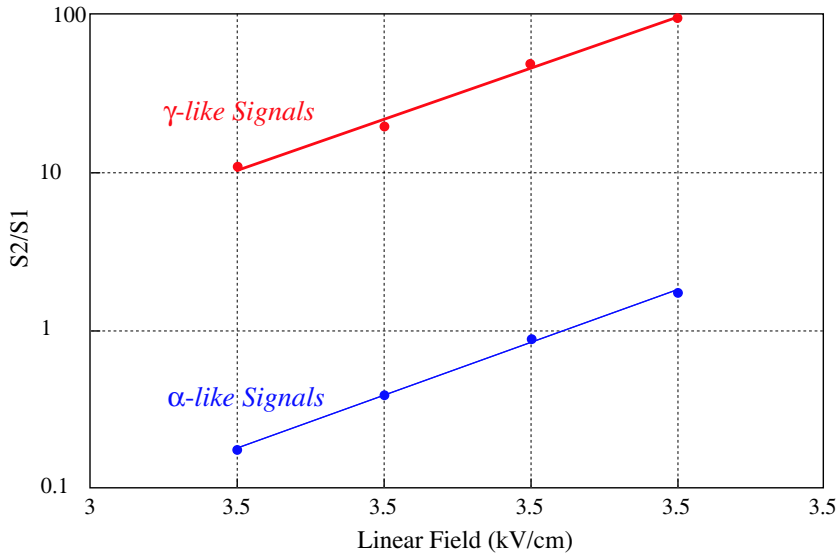


Figure 4.38: Values for $\gamma$-like and $\alpha$-like ratios $S2/S1$, as a function of the value of the linear multiplication field. Both signals evidence similar behaviours.

where $\rho$ is the multiplication gain expressed in *photons/electron*, function of the electric multiplication field, $\kappa_l$ and $\kappa_g$ are the average detection efficiencies for primary and secondary signals expressed in *photoelectrons/photon* and $n_{e,\alpha}$ and $n_{ph,\alpha}$ are the above introduced known quantities relative to $\alpha$-particles. The last two parameters have been obtained from a set of simulations on light collection[18] which provide $\kappa_l = (0.088 \pm 0.012)$ *phe/photons* and $\kappa_g = (0.118 \pm 0.014)$ *phe/photons*, almost independent from the position. On the basis of the measured $S2/S1$, to which the contribution from electroluminescence produced in the gaseous gap of the the extraction region has been subtracted, one obtains, through Eq. 4.26, the value of $\mathcal{M} = \rho(\mathcal{E}_m)/2$ *cm* associated with the multiplication process occurring in the 2 *cm* multiplication gap. The exponential behaviour of the results in Fig. 4.39 suggests that the ionization threshold introduced in Sec. 3.3.2 is overcome, in the vapor phase, for the applied fields intensities.

[18] In the simulations a reflectivity of 95% (see Sec. 4.1.1.2) and a PMT global efficiency of 20% on visible light have been assumed. The higher efficiency in the gas phase is essentially produced by the different refractive index between the two phases: since $n_g < n_l$, the light produced in gas and reaching the interface with an angle higher than the Brewster angle is reflected [102].

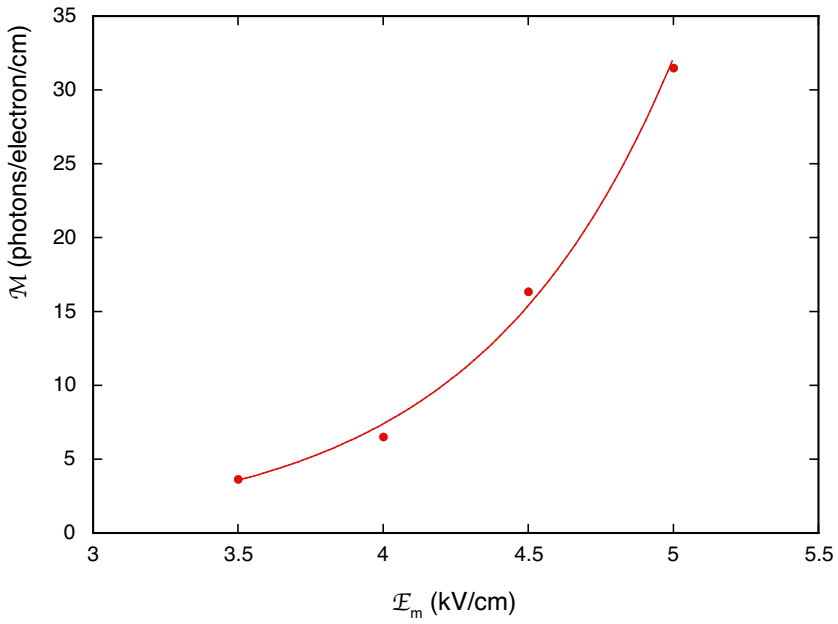


Figure 4.39: Multiplication gain $\mathcal{M}$ expressed in $phe/electron/cm$ as function of the applied $\mathcal{E}_m$. The result of an exponential fit is plotted too.

### Comparison between $\alpha$ and nuclear recoils

A direct comparison between nuclear recoils and $\alpha$-particles results cannot be executed due to the different experimental set-up since, in the first case, the population distributions were distorted by multiplication occurring near the wires, removed in the second set of measurements, and due to the different explored energy ranges. Nevertheless, from the data it follows that these two families behave roughly in a similar way. Particles range measurements for $\alpha$ and $Ar$ recoils provide very similar values of electronic stopping power and the measurement on primary scintillation light of Sec. 4.1.2.3 confirms the hypothesis of a recoil ionization density very similar to the one produced by $\alpha$-particles in the core of the track (see Sec. 3.2.3.1).

To roughly evaluate the expected behaviour of nuclear recoils in the new set-up one should consider in more details the number of photons and electrons produced by an $\alpha$ and by a nuclear recoil. These two quantities are in general

expressed by the equations

$$n_{ph} = \frac{E}{\left(\frac{W'_{l,ph}}{q_{nc}q_{el}}\right)} \tag{4.27}$$

and

$$n_e = \mathcal{R}\frac{E}{(W'_{l,\beta}/q_{nc})} \tag{4.28}$$

where $\mathcal{R}(\mathcal{E}_d)$ is the fraction of electrons surviving recombination and $q_{nc}$ $q_{el}(\mathcal{E}_d)$ are the previously introduced nuclear and electronic quenching. The explicit dependence from electric field of $n_e$ and $n_{ph}$ has been removed to lighten the formalism: the quantities have to be evaluated for $\mathcal{E}_d = 1\ kV/cm$. As a consequence the $n_e/n_{ph}$ ratio, strictly connected to the measured $S2/S1$ (see Sec. 4.1.2.3), can be expressed as

$$\frac{n_e}{n_{ph}} = \mathcal{R}\frac{W'_{l,ph}}{q_{el}(1\ kV/cm)\cdot W'_{l,\beta}} \tag{4.29}$$

leading to

$$\frac{(n_e/n_{ph})_R}{(n_e/n_{ph})_\alpha} = \frac{\mathcal{R}_R}{\mathcal{R}_\alpha}\cdot\frac{q_{el,\alpha}}{q_{el,R}} \approx 71\cdot\mathcal{R}_R \tag{4.30}$$

where the $q_{el,\alpha}(1\ kV/cm) \approx 0.71$ (see Sec. 3.2.3.1), $\mathcal{R}_\alpha(1\ kV/cm) \approx 0.02$ and $q_{el,R} \approx 0.5$ (see the previous section) have been replaced. According to the recombination parameter $\mathcal{R}_R$, the ratio of Eq. 4.30 can assume a wide range of values. As stated at the beginning of this section, the ionization density from recoils is similar to the one produced by $\alpha$ in the core of their track, as confirmed by scintillation measurements. On the other hand, referring to the concept introduced in Sec. 3.2.3.1, the recombination is affected also by the structure of the ionization track. For $\alpha$-particles, the penumbra (low density) and core (high density) region are well separated. For recoils they are expected to be continuous: the produced $\delta$-rays (secondary ionization electrons) should not be enough energetic to completely penetrate the core and hence, like in the fission fragments, a fairly undifferentiated core is produced. The global recombination effect for $\alpha$-particles is the superposition of the high recombination $\mathcal{R}_c$ occurring in high density region and of the reduced recombination $\mathcal{R}_p$ occurring in the penumbra ($\mathcal{R}_c < \mathcal{R}_p$). As obvious the global measured recombination parameter $\mathcal{R}$ is somehow increased by presence of the low density regions ($\mathcal{R}_\alpha > \mathcal{R}_c$). Since, for nuclear recoils track the low density region is not present, a parameter $\mathcal{R}_R$ slightly lower than $\mathcal{R}_\alpha$ ($\mathcal{R}_R \lesssim 0.02$) is expected,

suggesting a ratio $(n_e/n_{ph})_R/(n_e/n_{ph})_\alpha$ of the order of unity.

As a consequence, an $S2/S1$ almost equal or slightly lower than the one measured for $\alpha$-particles is expected for recoils, although in a completely different energy range ($S1$ is several order of magnitude lower for recoil events). For this reason, as soon as the experimental set-up is modified, a measurement of $S2/S1$ for $\alpha$ population can be used to roughly estimate the recoil region in the standard scatter plot.

## 4.2 WARP Prototype 2.3 *l*: phase II

Once verified the performance of the proposed technique and studied the extraction and multiplication mechanisms, the chamber has been refurbished and installed at the underground National Laboratory of Gran Sasso to study its behaviour in a low background environment. Particular attention has been given to internal detector gamma background measurements: the role of the $\beta$-emitter $^{39}Ar$ contamination has been investigated.

### 4.2.1 The modified experimental set-up

After the completion of the test program described in the previous sections, the 2.3 $l$ prototype has been refurbished by substituting the single 8 *inch* hemispherical photomultiplier with seven 2 *inch* phototubes (*mod. Electron Tubes EMI D743*, with sand blasted glass flat window). They are arranged on a hexagonal centered grid with nominal spacing of 65 $mm$, placed on top of the sensitive volume, in the argon gas phase, with the PMTs windows at about 40 $mm$ from the last grid. The $g2$ grid has been lifted up and placed at 27.5 $mm$ from $g1$: as in the previous case the interface is placed at about 4 $mm$ from $g1$. The applied voltage is used to provide both the extraction ($\mathcal{E}_{e,l}$) and multiplication fields ($\mathcal{E}_{e,g} \equiv \mathcal{E}_m$). To avoid ionization electrons loss, due to drift field un-uniformity in the proximity of racetracks, the sensitive volume has been reduced to a more inner region by the means of a PTFE ring, delimiting a truncated cone shaped drift volume (see Fig. 4.40): in this way, closed lines of forces between the racetracks are completely removed from the sensitive volume. The sensitive volume reduces from 2.3 $l$ to 1.87 $l$. It should be noted that the use of seven 2 *inch* PMTs reduces of about a factor 3 the overall photocathode coverage with respect to the single 8 *inch* hemispherical photomultiplier. This reduction is partially balanced by a higher quantum efficiency

Figure 4.40: Illustration of the modified 2.3 litres chamber inner layout, with the new array of 7 phototubes. The chamber has been tested in the LNGS laboratory for background measurements.

and a more uniform response of the smaller phototubes: differently from what observed for the hemispherical photomultiplier, the response of the 2 *inch* PMT is almost independent from the position of the impinging photons onto the photocathode. As in the previous set-up, all the internal surfaces of the prototype are covered with the wave-shifting/reflecting layer, while the photomultiplier glass windows are coated with *TetraPhenyl-Butadiene*. In some specific measurements the liquid argon has been doped with xenon behaving, as shown in Sec. 3.2.4, like a wavelength shifter from 128 $nm$ to 175 $nm$. In this case, instead of standard $VME + TPB$ system, a PTFE diffusive layer

has been adopted (estimated reflectivity 88% at 175 $nm$) [103].

The choice of inserting more than one PMT is essentially leaded by the request of working in a low energy region with few photoelectrons associated. In such a regime the stochastical noise of a single photomultiplier plays a crucial role. The only way, to decouple as much as possible the trigger rate from the PMTs noise and, at the same time, to obtain an enough low threshold, is provided by the use of a coincidence between several PMTs. Another meaningful and positive aspect, concerning the use of more than one phototube, is represented by the possibility of roughly locating the position of the interaction in the $x$-$y$ plane (normal to drift direction): the electroluminescence light, associated with a point-like event, occurs at the same $(x, y)$ as the ionizing interaction, since the electrons follow lines of force almost parallel to the chamber axis. Obviously the light distribution recorded by the seven PMTs is function of the direct solid angle and hence, since the $S2$ signal is produced in gas phase, the photomultiplier facing the multiplication specific location detects more light than the others. The granularity of the localization is obviously function of the phototubes dimensions and this information is more meaningful for large sized detectors for which $x$-$y$ localization can be used to cut a sensitive volume, far from the physical walls of the drift region, and hence to remove a large fraction of events associated with materials radioactivity.

The external set-up has been modified too. A 10 $cm$ lead shield has been installed to carry out the measurements concerning the internal radioactivity. This shield surrounds the whole experimental set-up and it is used to absorb the environmental $\gamma$'s. One should note that, although not airtight, the shield is enough shut to avoid a continuum circulation of air in the interspace between it and the argon bath: as soon as the LAr bath starts evaporating, the air that contains a high concentration of $\gamma$-emitters is largely substituted by argon gas, leading to a global decrease of radioactive contaminants in that region.

The last set-up modification concerns the use of a different filter for LAr electronegative purity. An $Hopkalit^{TM}$ cartridge has been used instead of standard $Oxisorb^{TM}$ since the latter is known to introduce radiochemical pollution in the purified liquid. This new filter offers performance similar to the previous one but it reduces the traces of heavy metals and other contaminants at its output (see Tab. 4.5). This precaution is crucial if internal $\gamma$- and $\beta$-backgrounds have to be measured.

| | | |
|---|---|---|
| Producer | Air Liquid | |
| Trade name | Hopkalit | |
| Purification capability | $< 0.1$ *ppb* $O_2$ *and* $CO$ | |
| Composition | 63% $MgO_2$ 37%$CuO$ | |
| Intrinsic radioactive contamination | $^{238}U$ | $(.12 \pm 0.01)$ *ppm* |
| | $^{228}Ra$ | $(.10 \pm 0.01)$ *ppm* |
| | $^{228}Th$ | $(.12 \pm 0.01)$ *ppm* |
| | $^{40}K$ | $(174 \pm 21)$ $Bq/kg$ |
| | $^{60}Co$ | 0.019 $Bq/kg$ |
| | $^{137}Cs$ | $.019 \pm .009$ $Bq/kg$ |
| Contamination at outlet (on $N_2$) | $^{23}Na$ | $(.031 \pm 0.013)$ *ppt* |
| | $^{24}Mg$ | $(.004 \pm 0.001)$ *ppt* |
| | $^{27}Al$ | $(.018 \pm 0.002)$ *ppt* |
| | $^{39}K$ | $(.021 \pm 0.007)$ *ppt* |
| | $^{52}Cr$ | $< 0.01$ *ppt* |
| | $^{63}Cu$ | $(.006 \pm 0.001)$ *ppt* |
| | $^{64}Zn$ | $(.017 \pm 0.003)$ *ppt* |
| | $^{75}As$ | $(.00050 \pm 0.00001)$ *ppt* |
| | $^{114}Cd$ | $(< .0003)$ *ppt* |
| | $^{202}Hg$ | $< .00006$ *ppt* |

Table 4.5: Main characteristics of the Hopkalit$^{TM}$ purifier.

One should note that due to the different altitude between the phase I measurements site and the LNGS site, the atmospheric pressure measured at LNGS is about 100 *mbar* lower than the other (920 *mbar abs* instead of 1020 *mbar abs*). As explained in Sec. 4.1.1.1, the internal pressure of the chamber tends to be equal to the external one and hence the gaseous argon presents a different density according to the measurement site. This, as shown later, will strongly influence the multiplication mechanism.

#### 4.2.1.1 New data acquisition and readout system

The readout and acquisition systems have been modified to count for the presence of the seven phototubes. The spectrum acquisition line is almost equivalent to the one shown in Fig. 4.13 apart from the possibility of summing up the pre-amplified analogue signals (see Sec. 4.1.1.4): this permits to acquire the primary scintillation spectrum detected by one up to seven phototubes. As before the calibration in photoelectrons is achieved by executing for each

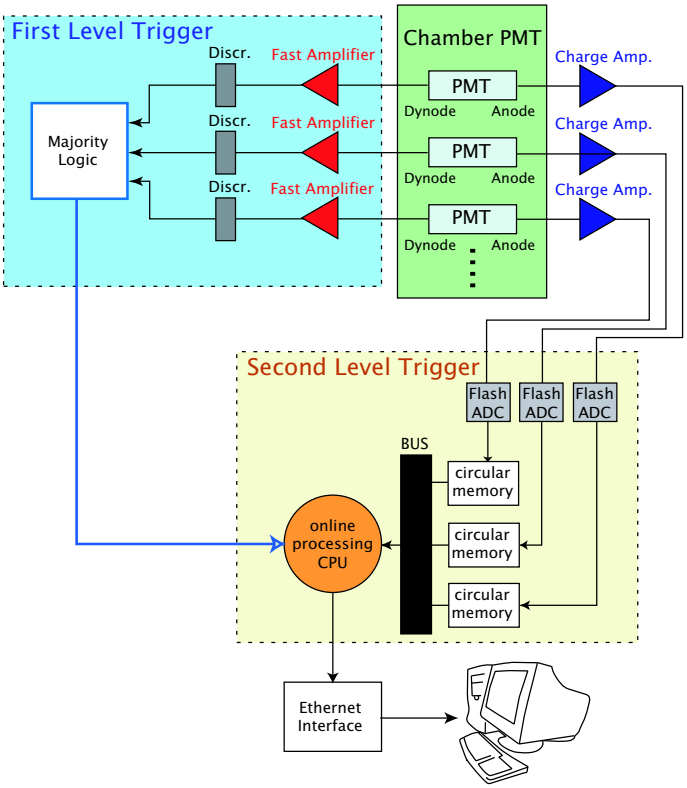


Figure 4.41: Data acquisition and readout system for the seven phototubes signals. See text for details.

PMT the relative SER measurement.

For what concerns the double signals acquisition a completely different scheme has been developed: as stated before, this new DAQ should foresee a trigger logic able to work on the coincidence of the several PMTs. At the same time, from the point of view of a long run acquisition, a second level trigger has been thought to reject those events clearly $\gamma$-like ($S2/S1 \gg 1$) and hence not belonging to the less abundant nuclear recoils class ($S2/S1 \approx 1$). For this reason a two level trigger has been implemented. The DAQ system is schematically described in Fig. 4.41. For each PMT, the $12^{th}$ dynode stage current output is extracted and sent to a *first level trigger unit*, controlling the acquisition of the anodic channels. On the other hand, the anodic pre-amplified signal of each PMT (with a Canberra 2005 charge preamplifier) is sent to a flash ADC and recorded to circular memory buffers. As digitizers, the CAEN $V789$ modified custom boards have been used with the pre-amplifier section

replaced by fast amplifiers. Inside the board the signal is splitted into two channels, one of those attenuated of a factor 10. The signal in each channel is then digitalized through a Flash ADC (10 $bits$ dynamical range and 20 $MHz$ sampling frequency) and recorded into a circular buffer. Pre-amplifiers and PMTs gain are almost equalized and adjusted in such a way that the single photoelectron amplitude corresponds to about 10 $ADC\ counts$ in the high gain channels (in the working conditions). The used width of the circular memory buffers is 4 $kBytes$ (about 204 $\mu s$ at 20 $MHz$) allowing the continuous recording of a full drift length ($\approx 50\ \mu s$). This board works together with a CAEN $V793$ trigger board and MVME 2100 CPU board. Each time the trigger board receives a signal from the first level trigger system, a command is sent to the CPU board, controlling the readout of the buffers, and the content of all the buffers is charged in the CPU memory. Once loaded in memory, a second level software trigger (that can be turned off) is performed by the $CPU$ onto the sum of the anodic signals (not attenuated channels). If also the second level trigger, based on an opportune algorithms, is passed, the content of the buffers is recorded onto a mass storage device. In these conditions the maximum sustained trigger rate, without dead time, is of the order of 15 $Hz$.

The *first level trigger* (*blue square* in Fig. 4.41) consists essentially of a PMT majority requesting that at least 4 PMTs detect a signal over threshold. For each photomultiplier the current signal of the last dynode is amplified through a standard inverting fast amplifier with gain $\approx 100$ and sent through a standard discriminator whose threshold is set, in the working conditions, to 1.5 photoelectrons (corresponding to different amplitude value according to PMTs gains). The logic output of each discriminator is then sent to a majority board requesting at least 4 signals over threshold. The $NIM$ output from the majority is sent to the trigger board (CAEN $V793$).

Since for some applications and calibration purposes only the sum of the PMTs signals is of interest, a data acquisition system similar to the one sketched in Fig. 4.15 has been implemented too, recording the sum of all photomultipliers and hence loosing a certain amount of informations. Differently from the previous condition the sampling is set to 200 $ns$.

| *Source* | *Activity* $kBq$ | $\gamma$*energy* $keV$ |
|---|---|---|
| $^{57}Co$ | 1.1 | 122 (90%)<br>137 (10%) |
| $^{137}Cs$ | 17 | 662 |
| $^{60}Co$ | 19 | 1173 (100%)<br>1332 (100%) |

Table 4.6: $\gamma$-ray sources used for the calibration of the detector.

### 4.2.2 Experimental results at LNGS

#### 4.2.2.1 $^{39}Ar$ activity measurement

Once installed at the National Laboratory of Gran Sasso, the chamber has been initially used as a pure scintillation counter to study in details the $\gamma$-background due to environmental and internal radioactivity. These measurements, performed in presence of the lead shield, have identified as major components of the internal radioactivity the $^{222}Rn$ and $^{39}Ar$ dissolved in LAr as shown further on. The following data have been obtained with xenon-doped LAr (see Sec. 4.2.1 for details).

The data have been obtained through the standard spectra acquisition system, recording the sum of the seven PMTs. A set of calibration measurements has been repeated both with the single photomultipliers and with their sum: the first were aimed to verify the uniform response (in terms of $phe/keV$) of all the phototubes, whose SERs were almost equalized. Once verified this uniformity, several primary scintillation spectra, sum of the seven PMTs, have been acquired in presence of $^{57}Co$, $^{137}Cs$ and $^{60}Co$ calibration sources, placed within the external LAr bath, facing the drift volume of the chamber. The characteristic of these sources are described in Tab. 4.6. The average photoelectrons yield has been used to calibrate in energy the primary scintillation axis for $\gamma$-like events.

The background spectrum measured with (red histogram) and without (blue histogram) the $\gamma$ shielding is shown in Fig. 4.42, 4.43, and 4.44 for different energy windows. The vertical scale for all spectra is expressed in $counts/keV/sec$; the horizontal scale corresponds to electron equivalent energy ($E_{ee}$). Since, as explained in Sec. 4.1.2.3, Radon and its daughters are dis-

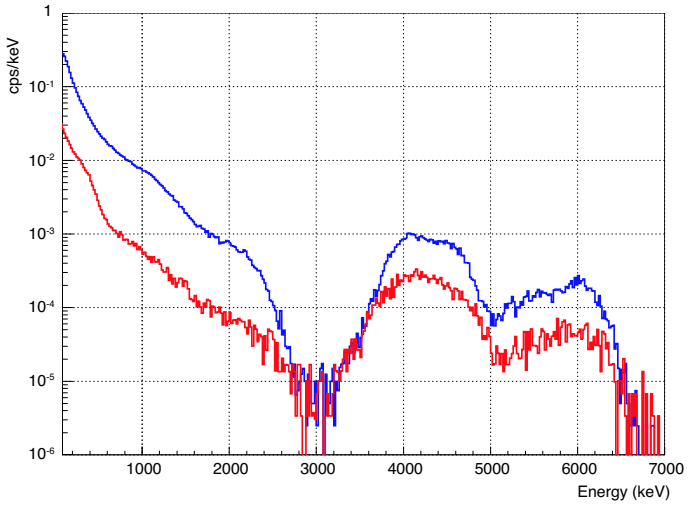


Figure 4.42: Background energy spectrum in the region 80-7000 $keV$ with (red) and without (blue) lead shielding at LNGS. The peak between 3.0 and 5.0 $MeV$ ($\alpha 1$ peak) are produced by $\alpha$-particles from $^{222}Rn$ and $^{218}Po$ decays. The peak between 5.0 and 6.5 $MeV$ ($\alpha 2$ peak) is produced by the $\beta - \alpha$ decay $^{214}Bi$ followed by $^{214}Po$.

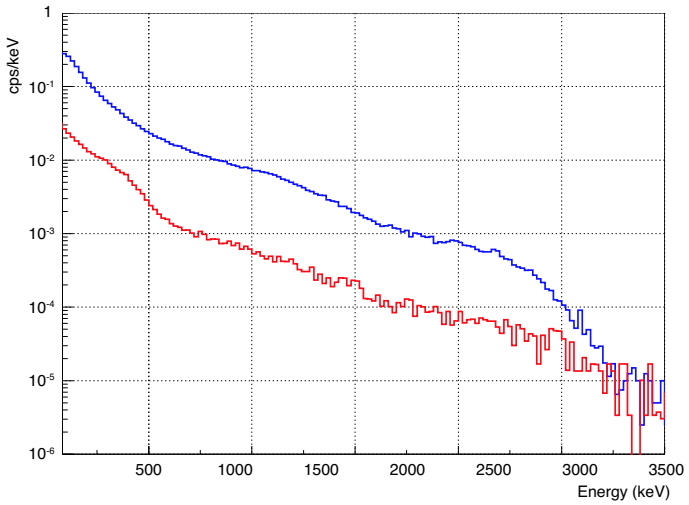


Figure 4.43: Background energy spectrum in the region 80-3000 $keV$ with (red) and without (blue) lead shielding at LNGS. The observed shoulder at about 2.4 $MeV$ is due to Compton edge of the 2615 $keV$ $\gamma$-line from $^{208}Tl$. The one at 1.2 $MeV$ to Compton edge of the 1460 $keV$ $\gamma$-line of $^{40}K$.

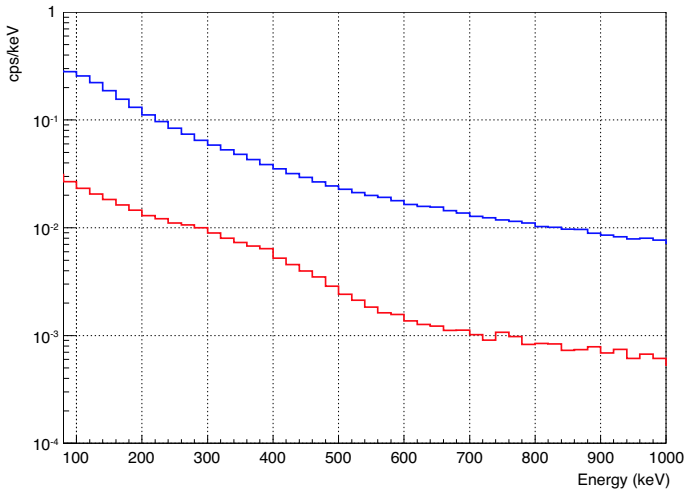


Figure 4.44: Background energy spectrum in the region 80-1000 $keV$ with (red) and without (blue) lead shielding at LNGS. The spectrum with shield installed presents a feature absent in the one acquired without shileding.

| *Energy range (keV)* | *No shield* | *Shield* | *Shield suppression* |
|---|---|---|---|
| 100-500 | 35.4 | 4.15 | 0.12 |
| 500-1000 | 6.5 | 0.56 | 0.09 |
| 1000-1500 | 2.22 | 0.17 | 0.08 |
| 1500-2500 | 0.78 | 0.081 | 0.10 |

Table 4.7: Total counting rates observed in different energy ranges of the spectra with and without shielding.

solved in the liquid argon inside the active volume, the observed peak between 3.0 and 5.0 $MeV$ ($\alpha 1$ peak) is traced back to $\alpha$-particles from $^{222}Rn$ and $^{218}Po$ decays while that between 5.0 and 6.5 $MeV$ ($\alpha 2$ peak) is connected to $\beta - \alpha$ decays from $^{214}Bi$ followed by $^{214}Po$. The values of the two peaks maxima can be used to evaluate the quenching of $\alpha$-particles with respect to the electron equivalent energy. The obtained value is about 0.75 in presence of xenon, to be compared to the one expected for pure liquid argon given by the ratio of the average quenching factor for electrons, with energy from 1 $MeV$ down to $few\ tens\ of\ keV$ ($q_{el}^{e} = 0.84$) and $\alpha$-particles characterized by $q_{el}^{\alpha} = 0.71$ (see Sec. 3.2.3.1), leading to a relative quenching of about 0.84 ($\alpha/\gamma$ ratio).

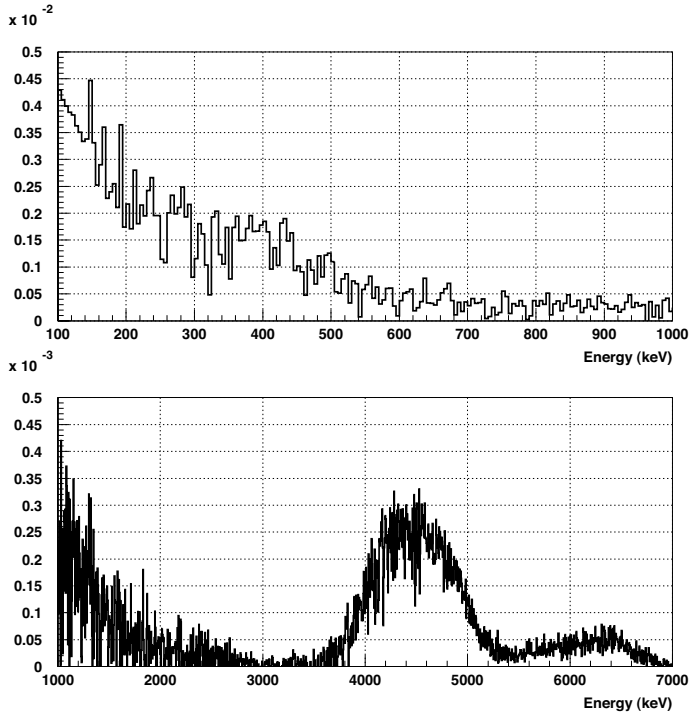


Figure 4.45: Energy spectrum shape of the events generated by internal $^{222}Rn$ and its daughters in the energy windows 100-1000 $keV$ (up) and 1000-7000 $keV$ (down). The spectrum is obtained by the difference of two spectra (few hours each), acquired at 8 days of distance.

The intensities of the $\alpha$'s peaks depend on the liquid argon $Rn$ content at the filling time and, as in the previous measurements, they are observed to follow the typical $^{222}Rn$ half-life. Below 2.5 $MeV$ most background is produced by environmental $\gamma$-rays interacting inside the chamber. Given the dimensions of the chamber and the relatively low $Z$ of $Ar$ atom, the spectrum is dominated by Compton interactions: two features easily recognizable are the Compton edges of the $^{208}$Tl line (2382 $keV$, from the 2615 $keV$ line) and of the $^{40}K$ line (1242 $keV$, from the 1460 $keV$ line). The background in this region is also due to $\gamma$-emission from $^{222}Rn$ and its daughters. The counting rates in different energy ranges are summarized in Tab. 4.7. As evident from the Fig. 4.43 (80-3000 $keV$), the lead shielding reduces the counting rate below 2.5 $MeV$ of one order of magnitude and the reduction factor is almost uniform in the range 600-2200 $keV$. Below 600 $keV$, as displayed in Fig. 4.44, a diffuse peak

starts to be evident in the measurement with the shielding installed. This feature is consistent with the signal from $^{39}Ar$ $\beta$-decays as discussed further on.

The internal $\gamma$-background from $^{222}Rn$ and its daughters can be estimated taking into account that its activity reduces according to an half-life of 3.82 $d$. Therefore the spectrum from $^{222}Rn$ can be extracted simply by subtracting two energy spectra acquired at different times during the same run. The difference of two spectra (few hours each), acquired at 8 days of distance, is plotted in Fig. 4.45: it represents the shape of the $^{222}Rn$ spectrum to be normalized in order to reproduce the counting rate of $\alpha$-peaks. This normalization for the spectrum with lead shielding, displayed in Fig. 4.46, evidently shows that the contribution from $\gamma$'s of $^{222}Rn$ is not negligible: obviously this contribution becomes less important if the spectrum is acquired several days after the chamber filling.

As stressed in Tab. 4.7, the shape of background spectra with and with-

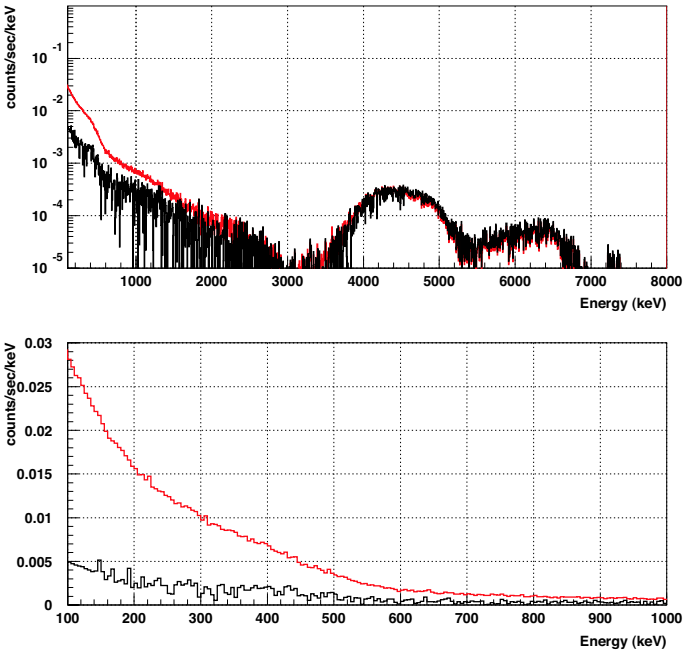


Figure 4.46: Comparison between the background spectrum observed with the lead shielding (red histogram) and that $Rn$ induced (black histogram), normalized with the $\alpha$-peaks rate. The two plots refers to 100-7000 $keV$ (up) and 100-1000 $keV$ (down) energy windows.

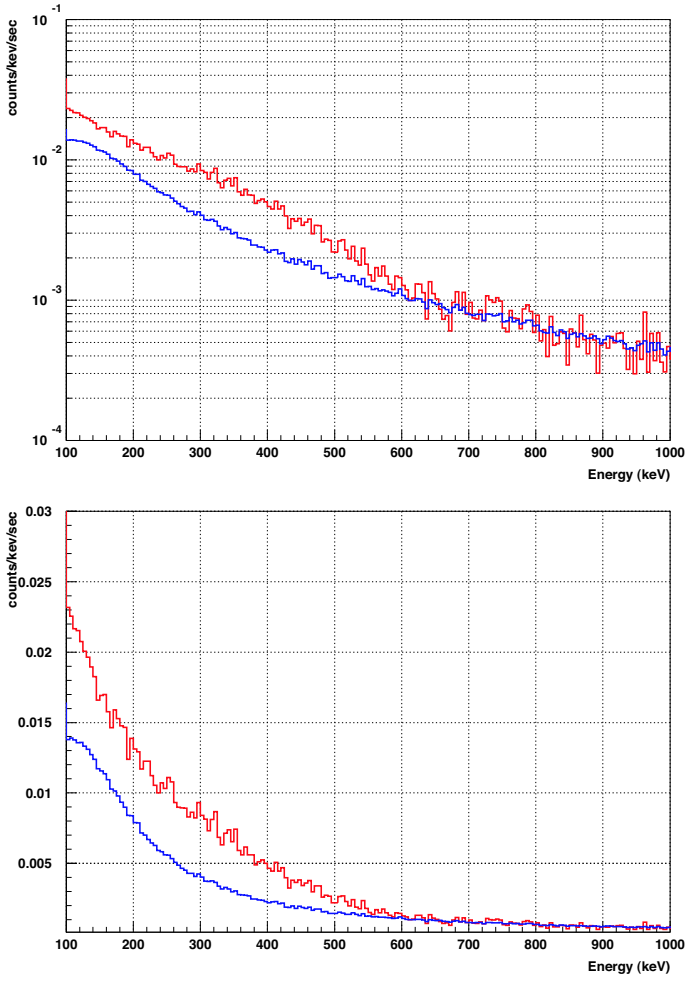


Figure 4.47: Comparison, in the range energy 100-1000 $keV$, between the background spectrum obtained with the lead shielding (red) and the one without shielding (blue) renormalized by a factor $\epsilon$ as discussed in the text. The two spectra are almost perfeclty superimposable for energy higher than 700 $keV$. The difference of the two spectra contains the major additional internal background component of LAr, mostly due to $^{39}Ar$ $\beta$-decays.

out lead shielding is remarkably similar in the energy range 600-2200 $keV$. This is understandeable if one assume that the spectrum in this energy region is dominated by environmental $\gamma$'s from Uranium, Thorium chain and Potassium, mainly coming from materials surrounding the sensitive volume of the detector. Without the shield the expected dominant contribution is from air, rock and concrete of the laboratory. On the other hand, with the shield

installed the expected dominant contribution is from residual air between the shielding and the dewar, the dewar and shielding themselves, and the walls of the chamber. In any case $\gamma$-rays are reaching sensitive volume from the surrounding, and a similar shape of the spectrum is expected. Under this assumption it is possible to empirically estimate the internal component of the background below 600 $keV$ by comparing the spectra acquired with and without shielding. Once subtracted the internal Radon contributions, these last two scintillation spectra, namely $S1_s(E_{ee})$ and $S1_{ns}(E_{ee})$, can be expressed as

$$S1_s(E_{ee}) = E_s(E_{ee}) + I(E_{ee}) \tag{4.31}$$

$$S1_{ns}(E_{ee}) = E_{ns}(E_{ee}) + I(E_{ee}) \tag{4.32}$$

where $E_n(E_{ee})$ and $E_{ns}(E_{ee})$ are the scintillation spectra from external sources respectively with and without lead shielding, and $I(x)$ is the spectrum from internal radioactivity. As stated before the two spectra are very similar in the energy range 600-2200 $keV$, apart from an overall scale factor $\epsilon$ evaluated by requesting $E_s(E_{ee}) = \epsilon E_{ns}(E_{ee})$: they results perfectly superimposed for $\epsilon = 0.09$. The internal background is hence obtained by

$$I(E_{ee}) = \frac{S1_s(E_{ee}) - \epsilon S1_{ns}(E_{ee})}{1-\epsilon}. \tag{4.33}$$

The results are plotted in Fig. 4.47, showing the excess spectrum $I(E_{ee})$ associated with internal radioactivity in the energy range up to approximately 600 $keV$.

The measured excess is compatible with $^{39}Ar$ $\beta$ spectrum (half-life of 269 $y$, end-point at 565 $keV$ and average energy at 220 $keV$). Figure 4.48 shows the internal radioactivity spectrum fitted, in the range 200-800 $keV$ by theoretical $\beta$ spectrum $B(E_{ee})$ convoluted with the resolution function

$$F(E_{ee}) = \int dE'_{ee} B(E'_{ee}) \cdot e^{-\frac{(E_{ee}-E'_{ee})^2}{2\sigma^2(E'_{ee})}}. \tag{4.34}$$

The resolution function, derived from calibration spectra, is expressed as

$$\sigma(E_{ee}) = \sqrt{a' E_{ee}^2 + b' E_{ee} + c'} \tag{4.35}$$

with

$$a' = 0.013 \quad b' = 3.6\ keV \quad c' = 529\ keV^2 \tag{4.36}$$

and where the first term takes into account non-uniformities in the light collection inside the chamber volume, the second term the statistical fluctuations

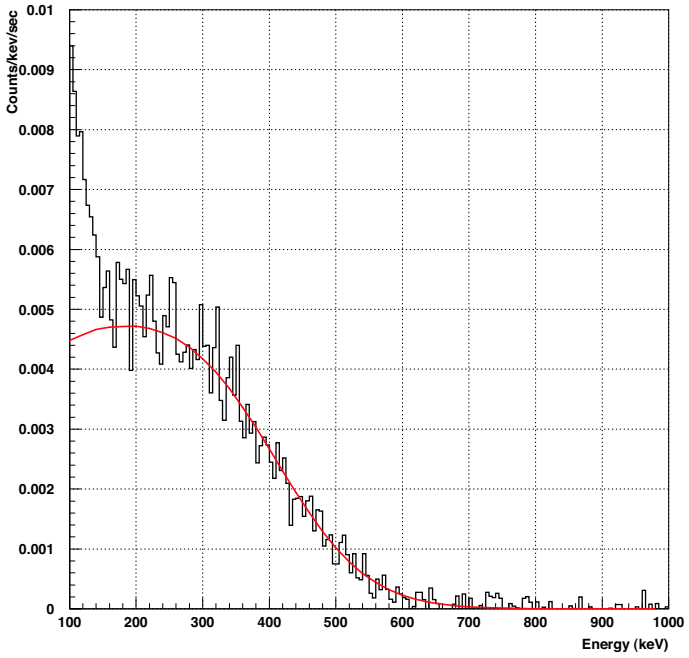


Figure 4.48: Fit of the residual spectrum $I(x)$ observed after subtraction of the internal $^{222}Rn$ signal and external $\gamma$-ray spectrum (the excess spectrum of Fig. 4.47). The fit function is the normalized $^{39}Ar$ $\beta$-spectrum.

in the number of photoelectrons and the third term is a constant contribution independent from energy. The results of the fit provide a rate of 1.1 $Hz$ in the fitted area 200-800 $keV$ (corresponding to 2.05 $Hz$ on all the spectrum) leading to an estimated activity of

$$A(^{39}Ar) = \frac{2.05\ Bq}{1.87\ l\ of\ LAr} = 1.1\frac{Bq}{l\ of\ LAr} = 0.76\frac{Bq}{kg\ of\ Ar} \qquad (4.37)$$

The estimated errors to the evaluated activity has to be searched in the systematics associated with $\gamma$-rays subtraction (0.3 $Bq$), energy calibration (0.2 $Bq$), internal radon subtraction (0.1 $Bq$)[19]. Together with the systematics, the statistical fluctuations in the counts in the 200-600 $keV$ fit region (0.02 $Bq$)

[19]For the evaluation of the systematic components produced by internal Rn and external gamma ray subtractions the absolute normalization parameters of the subtracted spectra has been changed within one standard deviation, and fitted the residual spectrum with the function $F(E)$. For the evaluation of the systematics connected with the energy calibration the calibration coefficients ($phe/keV$) of the spectra has been chaghed within one standard deviation and evaluated the difference in the fitted 39Ar spectra.

should be considered. By summing the above components in quadrature, the total uncertainty can be evaluated as 0.37 $Bq$. Including the evaluated uncertainties, Eq. 4.37 can be rewritten as

$$A(^{39}Ar) = (1.1 \pm 0.4)\frac{Bq}{l\ of\ LAr} = (0.76 \pm 0.28)\frac{Bq}{kg\ of\ Ar} \tag{4.38}$$

This value is in very good agreement with the determination by H.H. Loosli [104] according to which the $^{39}Ar$ content in natural argon is equal to $(8.1 \pm 0.3) \cdot 10^{-16}$, corresponding to a specific activity in LAr of $(1.4 \pm 0.05) Bq/l$.

One should note that a $\beta$-decay spectrum similar to the measured one can, in principle, be attributed to $^{85}Kr$ with end-point at 687 $keV$. However the typical $^{85}Kr$ activity in air is of the order of 1 $Bq/m^3$ leading, for any reasonable distillation process in the production of LAr, to a negligible activity if compared to the measured 1 $Bq/l$.

The obtained $^{39}Ar$ activity plays a crucial role in the realization of a bigger detector since it represents the unremovable $\gamma$-like background, intrinsically associated with the use of natural argon, and since its activity is not negligible. Although $\gamma$'s and nuclear recoils families are well separated, a high $\gamma$-like events rate could be problematic. Since, as shown later on, even the most performing discrimination technique at some level starts to fail, a too high $\gamma$-like events rate produces, in the detection window, a certain amount of $\gamma$-like events wrongly labeled as nuclear recoils. This represents the background surviving shielding and rejection methods and its rate roughly represents the maximum obtainable sensitivity (See Sec. 5.3). The only way to reduce this background is the depletion of natural argon from the 39 isotope through isotopic separation.

#### 4.2.2.2 Measurements on $\alpha$- and $\gamma$-family: $S2/S1$ and pulse shape discriminations

As stated before the argon internal pressure could deeply influence the mechanism of production of proportional light and, as a consequence, the ratio $S2/S1$. For this reason a $S2/S1$ ratios different from the one illustrated in Sec. 4.1.2.3 for $\gamma$-like and $\alpha$-particles families are expected to be measured at LNGS, even in the same fields configurations, due to the different atmospheric pressure (0.920 $bar\ abs$ and $T_b = 86.4\ K$). To evaluate this modification a double signals measurement has been conducted, in pure argon, with the DAQ system foreseeing the digital scope and the electric fields $\mathcal{E}_d = 1\ kV/cm$,

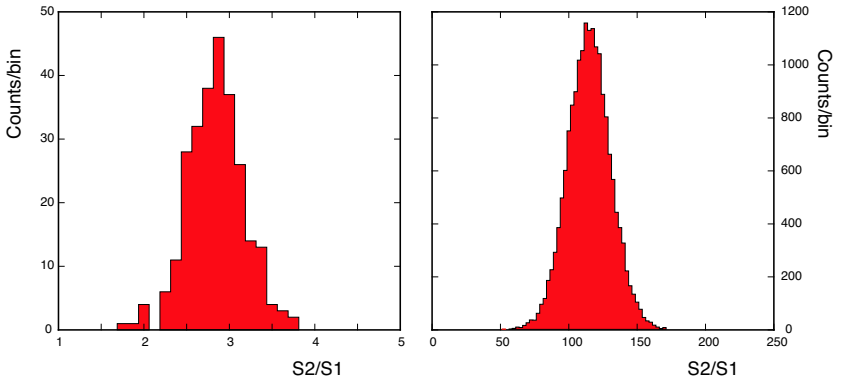


Figure 4.49: Histograms of the $S2/S1$ distribution. The two populations are clearly separated: $\alpha$-particles cluster (left) is centered around $S2/S1 \approx 2.9$ while $\gamma$-population (right) is peaked around $S2/S1 \approx 113$.

$\mathcal{E}_{e,l} = 2.78\ kV/cm$, $\mathcal{E}_{e,g} \equiv \mathcal{E}_m = 4.19\ kV/cm$. The results are plotted in Fig. 4.49 where the events of the scatter plot have been projected onto the $S2/S1$ axis: $S1$ and $S2$ are provided by the sum of the synchronous signals of all seven photomultipliers. Although, as in the previous measurements the $\alpha$- and $\gamma$-families are perfectly separated, an increase of about a factor 15 is observed for first family while a factor 10.5 is measured for $\gamma$-like events. This last distribution is unfortunately affected by saturation problems, due to the reduced dynamical range of the flash ADC, that apparently lower and to narrow the $\gamma$-family $S2/S1$ distribution[20]: this last observation explains the different multiplication factors observed for the two clusters and hence the measured suppression factor $(S2/S1)_\gamma/(S2/S1)_\alpha \approx 43$ different from the previously measured one approximately equal to 60 (see Sec. 4.1.2.3). This last quantity should, in principle, remain constant since a change in multiplication gain should not affect it. The corresponding multiplication gain, deduced from the not saturating $\alpha$-family, is about 40 $photons/electron/cm$ at $\mathcal{E}_m = 4.19\ kV/cm$ to be compared to 7 $photons/electron/cm$ measured with $\mathcal{E}_m = 4\ kV/cm$ at surface level (1.02 $bar\ abs$). As evident, the multiplication process is extremely sensitive to argon pressure.

Verified the change in the multiplication gain, the primary risetime of the

[20]The secondary signal of $\gamma$-events sometimes saturates the flash ADC. Since the saturated events are rejected, only those events with approximately $S_2/S_1 < S2_{sat}/S1$ can be plotted and an apparent decrease of the average $S_2/S_1$ value of the whole population is observed.

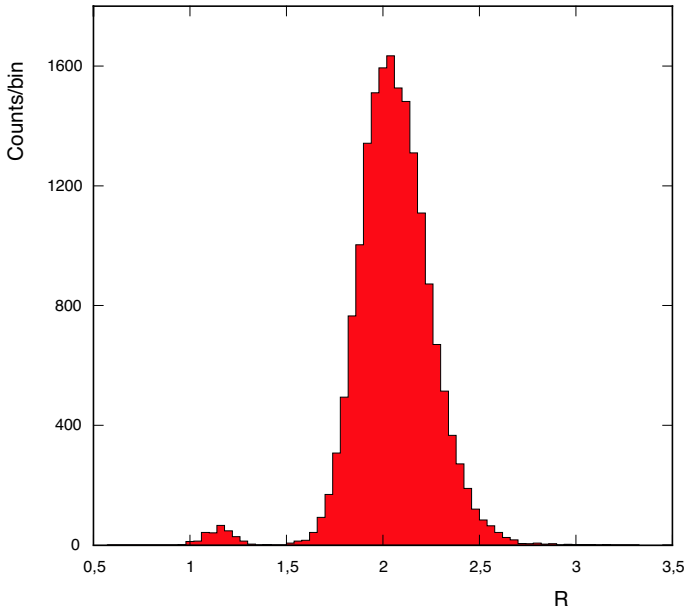


Figure 4.50: Distribution of the ratio $\mathcal{R} = S1/S1(\leqslant 400\ ns)$. Two well separated families are clearly distinguishable. The low $\mathcal{R}$ cluster is associated with $\alpha$ decays: as expected for this kind of events, the majority of light is produced within the first 400 $ns$, suggesting that the singlet component is dominant. The high $\mathcal{R}$ cluster is attributed to $\gamma$-like event.

two families have been investigated in details in order to verify the possibility of coupling to the standard $S2/S1$ discrimination a pulse shape discrimination. As stressed in Sec. 3.2.3, the scintillation light is constituted by two different components, the first $I_t$ associated with the first excited triplet state of the $Ar_2^*$ dimer and the other $I_s$ associated with the singlet: the two components are characterized by very different decay constants ($\tau_t \approx 1.5\ \mu s$ and $\tau_s \approx 6\ ns$). The relative intensity of these two components $I_s/I_t$ is, as explained in Sec. 3.2.3.2, function of the ionization density: $I_s/I_t \approx 0.3$ has been measured at zero drift field for relativistic electrons and $I_s/I_t \approx 1.3$ for $\alpha$-particles [74]. On the basis of this observation, a similar evaluation has been performed onto the acquired data. The selected acquisition has been performed with the DAQ system foreseeing the digital scope, in which the readout electronic records the integrated photomultipliers sum pulse every 200 $ns$: due to the fact that the clock signal is not synchronous to the signal pulse, the minimum time interval containing all the primary fast component

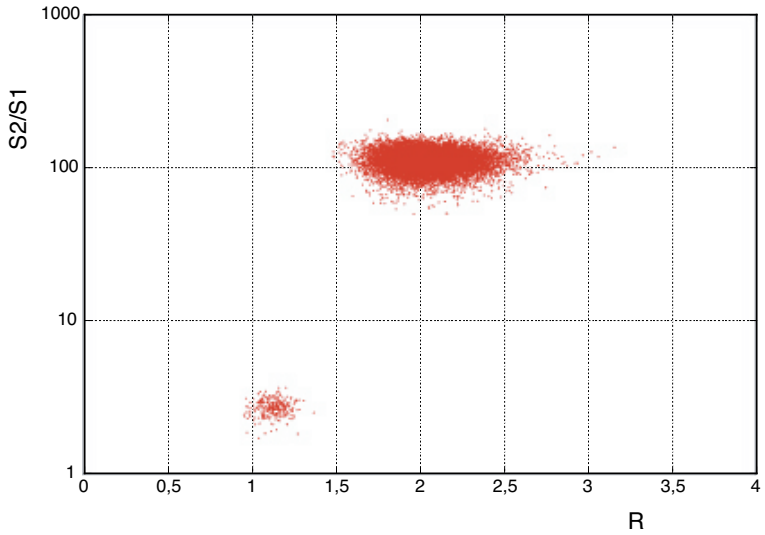


Figure 4.51: Mixed scatter plot $S2/S1$ *vs.* $\mathcal{R}$. An evident correlation is observed, indicating that the two techniques perfectly agree with each other, at least for the observed set of data containing about 17000 $\gamma$-like events.

is represented by two bin corresponding to 400 $ns$[21]. Such time interval is enough to fully contain the totality of the fast component and a fraction of the slow triplet component. The resulting distribution of the inverse of the fraction of total light measured within this time window, expressed by the ratio $\mathcal{R} = S1/S1(\leqslant 400\ ns)$, is plotted in Fig. 4.50 for the scanned events. Once again two completely separated populations are detectable. The average width of the two distributions is essentially dominated by the fact that, due to the asynchronism of the clock, the observed window could contain from a maximum of 400 $ns$ of integrated signal to a minimum of something more than 200 $ns$. This uncertainty could be reduced by the use of a more sampled readout system. In order to verify that the two clusters obtained with pulse shape discrimination are experimentally consistent with $\alpha$'s and $\gamma$'s populations (obtained using the $S2/S1$ method), the scatter plot $S2/S1$ *vs.* $\mathcal{R}$ has been elaborated. The results are shown in Fig. 4.51: a strict correlation is observed, indicating that the two techniques perfectly agree each other, at least

[21] Due to the asynchronism between clock and signal, it is possible that the signal starts at the end of the 200 $ns$ bin and hence, to be sure to fully contain the fast component, almost completely de-exciting within 30 $ns$ (5 decay constants), two successive bins should be considered (400 $ns$).

for the observed set of data containing about 17000 $\gamma$-like events. According to these data the the probability that a $\gamma$-like event populates the region labeled $\alpha$-like is lower than $10^{-4}$ ($< 1/17000$) for each discrimination technique, if only statistical fluctuations are considered. Since the two procedures are based onto two different phenomenologies, it follows that the probability of each one to fail is uncorrelated from the other, leading to a global rejection power higher than $10^{-8}$.

The obtained results are in good agreement with the expected behaviour described in Sec. 3.2.3.2 although they seem more consistent with $I_s/I_t \approx 2.7$ for $\alpha$-particles and $I_s/I_t \approx 0.6$ for $\gamma$-like events (if the standard values of the decay constants are assumed). This is not surprising since, as stressed before, the results of Ref. [74] refer to measurements carried out without electric field. Differently from $\gamma$-family, the majority of the light, induced by $\alpha$-decays ionizations, is produced within the first 400 $ns$ suggesting that the singlet component is dominant. For what concerns nuclear recoils, an $\mathcal{R}$ ratio approximately of the same order of the one measured for $\alpha$-particles is expected. This consideration is essentially guided by the observation that the argon recoils ionization density, influencing the relative intensity $I_s/I_t$, should be of the same order the one measured for $\alpha$-particles, as mentioned at the end of Sec. 3.2.3.1 and 4.1.2.3. One should note that in the energy region populated by nuclear recoils, characterized by a reduced number of detected photoelectrons, the statistical fluctuations become more significant and the pulse shape discrimination becomes obviously less performing.

The proposed signal shape discrimination is evidently enhanced by the great difference between the fast and slow component decay times ($few\ ns$ to 1.5 $\mu s$). The xenon-doping at concentration higher than $[Xe] \geqslant 1\%$ tends, as explained in Sec. 3.2.4, to reduce the slow decay time constant typical of pure LAr: this obviously can afflict the proposed shape discrimination power and hence concentrations lower than 1% should be used to avoid the deterioration of the rejecting power.

#### 4.2.2.3 Estimate of $S2/S1$ rejection power

After this first set of measurements aimed to investigate the $S2/S1$ ratio behaviour at the new working pressure and to select the opportune electronic amplification factors, a longer measurement in low background condition (lead shielding installed) has been performed. Xenon-doped argon has been used

| *Field* | *Field Intensity* ($kV/cm$) |
|---|---|
| $\mathcal{E}_d$ | 1.0 $kV/cm$ |
| $\mathcal{E}_{e,l}$ | 2.54 $kV/cm$ |
| $\mathcal{E}_m$ | 3.8 $kV/cm$ |

Table 4.8: Fields configuration.

($[Xe]$= 1000 $ppm$) together with PTFE reflective layer. The DAQ system of Fig. 4.41 is used to acquire the signal of each PMT with a trigger occurring when at least a 4 phototubes detect, within a 200 $ns$ time window, a signal above threshold, placed at 1.5 $phe$. The fields configuration is shown in Tab. 4.8. The data have been acquired with run of $few\ hours$, preceded and followed by SER measurements to evaluate the photomultiplier gain stability. The total acquired statistics is of 5 $million$ of triggers, corresponding to about 208.2 $hours$: the average trigger rate, with the lead shield installed, is of the order of 6.9 $Hz$. This trigger rate is sustained by the DAQ system without dead-time problems. No sensitive degradation of lifetime has been observed throughout the acquisition period.

The acquired data have been offline analyzed through a custom software dedicated to events reconstruction, working on the sum of the seven photomultipliers signals. The developed software proceeds as follows:

1. the signals from each photomultiplier, after check for saturation and photoelectron calibration, is summed. No light yield correction is applied since the seven PMTs present a quite uniform response, as suggested by the single phototube spectra acquired in presence of calibration gamma sources;

2. the resulting sum signal is differentiated and peaks above the baseline are searched with a given threshold (typical threshold is between $2 \div 5$ photoelectrons): output of this step is the number of signals found above threshold, their position and their width;

3. after a test on the pulses width to define whether the peaks are located, a fit is made on the non differentiated sum signal with prototype primary and secondary signals shapes in correspondence to the found peaks: output of this last step is the amplitude and position of the fitted primary

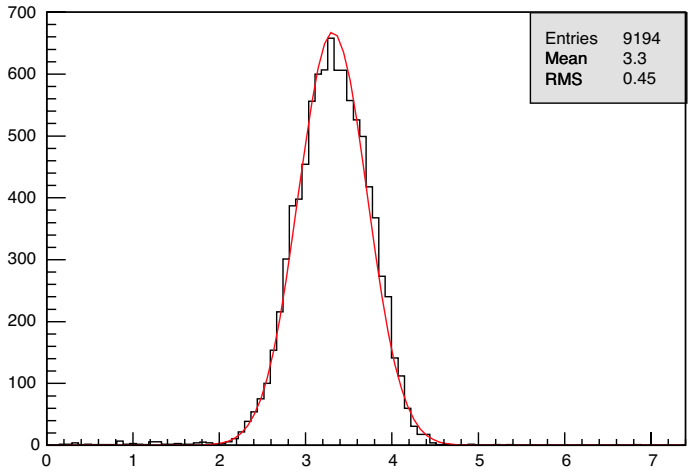


Figure 4.52: Ratio $S2/S1$ distribution relative to $\alpha$-particles. It is well fitted by a gaussian with $\mu = 3.3$ and $\sigma = 0.45$ ($\approx 14\%$).

and secondary signals and, for each individual fit, the parameter $\xi$, given by the sum of square deviation divided by the amplitude of the fitted peak. This last quantity is used to evaluate the goodness of fit.

The software returns a set of values characterizing the signal and the quantities used to carry out the analysis are: the primary risetime $\tau_{r1}$, the secondary risetime $\tau_{r2}$, the drift time $\tau_d$, the fitted primary and secondary amplitude $S1$ and $S2$ and $\xi$ of primary and secondary fit, respectively $\xi_1$ and $\xi_2$.

Following the strategy illustrated in Sec. 4.1.2.3, the position of $\alpha$-peaks is investigated to define the region of interest for recoils. The $S2/S1$ distribution relative to $\alpha$-particles is displayed in Fig. 4.52 and it presents a gaussian behaviour with $\mu = 3.3$ and $\sigma = 0.45$ ($\approx 14\%$). These results should be assumed as reference for the recoils region. Since, as stated in the next chapter, a threshold on primary light of 20 *phe* will be used in the 100 $l$ WARP detector, the rejection power has been evaluated from the recorded data in the region $20 \div 100$ *phe* of the scatter plot, corresponding in the optimal configuration to an argon recoil energy roughly in the range $30 \div 150$ $keV$ (the photoelectrons yield of a 65 $keV$ recoil has been assumed as reference for the energy scale). Since the photoelectrons yield provided by the used set-up for this particular measurement is lower than the nominal one (extrapolated by neutron gun measurements of Sec. 4.1.2.3), the selected $S1$ range ($20 \div 100$ *phe*) corresponds

to argon recoils of energy approximately higher than 250 $keV$ (instead of 30 $keV$) were essentially no recoils induced by natural radioactivity neutrons are expected[22]. For this reason each event occurring in *region A*, defined by 20 $phe < S1 < 100$ $phe$ and $S2/S1 < 3.3$, and surviving the cuts shown below, is assumed to be a "contaminant" $\gamma$-like event. The rejection power is hence defined as the ratio between the number $n_c$ of the surviving events in *region A* (after all the selected cuts have been applied) over the number $n_a$ of events occurring in the range 20 $phe < S1 < 100$ $phe$ and presenting at least one peak with the features of a primary signal: this request rejects noise events and signals constituted by only a secondary peak, since the relative $S1$, below threshold (and hence below 20 $phe$), is too small to be properly reconstructed by the software. This number number, equal to 1851364 events, can be also deduced from the primary light spectra shown in Sec. 4.2.2.1 opportunely corrected for the presence of the drift field.

A set of cuts on the above introduced quantities have been applied to reject from *region A* those events presenting features evidently not appropriate to expected nuclear recoils events. The performed cuts, apart from drift-time one, are enough relaxed to guarantee that the totality of nuclear recoils candidates survives them. For this reason, the obtained rejection powers have to be considered as conservative upper limits and, in principle, they can be ulteriorly lowered by applying more restrictive cuts. The following set of requests (further on referred as $Cut_a$) have been applied to determine the number of candidate contaminant events:

- The signal should present two peaks;
- The first peak should provide characteristic compatible with the typical prototype primary signal ($0 \leqslant \xi_1 \leqslant 1.0$). This cut is not strict;
- The second peak should provide characteristic compatible with the typical prototype secondary signal ($0 \leqslant \xi_2 \leqslant 10.$). This cut is very relaxed since secondary signals from recoils should differ from the prototype one if few photoelectrons associated with electroluminescence are produced;
- The $S1$ amplitude is contained in the range $20 \div 100$ $phe$;

[22]The expected neutron induced recoils spectrum in the 2.3 $l$ chamber has been estimated by simulating neutrons interaction by the means of the FLUKA package [105] and considering the $n - Ar$ cross section shown in Fig. 4.17. A neutron flux, associated with natural radioactivity and equal to the one measured in Hall C of LNGS [107], has been assumed.

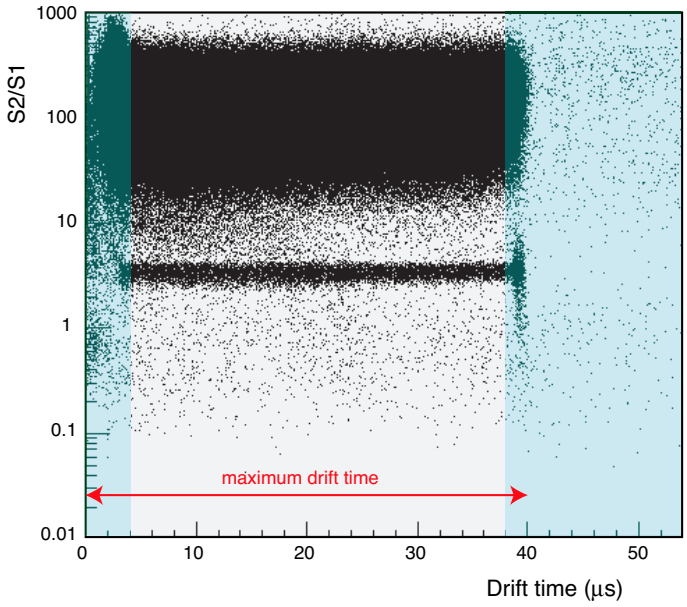


Figure 4.53: Scatter plot $S2/S1$ *vs. Drift time*. The effect of fiducial volume cut is evident (light blue region are rejected): it removes all the unphysical events characterized by a reconstructed drift time greater than the maximum drift time $\approx 40\ \mu s$ (spurious coincidence or misreconstructed events) and also those physical events occurring near the cathode or near the interface.

- The $S2/S1$ ratio should be lower than 3.3 (other $S2/S1$ limits for *region A* have been investigated as shown on Tab. 4.9);
- The drift time should be contained in the range $4 \div 38\ \mu s$. This cut eliminates unphysical events and intercations occurring near the cathode and near the interface[23]: it essentially reduces the sensitive volume of the chamber of about 18% and hence it can affect recoil candidate events too (according to the measured drift velocity the cut rejects the events occurring within 2 *mm* from the interface and within 1 *mm* from the cathode). The effect of this cut is shown in Fig. 4.53.

Of the surviving 577 events, the ones providing $S2/S1 < 1$ have been visually scanned (further on referred as $Cut_m$) and individual photomultiplier signals have been considered. In the region $20 \div 100$ *phe* and $S2/S1 < 1$, 200 events

[23]The events occurring near the interface are not easily reconstructable since it is not evident where the primary signal stops and secondary signal begins.

| *Kind of cut* | *region A* $S2/S1$ *limit* | $n_c$ | *Estimated rejection power* ($\times 10^{-4}$) |
|---|---|---|---|
| $Cut_a(\xi_2 < 10.) + Cut_m$ | 4.5 | 540 | 2.9 |
| | 3.3 | 409 | 2.2 |
| | 2.0 | 259 | 1.4 |
| | 1.0 | 132 | 0.7 |
| $Cut_a(\xi_2 < 1.) + Cut_m$ | 4.5 | 499 | 2.7 |
| | 3.3 | 377 | 2.0 |
| | 2.0 | 240 | 1.3 |
| | 1.0 | 116 | 0.6 |

Table 4.9: Rejection powers estimates for different value of the upper limit of *Region A* and for different requests on the secondary signal fit. Rejection powers of the order of $10^{-4}$ are evaluated. These values should be considered as upper limits since visual scanning has been performed only in the $S2/S1 < 1$ region.

over a total of 316 (63%) have been rejected after visual scanning. In the selected energy window mainly two classes of events have been rejected. The first category includes the events characterized by an unbalanced response of the single PMTs: the response from a single PMT (mostly the central one) is largely dominating above the others (by a factor $10 \div 20$). These events can be attributed to sparks on the phototubes or to decays or interactions in the PMTs windows. The second class is constituted by events most likely due to a double Compton interaction, ionizing both in the sensitive volume and in the gaseous region: this causes that multiplication associated to the interaction in gas produces a small secondary signal almost superimposed to the synchronous primary peaks. These are followed, after the normal drift time, by $S2$ signals associated with the ionization in liquid.

The results of the rejection power evaluations are summarized in Tab. 4.9 for different values of *region A* $S2/S1$ upper limits since, as stated before, the value $S2/S1 = 3.3$ provided by $\alpha$-particles should be considered just as a reference. The estimated rejection powers suffer two problems. First, only a fraction of the *region A* events has been visually scanned: for this reason the estimates should be considered as conservative upper limits, since the effect of visual scanning on rejection is expected to be not negligible (rejections from visual scanning of the order of 63% have been obtained in subregions).

On the other hand, in the nominal photoelectrons yield conditions, the region $20 \div 100$ *phe* will correspond to a lower energy portion of the $\gamma$'s spectrum, characterized by a slighlty lower $S2/S1$ value (due to recombination) if compared to the analyzed one (as shown in Sec. 4.1.2.3). This fact will tend to raise the upper limit. Nevertheless one should note that, in presence of xenon, a smearing in the $S2/S1$ resolution has been observed suggesting a higher rejection power for pure liquid argon measurements.

## 4.3 Summary

This chapter has been dedicated to the experimental tests performed with a small prototype of double phase argon detector (Sec. 4.1.1). This chamber, with a sensitive volume of 2.3 $l$, has been used to develop an experimental technique able to detect tiny energy deposition in the sensitive volume and to identify the nature of the interacting ionizing particle. As stressed in Chap. 2 this identification method has to be used to discriminate nuclear recoils (possibly induced by WIMPs interactions) from $\gamma$-like interactions (mainly associated to natural radioactivity) that are dominant in the detection region of interest, corresponding to a recoil energy included in $30 \div 100$ $keV$. The proposed technique is based on the simultaneous measurement of scintillation light and ionization induced by an interaction in liquid argon: an applied electric field is used to drift the ionization electrons (away from the interaction site) towards a gaseous region positioned above the liquid sensitive volume. Once reached the interface, the electrons cloud feels a stronger electric field used to fast extract it into the gaseous region and, by the means of a second electric field, it is accelerated in the vapor phase inducing the emission of VUV photons. In this way the tiny ionization signal can be luminously multiplied and hence amplified. As a consequence an interaction in the sensitive volume generates a scintillation signal (produced by the induced excitation and by the occurring recombination) and an electroluminescence signal, called proportional scintillation, produced by the acceleration in the gas phase of the ionization electrons survived recombination (Sec. 4.1.1.4). Both luminous signals are readout by a device sensitive to UV light, in this case a photomultiplier. Once produced by an almost point-like interaction, the secondary signal is delayed with respect to the prompt scintillation by a time equal to the time spent by the ionization electrons to drift towards the gas volume and to be luminously multiplied.

While both signals are obviously function of the deposited energy their relative ratio, for a fixed field configuration, assumes typical values according to the nature of the interacting particle that, in other words, determines the relationship between scintillation and ionization produced in the medium. As a consequence this ratio, as shown in Sec. 4.1.2.3, is used as discrimination criterion. Once determined the particle nature, the scintillation signal can be used to determine its deposited energy. This aspect is crucial since, as stated in Chap. 3, different particles of different energies, suffering different quenching processes, can produce the same luminous output. The same concept can be expressed by attributing a different photoelectrons yield, expressing the average number of photoelectrons produced for a unit energy deposition ($phe/keV$), for different particles.

After having verified the extraction process and characterized the production of electroluminescence light in the vapor phase, all the above mentioned properties of the experimental technique have been studied in details by exposing the chamber to several radioactive sources, including $\gamma$'s, $\beta$'s, $x$-rays and neutrons, these last able to induce, as WIMPs, nuclear recoils in the energy range of interest (Sec. 4.1.2). As expected, the amount of scintillation (signal $S1$) and ionization (signal $S2$) are function, other than the energy of the interacting particle, also of the nature of the particle itself. Nuclear recoils, for example, are characterized by a depleted ionization signal (if compared to minimum ionizing particles) since very intense electric fields are necessary to avoid recombination process (due to their induced high local ionization density). As far as scintillation is concerned, the photoelectrons yield for nuclear recoils is lower than that associated with $\gamma$-like events, due to the enhanced luminous quenching process: in particular while at a drift field of 1 $kV/cm$ a $\gamma$-like event of approximately 20 $keV$ produces 2.3 $phe/keV$, a nuclear recoil of about 65 $keV$ is characterized by a photoelectrons yield of 0.63 $phe/keV$ (a $recoil/\gamma$ $ratio \approx 0.3$). This last quantity has a crucial role for the energy calibration of the system leading to the existence of two different energetic thresholds, one valid for recoils and the other (lower) for $\gamma$-like interactions[24]. As a consequence, looking at the $S1$ $vs.$ $S2/S1$ scatter plot nuclear recoils populate a region separated from the one associated with other ionizing particles and, for example, different from the one populated by $\gamma$-particle. Similar

[24] As an example if a threshold for primary scintillation is set to 20 $phe$, this will correspond approximately to an energy loss of 9 $keV$ for $\gamma$-particles and 30 $keV$ for nuclear recoils.

consideration can be extended to $\alpha$-particles behaving in way similar to nuclear recoils due to high ionization density, although in a completely different energetic region. Several tests have been conducted onto this last population and, according to them, $\alpha$-events are characterized by a proportional signal approximately sixty times lower than that expected for a $\gamma$-like event producing the same amount of scintillation light. Similar values are expected for nuclear recoils too. The $S2/S1$ ratio can hence be used to discriminate the nature of the particles but, obviously, it will start to fail at some level, leading to $\gamma$-like events wrongly labeled as nuclear recoil. According to the performed measurements rejection power lower than $10^{-4}$ are obtained for $\alpha$-particles with respect to $\gamma$-like population: similar conservative upper limits have been obtained for nuclear recoils too[25]. On $\alpha$-particles population a second discrimination criterion, based on scintillation signal shape analysis, has been performed: in particular, as documented by several works found in literature, the relative intensities of the slow and fast component of the scintillation light is function of the impinging particle and, once again, of the ionization density. The test carried out on this subject has provided a rejection power better than $10^{-4}$ (Sec. 4.2.2.2). The two proposed techniques, since independent, can be coupled to obtain very performing rejections: dedicated tests in the case of nuclear recoils have to be performed.

Once verified the experimental technique performance, the 2.3 $l$ prototype has been installed at the National Laboratory of Gran Sasso to study the radioactive background (Sec. 4.2.2.1). The rejection power previously defined has to be compared to the $\gamma$-like events rate within the detection window to determine the expected background events able to mimic WIMP signature. As a consequence a set of scintillation measurements has been performed, studying the light spectrum and the possible radioactive contaminations of the used materials, especially of argon. Of particular interest is the result concerning $^{39}Ar$ $\beta$-emitter contamination (contained within the used liquid argon), providing an activity of 0.76 $Bq/kg\ of\ Ar$. As shown in the next chapter this dissolved radioactive source, unremovable if isotopic depletion techniques are not applied, will represent the main background source for nuclear recoils detection, requesting very performing discrimination techniques.

[25] A rejection power of $10^{-4}$ means that 1 $\gamma$-event each 10000 events produces a $S2/S1$ characteristic of nuclear recoils and hence it is wrongly labeles as nuclear recoil. One should note that the declared rejection power has to be considered as upper limits.

# Chapter 5

# WARP proposed 100 $l$ detector

The experimental results obtained with the 2.3 $l$ prototype have confirmed that the nature of an interacting particle can be effectively discriminated through the use of a double-phase argon detector, even for tiny energy depositions associated to nuclear recoils. In particular the studied $S2/S1$ technique has provided discrimination powers better than $10^{-4} \div 10^{-5}$ for $\gamma$-like events, as shown in Sec. 4.2.2.3. This method can be used together with a signal shape discrimination, introduced in Sec. 4.2.2.2, and whose rejection power in the low energy region should be ulteriorly investigated. Nevertheless, one should note that since the two methods refer to two fundamentally different phenomenologies, the probability of each one to fail is most likely uncorrelated and hence the global discrimination power (provided by the simultaneous use of both the techniques) is given by the product of the two independent discrimination powers. On the basis of these major results and of the observations on argon properties as target for WIMP interaction (see Sec. 2.4), the WARP collaboration has been proposed the realization of an argon 100 $l$ sensitive detector for dark matter search [41]. Obviously, as for the majority of rare events experiments, the consistent background to the signal should be reduced as much as possible. As a first step the detector has to be installed in an underground laboratory, in this case the Gran Sasso National Laboratory, to protect it from cosmic rays otherwise producing an overwhelming rate of interactions. As second step, the main sources of the background should be reduced: in this sense the radiopurity of the materials and the use of

some forms of shielding become absolutely necessary. As stressed in Chap. 2, WIMPs are in principle detectable in low background detector by the means of the nuclear recoils they should induce inside of it. For this reason the experimental technique should provide a way to highly efficiently discriminate nuclear recoils from other interactions (mainly electron-recoils) in the energy range of interest. Due to the consistent rate of this background, even in presence of very radiopure materials, such discrimination method should be really performing. A second dangerous background for this kind of dark matter direct detection experiment is represented by those processes leading to nuclear recoils, in principle indistinguishable from that WIMP-induced. This recoil events, that can mimic the WIMP signature, are mainly induced by neutrons and neutrinos. The former can be effectively reduced by reducing neutrons flux through the detector (neutron shield and radiopure materials) and/or developing an experimental technique able to exploit their stronger interacting nature (if compared to WIMP): as an example the detector could be dimensioned in order to provide a high probability that a neutron interacts more than once within the detector itself (differently from what it is expected for WIMP). As far as the neutrino-induced background is concerned, there is no way to reject these events. Fortunately, in the case of argon, the expected component of neutrino-induced nuclear recoils spectrum is really negligible above the selected threshold energy (see Sec. 5.2.3). The last possible recoil-source concerns the so-called *surface events*, particular processes occurring near the surface of the materials that can produce a single recoils within the sensitive volume: these events could be effectively removed by sensitive volume cuts, rejecting those interactions occurring in the peripheral region of the sensitive volume (see Sec. 5.2). A detailed study of the possible backgrounds for the proposed detector is described in Sec. 5.2 after the description of its main features.

## 5.1 The experimental layout

A conceptual layout of the argon based detector consists of a large volume of ultra-pure liquid argon. The liquid volume can be ideally divided, as shown in Fig. 5.1, into two separate parts, a central detection region surrounded by the rest of the liquid used as an anti-coincidence shield:

- the *central core* traces back the 2.3 *l* chamber inner structure. Above

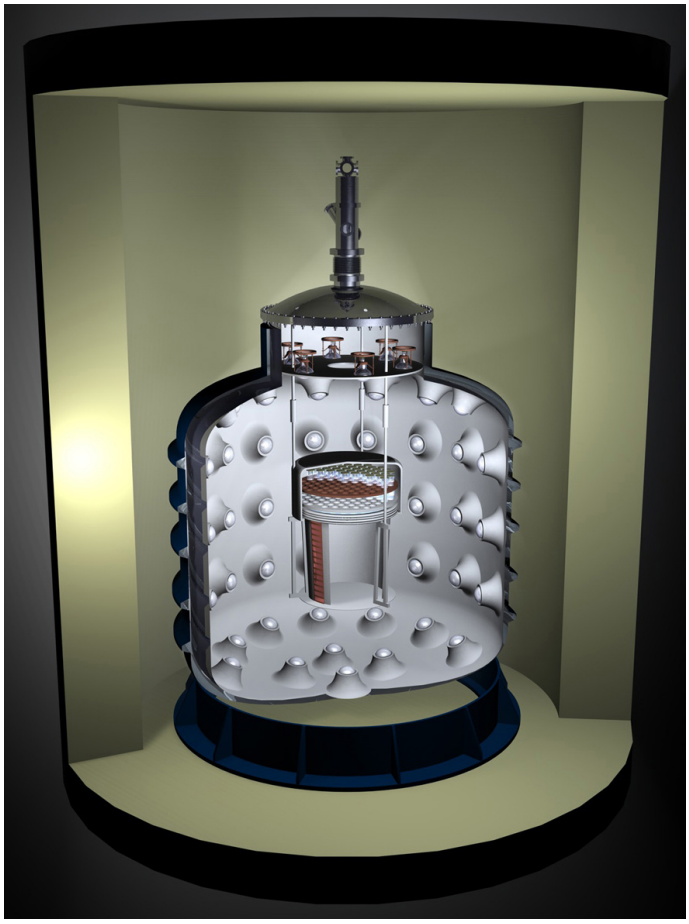

Figure 5.1: Artistic view of the conceptual layout of the argon detector. The inner detector is fully contained in an active anti-coincidence volume. The whole system is surrounded by $\gamma$'s and neutrons shields.

the liquid argon sensitive volume a gaseous gap is maintained, to provide a region where electroluminescence can occur. A set of race-tracks and grids is used to drift the ionization electrons, produced by an interaction in the sensitive volume, towards the liquid-gas interface and to extract and light multiply them. The region is equipped with phototubes to detect both primary and secondary scintillation light produced by an ionizing event: tridimensional localization of the event is provided, as briefly discussed in Sec. 4.2.1, by the time delay of the secondary signal ($z$) and by the distribution of the proportional light detected by the phototubes array ($x$-$y$). A threshold of at least 20 *phe* on primary

light is requested. This system is aimed to separate, in the low energy region, ionization signals ultimately produced by electron recoils from those associated with the nuclear recoils, potentially induced by WIMP's interactions. As stressed all along the work, these last ones are perfectly mimicked by neutrons elastic scattering over argon atoms, resulting in nuclear recoils. The structure used to define and support the sensitive volume should be as thin as possible and constituted by low activity materials;

- the *anti-coincidence volume* is simply readout by an adequate number of photomultipliers and it is used to reject those events due to neutrons or other particles penetrating from outside or travelling out from the central part (no electric fields are present in this region). Only events in which no signal is recorded by this component and producing a nuclear recoil event in the central core, are potential candidates for WIMP induced events. This volume should be dimensioned in order to make negligible the probability that a neutron, after having induced a recoil in the central region, does not produce a signal above threshold (at least 10 *phe* of primary light) in the anti-coincidence volume, within a few *hundreds of ns* time window. Evidently the central part and the anti-coincidence volume must be optically separate in order to avoid cross-talk. Once again, to efficiently use this surrounding volume as an anti-coincidence, the event rate should be as low as possible, requesting a high radioactive purity of the used materials.

In addition it is advantageous to add external $\gamma$ and neutron shields, these last aimed to absorb, or at least to thermalise, the environmental neutrons background (see Sec. 5.1.3).

Considering that the required thickness of the active shield to effectively reduce the neutrons background should be of the order of 40 $cm \div 60$ $cm$ (see estimate in Sec. 5.1.2), the proposed fiducial volume has been chosen in the range of about 100 $l$, corresponding to an active mass of about 140 $kg$.

### 5.1.1 Inner detector

The inner detector has been designed trying to minimize the amount of materials to be placed around the inner active volume and therefore to reduce

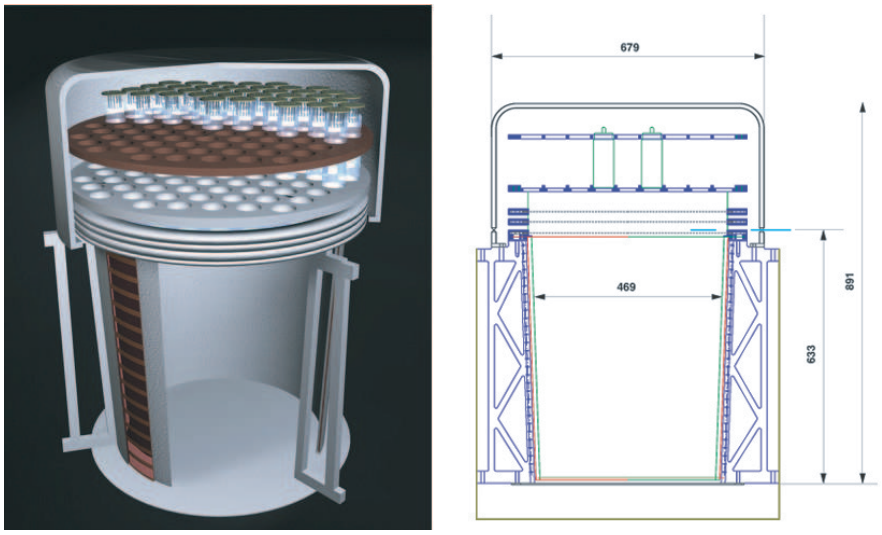


Figure 5.2: Artistic view (on the left) and drawing (on the right) of the inner detector layout. The distances are expressed in $mm$.

the radioactive contamination. Its structure is suspended in the middle a liquid argon volume. As shown in Fig. 5.2, it is mainly constituted by

- a *sensitive drift region*: this volume is limited at the bottom by a 3 $mm$ thick circular stainless steel plate ($\varnothing = 58\ cm$), laterally by a truncated conical shaped race-tracks system and at the top by a circular grid placed at about 470 $mm$ from the cathode. The race-tracks system is constituted by means copper strips printed on a $Kapton^{TM}$ substrate (1 $cm$ wide interspaced by 1 $cm$). The layer is enrolled in a truncated conical shape with the copper strips forming annular rings (the race-tracks) which are then connected to each other and to the cathode by means of a resistors chain (voltage degrader). The grid is composed by a stainless steel ring (internal diameter $\approx 50\ cm$, external diameter $\approx 58\ cm$, thickness 5 $mm$) holding a set of stainless steel wires ($\varnothing = 150\ \mu m$) 4 $mm$ pitched. The wires are enrolled on gold plated bushes, which are in turn inserted into opportunely shaped holes machined inside the stainless steel ring. The wires are mechanically tensioned to about 750 $g$. The whole structure is supported by a skeleton of $PEEK^{TM}$ dielectric rods. All the inner surfaces are covered with a reflecting/waveshifting layer for improving the light collection efficiency;

- an *extraction and multiplication gaseous region*: this region, placed above the first lower grid, is fully limited by a stainless steel cap used to contain the gaseous gap. This last is produced by the means of several heating resistors, placed in the liquid region and inducing its evaporation. A set of grids, identical to the lower one, is placed in this gas volume to provide the appropriate extraction and multiplication fields. The liquid interface is maintained at a fixed level by the means of a set of small holes, positioned all along the cap, in correspondence of the middle point between the first and the second grid. A small pipe will also be connected to the top cap to eventually re-pressurize the gas. The grids are separated by means of annular $PEEK^{TM}$ insulators and the voltage on each one is independently supplied by means of a dedicated $HV$ channel. Once again all the surfaces are covered with the reflective layer;

- an *array of photomultipliers*: a set of quartz or borosilicate window phototubes, eventually coated with TPB (see Sec. 4.1.1.2), is placed above the grids, within the gas gap, for the scintillation signals readout (both primary and secondary). To cover, as much as possible, the available surface, as displayed in Fig. 5.3, a $PEEK^{TM}$ structure supports 37 phototubes of which 6 are 2 *inches* and 31 are 3 *inches* large (diameter), providing a global photocathodic coverage equal to 10%. The selected photomultipliers are Electron Tubes Type D749U and D750U with 12 dynode stages and bialcali photocathode evaporated on platinum under-layer, to ensure good functionality at cryogenic temperatures (see Sec. 4.1.1.2). These phototubes, whose properties are summarized on Tab. 5.1, are characterized by a good response to single photoelectrons, allowing photon counting, and they are realized with specially selected low activity materials. The bases (a standard resistive divider chain plus loading capacitors welded on a circuit printed on Kapton$^{TM}$ substrate) are directly mounted on the phototube pins, thus minimizing the needs for cabling and cryogenic feed-through. The heat produced by the PMT bases (about 10 $W$ in total) contributes to the pressurization of the gas phase.

A foil of copper deposited on Kapton$^{TM}$ support externally surrounds the body of the internal detector. This external layer is put to ground and ensures that no residual field is present in the active veto region (see Sec. 5.1.2). All the

| *Inner detector* | |
|---|---|
| Overall External Dimensions | $Height = 90\ cm$<br>$Diameter = 75\ cm$ |
| LAr Volume (Sensitive Volume<br>Conical Shape) | $Height = 60\ cm$<br>$MaxDiameter = 50\ cm$<br>$MinDiameter = 46\ cm$ |
| Internal LAr Mass / Volume | $152\ kg/109\ litres$ |
| Number of readout 3 *inch* PMTs | 31 |
| Number of readout 2 *inch* PMTs | 6 |
| Total photocathode coverage of the<br>inner surface | 10% |
| Nominal reflectivity of the inner layer | 94% |
| Nominal drift field | $1\ kV/cm$ |
| Maximum drift field | $1.5\ kV/cm$ |
| Operating Voltage at nominal drift field | $-70\ kV\ to\ +10\ kV$ |
| Operating Voltage at maximum drift field | $-130\ kV\ to\ +10\ kV$ |
| *Photomultiplier* | |
| Diameter | 2” |
| Quantum Efficiency at Peak | 30% |
| Dynodes | $12\ LFBeCu$ |
| Nominal Anode Sensitivity | $500\ A/lm$ |
| Overall Voltage for nominal sensitivity | $1950\ V$ |
| Dark Current at $20°\ C$ at nominal sensitivity | $3\ nA$ |
| Gain at nominal A/lm | $7 \times 10^6$ |
| Maximum Gain | $3 \times 10^7$ |

Table 5.1: Nominal characteristics of the inner detector and of the phototubes (EMI Type D749U).

inner and outer surfaces of the central detector are covered with the highly diffusing material described in Sec. 4.1.1.2. It consists of a standard reflective dielectric multilayer film ($VM2000$) onto which a $TPB$ layer is evaporated: this material has to be coupled with $TPB$ coated phototubes. To provide the signal shape discrimination of Sec. 4.2.2.2 no xenon-doping can be applied, since it could modify the scintillation decay constants. If one assumes the

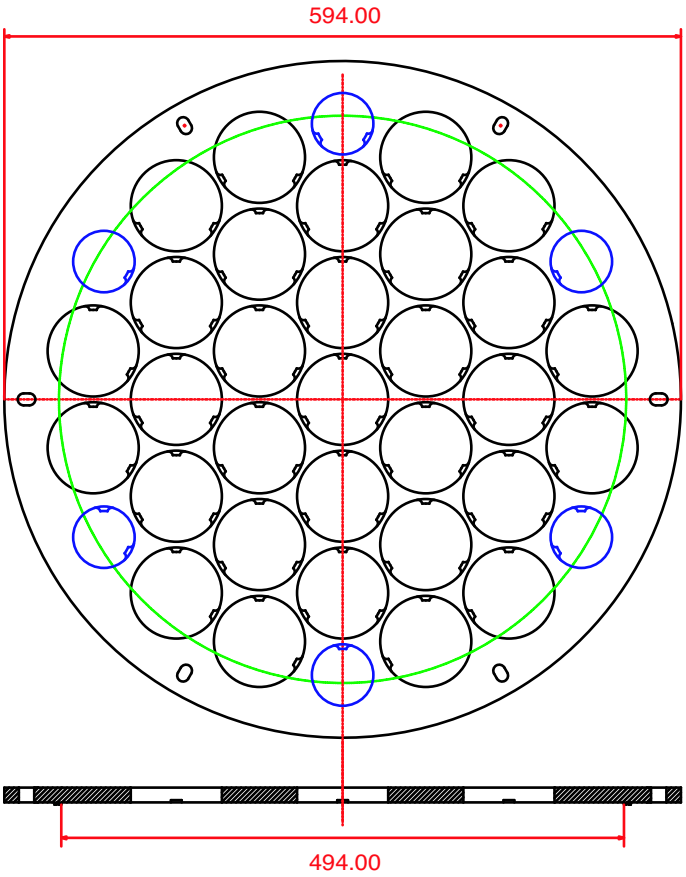


Figure 5.3: Geometry of the phototubes array of the inner detector (the distances are provided in $mm$). The sensitive area corresponding to the drift width is indicated by the green line.

results obtained with the 2.3 $l$ chamber[1] and the same diffusive layer performances, obviously rescaled for the different PMTs quantum efficiencies, for the different size of the detector and for the different photocathodic coverage, a global photoelectrons yields of about 3.5 $phe/keV$ (for 20 $keV$ electrons in pure LAr at zero field) is expected for the 100 $l$ inner detector (2.8 $phe/keV$ at 1 $kV/cm$).

A reasonable nominal threshold of at least 20 $phe$ of primary light is requested for energy deposition within the sensitive volume. Equation 4.19,

[1]For 20 $keV$ electrons a photoelectron yield of 2.9 $phe/keV$ has been measured with no applied field and 2.3 $phe/keV$ at 1 $kV/cm$, see Sec. 4.1.2.1

opportunely modified to count for the increased scintillation yield[2], leads to the equation

$$E_R(p) = 2.7\ keV \cdot \left(\frac{p}{1\ phe}\right)^{0.817} \tag{5.1}$$

that can be used to compute the minimum detectable recoil energy corresponding to the selected 20 *phe* threshold: the obtained threshold recoil energy is $E_R = 31\ keV$. On the basis of the assumptions outlined in Chap. 2, the potential WIMPs events should produce in argon a nuclear recoils spectrum up to 100 $keV$ corresponding, in term of primary signal, to about 90 *phe* (obtained from Eq. 4.19 with $A'_s = 0.3\ phe/keV$). The introduced $20 \div 90$ *phe* range corresponds, in terms of electrons recoils, to the energy range $8 \div 32\ keV$ and it will be referred, in the rest of the work, as acceptance window (the estimated value of 2.8 $phe/keV$, referred to 20 $keV$ electron recoils at 1 $kV/cm$, is assumed as reference[3]). One should note that the above introduced intervals are correct only if the measured photoelectrons yield for the 100 $l$ will correspond to the values extrapolated from the 2.3 $l$ results: if this is not the case, this energy ranges have to be slightly modified together with the following background estimates.

Strict requests on radiopurity of the selected materials has to be applied. The contamination of the main materials used in this central volume has been measured and the results are listed in Tab. 5.2.

### 5.1.2 Active anti-coincidence shield

The inner detector is completely submerged into an external liquid argon bath, contained inside a double wall cryogenic vessel insulated with vacuum and super-insulation and made of stainless steel ($AISI304LN$) selected for low radioactive contamination (specific activity from uranium and thorium contamination are displayed in Tab. 5.2). A large fraction of this volume is enclosed within the so-called active veto (active anti-coincidence liquid argon shield), optically separated by the remaining region and by the inner detector

[2]Since Eq. 4.19 has been obtained with the 2.3 $l$ chamber, characterized by a reference photoelectrons yield at zero field equal to 2.9 $phe/keV$ for a 20 $keV$ electrons, the $A_s$ value should be rescaled to count for the higher yield extrapolated for the 100 $l$ (3.5 $phe/keV$) and hence multiplied by a factor 1.2 (nominally $A'_s = 0.3\ phe/keV$).

[3]As shown in Fig. 3.10 a negligible modification of the quenching due to escaping electrons is expected passing from 8 to 32 $keV$ electron energies. The estimated photoelectron yield of 20 $keV$ electrons is hence used as reference.

| | | |
|---|---|---|
| Stainless steel for grids, | $^{238}U$ | $(3.7 \pm 0.7)10^{-10}$ $g/g$ |
| cathode and vessel | $^{232}Th$ | $(2.8 \pm 0.3)10^{-9}$ $g/g$ |
| | $^{40}K$ | $< 14$ $mBq/kg$ |
| | $^{60}Co$ | $6 \pm 1$ $mBq/kg$ |
| Kapton foil (covered with copper layer) | $^{238}U$ | $< 2.1 \times 10^{-3}$ $ppm$ |
| | $^{228}Ra$ | $< 0.0095$ $ppm$ |
| | $^{228}Th$ | $< 0.091$ $ppm$ |
| | $^{40}K$ | $0.17 \pm 0.08$ $Bq/kg$ |
| | $^{60}Co$ | $< 0.012$ $Bq/kg$ |
| | $^{137}Cs$ | $< 0.031$ $Bq/kg$ |
| Tetra-Phenyl-Butadiene | $^{238}U$ | $< 2.1 \times 10^{-3}$ $ppm$ |
| | $^{228}Ra$ | $< 0.0061$ $ppm$ |
| | $^{228}Th$ | $< 0.0057$ $ppm$ |
| | $^{40}K$ | $< 0.2$ $Bq/kg$ |
| | $^{60}Co$ | $< 0.012$ $Bq/kg$ |
| | $^{137}Cs$ | $< 0.010$ $Bq/kg$ |
| Mylar foil | $^{238}U$ | $< 6.4 \times 10^{-3}$ $ppm$ |
| | $^{228}Ra$ | $< 0.014$ $ppm$ |
| | $^{228}Th$ | $< 0.015$ $ppm$ |
| | $^{40}K$ | $0.27 \pm 0.14$ $Bq/kg$ |
| | $^{60}Co$ | $< 0.02$ $Bq/kg$ |
| | $^{137}Cs$ | $.014 \pm .008$ $Bq/kg$ |
| 3M reflecting foil | $^{238}U$ | $< 0.022$ $ppm$ |
| | $^{228}Ra$ | $< 0.034$ $ppm$ |
| | $^{228}Th$ | $< 0.035$ $ppm$ |
| | $^{40}K$ | $< 0.8$ $Bq/kg$ |
| | $^{60}Co$ | $< 8 \times 10^{-3}$ $Bq/kg$ |
| | $^{137}Cs$ | $.054 \pm .029$ $Bq/kg$ |
| Phototube | $^{39}K$ | $37$ $ppm$ |
| | $^{238}U$ | $10$ $ppb$ |
| | $^{232}Th$ | $36$ $ppb$ |
| PEEK | $^{238}U$ | $0.0021 \pm 0.0001$ $ppm$ |
| | $^{228}Ra$ | $0.0064 \pm 0.0004$ $ppm$ |
| | $^{228}Th$ | $0.0034 \pm 0.0001$ $ppm$ |
| | $^{40}K$ | $.059 \pm .006$ $Bq/kg$ |
| | $^{60}Co$ | $< 0.001$ $Bq/kg$ |
| | $^{137}Cs$ | $< 0.001$ $Bq/kg$ |

Table 5.2: Measured radioactive contaminations of constituent materials. Upper limits for $^{238}U$ and $^{232}Th$ are derived assuming secular equilibrium of the corresponding decay chains [108].

and readout by a set of 3 *inch* phototubes: this region is aimed to reject all those events producing, within a defined time window, both an interaction in the sensitive volume and in the anti-coincidence volume itself and hence

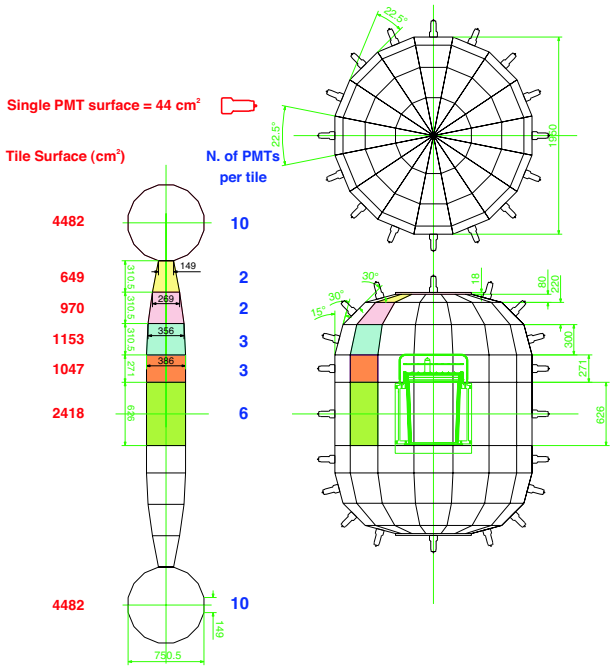


Figure 5.4: Active shield structure drawings. Quotes are expressed in $mm$. Details on one vertical slice of the veto surface are shown. For each tile size, the corresponding number of installed PMTs is indicated.

most likely not associated to a WIMP induced nuclear recoil. No electric field should be present in this active volume since an energy detection threshold, as low as possible, should be provided in this region: as shown in Sec. 3.2.3, the presence of an electric field induces a reduction of scintillation yield especially for $\gamma$-like events, leading, for a fixed photoelectrons threshold, to higher energetic limit. The high voltage regions of the inner volume should be electrostatically shielded by the means of a thin conductor layer surrounding the whole inner detector, grounded and covered with the reflecting film.

The active shield essentially consists of an array of 436 photomultipliers, 3 *inch* diameter, held in place by $PEEK^{TM}$ supports externally sustained by a thin stainless steel structure: this last structure is also used to prop up the whole veto boundary surface obtained, as displayed in Fig. 5.4, by the juxtaposition of several $PEEK^{TM}$ tiles, covered with reflective layers and presenting a certain number of holes through which the phototubes face the anti-coincidence region. Differently dimensioned tiles are foreseen with maximum size equal to $630 \times 390$ $mm^2$ (See Fig. 5.4 for details). The obtained

| | |
|---|---|
| Overall External Dimensions (including PMTs and sustaining structure) | $Height = 260\ cm$<br>$Diameter = 220\ cm$ |
| Active LAr Volume | $Height = 220 cm$<br>$Diameter = 180\ cm$ |
| Thickness of $VETO$ layer | $60\ cm$ |
| Internal LAr Mass / Volume | $7850\ kg / 5600\ litres$ |
| Number of readout 3" PMTs | 436 |
| Total photocathode coverage of the inner surface | 10% |

Table 5.3: Main characteristics of the active veto.

photocathodic coverage is of the order of 10% of the whole inner veto surface. This set-up leads to an expected photoelectron yield, at zero drift field, equal to 3 $phe/keV$ for electron recoil and approximately 0.65 $phe/keV$ for nuclear recoils, assuming that the quenching is not efficiently affected by fields of this intensity[4]. Once again a reasonable recoil energy for the active veto region is of the order of 30 $keV$ corresponding to about 20 $phe$ and hence to electron recoils of approximately 7 $keV$. The main feature of the anti-coincidence volume are summarized in Tab. 5.3.

The dimension of the active veto region has been selected in order to provide a minimal argon thickness of 60 $cm$ between the inner detector and the external not readout volume. According to the performed FLUKA simulation [105] of the apparatus (see Sec. 5.2.2), this depth is enough to reduce to less than $10^{-4}$ the probability that a fast neutron, coming from outside, produces a recoil over threshold in the inner detector without associated signals over threshold in the veto region. A more detailed definition of the threshold is presented in Sec. 5.2.

[4]Once again the data have been extrapolated by 2.3 $l$ measurements. Since no field is applied the $\gamma/recoil$ ratio is provided, in the case of the prototype, by the ratio of the photoelectron yields for $\gamma$ (2.9 $phe/keV$) and that for nuclear recoils at zero field. This last number is assumed to be approximately equal to that measured at 1 $kV/cm$ (0.63 $phe/keV$) since, as shown in Sec. 3.2.3.1, fields of this intensity should not effectively affect the scintillation quenching process for particles heavy ionizing, as nuclear recoils. The application of the same $\gamma/recoil$ ratio to the extrapolated 100 $l$ yield provides the declared 0.65 $phe/keV$ for nuclear recoils.

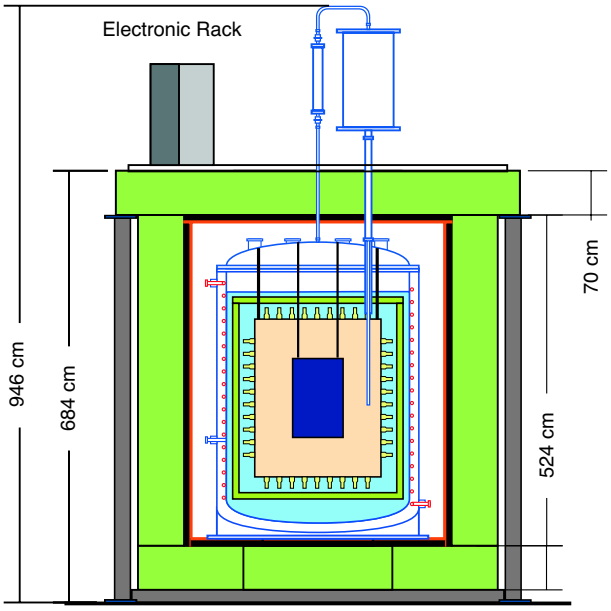


Figure 5.5: Side view of the detector layout with $\gamma$-rays and neutrons shields.

### 5.1.3 External passive shields

As previously stressed, two important components of the background to WIMP direct detection are represented by neutrons-induced nuclear recoils and $\gamma$-like events (referred in the rest of the work as $\gamma$-like background[5]). While the first can perfectly mimic the WIMP signature, the second could be effectively rejected by the proposed discrimination technique: obviously this last one could fails at some level, producing the misidentification of a $\gamma$-like event as a nuclear recoil. For this reason, together with the request of working in a low background environment (to avoid for example pile-up problems), a first reduction of these two backgrounds is guaranteed by the presence of external *neutrons* and $\gamma$ passive shields, to reduce the component of this background induced by natural radioactivity at the experimental site (see Fig. 5.5).

Fast neutrons from environmental radioactivity could induce nuclear recoils in the energy range of interest, where WIMP induced recoils are expected. One should observe that, if an elastic scattering is assumed, the maximum re-

[5] In other words the $\gamma$-background includes the contributions by both $\gamma$ and $\beta$ emitter.

| *Material* | *Activity* ($\mu Bq/kg$) | | |
|---|---|---|---|
| | $^{226}Ra$ ($U$ *chain*) | $^{228}Th$ ($Th$ *chain*) | $^{40}K$ |
| *Lead* | $\leqslant 29$ | $\leqslant 22$ | $440 \pm 140$ |
| *Copper* | $\leqslant 16$ | $\leqslant 19$ | $\leqslant 88$ |

Table 5.4: Typical value for lead and copper activity used in low background experiments [106].

coil energy produced by an impinging neutron of energy $E_n^i$ is given by

$$E_R^{max} = E_n^i \cdot \left[1 - \left(\frac{A-1}{A+1}\right)^2\right] \tag{5.2}$$

corresponding for $A = 40$ to a $E_R^{max} \approx 0.1 \cdot E_n^i$. According to this equation and assuming a threshold of the order of 30 $keV$ in the sensitive volume, one should note that neutrons do not need to be absorbed since only those with kinetic energy higher than 300 $keV$ can induce a recoil over threshold. On the basis of this observation the neutron shield has been dimensioned in order to effectively thermalize the fast neutrons flux from the environment and compress their induced recoils energy spectrum below threshold. A 70 $cm$ thick polyethylene shield will be installed. In the same way a standard low activity $\gamma$-shield will be installed between the external polyethylene shield and the cryostat to reduce the environmental $\gamma$-background and those $\gamma$'s produced by neutrons interaction in the polyethylene shield: it is constituted by a 10 $cm$ thick lead layer and 2 $cm$ thick OFHC copper layer (facing the inner volume). A high radiopurity is requested for this materials since their total weight is about 128 $ton$: typical value for good low activity lead and copper are summarized in Tab. 5.4. The interspace between the copper walls and the cryostat is air-tight and fluxed with nitrogen gas (or artificial air).

Once reduced these external contributions, the $\gamma$-like background remains dominated by the not negligible activity, due to the presence of $^{39}Ar$ in natural argon, of $(0.76 \pm 0.28)$ $Bq/kg\ of\ LAr$. This component is unremovable apart from using special isotopically separated $^{40}Ar$, depleting the $^{39}Ar$ content. From the point of view of the more dangerous neutrons background, the surviving main source is represented by the cryostat walls themselves, whose approximate weight is about 13 $ton$ (stainless steel is less radiopure than lead or copper). For this reason a second internal polyethylene shield,

| | |
|---|---|
| Main Dewar Internal Dimensions | $Height = 445\ cm$<br>$Diameter = 290\ cm$ |
| Main Dewar LAr Volume | 23000 $litres$ |
| Main Dewar Thermal Insulation | *Vacuum + Superinsulation* |
| Main Dewar and top flange Weight | $\approx 13000\ kg$ |
| Operating Pressure | 1.5 $bar\ abs$ |
| Operating Temperature | 88 $K$ |
| LAr Filling Speed | 500 $l/hour$ |
| Nominal Gas Recirc. Rate | 5 $l/hour$ |
| Maximum Gas Recirc. Rate | 20 $l/hour$ |

Table 5.5: Main characteristics of the cryogenic systems.

10 $cm$ thick, is installed inside the liquid argon volume, in the interspace between the stainless steel cryostat and the active veto region. A detailed study of the background and of the resulting projected sensitivity is presented in Sec. 5.2, together with the justifications for the chosen shield thicknesses.

### 5.1.4 Cryogenics and purification systems

The liquid argon volume is contained in a cylindrical stainless steel double wall cryogenic vessel (290 $cm$ large and 445 $cm$ high), insulated with vacuum and super-insulation and closed by a top flange ($\varnothing = 290\ cm$) whose tightness is ensured by a double sealing with an internal o-ring in $Kalrez^{TM}$ [6] and an external o-ring in $Viton^{TM}$. The corresponding total liquid argon volume is of the order of 23000 $l$. The cryostat dimensions have been selected to eventually host a 1 $ton$ sensitive volume providing at the same time a consistent anti-coincidence thickness. Its main fetaures are summarized in Tab. 5.5. On the top flange an ensemble of ports (ConFlat $CF200$ and $CF250$ flanged with copper o-rings sealing) have been foreseen for

- the electrical feed-throughs for phototubes high voltage supply and read-out, corresponding to about 2500 ceramic feed-throughs mounted on 8 $CF250$ flanges;

[6] They have been chosen both for the low permeability to Radon and for their large temperature application range.

- the electrical feed-throughs for cathode and grids high voltage supplies;
- the cryogenic system functional services such as vacuum pump system, argon purification system, gas recirculation unit, etc.;
- the auxiliary instrumentation such as LAr purity monitor and temperature probes;

The body of the vessel presents only a single port as the input to the liquid argon recirculation unit. The request on leak tightness of the dewar is of $10^{-8}$ $mbar\ l\ sec^{-1}$. Within the double wall interspace of the vessel, in contact with the internal face, a cooling serpentine (nitrogen circulating) is installed and used before and during filling procedure.

As explained in Sec. 3.2.5 and 4.1.1.1 electronegative impurities, capturing the drifting electrons, should be removed from commercial argon for TPC like applications. Moreover, due to out-gassing of the inner surfaces, the liquid argon should be continuously recirculated and purified in order to maintain a high enough and stable electron lifetime. For this reason the cryogenic plant should be ideally divided into two main units: the first is used to purify the commercial argon during the filling procedure while the second, responsible for gas recirculation and purification, is activated only once the vessel is filled and it should continuously work to maintain a high enough LAr purity. The cryogenic scheme is shown in Fig. 5.6. As stressed in Sec. 4.2.1, due to the reduced radiochemical pollution in the output liquid, the $Hopkalit^{TM}$ filter has to be preferred to standard $Oxysorb^{TM}$.

The filling procedure is regulated by the filling unit of Fig. 5.6 and it should start only once the cryostat has been cooled down by the means of the cooling serpentine. The argon contained in storage dewar is passed through an $Hopklite^{TM}$ filter cooled down by immersion in a liquid argon bath in order to proceed, after an initial transitory period, in liquid phase and hence at a constant rate of about 500 $l\ of\ LAr\ per\ hour$. The cooling down of the filter is necessary to directly inject liquid argon into the vessel: re-condensation strategy, as the one followed for the small prototype, requires too long time.

On the other hand, to maintain the LAr purity for long data acquisition, a continuous argon recirculation system has been implemented (see recirculation unit of Fig. 5.6). The gas produced by the continuous evaporation of the LAr in the dewar, caused by thermal losses from the cryostat and by the power dissipated by the phototubes, is taken from the top of the cryostat,

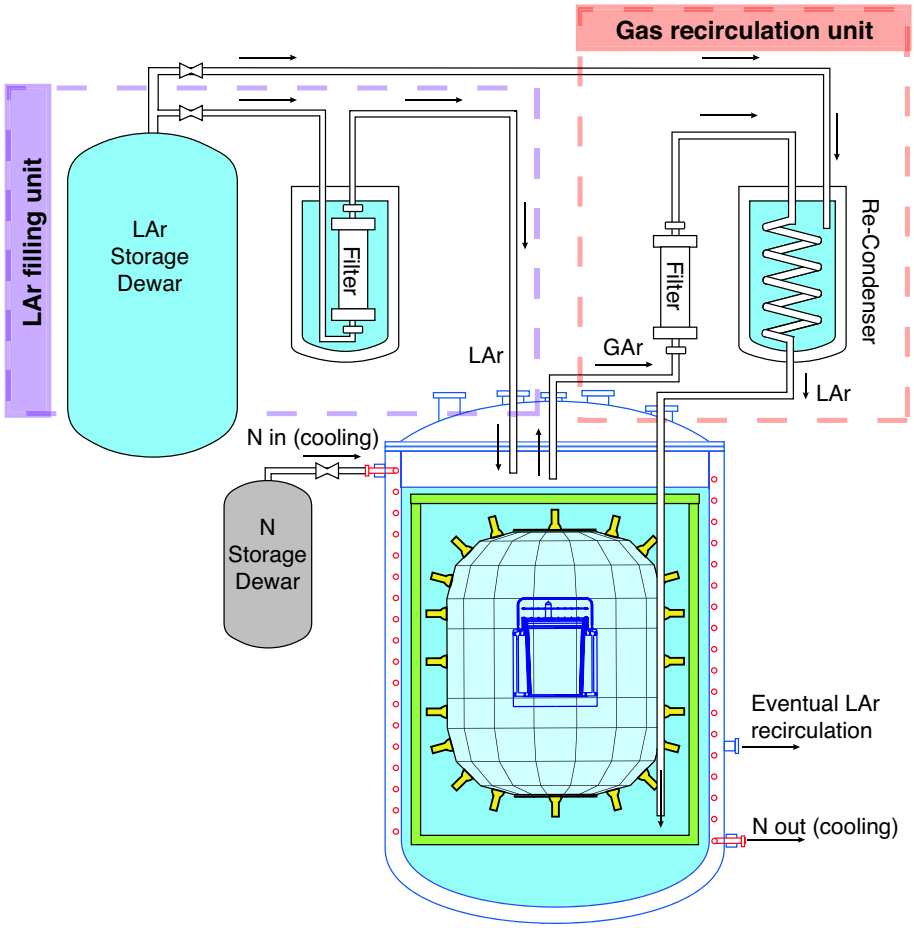


Figure 5.6: Schematics of the cryogenic plant.

passed through a filter (not cooled down), re-condensed into a LAr bath (re-circulation re-condenser) and re-enjected on the bottom of the cryostat. A minimum recirculation rate of about 5 $litres/hour$, that could be augmented by the means of a heating resistance located below the surface of the LAr, is expected.

The cryogenic plant is completed by two external storage dewars, the automatic filling system for the gas recirculation re-condenser and standard monitoring devices (temperatures and pressures).

### 5.1.5 Readout electronics and trigger system

A good *WIMP* candidate event should produce, only in the inner volume, primary scintillation light and proportional light in such a way that the ratio between the second and the first peak amplitudes, seen by the PMTs ($S2/S1$), is smaller than a given value which depends on the chosen multiplication field. On the basis of this discrimination technique, an online two levels trigger system has been developed. The conceptual DAQ scheme differs from the one implemented for the 2.3 $l$ measurements at LNGS since, in that case, no active veto was present (see Sec. 4.2.1.1). Although the ultimate acquisition system has not yet been decided, since ulterior investigations are needed, its main features are sketched in Fig. 5.7. For all the events evidently not $\gamma$-like and producing a signal over threshold into at least $n$ internal PMTs, the signal shape of each inner detector phototube is recorded together with a set of data representing the arrival time and the amplitude of the scintillation light signal (or signals) seen, within the acquisition time window, by each external photomultiplier: this information associated with the veto phototubes will be used offline as an anti-coincidence.

The sensitive volume and the active veto region are readout by two sets of phototubes. While in the sensitive region the photomultipliers signal shapes should be recorded to perform the offline analysis of the events, the PMTs of the active veto volume are just used to provide the anti-coincidence flag and, for each phototube, only the starting time and the amplitude of the primary peak (or peaks) have to be recorded[7]. For this reason the anodic and $12^{th}$ dynode (referred further on as dynodic signal) current signals are extracted for the inner detector PMTs while for veto ones only the anodic signal is needed. The dynodic signals of the inner detector photomultipliers are used to select only those events producing a signal over threshold into at least $n$ phototubes. Such a trigger system is implemented sending the dynode signal of each photomultiplier to an amplifier and then to a programmable discriminator: the obtained output is a logic signal, almost synchronous with the detected scintillation signal, indicating if the single PMT has recorded a signal over threshold. The ensemble of these logic signals is sent to a Xirix CPU system that can be easily programmed to compute the above described $n$-majorities, within a defined coincidence window: a logic output is provided by the Xirix CPU unit

[7]Since no field is applied in the veto volume, no secondary signal occurs

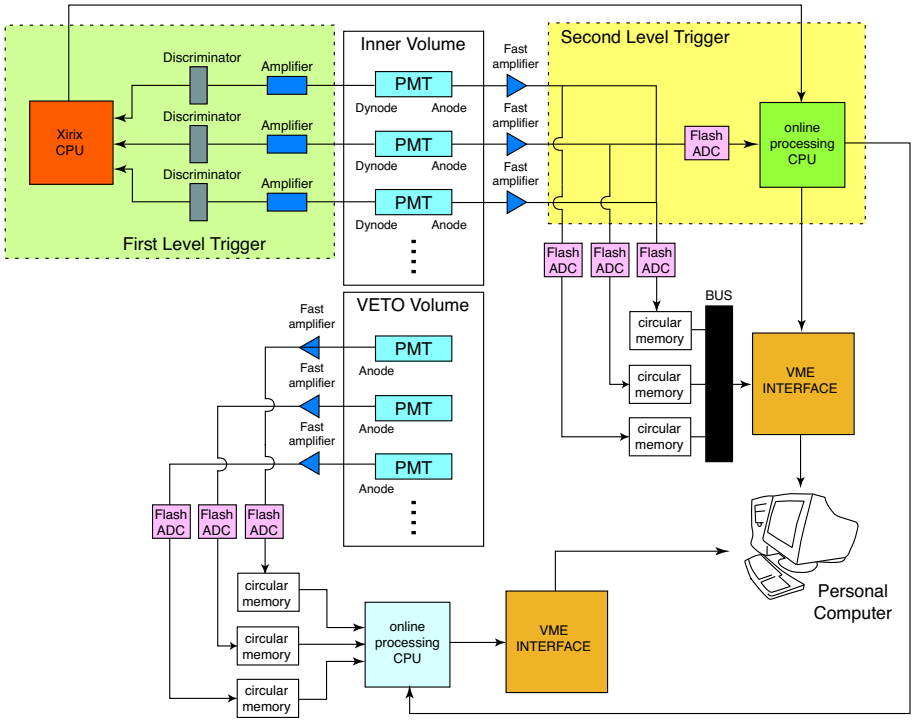


Figure 5.7: Trigger and readout system conceptual scheme.

that is used as a *first level trigger*. Of all these events only those presenting two peaks with the right ratio and risetimes are of interest and an online signal processing becomes favorable. To provide such *second level trigger*, the analogue sum of all the inner photomultipliers anode signals is sent to a flash ADC and then to a programmable CPU. This last, opportunely programmed, is used to process the signal and to calculate the ratio of the peaks amplitudes, once the first level trigger has hit. In this way a substantial fraction of the $\gamma$-like background can be rejected since those signals evidently $\gamma$-like shaped do not overcome this second level trigger. Flash ADCs with online programmable CPUs are easily available on the market in a number of versions with speed and flexibility.

Each anode signal from inner and outer volume PMTs is sent to a flash ADC and recorded to circular memory buffers. As digitizers, the custom CAEN 789 boards with the pre-amplifier section replaced by fast amplifiers could be used (see Sec. 4.2.1.1 for details). Fast amplifiers and PMTs gain will be adjusted in such a way that the single photoelectron amplitude will be

in the range of 50 *ADC counts* (the Flash ADCs of the boards have a depth of 10 *bits* and work at 20 $MHz$). The width of the circular memory buffers is 16 *kBytes* corresponding, at 20 $Msample/s$, to about 820 $\mu s$ and allowing the continuous recording of a full drift length ($\approx 400$ $\mu s$). The second level trigger CPU controls the readout of the circular memory buffers through *VME interface*. The inner phototube signal shapes are recorded onto a mass storage device. A second CPU performs an algorithm onto the external phototubes signal shapes recorded onto the flash ADC memory buffers: for each of them, the arrival time (with respect to a common clock) and the amplitude of the primary scintillation peaks, detected within a time interval centered around the trigger time, are recorded onto the mass storage device once the inner detector signal has overcome the second level trigger.

Once recorded the data onto a mass storage each single event will be offline analyzed. Evidently, in order to avoid data loss, the second level trigger criterion should be not too strict since it is aimed to reject only those events clearly $\gamma$-like. For this reason, each single event will be offline analyzed applying once again $S2/S1$ and signal shape discrimination criteria, both aimed to remove those events not classified as nuclear recoils. Once separated these events, the data from the veto region will be used as anti-coincidence for good WIMPs candidates. As stressed before an elastic recoil induced by a neutron will be most-likely characterized by a nuclear recoil shaped signal in the inner detector, with an associated signal in the veto volume occurring within a $few\ hundreds\ ns$ window, centered around the starting time of the primary peak detected by the internal phototubes. Only those events with no associated signals in the veto, within the coincidence window, will be considered as WIMPs induced events. The implemented scheme provides the remarkable possibility to study the neutron-induced recoils background itself, since these events are not hardware rejected by the trigger logic (anti-coincidence is just used to flag the event). One should note that the applied hardware thresholds will be evidently lower than that declared in the previous sections. These last ones should be considered as the threshold value for data analysis.

## 5.2 Background estimate

As previously justified, only the primary signal range $20 \div 90$ *phe* will be explored, corresponding to nuclear recoils approximately in the energy range

$30 \div 100\ keV$ and to electrons recoils included in the energy window $8 \div 32\ keV$. One should note that these data have been obtained assuming the light yield extrapolated from the prototype results: different measured photoelectrons yields should affect this energy ranges. In absence of direct measurements the introduced acceptance windows have been used to perform the following computations. Two essentially different backgrounds to the proposed WIMP detection are expected. One is represented by those interactions inducing a $\gamma$-like event in the sensitive volume that, according to the $\gamma$-like rejection power ($S2/S1$ and pulse shape discrimination), could be wrongly labeled as a nuclear recoil even if it is physically an electron-recoil. As shown in Sec. 5.2.1 the rate of these events is dominated by $^{39}Ar$ activity and by the rejection method capacity. The other source of background is constituted by those interactions inducing a nuclear recoil in the sensitive volume exactly as in the case of a WIMP. As shown further on, this category includes those events producing an argon recoil or a nuclear recoil of a different nucleus in the core detector: the former is essentially produced by elastic scattering of neutrons and neutrinos on argon nuclei, leading to a recoiling argon atom. The latter is constituted by some spurious events associated with the inner detector material contamination, that leads to the emission of a nuclear recoil due to the particular topology of the event (surface event): as an example it is possible to imagine an $\alpha$-decay, occurring at the surface of the material, whose $\alpha$-particle is emitted towards the bulk of the material while the associated recoiling nucleus is emitted towards the liquid argon volume.

As far as argon recoils is concerned, the neutrino-induced recoils spectrum is expected to populate the energy region below the selected threshold ($30\ keV$) and hence its role within the acceptance window is completely negligible (see details in Sec. 5.2.3). As regards neutrons-induced background, from a preliminary estimate, partially performed with a FLUKA simulation of the experimental set-up, it seems to be possible to bring its rate to a level better than 1 *event* each 100 *days* by the means of an opportunely dimensioned active veto and neutrons shielding and applying strict requests on materials radiopurity.

As previously explained a second source of background is represented by nuclear recoils of an element different from argon, occurring within the LAr sensitive volume. These events are in principle characterized by a signal very similar to that measured for argon recoil and they could be hardly distin-

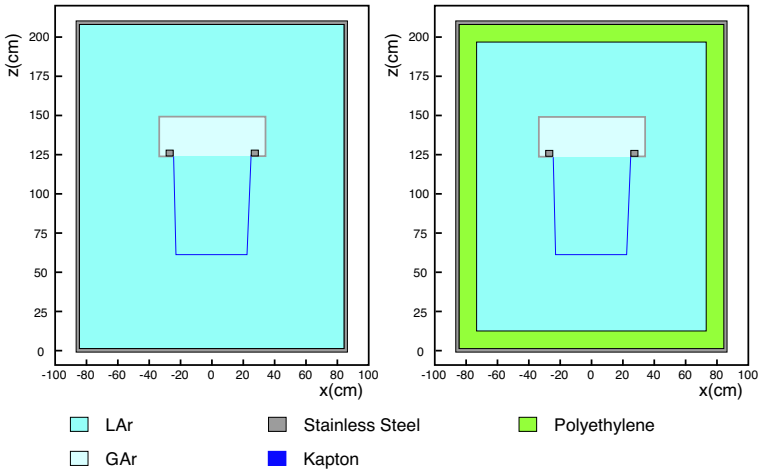


Figure 5.8: Basic geometries without (left) and with (right) the internal shield. The geometry with the shield will be referred as enhanced geometry. Different thicknesses have been implemented: 2.5 $cm$, 5.0 $cm$, 7.5 $cm$, 10.0 $cm$ and 12.5 $cm$.

guished. They can be imagined to occur only along the internal surface of the sensitive volume otherwise, if they occur in the middle of the volume, the signal produced by the other emitted particle (in the described process the $\alpha$-particle) would be detected together with the recoil signal, favoring the rejection of the event itself. Since these recoiling atoms have a typical range in liquid argon of less than one $\mu m$, they should occur in the very peripheral region of the sensitive volume: for this reason they are called surface events. The proposed fiducial volume cut, obtained through drift time and $x$-$y$ localization selection, removes efficiently all these events, selecting a sensitive volume far enough from this surfaces. In the rest of the work this kind of background will be considered completely removed by the fiducial volume cut technique.

The computations of $\gamma$-like and neutrons expected backgrounds have been in part obtained by a simulation performed with the FLUKA package. Several different geometries for the experimental apparatus have been tested. The presented results refer to the two simulated geometries sketched in Fig. 5.8, one of those presenting a neutrons shield contained in the main LAr vessel (this is the internal shield described in Sec. 5.1.3) with variable thickness (five values from 2.5 $cm$ to 12.5 $cm$ have been investigated). The inner detector is described as a LAr 63.0 $cm$ high cone with 22.5 $cm$ and 23.8 $cm$ radii and placed below a gaseous cylindrical volume, 25.6 $cm$ height and 66.0 $cm$ diam-

eter. The inner detector is contained within a stainless steel cap, 2 $mm$ thick, and a thin Kapton$^{TM}$ layer. A 2 $cm$ thick stainless steel cylinder, 210.0 $cm$ height and 180.0 $cm$ diameter, represents the vessel and encloses the LAr bath defining, at the same time, the veto region surrounding the sensitive volume. Differently from the real set-up the vessel is supposed to be as large as the veto region (60 $cm$ deep liquid argon shell surrounding the inner detector)[8]. In the enhanced set-up an internal polyethylene shield with five different thickness (from 2.5 $cm$ to 12.5 $cm$) is placed between the veto and the vessel.

### 5.2.1 Estimate of $\gamma$-like background

In order to estimate the requests on $\gamma$-like events rejection power, the expected $\gamma$-like background has been evaluated. With the installation of a passive $\gamma$-shield, realized with low background materials (10 $cm$ lead plus 2 $cm$ copper OFHC), the external $\gamma$ background, dominated by the $^{222}Rn$ decay chain (200 $Bq/m^3$) [109], is very effectively removed leaving, as dominant contribution, the surviving $\gamma$-like background associated with the presence of radioactive impurities, both dissolved in the LAr or contained in the inner detector materials. As stressed several times along this work, a $\gamma$-like event is a ionization event ultimately produced by an electron recoil: this kind of event could be produced by a primary $\gamma$, through Compton or photoelectric effect, or by the direct emission an electron (attributable to $\beta$-emitters). The expected rate associated with that component of the background produced by $\beta$-emitters can be directly evaluated on the basis of their estimated content within the materials: due to the nature of the emitted particle, these events are characterized by a single interaction in the sensitive volume since the emitted electrons release all their energy in the medium producing a unique track. On the other hand, the rate induced by $\gamma$-emitters is not easily estimable since, differently from the previous one, the emitted photon can interact more than once and hence the event could be rejected by the means of the active veto. For this reason this last background, differently from that originated by $\beta$-decays, is strongly affected by the performance of the anti-coincidence that can be evaluated only through a Monte Carlo simulation.

As regards LAr contaminants, $^{39}Ar$, $^{41}Ar$, $^{42}Ar$, $^{42}K$, $^{85}Kr$ and $^{222}Rn$ should be investigated. According to 2.3 $l$ measurements, $^{39}Ar$ ($\beta$-emitter) and

[8] In the projected set-up the vessel is larger than the veto region and an ulterior liquid argon layer separate the vessel from the veto, although not readout by the phototubes.

$^{222}Rn$ ($\gamma$-emitter) induced events dominate within the energy range of interest (see Sec. 4.2.2.1), at least if "fresh argon" is considered: the contamination by Radon occurs during storage dewar filling and hence, due to its short half-life of 3.82 *days*, its contribution tends to become negligible within few days from the filling of the chamber. On the other hand $^{39}Ar$ half-life is of the order 269 *years* and hence its contribution is not expected to significantly change with time. According to the $^{39}Ar$ $\beta$-spectrum, the fraction of $\beta$-decays falling in the acceptance energy window, corresponds to about 5.0%[9]. Consequently, the global expected interaction rate within the 100 $l$ sensitive volume and due to this isotope activity is given by

$$100\ l \times \left(1.1\frac{Bq}{l} \times 0.05\right) \approx 5.5\ cps = 3.16 \times 10^3\ iru \tag{5.3}$$

where the $^{39}Ar$ activity measured with the 2.3 $l$ prototype has been used (see Sec. 4.2.2.1) and the integrated rate unit *iru* (*events*/*kg*/*day*) has been introduced (see Chap. 2 for definitions).

In order to reduce the number of $^{39}Ar$ events wrongly labeled as nuclear recoils to a conservative maximum number of 1 *event in* 100 *days*, a rejection power of the order of $2.1\times10^{-8}$ should be provided ($4.7\times10^7$ events due to $^{39}Ar$ electron recoils are produced within the selected energy window in the whole detector in 100 *days*). A level of rejection of this order, once $S2/S1$ ratio and signal shape discriminations have been applied, has been already estimated between $\gamma$-like and $\alpha$-events families in the 2.3 $l$ chamber (see Sec. 4.2.2.3). As far as nuclear recoils and low energy $\gamma$-like events is concerned, only $S2/S1$ rejection power has been experimentally estimated, providing a rejection factor better than $10^{-4}$-$10^{-5}$ with the prototype: the effect of the application of the double discrimination technique has to be experimentally verified, directly with the 100 $l$ detector[10]. Incidentally, one should note that while the recoil spectrum is decaying exponentially, the $\beta$-spectrum within the acceptance

[9] The fraction of decays falling within the acceptance window have been evaluated directly from the normalized $\beta$-spectrum measured in Ref. [110] for each considered $\beta$-emitter.

[10] Since this 100 $l$ detector has been designed with some new technical features, the resulting $S2/S1$ rejection power could be better, in principle, than that measured with the prototype: as an example the recoil region could have been populated, in the 2.3 $l$ measurement, by those electron recoils, associated to interactions near the lateral wall of the drift volume, for which some ionization loss has occurred. As stated in the text, for the 100 $l$ detector all these peripheral regions can be removed by volume cut and hence a stronger rejection power could in principle be achieved.

window is rising approximately parabolically: *hence an eventually residual background signal, if present, should be easily identified and subtracted*. Due to the required large discrimination power, the possibility of isotopic separation of commercial argon has been investigated too, such as to reduce the background due to this contamination: $^{39}Ar$ depletion factors of $10^2 \div 10^3$ seems to be reachable by the means of diffusion or centrifugation processes, permitting to slightly release the requests on the discrimination power. Obviously $^{39}Ar$ decays are produced within the veto region too and a total rate of 6.6 $kHz$ is expected. Since as described in Sec. 5.1.5 the anti-coincidence window for the offline analysis is of the order of $few\ hundreds\ of\ ns$ a dead time of the order 0.1% is expected.

As far as $^{41}Ar$ is concerned, it is presence in LAr is essentially due to $^{40}Ar$ neutron capture. This isotope is a $\beta$-emitter, with half-life 109 $m$, end-point at 2491 $keV$ and with a huge specific activity of $1.517 \cdot 10^{18}\ Bq/g$ [110]. In the 99.1% of the decays a $\gamma$ peaked at 1294 $keV$ is emitted too [110]. The fraction of electrons within the acceptance window is 1.7% of the total number of $\beta$-decays and in 99.1% of the cases they can be rejected due to simultaneous high energy $\gamma$-ray [110]. The expected total rate within the detector can be expressed as function of its abundance $\xi$ ($g\ of\ ^{41}Ar/g\ of\ ^{40}Ar$) as

$$R(^{41}Ar) = 140\ kg\ of\ ^{40}Ar \times \left(\xi \frac{g\ of\ ^{41}Ar}{g\ of\ ^{40}Ar}\right) \times \tag{5.4}$$

$$\times \left(1.517 \cdot 10^{18} \frac{Bq}{g\ of\ ^{41}Ar}\right) \times 0.017 \times 0.009 \approx 3.48 \times \xi \times 10^{19}\ Bq. \tag{5.5}$$

An extremely conservative and rough upper limit of this rate can be evaluated assuming a neutrons flux through the sensitive volume of 1 $neutron/s$ and a global capture probability of 100%. Both these value are several orders of magnitude higher that the expected ones (see Sec. 5.2.2)[11] On the basis of these

[11] The main neutron source, in terms of flux, is represented by environmental neutrons associated with natural radioactivity. The low energy component of the this flux is efficiently captured by the 70 $cm$ thick polyethylene external shield, while the high energy part of the spectrum is partially captured and partially thermalized. If one supposes, to be conservative, that this fast neutrons component is simply thermalized and not captured, an integrated flux of the order of $4.33 \times 10^6\ neutrons\ cm^{-2}\ s^{-1}$ is expected [117], approximately corresponding to $10^{-2}\ neutrons\ s^{-1}$ crossing the sensitive volume (once assumed that no capture by neutrons shield occurs). This rate is about a factor 100 lower than the assumed one. On the other hand the capture probability is strongly favored only for thermal neutrons [99] and once again the assumed capture probability is very conservative.

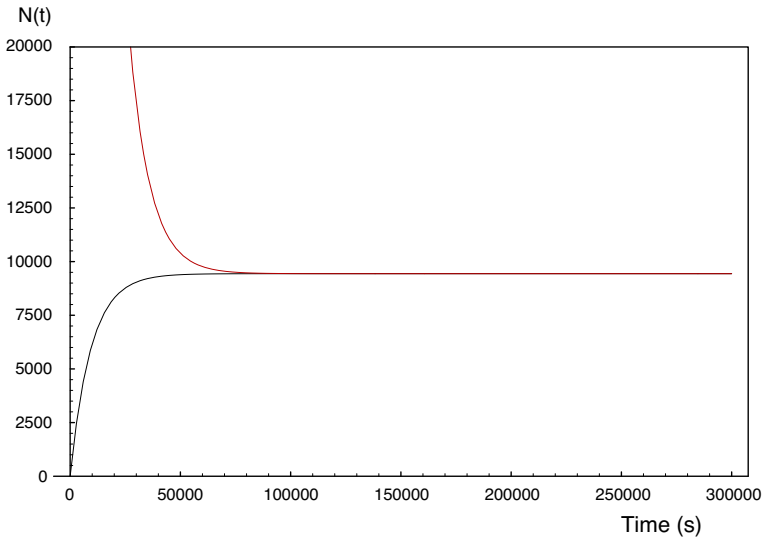


Figure 5.9: Solutions of Eq. 5.4 representing the average number of $^{41}Ar$ atoms within the sensitive volume for different values of $N(0)$, the average number of $^{41}Ar$ atoms present at the moment $t = 0$, instant in which the LAr starts to be exposed to the neutron flux responsible for the specific creation rate $b$. Its equilibrium number depends essentially on the production rate $b$ of Eq. 5.4, while the time spent to reach the equilibrium depends on the nuclide half-life and on its initial abundance. The two plots refer to $N(0) = 0$ and $N(0) = 2 \times 10^5 atoms$. The time spent to reach the equilibrium is in the range from few hours up to few days, for reasonable values of $N(0)$: even for $N(0) = 10^{12}$ $atoms$ the requested time is approximately 55 $hours$. In other words after a reduced time interval, the $^{41}Ar$ content becomes dominated by its production rate, independently from its initial amount.

considerations the expected contamination can be obtained by estimating the average number $N$ of $^{41}Ar$ atoms contained in the sensitive volume through equation

$$\frac{dN(t)}{dt} = -aN + b \tag{5.6}$$

where $a = 6 \times 10^{-5}$ $s^{-1}$, obtained from half-life, and $b = 1$ $atoms$ $s^{-1}$ is the production rate of $^{41}Ar$ (obtained from the assumed neutron flux and capture probability). Independently from the initial conditions, the average number of $^{41}Ar$ atoms, described by the above equation, reaches the equilibrium within a limited number of hours as shown in Fig. 5.9 for two completely different $N(0)$ values. The average number of $^{41}Ar$ atoms at equilibrium is of the order of $10^4$ $atoms$ within the whole inner detector (this value obviously decreases

if lower $b$ value are assumed and it can be used to evaluate the $\xi$ value upper limit). The comparison between this amount and the number of $^{40}Ar$ atoms contained in the sensitive volume produces, through Eq. 5.4, a conservative upper limit for the decay rate equal to $R(^{41}Ar) \approx 1.5 \times 10^{-4}$ *cps*. This upper limit makes this contribution extremely negligible, especially if compared to the provided rejection power, leading to a background rate several order of magnitude lower than 1 *event* in 100 *days*.

The contamination from $^{42}Ar$ can be estimated on the basis of the results found in literature, although no direct measurements have been performed with the small prototype. This $\beta$-emitter with specific activity 34.1 $Ci/g$ (9583 GBq/g), half-life 32.9 *years* and $\beta$-spectrum end-point at 600 $keV$ is contained in the atmosphere essentially due to thermonuclear tests [110]. According to the results found in literature [111], its concentration in earth atmosphere is less than $6 \times 10^{-21}$ $^{42}Ar$ $atoms/^{40}Ar$ $atoms$ ($2\sigma$ upper limit). The expected $^{42}Ar$ rate within the acceptance window containing 4.6% of the global spectrum, is hence less than

$$140\ kg\ of\ ^{40}Ar \times \left(6 \cdot 10^{-21} \frac{g\ of\ ^{42}Ar}{g\ of\ ^{40}Ar}\right) \times \tag{5.7}$$

$$\times \left(9583\ \frac{GBq}{g\ of\ ^{42}Ar}\right) \times 0.046 \approx 4 \cdot 10^{-4} cps = 0.23\ iru. \tag{5.8}$$

$$\tag{5.9}$$

This estimate suggests that the contribution to the background from $^{42}Ar$ is completely negligible if compared to that associated with $^{39}Ar$. A similar consideration can be performed for $^{42}K$, daughter of $^{42}Ar$. It is a short living (12.36 *hours*) $\beta$-emitter with spectrum end-point at 3525.4 $keV$. The 18% of the decays occurs together with a 1524.7 $keV$ $\gamma$-emission. Due to its short half-life (if compared to that of the parent nuclide), the expected number of decays at equilibrium has to equal that of $^{42}Ar$, leading to a rate upper limit of $\approx 5 \cdot 10^{-6}$ *cps*, once the fraction of decays falling in the acceptance window is considered (0.33%) [110].

The last considered $\beta$-contaminant is represented by the $^{85}Kr$ isotope, half-life 10.7 *years*, $1.450 \times 10^4$ $GBq/g$ of specific activity and end point at 687.1 $keV$ (5.4% of the decays within the acceptance window) [110]. According to the results found in literature the typical activity of $^{85}Kr$ in air is of the order of 1 $Bq/m^3$ [112], roughly corresponding to $4 \times 10^{-15}$ $g\ of\ ^{85}Kr/g\ of\ ^{40}Ar$ in air. Due to the distillation process a successive reduction of this contami-

nation is expected essentially due to the significantly different boiling points (fraction distillation is usually used). This rough estimate leads to

$$140\ kg\ of\ ^{40}Ar \times \left(\rho \cdot 4 \cdot 10^{-15} \frac{g\ of\ ^{85}Kr}{g\ of\ ^{40}Ar}\right) \times \tag{5.10}$$

$$\times \left(1.45 \times 10^4\ \frac{GBq}{g\ of\ ^{85}Kr}\right) \times 0.054 \approx 4.7 \cdot \rho \times 10^2 cps \tag{5.11}$$

$$\tag{5.12}$$

where with $\rho$ has been indicated the reduction to contamination due to distillation process, whose filtering procedure should more effectively select the argon than the kripton. A typical $\rho$ value provided by distillation processes should be at least of the order of $10^{-3}$, making negligible this contribution to the background, once the high rejection power is considered. If this estimate will not be confirmed by specific measurements, an additional fractional distillation of argon may be required.

As far as $\gamma$ contamination of internal materials is concerned mainly uranium, thorium and Potassium decays (mosly contained in race-tracks structure and photomultipliers) dominates the low energy $\gamma$ background. The active anti-coincidence shield, which is supposed to veto all events in which there is an additional energy loss in the veto volume of the order of at least 7 $keV$ (for electrons recoils), plays a crucial role in the rejection of these $\gamma$-induced events as shown by the results of a dedicated Monte Carlo simulation. The output of the simulation can be summarized by the following qualitative considerations

- Low energy $\gamma$-rays ($\leqslant 40\ keV$) deposits their full energy in the sensitive volume through the photo-electric effect, dominating the $\gamma - Ar$ cross section in this energy range. These events are strongly peaked around the periphery of the sensitive volume and they can be eventually eliminated by a geometrical cut obtained by $x$-$y$ localization;

- Higher energy $\gamma$-ray events are detectable on the other hand by a Compton effect with a low energy electron recoil in the sensitive energy domain. However such events are very likely to produce additional Compton scatterings either in the way in or in the way out of the prescribed event. At high energies, the spatial distribution is uniform, but the anti-coincidence signature is very efficient in rejecting the associated events with the help of additional secondary collisions.

| *Energy* (keV) | *Energy threshold in the veto region* | |
|---|---|---|
| | 3 *keV* | 6 *keV* |
| 50 | $(7.7 \pm 0.2) \times 10^{-3}$ | $(7.7 \pm 0.2) \times 10^{-3}$ |
| 100 | $(2.74 \pm 0.05) \times 10^{-2}$ | $(2.75 \pm 0.05) \times 10^{-2}$ |
| 250 | $(1.60 \pm 0.13) \times 10^{-3}$ | $(1.61 \pm 0.13) \times 10^{-3}$ |
| 500 | $(1.2 \pm 0.3) \times 10^{-4}$ | $(1.2 \pm 0.3) \times 10^{-4}$ |
| 1000 | $(7 \pm 3) \times 10^{-5}$ | $(7 \pm 3) \times 10^{-5}$ |
| 1500 | $(2.0 \pm 1.4) \times 10^{-5}$ | $(2.0 \pm 1.4) \times 10^{-5}$ |
| 2000 | $(5 \pm 2) \times 10^{-5}$ | $(6 \pm 2) \times 10^{-5}$ |
| *Energy* (keV) | *Energy threshold in the veto region* | |
| | 9 *keV* | 12 *keV* |
| 50 | $(7.7 \pm 0.2) \times 10^{-3}$ | $(7.7 \pm 0.2) \times 10^{-3}$ |
| 100 | $(2.76 \pm 0.05) \times 10^{-2}$ | $(2.77 \pm 0.05) \times 10^{-2}$ |
| 250 | $(1.63 \pm 0.13) \times 10^{-3}$ | $(1.64 \pm 0.13) \times 10^{-3}$ |
| 500 | $(1.2 \pm 0.3) \times 10^{-4}$ | $(1.2 \pm 0.3) \times 10^{-4}$ |
| 1000 | $(7 \pm 3) \times 10^{-5}$ | $(7 \pm 3) \times 10^{-5}$ |
| 1500 | $(2.0 \pm 1.4) \times 10^{-5}$ | $(2.0 \pm 1.4) \times 10^{-5}$ |
| 2000 | $(6 \pm 2) \times 10^{-5}$ | $(6 \pm 2) \times 10^{-5}$ |

Table 5.6: The fraction of events $\gamma$-like producing a signal below 30 *keV* ($E_{ee}$) in the sensitive volume and no signal above threshold in the active veto (referred to the produced $10^5$ *photons*) for different energies and for several values of veto threshold.

As a proof of the above considerations, the results of the simulation is reported in the case of the events induced by emitted photons from the PMTs. The simulated geometry is displayed in Fig. 5.8 and described at the beginning of Sec. 5.2. For this specific computation, the photons source has been assumed as uniformly distributed all along the inner detector photomultipliers plane, positioned at 7 *cm* from the interface level. Seven different photons energies have been considered and $10^5$ photons for each energy value have been produced with random direction: the fraction of events producing a signal below 30 *keV* ($E_{ee}$ corresponding to $E_R \approx 100$ *keV*) in the sensitive volume and no signal above threshold in the active veto (within the coincidence window) are reported in Tab. 5.6 for different energies and for several values of veto threshold. The probability of occurrence of these events is contained in the range

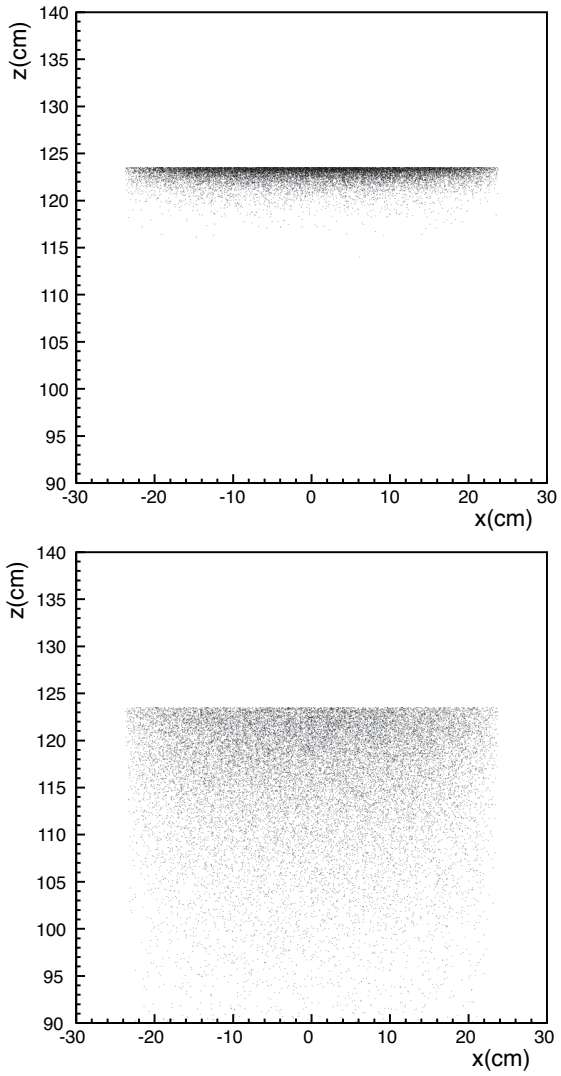


Figure 5.10: Spatial distributions of the events obtained simulating $\gamma$-rays emission from phototubes with energies 50 $keV$ (up) and 500 $keV$ (down). The liquid-gas interface level corresponds, in the used geometry, to $z = 123$ $cm$ while the cathode to $z = 60$ $cm$.

$2 \cdot 10^{-5} \div 3 \cdot 10^{-2}$ for the evaluated energies and obviously it is lower for higher energy photons. The maximum probability $3 \cdot 10^{-2}$ is obtained for 100 $keV$ photons: as stated above, for low energy $\gamma$-induced events the barycentre of the energy depositions is positioned on average in the peripheral region (in the case of 100 $keV$ $\gamma$-rays within 1 $cm$ from the interface). As example the

spatial distribution of the events induced by $\gamma$-rays from phototubes is displayed in Fig. 5.10 for photons energy of 50 $keV$ and 500 $keV$. Once again, assuming the contamination of materials summarized in Tab. 5.2 and using the indicative results obtained with the performed Monte Carlo, it is evident that those events induced by $\gamma$ contamination are efficiently rejected with the use of the veto and their associated background can be estimated as negligible if compared to that produced by $^{39}Ar$.

To conclude, in presence of passive and active shielding the dominant contribution comes from $^{39}Ar$ requesting a global rejection power (both $S2/S1$ and shape discrimination) of the order of $10^{-8}$ or $10^{-7}$ to reduce the $\beta$-events wrongly labeled as nuclear recoil respectively to less than 1 *event* in 100 *days* or 1 *event* in 10 *days*. In the eventuality of a further reduction of such events of more than two orders of magnitude, because of isotopic separation of the liquid Argon, other backgrounds may become dominant even in presence of an active anticoincidence veto. For this reason an overall rejection power of the $\gamma$-like background must be under any circumstance of the order of $10^{-4} \div 10^{-6}$ even in case of depleted argon.

### 5.2.2 Estimate of neutrons-induced background

As previously stated neutrons-induced nuclear recoils can perfectly mimic the signature within the inner detector expected for WIMP. The great difference is represented by the higher $n$-$Ar$ total cross section, implying an extremely higher probability of multiple interactions within the inner detector and veto volume and hence permitting the discrimination of a substantial fraction of those nuclear recoils induced by neutrons. The neutrons interacting within the sensitive volume could be emitted by contaminated internal materials or they could come from the external of the detector, being associated to environmental radioactivity.

The number of neutrons produced within the detector is mainly associated to spontaneous fission (SF) or ($\alpha$,n) reactions induced by uranium and thorium impurities contained within the internal materials or, alternatively, to those unstable nuclides eventually produced by cosmic rays within liquid argon volume. As far as thorium and uranium contamination is concerned, very strict requests have to be applied to all the internal materials: particular attention has to be given to the radiopurity of the vessel stainless steel (13 $ton$) and of lead and OHFC copper for the $\gamma$ shield (128 $ton$), represent-

| *Thickness of polyethylene (cm)* | *Energy threshold in the veto region* | |
|---|---|---|
| | 10 *keV* | 20 *keV* |
| 0.0 | $(1.24 \pm 0.08) \times 10^{-4}$ | $(2.0 \pm 0.1) \times 10^{-4}$ |
| 2.5 | $(8.2 \pm 0.6) \times 10^{-5}$ | $(1.30 \pm 0.08) \times 10^{-4}$ |
| 5.0 | $(4.4 \pm 0.5) \times 10^{-5}$ | $(5.8 \pm 0.5) \times 10^{-5}$ |
| 7.5 | $(1.4 \pm 0.3) \times 10^{-5}$ | $(2.3 \pm 0.3) \times 10^{-5}$ |
| 10.0 | $(9.5 \pm 0.3) \times 10^{-6}$ | $(1.4 \pm 0.3) \times 10^{-5}$ |
| 12.5 | $(8.0 \pm 0.2) \times 10^{-6}$ | $(1.0 \pm 0.2) \times 10^{-5}$ |
| *Thickness of polyethylene (cm)* | *Energy threshold in the veto region* | |
| | 30 *keV* | 40 *keV* |
| 0.0 | $(2.8 \pm 0.1) \times 10^{-4}$ | $(3.6 \pm 0.1) \times 10^{-4}$ |
| 2.5 | $(1.70 \pm 0.09) \times 10^{-4}$ | $(2.2 \pm 0.1) \times 10^{-4}$ |
| 5.0 | $(7.7 \pm 0.6) \times 10^{-5}$ | $(9.1 \pm 0.7) \times 10^{-5}$ |
| 7.5 | $(3.3 \pm 0.4) \times 10^{-5}$ | $(4.3 \pm 0.5) \times 10^{-5}$ |
| 10.0 | $(2.1 \pm 0.3) \times 10^{-5}$ | $(2.6 \pm 0.4) \times 10^{-5}$ |
| 12.5 | $(1.2 \pm 0.2) \times 10^{-5}$ | $(1.4 \pm 0.3) \times 10^{-5}$ |

Table 5.7: Number of events per emitted (fission) neutron from the cryostat with an energy deposition between 20-100 *keV* in the sensitive volume and below the threshold in the veto region.

ing, due to the large masses, the main internal sources of neutrons-induced background. For this reason an internal polyethylene shield, placed between the cryostat and the veto region, has been foreseen in order to reduce as much as possible the number of neutrons, emitted by the cryostat walls and by the shield and able to reach the inner sensitive volume. The effect, onto the spontaneous fission background component, of this internal shielding (for which different thicknesses have been implemented) and of the active veto have been simulated according to the geometry described in Sec. 5.2: a fission neutrons source uniformly distributed in the bulk of the cryostat walls and shield has been assumed. For each configuration $2 \times 10^6$ *neutrons* have been produced according to the typical fission spectrum of uranium and thorium chain and with random directions. The associated particles releasing energy in the internal volume are mainly neutrons and photons coming from neutron captures. The presence of the internal shielding obviously increases the

fraction of events due to photons. Within the total amount of events, only those producing an energy deposition in the sensitive volume of 20-100 $keV$, with an associated energy deposition below threshold in the veto region, are treated as background events. Obviously this evaluation is extremely conservative since this background category includes not only single nuclear recoils (representing the real background) but also neutron induced inelastic events and multiple events within the sensitive volume, respectively rejectable with the $S2/S1$ discrimination criterion or by topology of the signal (more than one secondary peak). Four different veto thresholds ($10 \div 40$ $keV$) have been considered. Obviously the number of background events decreases with the veto energy threshold, as shown in Tab. 5.7, summarizing the fraction of total produced events ($2 \times 10^6$ $neutrons$ for each configuration) satisfying the above described conditions. According to these results the probability that a fission neutron from the cryostat produces a background event varies in the range $8.0 \times 10^{-6} \div 3.6 \times 10^{-4}$, corresponding respectively to the better (12.5 $cm$ thick shielding and lowest veto threshold) and worst configurations (no shield and 40 $keV$ threshold in the anti-coincidence). Since the radiopurity of low background lead and copper is several order of magnitude better than that of the vessel stainless steel and since auto-absorption from lead is more effective, their contribution to the neutrons background can be neglected. Assuming a global stainless steel mass of 13 $ton$ (corresponding to the vessel and to the top flange), an uranium contamination of the order of that listed in Tab. 5.2 and the $^{238}U$ spontaneous fission branching ratio of $5.45 \times 10^{-7}$, the expected background rate associated with spontaneous fission neutrons from the vessel is of the order of 1 $event$ each $600 \div 27800$ $days$, according to the various veto threshold and shield thicknesses. A consistent fraction of these background events can be rejected by requesting a single secondary peak (resolved not multiple event). For the aim of the simulation two hits in the sensitive volume have been considered resolved if separated by at least 2 $cm$ in the $x$-$y$ plane or 0.5 $cm$ in the $z$ drift direction. The analysis of the 555 background events, obtained with the configuration foreseeing no shielding and 30 $keV$ veto threshold, has shown that 52% of the events undergoes to more than one interaction. Of the surviving ones, only a fraction of energy depositions will end up in single nuclear recoils (depending on the $n$-$Ar$ cross section for that specific neutron energy) while the remaining part will produced inelastic scattering effectively rejected by the particle discrimination techniques. According

| Source | *Energy threshold in the veto region* | |
|---|---|---|
| | 10 $keV$ | 20 $keV$ |
| Cathode | $(1.17 \pm 0.02) \times 10^{-2}$ | $(1.49 \pm 0.02) \times 10^{-2}$ |
| Cap | $(3.0 \pm 0.1) \times 10^{-3}$ | $(3.6 \pm 0.1) \times 10^{-3}$ |
| Source | *Energy threshold in the veto region* | |
| | 30 $keV$ | 40 $keV$ |
| Cathode | $(1.90 \pm 0.03) \times 10^{-2}$ | $(2.09 \pm 0.03) \times 10^{-2}$ |
| Cap | $(4.5 \pm 0.1) \times 10^{-3}$ | $(5.2 \pm 0.1) \times 10^{-3}$ |

Table 5.8: Number of background events (as defined in the text), per emitted (fission) neutron. For cathode and cap have been produced, for each configuration, $2 \times 10^5$ neutrons and $3.3 \times 10^5$ neutrons using the geometry without polythene shielding (whose presence is essentially not affecting the simulation).

to the adopted geometrical configuration of 10 $cm$ thick internal polyethylene shield and a veto threshold equal to 30 $keV$, the very conservative upper limit 1 *event* each 10000 *days* is obtained, before applying topological or $S2/S1$ discrimination.

A similar simulation has been performed to count for the contamination of the stainless steel used for cathode and cap (for gaseous gap enclosure), representing the majority of the inner detector structure mass. Differently from the above geometry no neutron shielding separates the sensitive volume from the neutron source, supposed as uniformly distributed in the core of the cap and cathode materials. As in the previous case, the background events are defined as those events releasing within the sensitive volume an energy in the range 20-100 $keV$ and an amount of energy below threshold within the veto volume: once again no cut on multiple interactions within the sensitive volume and on the nature of the neutrons induced events is considered (not only nuclear recoils are counted). The probability that an emitted neutron falls in the background region is summarized in Tab. 5.8 for different values of the veto threshold. Assuming for a mass of 6.3 $kg$ and 9.6 $kg$ respectively for cathode and cap, an uranium contamination of the order of that listed listed in Tab. 5.2 and the $^{238}U$ spontaneous fission branching ratio of $5.45 \times 10^{-7}$, the simulations suggest 1 *background event* each $22000 \div 40000$ *days* associated with cathode and 1 *background event* each $57800 \div 100000$ *days* associated

with cathode. As stated before this evaluation has to be considered as a conservative upper limits. According to these results probably more relaxed requests on stainless steel radiopurity can be applied.

Another possible internal neutron source is represented by those unstable nuclides, produced by cosmic rays interactions within the LAr itself, eventually leading to a delayed neutron emission. Those events, for which the neutron emission is coupled to the emission of another particle (such as $\gamma$ or $X - ray$ or $\alpha$'s), are effectively rejected due to the identification of multiple ionizations or by particle discrimination techniques. Of the surviving events only those ending-up in a single recoil without associated signal in the veto represent a possible background. One should note that due to the reduced cosmic rays rate in the underground laboratory (1 $m^{-2}$ $h^{-1}$) and to the dimension of the active veto, this background should be reduced to less than 1 *event* in 100 *days*. Nevertheless a detailed Monte Carlo simulation has to be implemented in order to correctly estimate such component.

The emission of neutrons within the inner detector may be also induced by material radioactivity through $(\alpha, n)$ reactions instead of spontaneous fission. The main $\alpha$-emitters contained in the selected material are, once again, part of the thorium and uranium chain. As a consequence, the intensity of this background contribution is function of the amount of uranium and thorium contained in the more abundant materials of the detector and of the $(\alpha, n)$ cross sections relative to these materials. Although a dedicated simulation should be developed to estimate this component of the neutrons-induced background, a rough evaluation of its order of magnitude can be computed as it follows. The more abundant materials contained in the core of the detector are represented by the argon itself and by the stainless steel of the vessel (lead, although abundant, is much less contaminated than stainless steel). If the $(\alpha, n)$ process occurs in liquid argon the signal associated to the emitted neutron, even in the case of a single recoil, will overlap that associated to the $\alpha$-particle ionization, leading to the rejection of the event itself. As far as stainless steel is concerned at a first approximation it could be treated as iron (its main component) for which the neutron yield for $(\alpha, n)$ reaction has been measured [113]. This work provides the number of emitted neutrons per incident $\alpha$-particle as function of the $\alpha$'s energy: since $(\alpha, n)$ reaction is a threshold process, it starts occurring in iron for $\alpha$ energies higher than 4.6 $MeV$. The value of the neutron yields for iron is listed in Tab. 5.9 for all the $\alpha$-emitters of the two

| *Uranium chain* | | | |
|---|---|---|---|
| $\alpha$-*emitters* | $\alpha$-*energy* ($MeV$) | *Neutron yield* (*neutrons per* $\alpha$) | *Total neutron yield* (*neutrons per* $\alpha$) |
| $^{238}U$ | 4.2 | *below thr.* | $5.6 \times 10^{-7}$ |
| $^{234}U$ | 4.7 | $1.6 \times 10^{-10}$ | |
| $^{230}Th$ | 4.6 | *below thr.* | |
| $^{226}Ra$ | 4.8 | $1.6 \times 10^{-10}$ | |
| $^{222}Rn$ | 5.5 | $5.9 \times 10^{-10}$ | |
| $^{218}Po$ | 6.0 | $4.2 \times 10^{-9}$ | |
| $^{214}Po$ | 7.7 | $5.5 \times 10^{-7}$ | |
| $^{210}Po$ | 5.3 | $2.8 \times 10^{-10}$ | |
| *Thorium chain* | | | |
| $\alpha$-*emitters* | $\alpha$-*energy* ($MeV$) | *Neutron yield* (*neutrons per* $\alpha$) | *Total neutron yield* (*neutrons per* $\alpha$) |
| $^{232}Th$ | 4.0 | *below thr.* | $1.6 \times 10^{-6}$ |
| $^{228}Th$ | 5.4 | $2.8 \times 10^{-10}$ | |
| $^{224}Rn$ | 5.7 | $2.1 \times 10^{-9}$ | |
| $^{220}Rn$ | 6.3 | $1.6 \times 10^{-8}$ | |
| $^{216}Po$ | 6.8 | $5.2 \times 10^{-8}$ | |
| $^{212}Bi$ (35%) | 6.0 | $4.2 \times 10^{-9}$ | |
| $^{212}Po$ (65%) | 8.8 | $2.4 \times 10^{-6}$ | |

Table 5.9: Neutrons yield produced by ($\alpha$,n) reaction in thick iron target [113] for the $\alpha$-emitters of the Uranium and Thorium chains. The relative intensities of the $\alpha$-lines referred to $^{238}U$ activity, when differing from 100%, are displayed in parenthesis. For the different nuclides only the dominant $\alpha$-energy is reported. Those emitters unable to induce ($\alpha$,n) reactions are indicated as *below thr.*. The total neutrons yield has been obtained by summing up the various contributions weighting them for the respective relative intensities. This value, multiplied for the $^{238}U$ and $^{232}Th$ activity in 1 $kg$ of iron (assuming the stainless steel contamination summarized in Tab. 5.2 and treating stainless steel as iron), provides a rough estimate of the total number of emitted neutrons induced by ($\alpha$,n) reactions per iron $kg$.

radioactive chains with energy above $(\alpha, n)$ threshold. Assuming the chains in secular equilibrium, a total mass of 13000 $kg$ of iron (representing the vessel) and a contamination equal to that presented in Tab. 5.2 for stainless steel, the

above values lead to a neutron production rate equal to $3.4 \times 10^{-5}$ $neutrons/s$ in the case of uranium and $1.3 \times 10^{-6}$ $neutrons/s$ for thorium chain. These neutrons are emitted in the bulk of the stainless steel vessel and, in order to effectively contribute to the background, they should overcome the internal 10 $cm$ polyethylene shielding and release from $20 - 100$ $keV$ in the inner detector without associated signals above threshold in the veto: in order to estimate the expected background rate, the probability that this occurs should be evaluated. As a first approximation it is quite intuitive to assume that this probability should not differ too much from that obtained simulating the propagation, within the detector, of the spontaneous fission neutrons from the same vessel (see Tab. 5.7). To be conservative a probability equal to $10^{-4}$ can be assumed (almost one order of magnitude higher than the value obtained for the simulated fission neutrons with the nominal conditions, 10 $cm$ thick shield and 30 $keV$ veto threshold). According to this rough estimate, the expected background rate associated to ($\alpha$,n) reactions in the vessel should be much lower than 1 $event$ each 100 $days$.

Another important component of the neutron-induced background is represented by those neutrons associated with natural environmental radioactivity and impinging onto the detector. Several measurements of the fast neutrons flux in LNGS halls have been performed [107, 114, 115]: they are almost consistent with an integrated total flux of the order of $0.7 \times 10^{-6}$ $cm^{-2}$ $s^{-1}$, for energies above 1 $MeV$. For the simulation of this background contribution, neutrons have been emitted in such a way to generate a uniform and isotropic fluence inside a sphere of 2.0 $m$ of radius surrounding the detector, with a flat energy spectrum in six different energy bins: 0-0.5 $MeV$, 0.5-1 $MeV$, 1-2 $MeV$, 2-4 $MeV$, 4-8 $MeV$ and 8-16 $MeV$. The expected background events for a unit incident flux ($event$ $cm^2$), releasing in the sensitive volume an energy between 20-100 $keV$, with an associated energy deposition below threshold in the veto region, is listed in Tab. 5.10 for the different neutrons energy groups, for different geometrical configurations (with and without an internal polyethylene shield of different thicknesses) and as function of several veto thresholds. As evident from the results, the role of the internal shielding, positioned between the neutrons source and the detector, is once again determinant: the presence of a 5 or 10 $cm$ thick polyethylene shield reduces the expected total number of background events of one or two order of magnitude for neutrons in the range $0 \div 1$ $MeV$, making their associated background neg-

| *No shield* | | | | |
|---|---|---|---|---|
| *Energy group* | *Energy threshold in the veto region* | | | |
| $(MeV)$ | 10 $keV$ | 20 $keV$ | 30 $keV$ | 40 $keV$ |
| $0-0.5$ | $31.7 \pm 1.4$ | $51.0 \pm 1.8$ | $73.3 \pm 2$ | $95.3 \pm 2$ |
| $0.5-1.0$ | $34.1 \pm 1.5$ | $48.8 \pm 1.8$ | $61.4 \pm 2$ | $75.3 \pm 2$ |
| $1.0-2.0$ | $3.2 \pm 0.5$ | $4.7 \pm 0.5$ | $7.0 \pm 0.7$ | $9.6 \pm 0.8$ |
| $2.0-4.0$ | $0.7 \pm 0.2$ | $1.2 \pm 0.3$ | $1.8 \pm 0.3$ | $2.2 \pm 0.4$ |
| $4.0-8.0$ | $1.0 \pm 0.2$ | $1.4 \pm 0.3$ | $2.0 \pm 0.3$ | $2.3 \pm 0.4$ |
| $8.0-16.0$ | $0.9 \pm 0.2$ | $1.3 \pm 0.3$ | $1.6 \pm 0.3$ | $1.7 \pm 0.3$ |
| 5 *cm thick shield* | | | | |
| *Energy group* | *Energy threshold in the veto region* | | | |
| $(MeV)$ | 10 $keV$ | 20 $keV$ | 30 $keV$ | 40 $keV$ |
| $0-0.5$ | $1.3 \pm 0.4$ | $2.2 \pm 0.5$ | $2.9 \pm 0.6$ | $3.3 \pm 0.6$ |
| $0.5-1.0$ | $3.9 \pm 0.7$ | $7.0 \pm 0.9$ | $8.2 \pm 1.0$ | $9.6 \pm 1.1$ |
| $1.0-2.0$ | $3.2 \pm 0.6$ | $4.9 \pm 0.8$ | $6.5 \pm 0.9$ | $8.1 \pm 1.0$ |
| $2.0-4.0$ | $2.2 \pm 0.5$ | $3.7 \pm 0.7$ | $4.7 \pm 0.8$ | $5.8 \pm 0.9$ |
| $4.0-8.0$ | $1.1 \pm 0.4$ | $1.6 \pm 0.5$ | $3.0 \pm 0.6$ | $3.8 \pm 0.7$ |
| $8.0-16.0$ | $1.9 \pm 0.5$ | $2.4 \pm 0.5$ | $2.5 \pm 0.6$ | $3.2 \pm 0.6$ |
| 10 *cm thick shield* | | | | |
| *Energy group* | *Energy threshold in the veto region* | | | |
| $(MeV)$ | 10 $keV$ | 20 $keV$ | 30 $keV$ | 40 $keV$ |
| $0-0.5$ | $< 0.1$ | $< 0.1$ | $< 0.1$ | $< 0.1$ |
| $0.5-1.0$ | $0.5 \pm 0.2$ | $0.6 \pm 0.3$ | $0.6 \pm 0.3$ | $0.8 \pm 0.3$ |
| $1.0-2.0$ | $1.5 \pm 0.4$ | $1.8 \pm 0.5$ | $2.2 \pm 0.5$ | $2.4 \pm 0.6$ |
| $2.0-4.0$ | $1.9 \pm 0.5$ | $2.5 \pm 0.6$ | $3.5 \pm 0.7$ | $4.0 \pm 0.7$ |
| $4.0-8.0$ | $1.6 \pm 0.5$ | $2.3 \pm 0.5$ | $2.6 \pm 0.6$ | $3.3 \pm 0.6$ |

Table 5.10: Expected background events for a unit incident flux ($event\ cm^2$) with an energy deposition between $20-100$ $keV$ in the sensitive volume and below the threshold in the veto region, for the different energy bins and for the geometries with and without shield (5 and 10 $cm$ thick). The simulation has been performed generating $2 \times 10^6$ neutrons for the geometry without the internal shield and $1 \times 10^6$ for the geometries foreseeing the shielding. The effect of the polyethylene shield is evident: the number of background events associated with the $0-1$ $MeV$ component of the flux is reduced of one and two order of magnitude, with 5 and 10 $cm$ shield.

ligible. As far as neutrons above 1 $MeV$ is concerned, a rough estimate of the expected background in presence of the internal shield can be obtained assuming a relative weight between the energy groups. On the basis of the results

presented in Ref. [107], an equal weight has been assumed for the three energy groups in the range 1-8 $MeV$ while the contribution to the flux of the group above 8-16 $MeV$ has been set to zero. In other words the total integrated flux has been assumed as constituted only by 1-8 $MeV$ neutrons. The resulting estimated background consist of 1 *event* in 0.9 *days* or in 2.5 *days* for the 5 *cm* thick shield geometry and 1 *event* in 1.7 *days* or in 3.3 *days* for the 10 *cm* configuration. Once again this background rates have been evaluated without requesting nuclear recoils or single event in the sensitive volume and hence they have to be considered as very conservative upper limits. One should ulteriorly note that the computation have been evaluated just in presence of an internal shield: the projected geometry for the 100 $l$ detector foresees a 10 *cm* thick internal shield coupled with an external 70 *cm* thick polyethylene shield. This double shielding will obviously drop down this background component making it negligible with respect to neutrons produced internally.

According to the performed simulations, the number of recoils induced by neutrons, from internal contamination or external environmental radioactivity, is expected to be reduced, with the help of internal and external neutron shields (respectively 10 and 70 *cm* thick), of the liquid argon active veto region (60 *cm* thick) and of the sensitive volume cuts (removing the peripheral region directly facing the contaminated materials), to less than 1 *event* in 100 *days*. Nevertheless a more specific simulation representing the detailed proposed geometry has to be implemented to confirm or even lower such limit.

### 5.2.3 Estimate of neutrinos-induced background

The last investigated possible source of background is represented by those nuclear recoils induced by neutrino-nucleus elastic scattering [116] represented symbolically by the reaction

$$\nu + (A, Z)_{at\ rest} \rightarrow \nu + (A, Z)_{recoil} \tag{5.13}$$

where $A$ is the target nucleus, with $N$ neutrons and $Z$ protons (with atomic mass $M_T$), and the neutrino has momentum $p_\nu$. The cross section of this process, for $\sin(\theta_\omega) \approx 1/4$, is essentially proportional to $N^2$ [116], with only the vector current contributing. Neglecting the effects associated to the nuclear form factor, the differential cross section in terms of the momentum transfer

to the nucleus $q^2 = 2 \cdot M_T E_R$ is given by

$$\frac{d\sigma}{dq^2} = \frac{G^2}{8\pi} N^2 \left[1 - \frac{q^2}{q^2_{max}}\right] \qquad q^2_{max} = 4p^2_\nu. \tag{5.14}$$

The cross section applies to all neutrino species equally. In such approximation the integrated cross section and the maximum recoil energy are given by

$$\sigma \approx 0.42 \times 10^{-44} N^2 \left(\frac{p_\nu}{1MeV}\right)^2 \qquad E_R^{max} = \frac{2}{A}\left(\frac{p_\nu}{1MeV}\right)^2 keV \tag{5.15}$$

According to a Monte Carlo simulation implemented with the Fluka Package, the above cross section, folded in with the solar neutrino spectrum [116, 117], provides the following approximate rates: 3.5 *evenets/ton/day* for *p-p* neutrinos ($E_R^{max} \approx 8.4\ eV$), 0.23 *events/ton/day* for $^8B$ neutrinos ($E_R^{max} \approx 11.25\ keV$) and 0.0063 *events/ton/day* for pep and hep neutrinos. The predicted recoil spectrum is a fast falling function of $E_R$, as shown in Fig. 5.11. Therefore with an appropriate minimum threshold in the recoil energy, background events due to solar neutrinos are effectively rejected.

The total cosmic neutrinos flux has been estimated to be [117]

$$\phi \approx 11.5\ cm^{-2}s^{-1}. \tag{5.16}$$

Cosmic neutrinos present higher energies, in the region of *hundreds of MeV*. Therefore for recoils within the acceptance window, the approximation holds and the differential cross section 5.15 predicts a recoil spectrum practically flat in energy, almost independent from the neutrino momentum $p_\nu$ and equal, for argon, to

$$\frac{d\sigma}{dE_R} = 0.42 \times 10^{-44} N^2 A\ cm^2 keV^{-1} = 0.81 \times 10^{-40}\ cm^2 keV^{-1}. \tag{5.17}$$

Introducing the previously omitted nuclear form factor $F^2(q^2)$, the number of recoil events above a preset threshold and with $E_R < 80\ keV$ (for this evaluation this upper limit has been assumed) is given by

$$\int_{E_R^{th}}^{80\ keV} E_R \cdot \frac{d\sigma}{dE_R} \cdot F^2(2M_{Ar}E_R) \cdot \phi \cdot N\ dE_R \tag{5.18}$$

where $N$ is the numeric density of $Ar$ atoms per unit mass. The solution of the above equation, as function of recoil threshold energy $E_R^{th}$, is plotted in Fig. 5.11.

The irreducible neutrino associated background within the recoil energy

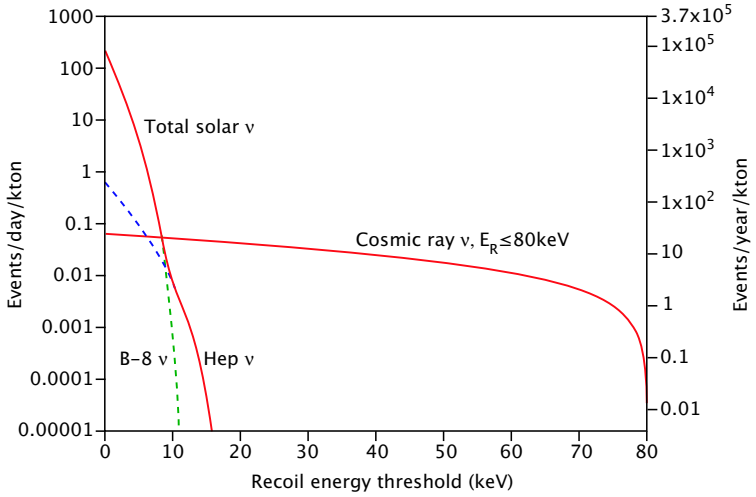


Figure 5.11: Irreducible background rates due to solar and cosmic neutrinos, as a function of the detection threshold. In the case of the cosmic neutrinos, which exhibit an essentially flat recoil energy distribution, an upper limit in the detection $E_R < 80\ keV$ has been introduced, in order to delimit the useful energy range for a *WIMP* search. The solar neutrinos from the main *p-p* cycle is not shown, since their recoil energies are in the region of a few $eV$.

window suitable for a *WIMP* search ($30\ keV \leq E_R \leq 100\ keV$) is of the order of $few\ 10^{-6}\ ev/day$ in the case of 140 $kg$ of argon. Obviously a decrease of the detection threshold, eventually achievable by the means of more performing phototubes producing a higher photoelectrons yield, would increase the neutrino background.

## 5.3 Projected experimental sensitivity

On the basis of the rough estimate of the background above performed and recalling the calculation of Sec. 2.4 it is possible to evaluate the projected sensitivity for the 100 $l$ WARP detector. As stressed before the dominant background is represented by $^{39}Ar$ contamination and, according to the achieved rejection power, it can be kept to a rate from 1 *to* 10 *events in* 100*days*. As far as the other background sources it seems possible to keep them at a level of less than 1 *event in* 100 *days*. As shown in Sec. 2.3, if no background sub-

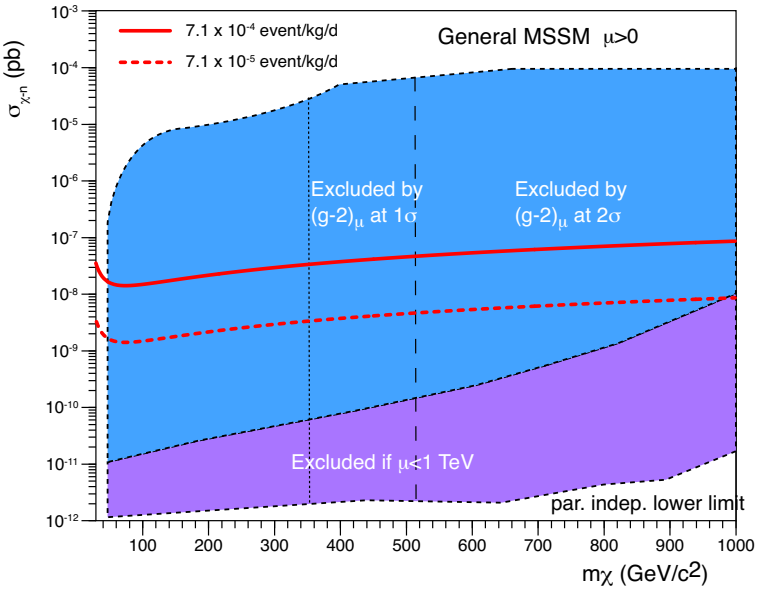


Figure 5.12: Expected maximum sensitivity curves, expressed as iso-rate curves in the $\sigma_{\chi\text{-}n}$-$m_\chi$ parameter space, in the hypothesis of a detection threshold $E_R = 30\ keV$ and an upper limit $E_R = 100\ keV$. The curves are obtained following the calculations shown in Sec. 2.2 and in caption of Fig. 2.6. The iso-rate curves corresponding to $7.1 \times 10^{-4}$ *iru* (unbroken red line) and $7.1 \times 10^{-5}$ *iru* (dashed red line) are indicated. For comparison, the allowed region of Fig. 2.3 is also reported.

traction techniques are applied[12], the sensitivity of the experiment is inferiorly limited by the background rate itself: this means, in the case of the proposed WARP detector, that the projected maximum sensitivity is of the order of $7.1 \times 10^{-5} ev\ kg^{-1}\ d^{-1}$ (1 *event in* 100 *days*) if a rejection power of $10^{-8}$ is obtained and of $7.1 \times 10^{-4} ev\ kg^{-1}\ d^{-1}$ (10 *event in* 100 *days*) if rejections of about $10^{-7}$ are achieved. The corresponding sensitivity curves, expressed as iso-rate curves in the spin-independent space parameters, are shown in Fig. 5.12. In the framework of spin-independent interaction, *these sensitivities correspond to the possibility of exploring WIMP-nucleon cross sections down to* $10^{-8} \div 10^{-9}$ *pb, approximately two order of magnitude lower than actual experimental limits.*

[12] In principle, since the main source of background is represented by $^{39}Ar$ whose spectrum is known, a background subtraction could be used to improve the sensitivity once reached the background rate (see Sec. 2.3).

# Bibliography


[1] R. M. Wald, *General Relativity*, Ed. University of Chicago Press;

[2] M.S. Turner & E.W. Kolb, *The early Universe (Frontiers in Physics)* (1990);

[3] P. Salucci, M. Persic, *ASP Conf. Ser. 117: Dark and Visible Matter in Galaxies and Cosmological Implications*, Brigham Young University, Provo UT (1997), 1-27;

[4] G. Jungman, M. Kamionkowski, K. Griest, *Phys. Rep.* **267** (1996), 195;

[5] B. Fuchs, astro-ph/9812048 (1998);

[6] M. Roncadelli, *Aspetti Astrofisici della Materia Oscura*, Ed. Bibliopolis (2004);

[7] M. Girardi *et al.*, *Astrophys. J.* **505** (1998), 74;

[8] H. Katayama, K. Hayashida, astro-ph/0405363 (2004);

[9] H. Bohringer, *Conference Proceedings Dark '96*, Ed. World Scientific (1997), 64;

[10] P. de Berbardis *et al.*, *Astrophys. J.* **564** (2002), 559;

[11] C. L. Bennett *et al.*, *Astrophys. J.* **583** (2003), 1;

[12] A. Balby *et al.*, *Astrophys. J.* **545** (2000), L1;

[13] A.G. Riess *et al.*, *Astron. J.* **116** (1998), 1009;

[14] S. Perlmutter *et al.*, *Astrophys. J.* **517** (1999), 565;

[15] R. R. Caldwell, R. Dave, P. J. Steinhardt,*Phys. Rev. Lett.* **80** (1998), 1582;

[16] R.J. Scherrer & M.S. Turner, *Phys. Rev. D* **33** (1986);

[17] D.N. Schramm *et al.*, *Rev. Mod. Phys.* **70** (1998), 303;

[18] R. Partridge, *3K: the cosmic microwave background radiation (Cambridge Astrophysics)* (1995);

[19] M. Merrifield, *Astron. J.* **103** (1992), 1552;

[20] M. W. Goodman, E. Witten, *Phys. Rev. D* **31** (1985), 3059;

[21] D. Dixon *et al.*, *New Astronomy* **3** (1998), 539;

[22] J. Ahrens *et al.*, *Phys. Rev. D* **66** (2002), 32006;

[23] S. Orito *et al.*, *Phys. Rev. Lett.* **84** (2000), 1078;

[24] J.D. Lewin, P.F. Smith, *Astropart. Phys.* **6** (1996), 87;

[25] R.H. Helm, *Phys. Rev.* **104** (1956), 1466;

[26] Y.G. Kim, T. Nihei, L. Roszkowski and R. Ruiz de Austri, *JHEP* **0212** (2002), 034;

[27] S. R. Golwala, Ph.D. Thesis, Univ. of Berkeley (2000);

[28] M. Altmann *et al.*, astro-ph/0106314 (2001);

[29] L. Baudis *et al.*, *Phys. Rep.* **307** (1998), 291;

[30] D. S. Akerib *et al.*, *Phys. Rev. Lett.* **93** (2004), 211301;

[31] V. Sanglard *et al.*, astro-ph/0503265 (2005);

[32] J. C. Barton *et al.*, *4th Int. Workshop on Identification of Dark Matter*, Ed. World Scientific (2003), 302;

[33] R. Bernabei *et al.*, *Int. J. Mod. Phys. D* **13** (2004), 2127;

[34] R. Bernabei *et al.*, *Phys. Lett. B* **389** (1996), 757;

[35] R. Bernabei *et al.*, *Phys. Lett. B* **480** (2000), 23;

[36] G. Angloher *et al.*, *Astropart. Phys.* **23** (2005), 325;

[37] R. Bernabei *et al.*, *Nucl. Phys. B (Proc. Suppl.)* **138** (2005), 48;

[38] D. B. Cline *et al.*, *4th Int. Symp. Sources and Detection of Dark Matter/Energy in the Universe*, Ed. Springer (2001), 453;

[39] J. V. Dawson *et al.*, *4th International Heidelberg Conference On Dark Matter In Astro and Particle Physics*, Ed. Springer (2002), 485;

[40] Y. Takeuchi, *ICHEP 04: 32nd International Conference on High Energy Physics*, Beijing, China (2004);

[41] Brunetti *et al.*, *WARP: Wimp Argon Programme* Experimental proposal, LNGS P 36/04 (2004), see also webpage http://warp.pv.infn.it; R. Brunetti *et al.*, *WARP liquid argon detector for dark matter survey*, to be published in the Conference proceedings of the *DM2004, the 6th UCLA Symposium on Sources and Detection of Dark Matter in the Universe*, Marina del Rey (2004); Brunetti *et al.*, *WARP: a wimp double phase Argon detector*, to be published in the Conference proceedings of the *IDM2004: 5th International Workshop on the Identification of dark matter*, Edimburgh (2004);

[42] P. Benetti *et al.*, *Nucl. Instr. and Meth. A* 327 (1993) 203;

[43] Icarus Collaboration, ICARUS I: *An Optimized Real Time Detector of Solar Neutrinos*, Experiment Proposal, LNF-89/005(R) (1989); S. Amerio *et al.*, *Design, construction and tests of the ICARUS T600 detector*, *Nucl. Instr. and Meth. A* **527** (2004), 329;

[44] A.F. Borghesani *et al.*, *J. Phys. Condes. Matter* **9** (1997), 5057;

[45] L. S. Miller *et al.*, *Phys. Rev.* **166** (1968), 871;

[46] M. Mijajima *et al.*, *Phys. Rev. A* **9** (1974),1438;

[47] T. Doke, K. Masuda, *Nucl. Instr. and Meth. A* **420** (1999), 62;

[48] W. R. Leo, *Techniques for Nuclear and Particle Physics Experiment*, Ed. Springer;

[49] J. Lindhard *et al.*, *Mat. Fys. Medd. Dan. Vid. Selsk.* **33** n. 10 (1963); J. Lind-hard *et al.*, *Mat. Fys. Medd. Dan. Vid. Selsk.* **33** n. 14 (1963);

[50] W. P. Jesse, J. Saduaskis, *Phys. Rev.* **90** (1953), 1120;

[51] J.A. Phipps, *Phys. Rev.* **135** (1964), A36;

[52] G. L. Cano, *Phys. Rev.* **169** (1968), 277;

[53] R. L. Platzman, *Int. J. Applied Radiat. and Isot. Vol.* **10** (1961), 116;

[54] T. Takahashi *et al.*, *Phys. Lett. A* **44** (1973), 123;

[55] M. J. Berger, J. S. Coursey and M. A. Zucker, *Stopping-Power and Range Tables for Electrons, Protons, and Helium Ions*, http://physics.nist.gov/PhysRefData/Star/Text/contents.html;

[56] R.T. Scalettar, *Phys. Rev. A* **25** (1982), 2419;

[57] E. Shibamura *et al.*, *Jpn. J. Appl. Phys.* **34** (1995), 1897;

[58] S. Amoruso *et al.*, *Nucl. Instr. and Meth. A* **523** (2004), 275;

[59] G. Jaffé, Ann. Phys. 42 (1913), 303; G. Jaffé, *Phys. Rev.* **58** (1940), 968;

[60] L. Onsager, *Phys. Rev.* **54** (1938), 554;

[61] J. Thomas and D.A. Imel, *Phys. Rev. A* **36** (1987), 614;

[62] J. Thomas and D.A. Imel, *Phys. Rev. A* **38** (1988), 5793;

[63] S. Kubota *et al.*, *Phys. Rev. B* **20** (1979) 3486;

[64] E. Shibamura *et al.*, *Nucl. Instr. and Meth. A* **260** (1987), 437;

[65] S. Kubota *et al.*, *Phys. Rev. B* **17** (1978) 2762;

[66] T. Doke *et al.*, *Nucl. Instr. and Meth. A* **291** (1990), 617;

[67] M. Suzuki *et al.*, *Nucl. Instr. and Meth. A* **327** (1993), 67;

[68] G. Bressi *et al.*, *Phys. Lett. A* **278** (2001) 280;

[69] T. Doke *et al.*, *Nucl. Instr. and Meth. A* **269** (1988), 291;

[70] A. Hitachi *et al.*, *Phys. Rev. B* **46** (1992), 11463;

[71] A. Hitachi *et al.*, *Phys. Rev. A* **35** (1987), 3956;

[72] A. Hitachi, A. Mozumder, *Proceedings of 46th Japan. Soc. Radiation Chemistry*, Hakon (2003), 148;

[73] A. Hitachi, *Proceedings of IDM2004*, Edinburgh (2004);

[74] A. Hitachi *et al.*, *Phys. Rev. B* **27** (1983), 5279;

[75] O. Cheshnovsky *et al.*, *J. Chem. Phys.* **57** (1972), 4628;

[76] E. Conti *et al.*, *Nucl. Instr. and Meth. A* **382** (1996), 475;

[77] S. Kubota *et al.*, *Phys. Rev. B* **13** (1976), 1649;

[78] T. Doke *et al.*, Chem. *Phys. Lett.* **115** (1985), 164;

[79] A. Hitachi *et al.*, *Phys. Rev. B* **46** (1992), 540;

[80] P. Cennini *et al.*, *Nucl. Instr. and Meth. A* **345** (1994), 230;

[81] E.M. Gushchin *et al.*, *Sov. Phys. JETP* **55** (1982);

[82] A.F. Borghesani *et al.*, *Phys. Rev. A* **149** (1990), 481;

[83] B.A. Dolgoshein *et al.*, *JETP Lett.* **11** (1970), 513; B.A. Dolgoshein *et al.*, *Fyz. Elem. Chastits At. Yadra* **4** (1973), 167 [*Sov. J. Part. Nucl.* **4** (1973), 70];

[84] A.I. Bolozdynya, *Nucl. Instr. and Meth. A* **422** (1999), 314; A.I. Bolozdynya, IEEE Trans. Nucl. Sci. **42** (1995), 565;

[85] D.F. Anderson, *Nucl. Instr. and Meth. A* **261** (1987), 445;

[86] F. Sauli, CERN Yellow Book 77-09 (1977);

[87] K. Masuda *et al.*, *Nucl. Instr. and Meth.* **160** (1979), 247;

[88] C. M. B. Monteiro, *IEEE Trans. Nucl. Sci.* **48** (2001), 1081;

[89] A. Bondar, *Nucl. Instr. and Meth. A* **524** (2004), 130;

[90] Air Liquide, *Gas Encyclopaedia*, Ed. Elsevier (2002);

[91] M. Ichige *et al.*, *Nucl. Instr. and Meth. A* **327** (1993), 144;

[92] P. Benetti *et al.*, *Nucl. Instr. and Meth. A* **505** (2003), 89;

[93] , Hamamatzu Photonics K. K., *Photomultiplier tube*, Japan (1994);

[94] D. N. McKinsey *et al.*, *Nucl. Instr. and Meth. B* **132** (1997), 351;

[95] C. H. Lally, *UV Quantum efficiences of Organic Fluors*, Imperial College Internal Note IC/HEP/94-11 (1994);

[96] M. C. Prata *et al.*, *Characterization of ETL 9357FLA Photomuliplier Tubes for Cryogenic Temperature Applications*, Internal Note of the Department of Nuclear and Theoretical Physics FNT/AE 04/23 (2004);

[97] O. Bunemann *et al.*, *Can. J. of Res.* **27**, 191;

[98] P.L. Beach, R.W. Finlay, R.L. Cassola and R.D. Koshel, *Phys. Rev.* **156** (1967), 1201.

[99] *JENDL 3.3 Database from URL http://wwwndc.tokai.jaeri.go.jp/jendl/j33/j33.html*;

[100] R. Veenhof, CERN (EP) and GSI (Darmstadt, Germany), *Garfield 8.0*;

[101] Sodern, *Mod. Genie 16T, Computerized Command Version, Manual n. 4011 143 6934 0C*, 584;

[102] R. Feynman, R. B. Leighton and M. Sand, *The Feynman: Lectures on Physics*, Publ. Addison-Wesley;

[103] P. Benetti *et al.*, *A test of Polytetrafluoroethylene (PTFE) reflector for LXe proportional scintillation detector*, Icarus internal note (1994);

[104] H. H. Loosli, *Earth and Planetary Science Letters* **63** (1983), 51;

[105] A. Fass, A. Ferrari, J. Ranft and P. Sala, *FLUKA a Monte Carlo simulation Package*;

[106] G. Heusser *et al.*, *Low-level germanium gamma spectroscopy at the microBq level and future developments towards higher sensitivity*, to be published in the IAEA Conference proceedings of the *International Conference on Isotopes in Environmental Studies*, Monaco (2004), by Elsevier as special issue of "The science of the total environment";

[107] F. Arneodo *et al.*, *Il Nuovo Cimento A* **8** (1999), 819;

[108] C. Arpesella *et al.*, *Astropart. Phys.* **18** (2002), 1;

[109] A. Esposito, *Laboratori di Frascati Internal Note* LNF-86/60(R) (1986); *Nucl. Phys. B (Proc. Suppl.)* **28** (1992), 420;

[110] L. P. Ekstrm and R. B. Firestone, *WWW Table of Radioactive Isotopes, database version 2/28/99 from URL http://ie.lbl.gov/toi/index.htm*;

[111] V. D. Ashitkov *et al.*, *Nucl. Instr. and Meth. A* **416** (1998), 179;

[112] J. A. Formaggio, C.J. Martoff, *Annu. Rev. Nucl. Part. Sci.* **54** (2004), 361;

[113] R. Heaton *et al.*, *Nucl. Instr. and Meth. A* **276** (1989), 529;

[114] P. Belli *et al.*, *Il Nuovo Cimento A* **101** (1989), 959;

[115] P. Rindi *et al.*, *Nucl. Instr. and Meth. A* **272** (1988), 871;

[116] D.Z. Freedman, *Phys. Rev. D* **9** (1974) 1389; A. Drukier and L. Stodolsky, *Phys. Rev. D* **30** (1984) 2295; J.N. Bachall, *Neutrino Astrophysics*, Cambridge University Press, 1990;

[117] G. Battistoni *et al.*, *Astropar. Phys.* **19** (2003), 269;